# 論文 / 著書情報
# Article / Book Information

| | |
|---|---|
| 題目(和文) | 地盤材料の粒子破砕による時間依存挙動に関する基礎的研究 |
| Title(English) | Time-dependent behavior of geomaterials due to particle crushing |
| 著者(和文) | 武井正孝 |
| Author(English) | |
| 出典(和文) | 学位:博士(工学),<br>学位授与機関:東京工業大学,<br>報告番号:甲第4686号,<br>授与年月日:2001年3月26日,<br>学位の種別:課程博士,<br>審査員:日下部 治 |
| Citation(English) | Degree:Doctor (Engineering),<br>Conferring organization: Tokyo Institute of Technology,<br>Report number:甲第4686号,<br>Conferred date:2001/3/26,<br>Degree Type:Course doctor,<br>Examiner: |
| 学位種別(和文) | 博士論文 |
| Type(English) | Doctoral Thesis |

# TIME-DEPENDENT BEHAVIOR OF GEOMATERIALS

# DUE TO PARTICLE CRUSHING

Masataka Takei

March 2001

# ABSTRACT

This dissertation is entitled "**Time-dependent behavior of geomaterials due to particle crushing**" and consists of 7 chapters.

In Chapter 1, entitled "**Introduction**", the backgrounds and objectives of this study are explained. Time-dependent behavior of geomaterials may be due to 1)primary consolidation, 2)creep behavior of geomaterials themselves and 3)particle crushing. The main literatures dealing with the facts that particle crushing of geomaterials and indicating the time-dependent behavior due to particle crushing were reviewed. Time-dependent behavior due to particle crushing is considered to progress by occurring a chained-event of "particle crushing" and subsequent "rearrangement of fragments" and "stress redistribution". From the literature review, the author indicates that detailed mechanism of time-dependent behavior due to particle crushing has not been clarified. To clarify the detailed mechanism and modeling of the phenomena are the purposes of this study.

In Chapter 2, entitled "**Observations of time-dependent settlement of plate loading tests on weathered granite ground**", reappraisals of plate loading tests conducted on weathered granite grounds were performed. Occurrence of particle crushing beneath the plate had already been confirmed by observation of a polarization-microscope. From the results of the reappraisal, time-dependent settlement of the plate was observed in each loading stage, and it was proportional to the common logarithm of time. The gradient of the settlement – log time curve increased with increasing of sustained load. Relationships between the gradient, that is called the rate of creep settlement, and soil parameters were also investigated.

In Chapter 3, entitled "**Properties of crushable materials and single particle crushing tests**", firstly, four types of crushable materials used in experiments of Chapters 4 and 5 (cylindrical chalk bar, cylindrical talc bar, glass bead and quartz particle from weathered granite ground) were introduced. Secondly, single particle crushing tests of the crushable materials were performed in order to obtain basic information about particle crushing and rearrangement. Crushing strength and characteristic initial stiffness of each crushable particle were estimated from the tests. Statistical values (mean value and standard deviation)

of the strength and the stiffness were calculated. The crushing behavior during the test was different according to the materials. The crushing strength of the four crushable materials could be explained by the Weibull distribution. The statistical trends of a numbers of fragments after crushing were also discussed.

In Chapter 4, entitled "**Time-dependent behavior of four crushable materials in one-dimensional compression tests**", one-dimensional compression tests of the four crushable materials were conducted in order to clarify the mechanism of time-dependent behavior due to particle crushing. In the tests of chalk bar specimen and talc bar specimen, particle crushing phenomena were visualized by using the specimen in which the chalk bars or talc bars were plied up two-dimensionally. From the observations, it was verified that the time-dependent compression due to particle crushing is, in general, stemmed from progressive nature of a chained-event of "particle crushing" and subsequent "rearrangement of particles" and "stress redistribution" under the condition of one-dimensional compression. It was found that the detailed mechanism of each event for the four materials was different, depending upon the crushing characteristics of single particle.

In the case of chalk bar specimen, in order to clarify the amount of component of particle crushing, the measured compression strain of the specimen were separated into instantaneous strain, strain due to material creep and other strain that means the strain due to particle crushing. Creep tests of a single chalk bar were used for the separation. From the results of the separation, the amount of the compression strain due to particle crushing was significant in the loading stage near the yield load.

In Chapter 5, entitled "**Model footing loading tests on chalk bar ground**", footing loading tests were conducted on model ground made of chalk bars in order to discuss the mechanism of time-dependent behavior due to particle crushing as an example of boundary value problems. Visualization of crushing phenomena in the model ground was attempted as well as the one-dimensional compression test of chalk bar specimen. From the tests, it was verified that the footing settled time-dependently, and the settlement would be due to the chained-event. However, crack openings were observed in some crushed chalk bars under a sustained load of each loading stage. It is considered that the crack opening would be caused by gradual collapsing of the angular edges formed in crushed chalk bars, and that the small confining contact forces around a crushed chalk bar enabled the crack opening.

In Chapter 6, entitled "**Modeling of crushing phenomena and analysis by distinct element method**", a modeling method was proposed for analyzing the time-dependent behavior due to particle crushing, then the one-dimensional compression test of chalk bar specimen was analyzed by distinct element method (DEM) that the proposed model was included. A crushable particle was modeled by an aggregate of rigid micro particles connected each other with a bonding strength, and the contact constitutive model between rigid particles did not include viscous effect. The values of parameters of the contact constitutive model and the bonding strength were determined by analyses of the single particle crushing test that were repetitively performed. From the analysis of one-dimensional compression test, it was clarified that the proposed model could represent the chained-event and that the progresses of the chained-event involved a time interval, though the time interval was very short. More investigations would be required to determine the values of parameters used in the analyses.

In Chapter 7, entitled "**Conclusions**", the conclusions of this dissertation were drawn, and the subjects for future studies were explained.

CONTENTS

# CHAPTER 1

# INTRODUCTION

## 1.1 Background of this study

In traditional soil mechanics, it has been assumed that soil particles are rigid and not crushed. Under the assumptions, it has been considered that compression or shear deformation of soil occurs resulting from deformation or breakdown of soil skeleton.

On the other hand, to be described later, crushing phenomenon of soil particles has been recognized from as early as 1960's. However, the particle crushing has been treated as peculiar phenomenon in traditional soil mechanics. The reason is that the traditional soil mechanics has covered the soils composed of hard particles such as silica sand, and that the magnitude of stress applied to ground by structures has been low levels of about 0.1MPa to 10MPa.

But, in recent years, particle crushing is recognized as usual phenomenon in soil mechanics. Soil mechanics is required to cover the crushable geomaterials that are crushed under low stresses such as 0.1 to 10MPa. Soil mechanics is also required to take into account geomaterials subjected to high stresses over 100MPa: hard particles are crushed under such a stress level. In future, particle crushing will be incorporated into soil mechanics systematically.

Crushable soils such as volcanic materials, residual materials, and carbonate materials are found in many parts of the world and are used extensively as construction materials for roads, embankments, and to support foundations of structures. It is considered that the maturity of society demands to construct structures on crushable geomaterials.

Soils under large-scale structures or under pile tips are likely to be subject to the high pressures, and the particles in these soils are easy to crush. Becoming large-scale or becoming deep of structures has been demanded by maturity of society, and advance in the state of the art of civil engineering makes possible the construction of large-scale structures and deep structures.

One thing which the author would like to stress here is that particle crushing is progressive phenomenon. To be described later, it has been indicated and investigated experimentally by several researchers that particle crushing progresses time-dependently. However, it is only investigated phenomenologically, that is to say, the mechanism of time-dependent behavior due to particle crushing has not been investigated from the viewpoint of microstructure of soils. The main purpose of this study is to clarify the mechanism of time-dependent behavior due to particle crushing.

It is considered that time-dependent behavior of geomaterials may be due to the following three factors :

1) Primary consolidation (Flow of pore water),

2) Creep behavior of geomaterials themselves, and

3) Particle crushing.

Time-dependent behavior of a soil (or a structure founded on a ground) would be due to all the three factors. The time-dependent strain or settlement would consist of the following three components: primary consolidation, creep and particle crushing. Thus it is necessary to estimate the amount of each component. In the next section, the outline of the past studies about physical understanding of each factor is described.

Needless to say, prediction of time-dependent deformation of soils is an important problem. The problems of poor bearing capacity or excessive settlement would result in malfunction of the structures. In design of foundation structures, it is needed to predict both instantaneous and long-term settlements of the structures. The prediction of the latter settlement would be useful for the structures in estimating service life, calculating life time cost and maintaining.

The clarification of the mechanism of time-dependent behavior due to particle crushing would contribute to the prediction of immediate and long-term settlements of the structures.

## 1.2 Mechanism of time-dependent behavior of ground

In this section, the outline of physical understanding of each factor is described.

### 1.2.1 Primary consolidation ( flow of pore water )

If a specimen made of saturated clay is under a sustained load, the specimen exhibits time-dependent compression. This is known as consolidation. This time-dependent compression is considered to consist of 1)primary consolidation, 2)secondary consolidation, and 3)others. Most of the compression is primary consolidation. The time-dependency of primary consolidation is due to the very low permeability of clay. As a consequence, a long time is needed for draining the pore water out. As pore water is drained, soil skeleton deforms. In the primary consolidation, the deformation of soil skeleton would be occurred without relative movement of particles and slippage between particles. During primary consolidation, the magnitude of pore water pressure decreases, that is to say, effective stress increases.

Terzaghi(1923) modeled one-dimensional consolidation phenomenon through the device shown in Figure 1.1. The model consists of a cylindrical vessel that contains a series of pistons separated by springs. The space between the pistons is filled with water, and the pistons are perforated. When a pressure $p$ per unit of area is applied to the surface of the uppermost piston, the height of the springs is at the first instant unchanged, because sufficient time has not yet elapsed for the escape of any water from between the pistons. With the passage of time, some water drains from the perforations of uppermost piston, and the volume of the compartments between the pistons decreases. This model is expressed by Equation (1.1):

$$\frac{\partial u}{\partial t} = c_v \frac{\partial^2 u}{\partial z^2} \tag{1.1}$$

where $u$ is excessive pore water pressure, $t$ is time, $c_v$ is coefficient of consolidation, $z$ is axis.

Mikasa(1963) derived a more general consolidation equation expressed by Equation(1.2) on the condition that coefficient of permeability $k$ and coefficient of volume compressibility $m_v$ changes with progress of consolidation.

$$\frac{\partial \varepsilon}{\partial t} = \frac{\partial}{\partial z}\left( \frac{k}{m_v \gamma_w} \frac{\partial \varepsilon}{\partial z} \right) \tag{1.2}$$

where $\varepsilon$ is strain, and $\gamma_w$ is unit weight of pore water. The upper two equations are the models for primary consolidation.

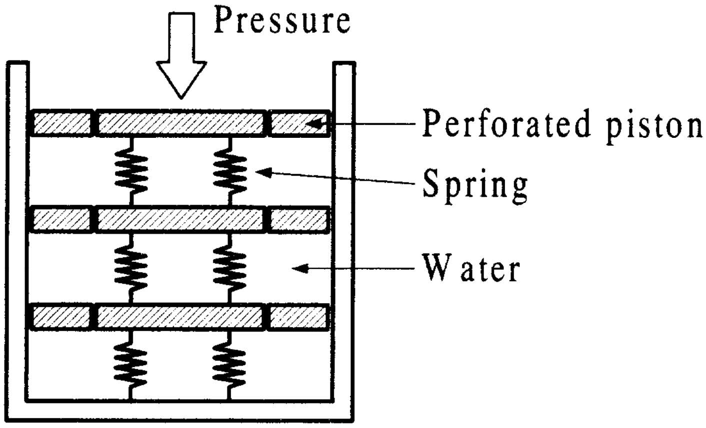


**Figure 1.1 Terzaghi's model for one-dimensional consolidation**

### 1.2.2 Creep behavior of geomaterials themselves

Creep behavior of geomaterials themselves means time-dependent deformation of soils under a constant effective stress. Secondary consolidation is a sort of the creep behavior of geomaterials. Many researchers have investigated the creep behavior, and proposed the modeling methods of the behavior. The investigations by the researchers are not reviewed in this study. It has been considered that the microscopic mechanism of the creep behavior would be related to relative movements of soil particles, that is to say, viscofrictional sliding between particles that may often lead to rearrangements of particles. This viscosity may be originated from adsorbed water, of which the coefficient of viscosity is higher than free water. It should be noted that the following assumption has been made in almost all studies of the creep behavior of soils: crushing or wearing of particles does not occur under the creep behavior.

### 1.2.3 Time-dependent behavior due to particle crushing

This behavior is based on the fact that particle crushing is a progressive phenomenon.

Figure 1.2 shows the considered mechanism of the time-dependent behavior due to particle crushing. Time-dependent behavior due to particle crushing may be considered to progress by occurring "particle crushing" and subsequent "rearrangement of fragments" and "stress redistribution". If a tensile stress in a particle induced by added forces exceeds a tensile strength of the particle, the particle will crush. Once crushing appears, an equilibrium state of forces in the ground collapses, and some crushed fragments will be generated and rearranged. Those fragments have been moving into the pore of soils until every particle and fragment reach the new equilibrium state of forces. Under this new condition, the crushing and redistribution occur again. Bonding between particles and existence of groundwater may also influence the nature of particle crushing behavior.

Time-dependent behavior due to particle crushing has also been indicated from 1960s by several researchers with the fact of particle crushing itself. But the detailed mechanism of the behavior has not been investigated. The indications of time-dependent behavior due to particle crushing by several researchers will be summarized in Subsection 1.3.2.

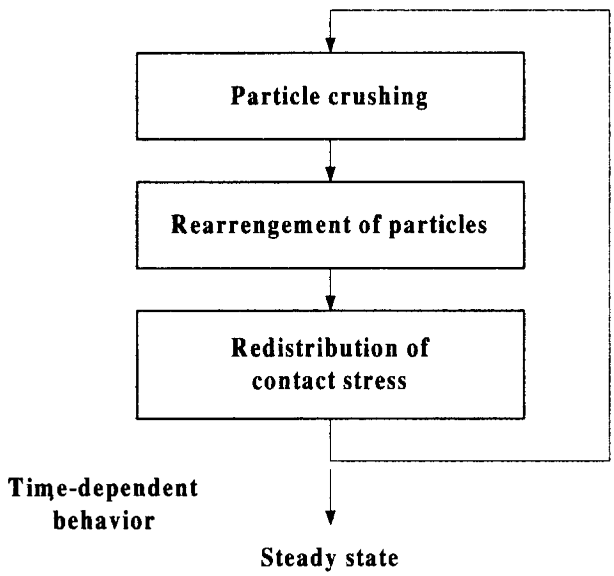


**Figure 1.2 Considered mechanism of time-dependent behavior due to particle crushing**

## 1.3 Review of studies about particle crushing and its time-dependency

In this Section, the studies that indicated the time-dependent behavior due to particle crushing will be reviewed in Subsection 1.3.2. Prior to the review, principal studies about particle crushing of geomatrerials will be also outlined in Subsection 1.3.1.

### 1.3.1 Particle crushing of geomaterials

**(1) Piles or other foundations set in granular ground**

The importance of the phenomenon of particle crushing in high pressure ranges has been recognized from as early as the 1960s in geotechnical engineering, in particular, in relation to pile foundation.

de Beer(1963) conducted two interesting experiments to investigate the influence of the crushing of grains on the penetration resistance of pile. The first experiment was a high pressure consolidation test by means of a simple apparatus shown in Figure 1.3(a). The second experiment was a penetration test (up to 280MN/m$^2$) using an apparatus shown in Figure 1.3(b). In the latter test, a very rigid cylindrical steel container with a height of 240mm and a diameter of 300mm was filled with Mol sand having an initial porosity $n_c$ of 39%. The surface of the sand was covered with a steel plate with a thickness of 20mm and a central borehole of 40mm diameter. In the borehole a piston with a 40mm diameter belonging to a hydraulic press of 300N was introduced, in order to subject the sand to increasing loads. In the first test, marked particle crushing was observed beyond the load of 45MN/m$^2$, and the settlement of the piston increased beyond the load. While, in the latter test, even under the pressure of 3 to 5 MN/m$^2$, already settlements of about 10mm could be observed, although any lateral upward movement was prevented (The pressure of the plate was about 0.12MN/m$^2$). This large compression would be due to particle crushing. From these experiments, the following conclusions could be drawn: 1) there is a marked compression of sand under a mean effective principal stress of over thousands of kN/m$^2$, by applying some shear stress, and 2) this compressibility is due to particle crushing and the magnitude of the compression is depend on mean effective principal stress and shear stress.

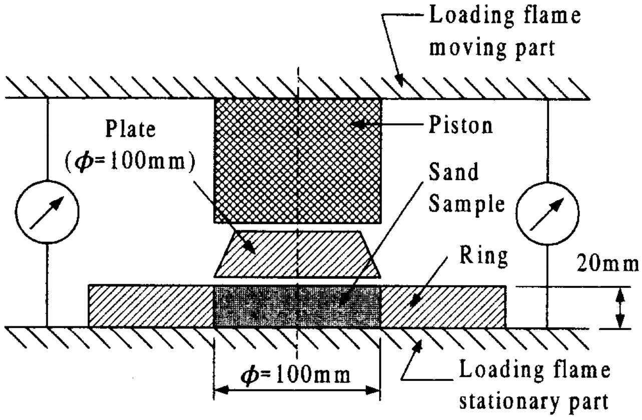


**(a) High pressure consolidation test**

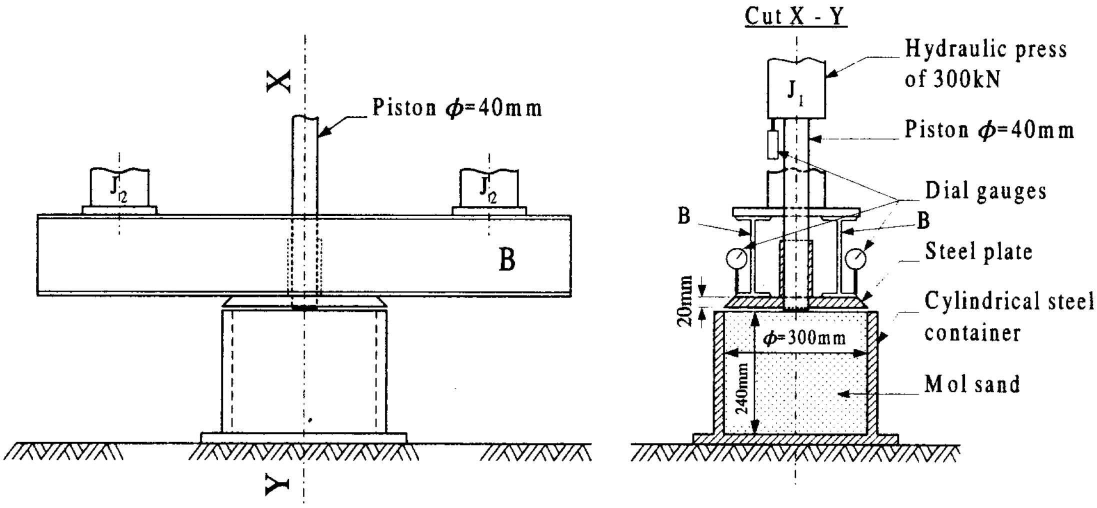


**(b) Penetration test**

**Figure 1.3 Experimental apparatuses of de Beer(1963)**

BCP(Bearing Capacity of Piles) Committee(1971) conducted a series of field load tests on piles in medium dense and dense sands. In these experiments, each pile that had a diameter of 200mm was loaded and settled over 1000mm (5 times of pile diameter) and was estimated the ultimate baring capacity. After each test, the pile was pulled out and the ground beneath the pile tip was investigated in detail : for example, grain size analyses on a block sample of dense sand directly below the pile tip and tri-axial compression tests on a block sample obtained from the test ground. The main conclusions of the field load tests about particle crushing were as follows : 1) A core of highly compacted soil was formed directly below the pile tip and the sand underneath the core underwent marked reduction in volume accompanied by considerable crushing of the particles, 2) the degree of particle crushing of the sand immediately outside the compacted core corresponded to that caused by the triaxal shear under a cell pressure of 10MN/m$^2$ .

Miura(1985) investigated the effect of particle crushing on the point resistance of piles by a series of model pile-loading tests on sandy ground. The model pile was a steel pile of 50mm in diameter and 320 mm in length. The ground was made of air-dried sand compacted in 280mm thick in a dense state (void ratio was 0.6 and wet density was 1.66Mg/m$^3$) in a steel container. He established the fact that the point resistance of piles in sand greatly depends on the particle crushing property of sand below the pile tip to a depth of several times the pile diameter.

Yasufuku and Hyde(1995) also conducted model pile tests to investigated the relationships between the stress-strain properties of a soil and the corresponding model pile end-bearing capacity using a spherical cavity expansion theory. The model pile was 20mm in diameter and made from chromium plated steel. The model ground was made in a calibration chamber of 330mm in diameter and 410mm in height. A carbonate sand, weathered granite sand, and silica sand were used. They concluded that the use of spherical cavity expansion methods offers potential for better prediction of end-bearing capacities by taking account of soil crushability.

Ohno and Sawada(1999) discussed the influence of the initial stress condition on the bearing capacity in sands based on the loading tests of model pile in two types of sands having different crushabilities of sands. They showed that there is a unique relationship between end bearing capacity and mean effective stress and a unique relationship between the skin friction and the horizontal stress, regardless of the crushablity of sands.

Randolph et al.(1993) provided an overview of the performance of piled foundations in calcareous sediments, which is one of the crushable geomaterials. They indicated that the low capacity of driven piles is due to particle crushing and rearrangement of the soil, and the formation of a zone of low effective stress immediately around the pile during the driving process. They also indicated that a narrow 'rubble' zone is created immediately around the pile in the case of drilled and grouted pile when the pile is subjected to cyclic loading, and that the calcareous soil in the rubble zone is finally broken down allowing failure of the pile.

Kusakabe et al.(1992), Ohuchi et al.(1994), and Miyake and Kusakabe(1997) conducted three loading tests of square footing (0.2, 0.3, 0.4m) in a pneumatic caisson being constructed 8.7m below the ground surface on naturally deposited granular materials. After the loading tests, visible shear bands were observed. A detailed examination revealed that the shear bands beneath the footing under high pressure were formed with densification by particle crushing, whereas the shear bands in passive zones under small pressure loosen by positive dilatancy.

**(2) Effects of particle crushing on mechanical properties obtained from triaxial or one-dimensional compression tests**

Haruyama(1969) investigated the shear characteristics of Shirasu, that is one of the crushable volcanic materials, by means of triaxial compression tests. Figure 1.4 shows a failure envelope with Mohr circles obtained from the triaxial tests of air dried Shirasu specimens. The envelope is a curve with decreasing slope with an increase in confining pressure. He considered that the reason why the envelope became a curved line with progressively flatter slope was (1)the effect of crushing of particles in shearing and (2)the effect of structure. Such a curved envelope was also observed in triaxial tests on sands under high confirming pressures performed by several researchers (for example, Bishop et al.,1965, Lee et al., 1967).

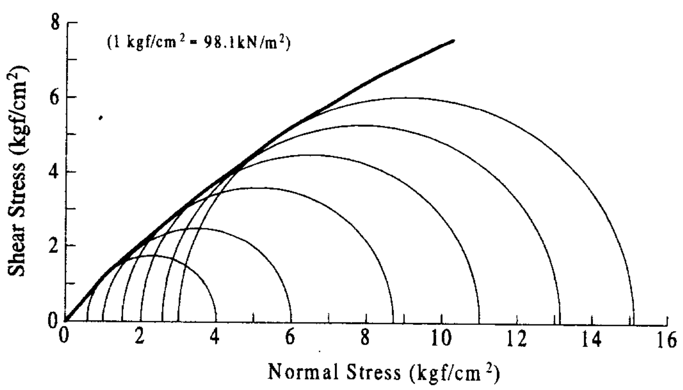


**Figure 1.4 Mohr circles and a failure envelope for air dried Shirasu (Haruyama, 1969)**

Miura and his associates conducted pioneering work on the effect of particle crushing on the compressive and shear characteristics of granular materials, including Toyoura sand, a decomposed granite and other materials. Miura and Yamanouchi(1971) investigated drained shear characteristics of Toyoura sand under high confining pressures (2.5 – 50MN/m$^2$) with the use of triaxial compression test apparatus. From the results of the tests and observation of particle crushing using microscope, they estimated the degree of contribution of the effect of particle crushing and rearrangement to shear strength as shown in Table 1.1.

**Table 1.1 Effect of particle crushing on shear strength under high pressures**
**( This table summarizes the results of Miura and Yamanouchi, 1971 )**

| | Confining stress ($MN/m^2$) | 7.5 - 12.5 | 15 - 50 | 50 |
|---|---|---|---|---|
| **A** | Dense specimen | 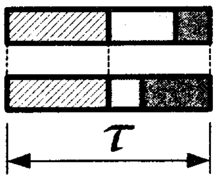 | 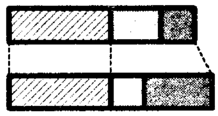 | 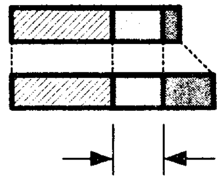 |
| **B** | Loose specimen | | | |
| Comments | | Shear strengthes ($\tau$) of A and B are equal. D. effect of A is larger than that of B. P. effect of A is smaller than that of B. | Dilatancy effect and particle crushing and rearrangement effect are intermediate of the both neighbors. | Dilatancy effects of A and B are equal. Particle crushing and rearrangement effect of B is larger than that of A. |

Legend ; $\tau$: Shear strength or maximum deviator stress

$\tau$ is composed of the following three components :

- Strength originated from friction between particles
- Dilatancy effect (D. effect)
- Particle crushing and rearrangement effect (P. effect)

Miura and Yamanouchi(1977) and Miura and O-hara(1979) investigated the effect of particle-crushing on the shear characteristics of Toyoura sand and a decomposed granite soil by a triaxial compression test and a repeated triaxial test. The amount of particle crushing was estimated using the increase of surface area $\Delta S$. The particle crushing property of a sample under shear stresses is defined by the rate of increase of the surface area $S$ to the plastic work gone $W$ ($dS/dW$), which is called the "particle-crushing rate". A close relation was found between the particle-crushing rate and the dilatancy rate or the shear strength.

Miura et al.(1984) proposed a constitutive model for sand in a particle crushing range based on plasticity theory and on an expression for the energy dissipation per unit volume $\delta W$ that they proposed.

$$\delta W = p'\sqrt{(\delta v^p)^2 + (M\delta\varepsilon^p)^2 - (M\eta)^2 \delta v^p \delta\varepsilon^p} \tag{1.3}$$

where $p'$ is effective principal stress, $\delta v^p$ is a plastic volumetric strain increment, $\delta\varepsilon^p$ is a plastic shear distortional strain increment, $M$ is gradient of critical state line, $\eta$ is stress ratio. Using the Equation(1.3), they gave a constitutive model for sand in a particle crushing range :

$$\begin{aligned} \delta v &= \frac{\lambda}{1+e}\left[\frac{\delta p}{p'} + \left(1-\frac{\kappa}{\lambda}\right)\frac{(2+M^2\eta)\eta}{M^2\eta^3+\eta^2+M^2}\delta\eta\right] \\ \delta\varepsilon &= \frac{\lambda-\kappa}{1+e}\left[\frac{\delta p}{p'} + \frac{(2+M^2\eta)\eta}{M^2\eta^3+\eta^2+M^2}\delta\eta\right]\times\left[\frac{(2+M^2\eta)\eta}{M^2-\eta^2}\right] \end{aligned} \tag{1.4}$$

where $\delta v$ is volumetric strain increment, $\delta\varepsilon$ is strain increment, $e$ is void ratio, $\lambda$ is compression index, $\kappa$ is swelling index.

In recent years, a number of experimental results have reported the characteristics of crushable materials such as volcanic materials, residual materials, and carbonate materials.

Kusakabe et al.(1991) investigated strength and deformation characteristics of an undisturbed scoria, that is one of the volcanic materials, through triaxial compression tests and plane strain compression tests in undisturbed and disturbed states. They showed that the behavior of the undisturbed scoria changes from that of a dilatant brittle material to that of a plastic material in the confirming pressure range of 700 to 1500 kPa, exhibiting volume reduction with particle crushing.

Miura et al.(1996) and Miura and Yagi(1997) investigated the particle breakage properties of volcanic coarse-grained soils, produced by fall deposition in Hokkaido, Japan, at consolidation and shearing, through a series of one-dimensional and isotropic consolidation tests. They showed that the particle breakage characteristics of volcanic soils depended strongly on the effective stress path during consolidation and shearing, and that an index of $\Delta F_c$, that was an increment of finer (not more than 75μm) content, could be estimated only by effective mean principal stress and effective stress ratio.

Barksdale and Blight(1997) outlined the compressibility and settlement of residual soils. According to their outline, all residual soils behave as if overconsolidated. Their compressibility is relatively low at low stress levels. Once a threshold yield stress or equivalent preconsolidation stress has been exceeded, the compressibility increases. In most cases, the stress range will be such that the soil will remain within the pseudo-overconsolidated range of behavior.

Brenner et al.(1997) listed special features encountered with residual soils which are mainly responsible for the difference in stress-strain and strength behavior in comparison with transported soils. Table 1.2 shows the list.

**Table 1.2 Comparison of residual and transported soils with respect to various special features that affect strength (Brenner et al., 1997)**

| Factor affecting strength | Effect on residual soil | Effect on transported soil |
|---|---|---|
| Stress history | Usually not important | Very important, modifies initial grain packing, causes overconsolidation effect |
| Grain/particle strength | Very variable, varying mineralogy and many weak grains are possible | More uniform; few weak grains because weak particles become eliminated during transport |
| Bonding | Important component of strength mostly due to residual bonds or cementing: causes cohesion intercept and results in a yield stress; can be destroyed by | Occurs with geologically aged deposits, produces cohesion intercept and yield stress, can be destroyed by disturbance |
| Relict structure and discontinuities | Develop from pre-existing structure or structural features in parent rock, include bedding, flow structures, joints, slickensides etc. | Develop from deposition cycles and from stress history, formation of slickensided surfaces possible |
| Anisotoropy | Usually derived from relict rock fablic, e.g. bedding | Derived from deposition and stress history of soil |
| Void ratio/density | Depends on state reached in weathering process, independent of stress history | Depends directly on stress history |

Hattori et al.(1998a) investigated the mechanical behavior of Hiroshima decomposed granite, that is one of the residual materials, by performing oedometer tests and drained and undrained triaxial tests. Further tests were performed on individual rock forming minerals : quartz, orthoclase, and clay(feldspar and biotite). Based on the results of oedometer tests, they indicated that particle crushing ensues when the pressure exceeds the yield stress. They also indicated based on the tests that the mechanical characteristics of one-dimensional compression and shear were governed by those of clay under the pressure of not over 900MPa, while the characteristics were governed by those of quartz and orthoclase under the pressure of over 900MPa.

Airey et al.(1988) conducted a series of oedometer tests and triaxial tests for two carbonate sands obtained from two locations in Australia's Bass Strait. Figure 1.5(a) shows $e$ – log $p$ curves of a sand in one-dimensional(oedometer) tests and isotropic(triaxial) compression tests. The sand is less compressible when compressed isotropically than when compressed one-dimensionally. It is generally found that the isotropic normal compression response lies to the right of the one-dimensional response in $e$, $p'$ space so that a greater stress is required to reach the normally compressed state. They described that the normally compressed state is associated with particle crushing, and that the additional shear stresses in one-dimensional compression appear to lower the mean stress at which crushing occurs. Figure 1.5(b) shows relationship between mobilized angle of friction ($\phi'_m$) and rate of dilation ($-d\varepsilon_v/d\varepsilon_1$) obtained from the triaxial tests. For each sand, all data lie within a narrow band. That is to say, there is no discernible effect due to changing confining stress, which suggests that particle crushing does not affect the fundamental relationship between the mobilised angle of friction and the rate of dilation. They also showed that the two sands behaved in accordance with the stress-dilatancy theory of Rowe(1962).

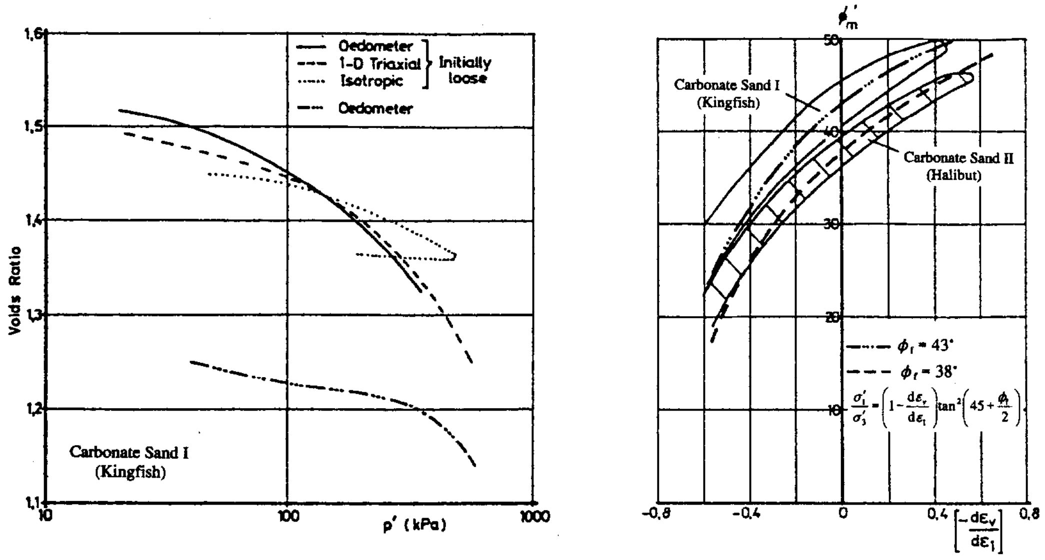


**(a) $e - \log p$ curves of isotropic and one-dimensional compression tests**

**(b) Relationship between mobilized angle of friction and rate of dilation**

**Figure 1.5 Results of oedometer tests and triaxial tests (Airey et al., 1988)**

Hull et al.(1988) investigated the behavior of various calcareous sediments in isotropically consolidated drained triaxial tests. Seven sands were tested; one silica sand and two processed sands that had a uniform size of grains, and four naturally occurring calcareous sands that contained a larger range of particle sizes and are generally finer. From the consideration of the tests, they isolated the crushing of particles as a major factor for controlling the performance of the sediments in standard triaxial tests.

Fukumoto(1992) considered a change in particle size distribution during several types of soil tests; triaxial compression, one-dimensional compression, gyratory and compaction test. The samples used in these tests included various rock qualities ranging from brittle mudstone to considerably stronger quartz granular materials. Figure 1.6 shows two examples of grain size distribution curve. Changes in particle size distribution were observed during all types of test. He showed that the grain size distribution curves obtained after each of the tests depend greatly on the type of tests and the testing conditions. Fukumoto(1990) had also proposed a grading equation that was derived mathematically based on considerations related to the weathering process of rocks. He indicated that the grading equation could be applied with good accuracy to artificial particle breakage (that is to say, particle breakage during the soil tests). The curves calculated from the equation are also shown in Figure 1.6.

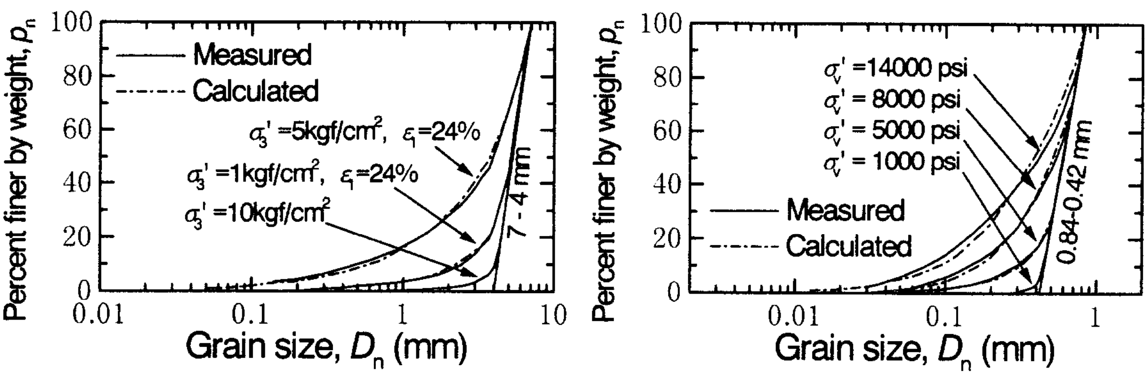


**(a) Isotropic consolidation** **(b) One-dimensional compression**

**Figure 1.6 Change in particle size distribution in one-dimensional compression tests (Fukumoto, 1992)**

Yoshida(1995) thought that particle crushing of geomaterials is one of the important factors about the relationship between stress and strain in share bands. He conducted one-dimensional compression tests of sand, gravel and glass beads specimen to obtain basic information about particle crushability. From the one-dimensional compression tests, he defined a crushing stress $p_c$ that is a intersection of a tangent $m_i$ of the initial part of the axial stress – plastic axial strain curve and a tangent $m_c$ of the subsequent straight part of the curve, and indicated that particle crushing occurred very little before the axial stress reached the $p_c$, and that particle crushing occurred remarkably after the axial stress was beyond the $p_c$. He also indicated that $m_i$ decreased with increase of $p_c$ as shown in Figure 1.7(a), and used $m_i$ as an index of crushability. Based on the above-mentioned experimental results, he conducted plane strain compression tests with the use of the same particulate materials as the one-dimensional compression tests, and investigated the influence of particle crushing on the magnitude of strain in shear band. Figure 1.7(b) presents the test results. It is obvious that under a small confined pressure($\sigma_3$'=0.08MN/m$^2$ ) the characteristic strain of shear band

$(u_s*)_{res}/t_0$ (where $(u_s*)_{res}$ means the shear deformation of the shear band until the shear stress of the shear band reaches the residual strength after a peak stress, $t_0$ means thickness of the shear band.) did not influenced from crushability $m_i$ and $F_{20}$ (that is a sort of configuration index : The more angular the configuration is, the larger the $F_{20}$ is, and $F_{20}$=0 when the configuration is in spherical.), and that under a large confined pressure( $\sigma_3$'=0.4MN/m$^2$ ) $(u_s*)_{res}/t_0$ influenced from crushability $m_i$.

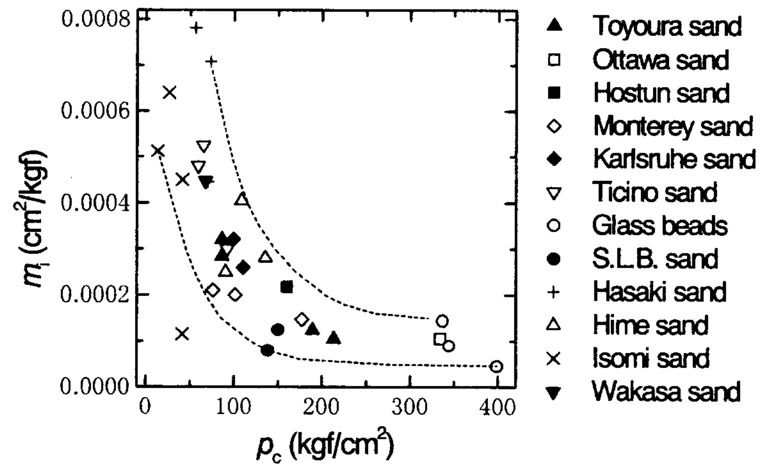


**(a) Relationship between $m_i$ and $p_c$**

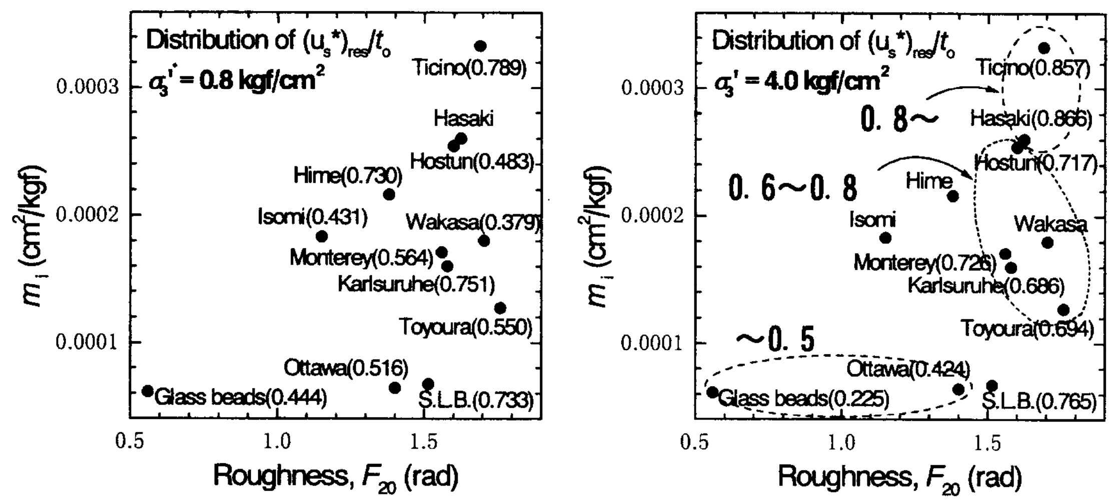


**(b) Relationships between crushability($m_i$) and angularity($F_{20}$)**

**Figure 1.7 Results of Yoshida(1995)'s laboratory tests**

### (3) Characteristics obtained from single particle crushing tests

The fracture of a single particle has been experimentally examined for various materials by several researchers. Lee(1992) conducted single particle crushing tests in such a manner shown in Figure 1.8(a). He defined a characteristic tensile stress $\sigma$ induced within it as :

$$\sigma = \frac{F}{d^2} \tag{1.5}$$

where $F$ is the platen load shown in Figure 1.8(a), $d$ is a particle diameter. Figure 1.8(b) shows a typical plot of platen load $F$ as a function of the platen displacement $\delta$. Particle crushed catastrophically at the maximum load of $F_f$. He calculated a tensile strength of the particle as

$$\sigma_f = \frac{F_f}{d^2} \tag{1.6}$$

where the subscript f denotes failure.

He found that the average tensile strength of single particles that are made of a single mineral is a function of particle size : the logarithmic value of the tensile strength is inversely proportional to the logarithmic value of particle size (Figure 1.8(c)).

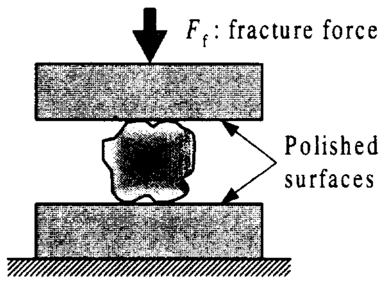


**(a) Test set-up**

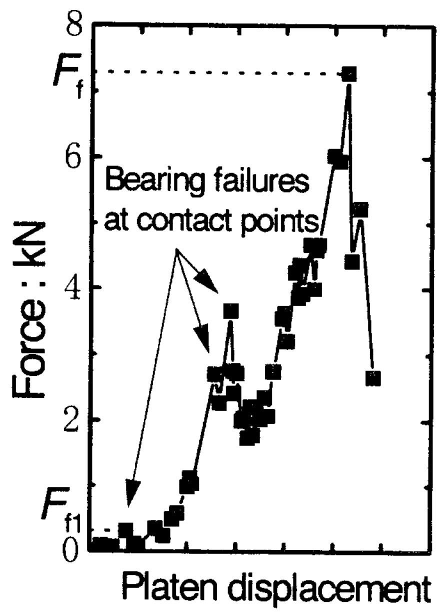


**(b) Typical load – deflection plot**

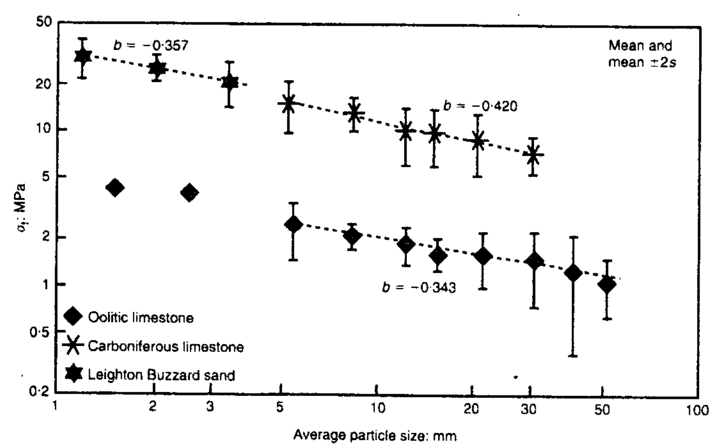


**(c) Mean tensile strength as a function of particle size**

**Figure 1.8 Outline of single particle crushing tests (Lee, 1992)**

Attempts have been made to relate the characteristics obtained from single particle crushing tests to the characteristics obtained from one-dimensional compression tests or triaxial compression tests.

Yasufuku and Kwag(1999) conducted a series of single particle fragmentation(crushing) tests and isotropic compression tests for four different types of sands in order to clarify the characteristics of both the single particle fragmentation strength and the particle crushing under the isotropic compression process, as related to soil crushability. About isotropic compression tests, they indicated the unique relationship between yielding stress ($p'_c$) and relative density ($D_r$).

$$\log p'_c = K + 2.27D_r \tag{1.7}$$

The constant $K$ is the material coefficient and decided by the value of log $p'_c$ when $D_r$ is equal to 0%. They regarded $K$ as an index to represent the degree of crushability of sands. About single particle fragmentation tests, they indicated the relationship between a strength characteristic and mean particle size($d_m$).

$$\frac{P_{f1}}{A} = zd_m^b \tag{1.8}$$

where $P_{f1}$ is the first peak force of force($F$) – displacement($\delta$) curve obtained from the single particle fragmentation test, $A$ is a characteristic area that calculated as $\pi d_{mi}^2/4$ ($d_{mi}$ is mean particle size of individual particle, $d_m$ is the mean value calculated from the values of $d_{mi}$ ) for rounded and angular particles and as $tL$ ($t$ is mean thickness of a particle, $L$ is the same as $d_{mi}$ ) for flat particles. $z$ and $b$ are material constants which represent the value of $P_{f1}/A$(MPa) at $d_m$=1.0(mm) and the slope of the plot, respectively. Finally, they indicated that the values of representative fragmentation particle strength ($P_{f1}/A$ (at $d_{50}$), $d_{50}$ means the particle size corresponding to 50%, by weight, of grains smaller than the size denoted by the abscissa of the grain size distribution curve) and the crushable index ($K$) have a strong correlation with each other. They suggested that the representative fragmentation strength could be a key factor in preliminary parameters for evaluating the soil crushability.

Nakata et al.(1999) carried out single particle crushing tests and triaxial compression tests of a sand, in order to clarify the relationships between the mechanical characteristics of a sand and particle crushing. The results of the single particle crushing tests were analyzed and compared using particle survival probability curves. The probability of survival ($P_{sc}$) at a given crushing stress $\sigma_c$ is given by

$$P_{sc} = \frac{\text{number of particles crushing at } \sigma \geq \sigma_c}{\text{total\_number of particles tested}}. \tag{1.9}$$

where $\sigma_c$ is a characteristic stress $\sigma_c = F_{f1}/d^2 (F_{f1}$ is the first peak of $F - \delta$ curve: refer to Figure 1.8(b)). Figure 1.9(a) shows the survival probability curve. From the triaxial tests, they expressed the degree of crushing in a specimen as a particle breakage factor $B_f$ that defined in terms of the evolution of the particle size grading curve. The factor $B_f$ is $R/100$ and $R$ is the percentage of particles smaller, after testing, than the minimum particle size in the original sand as shown in Figure 1.9(b). Figure 1.9(a) also shows the value of $(1 - B_f)$ against the $\sigma_{sp}$. $\sigma_{sp}$ is the maximum characteristic stress estimated for the individual particles embedded in the test specimen using a simplified analysis. There appears to be a good fit between the survival probability curve and the $(1-B_f) - \sigma_{sp}$ curve. Finally, as shown in Figure 1.9(c), they related the factor $B_f$ with the maximum value of the mean normal effective principal stress on the yield surface ($p'_0$) that estimated from the modified Cam Clay yield surface for soils proposed by Roscoe and Burland(1968).

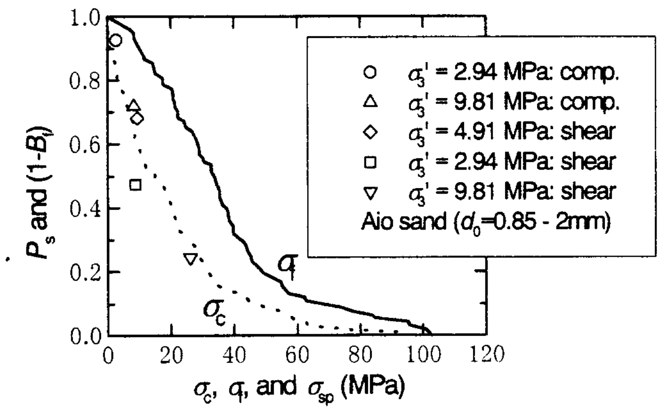


**(a) Survival probability curve and $(1 - B_f) - \sigma_{sp}$ curve**

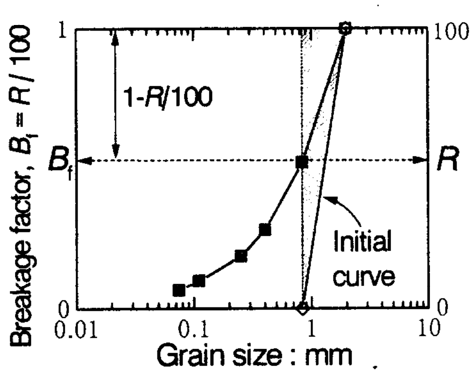


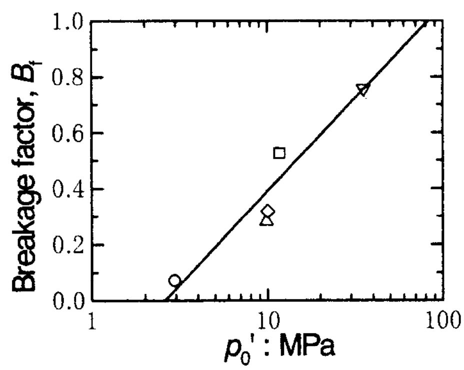


**(b) Definition of a factor $B_f$** **(c) $B_f$ versus $p'_0$**

**Figure 1.9 Relationship between a particle breakage factor and the maximum value of mean normal effective stress($p'_0$) for a given yield surface (Nakata et al., 1999)**

McDowell and Bolton (1998) gave a set of theoretical interpretations for major features observed by single particle test and one-dimensional compression test from the view of micromechanics.

Firstly, they applied Weibull statistics to the results of the single particle crushing tests conducted by Lee(1992) (shown in Figure 1.8).

$$P_s(d) = \exp\left[-\left(\frac{d}{d_0}\right)^3\left(\frac{\sigma}{\sigma_0}\right)^m\right] \tag{1.10}$$

where $P_s(d)$ is the survival probability of the particle, $\sigma_0$ is the value of $F/d^2$ at which 37% of the tested particles survive. $d_0$ is the initial particle size ('initial' means 'before crushing'), and it is related to the mean tensile strength of $\sigma_0$ by the relation of Figure 1.8(c), that is to say, $\sigma_f \propto d^{-b}$.

Secondly they explained the influence of grain strength on angle of internal friction. Figure 1.10 shows dilatational component of angle of internal friction ($\Delta\phi$) plotted against mean effective stress $p'$ normalized by the grain tensile strength($\sigma_0$). $\Delta\phi$ reduced logarithmically with $p'/\sigma_0$ . From Figure 1.10, McDowell(1999) suggested that the tensile strength of soil grains was considered to be of great significance in studying the macroscopic behavior of soils and rockfills.

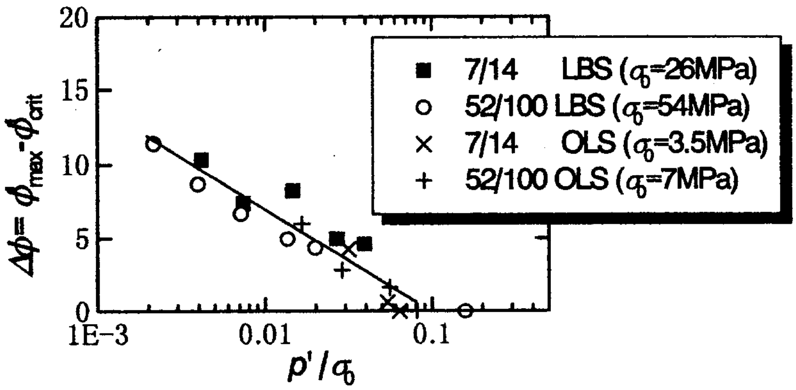


**Figure 1.10 Dilatational component of angle of internal friction plotted against mean effective stress normalized by grain tensile strength (McDowell and Bolton, 1999)**

Finally, they explained the fact that a linear normal compression line emerges when void ratio is plotted against the logarithm of vertical effective stress. They involved a fractal geometry in the explanation : the particle size distributions of broken and crushed granular materials are often fractal (Turcotte, 1986). The explanation has three ingredients mentioned after.

(i) Introduction of a work equation

The following work equation was introduced : the equation is the original Cam Clay work equation (Schofield and Wroth, 1968) added a term of energy dissipation for particle crushing :

$$q\delta\varepsilon_q + p'\delta\varepsilon_v = \mathrm{M}p'\delta\varepsilon_q + \frac{\Gamma dS}{V_s(1+e)} \tag{1.11}$$

The left-hand side represents the plastic work done per unit volume by deviatoric stress $q$ and mean effective stress $p'$ (with corresponding irrecoverable strain increments $\delta\varepsilon_q$ and $\delta\varepsilon_v$ ). $Mp'\delta\varepsilon_q$ is identified as internal frictional dissipation. M is the generalized friction coefficient. The second term of the right-hand side is the term indicating energy dissipation for particle crushing. d$S$ is the increase in surface area of a volume $V_s$ of solids distributed in a gross volume $V_s(1+e)$, and $\Gamma$ is the surface energy related to the critical strain energy release rate $G_c$ by $\Gamma=G_c/2$.

(ii) Introduction of a fractal

The fractal geometry was introduced to the total surface area of particles in a sample ($S$) and the volume of solids in the sample ($M$).

$$S(L > d_s) = 5\beta_s A d_s^{-1/2} \tag{1.12}$$

$$M(L < d_0) = 5\beta_v A d_0^{1/2} \tag{1.13}$$

where $d_s$ is the smallest particle size, $\beta_s$ is the surface shape factor, $A$ is a constant, $\beta_v$ is the volume shape factor, and $d_0$ is the largest ('initial') particle size in the sample of one-dimensional compression test.

(iii) Relating the smallest particle size $d_s$ with macroscopic stress $\bar{\sigma}$

The smallest particles of size $d_s$ may be considered to have a characteristic tensile stress which is proportional to the macroscopic stress $\bar{\sigma}$. If the splitting of grains is governed by linear elastic fracture mechanics, then the only dimensionless group that can be formed from these parameters is $\bar{\sigma}\sqrt{d_s}/K_{Ic}$, where $K_{Ic}$ is the fracture toughness. From the above-mentioned point, the following equation was derived :

$$\bar{\sigma}\sqrt{d_s} \propto \bar{\sigma}_0\sqrt{d_0} \tag{1.14}$$

where $\bar{\sigma}_0$ is called a clastic yield stress by McDowell and Bolton. The clastic yield stress $\bar{\sigma}_0$ is considered to be defined as the value of macroscopic stress which causes the maximum rate of grain fracture under increasing stress, for particles loaded in the sample of one-dimensional compression test.

From the aforementioned ingredients of (i)(ii)(iii), the following equation was obtained :

$$\lambda = \frac{1}{1-\mu}\frac{\beta_s}{\beta_v}\frac{\Gamma}{\overline{\sigma}_0 d_0} \tag{1.15}$$

where $\lambda$ is the slope of the normal compression line, $\mu$ is a weak function solely of the angle of internal friction. Equation (1.15) suggests that the tensile strength of particles governs the normal compression.

### (4) Others

Mukunoki et al.(1999a,b, 2000) have been attempted to visualize the change of density in crushable ground under pile loading without any destruction using industrial X-ray CT scanner, and estimate the results quantitatively. They conducted model pile loading tests on model ground made of decomposed granite soil or garnet particles that were very hard particles. Scanning by the CT scanner was conducted before, on the way and after each test. X-ray absorption coefficients called "CT-value" at each pixel were derived from the scanning. The coefficients of variation in each range in a picture are calculated and used for index of degree of particle crushing, since the decrease of the coefficient of variation reflects the increase of density in each range. From a series of experiments, they suggested that the coefficient of variation would have the potential of estimating the particle crushing quantitatively.

### (5) Summary of Subsection 1.3.1

As mentioned above, particle crushing phenomena is studied actively in recent years. Almost all studies were fundamental studies through laboratory tests. However, in all studies described in this subsection, there is no point of view of time-dependency.

### 1.3.2 Time-dependent behavior of geomaterials due to particle crushing

A limited amount of literature is available on time-dependent behavior related to particle crushing. As far as the author is aware of, Lee and Farhoomand(1967) were the first to indicate time-dependent behavior due to particle crushing. They conducted isotropic and anisotropic triaxial compression tests of granular soil to investigate the compressibility of granular soil and the possible effects of particle crushing at high pressures as applied to the design of gravel drains and soil filters for use in high earth dams. They heard occasional cracking sounds coming from a triaxial cell after a load was applied, and indicated that crushing as well as compression is a time-dependent phenomenon.

Vesic and Clough(1968) were the first to experimentally demonstrate the time-dependent behavior of granular materials under high pressure ranges as high as 62 MPa. From the plots of volumetric strain (degrees of consolidation) vs. logarithmic time during isotropic compression of a test with an air-dry sample (Figure 1.11), it was observed that the time required to reach convergence of consolidation increases as confined pressure is increased. No reasonable interpretation was possible for this phenomenon by means of the theory of primary consolidation. They maintained that these curves were not surprising in view of the character of deformation which is predominantly breakdown of particles, and that a similarity with the phenomenon of secondary consolidation should be expected.

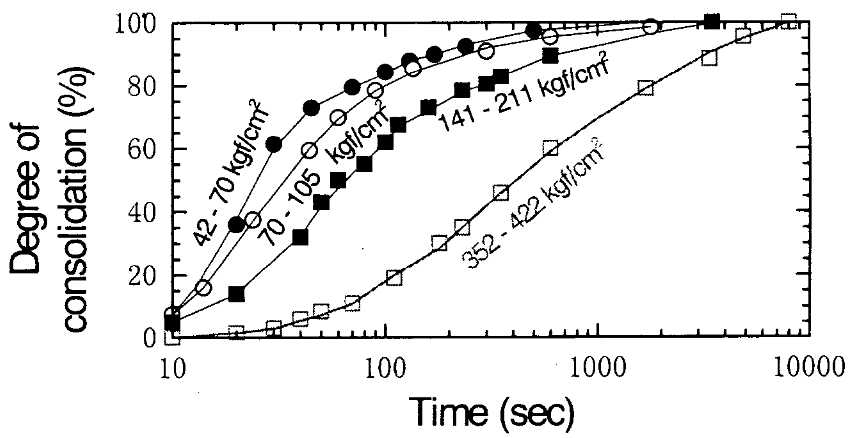


**Figure 1.11 Progress of volumetric strain with time during isotropic compression (Vesic and Clough, 1968)**

Miura and Yamanouchi(1972) investigated time-dependent compression of specimens made of Toyoura sand under high pressure by isotropic compression tests. Figure 1.12 shows relationships between degree of compression and elapsed time. There are two inflection points on each curve. They also conducted sieve analyses of each specimen before and after the test, and indicated that there was no significant difference between the grading curve obtained at the time of the first inflection point, and the curve obtained at tens of hours after compression start. From the above-mentioned results, they considered that the compression of specimen would progress due to particle crushing before the first inflection point, and that the compression of specimen would progress due to slips between particles after the first inflection point.

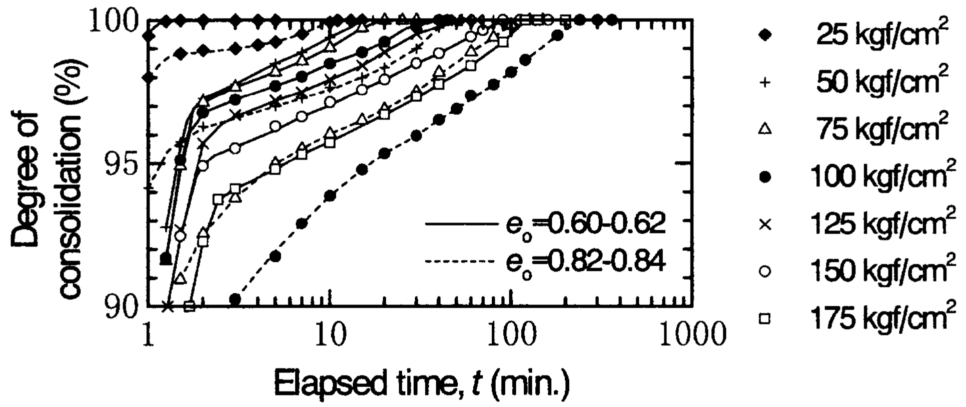


**Figure 1.12 Relationships between degree of compression and elapsed time (Miura and Yamanouchi, 1972)**

Sharp and Seters(1988) conducted a series of plate loading tests(PLT) on calcareous sediments to obtain the bearing capacity and load settlement characteristics of the ground (Figure 1.13(a)). The settlement – logarithmic time curve of a loading stage (Figure 1.13(b)) appeared to be characterized by an initially curved portion, thereafter followed by a straight line. These portions might well represent primary and secondary consolidation, respectively. The slope on a log time basis of the secondary settlement was usually greater than that of the primary portion. What they observed was contrary to normal soil behavior. They suggested that particle breakdown releases sufficient intra-particle fluid to assist creep.

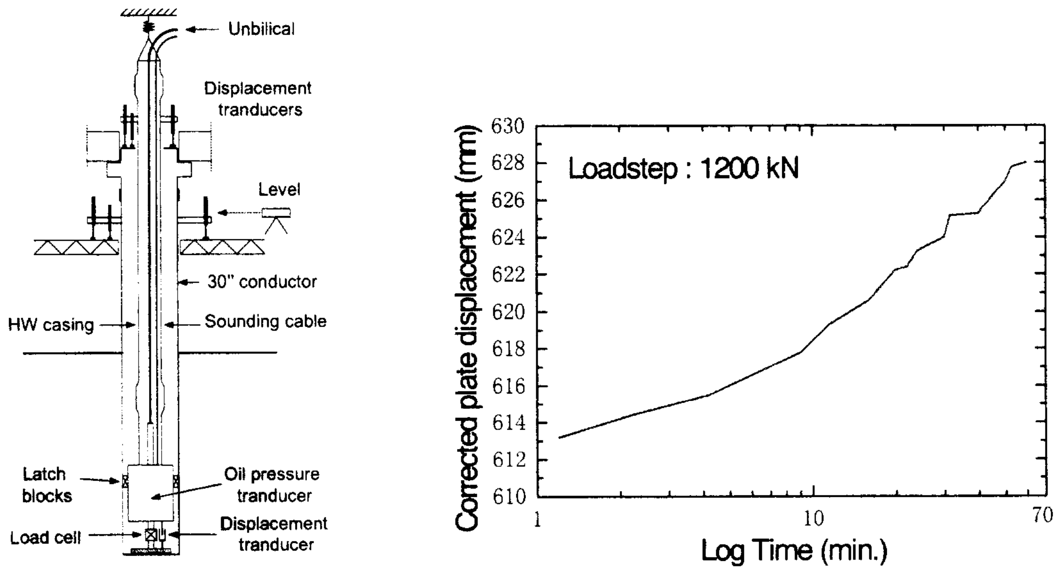


**(a) Outline of PLT** **(b) Settlement vs. log time of a loading stage**

**Figure 1.13 PLT on the Calcareous ground (Sharp and Seters, 1988)**

Leung et al.(1996) and Yet et al.(1996) carried out a centrifuge study to investigate the time-dependent behavior of piles under sustained loads. The model pile was a solid cylindrical rod made of aluminum alloy and jacked into the model ground of a uniform, angular, fine silica sand prepared by the air-pluviaton method (Figure 1.14(a)). The load on the pile was gradually increased until the desired load was reached, then maintained for a duration of up to 1 hour. The plots of settlement-logarithmic time (Figure 1.14(b)) indicated that the creep settlement of the pile increases almost linearly with logarithm of time. They defined a creep coefficient as the magnitude of pile settlement to one logarithmic (to base 10) time cycle. As can be seen, the creep coefficient increases with the load ratio, which was defined as a ratio of the maintained load to ultimate capacity of the pile.

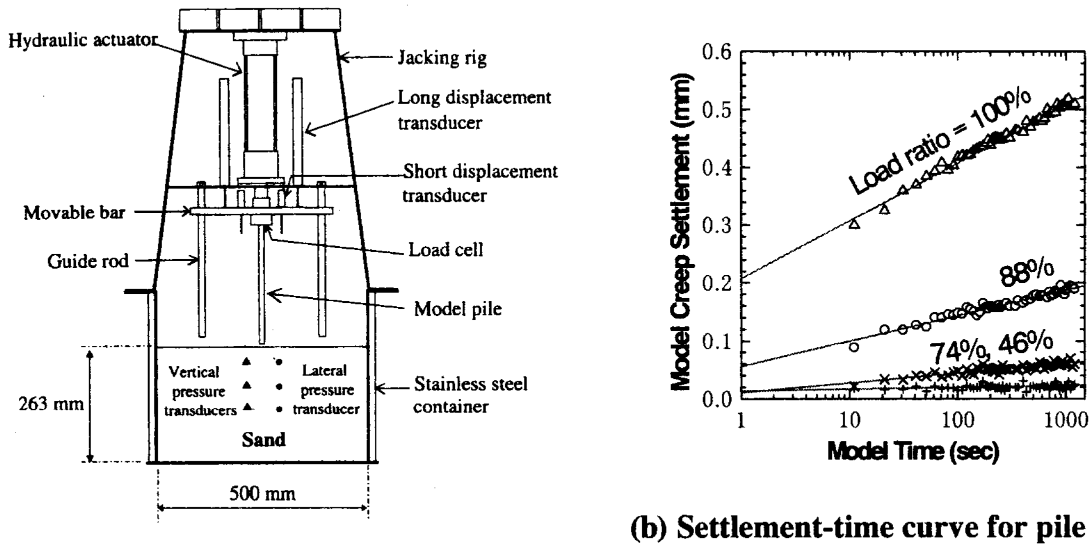


(a) Outline of centrifuge model

(b) Settlement-time curve for pile at various load ratios

**Figure 1.14 A centrifuge study of time-dependent behavior in pile creep in sand (Leung et al., 1996 and Yet et al.,1996)**

Leung et al.(1996) presumed that one possible reason for the creep phenomenon might be particle breakage. With greater load, the interlocking particle stress is larger and hence more particle breakdown occurs and the creep coefficient increases. They also conducted one-dimensional compression tests on the tested material to investigate the possible link between sand creep that may occur beneath the pile tip and particle breakage. From measured creep settlement (Figure 1.15(a)) and particle breakage observed by microscope (Figure 1.15(b)), they concluded that particle breakage would cause the increase in pile settlement with time.

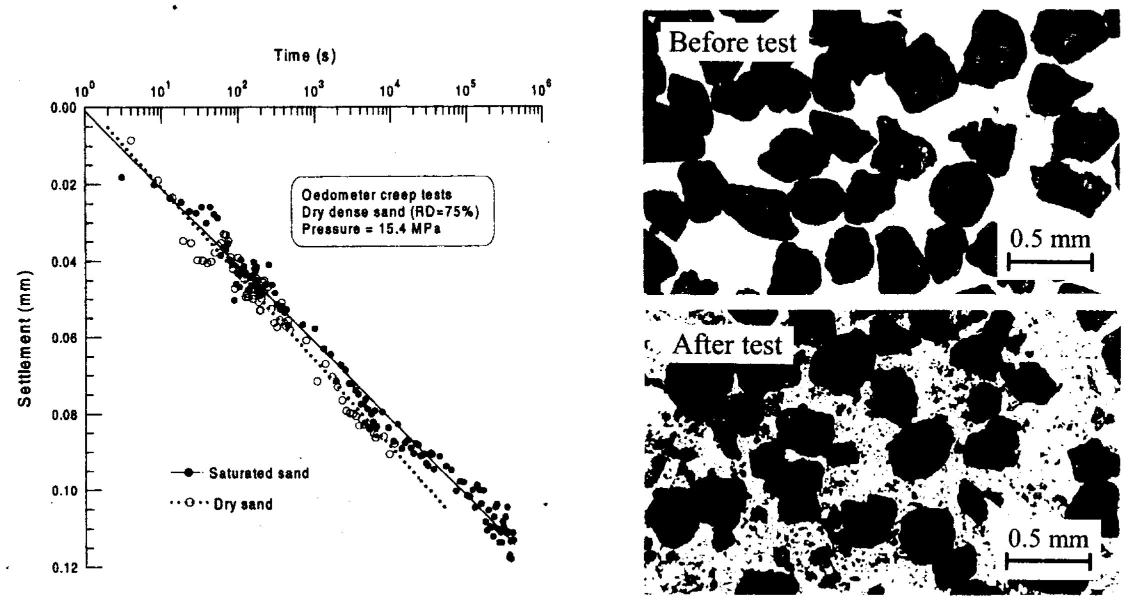


(a) Settlement vs. log time

(b) Observations of sand particles

**Figure 1.15 One-dimensional compression tests of a silica sand (Leung et al.,1996)**

Barksdale and Blight(1997) introduced some examples of field observation of time-dependent settlement of structures founded on residual soils (Figure 1.16(a)). The settlement had been monitored over several years. The settlement had progressed after the end of construction of buildings (Figure 1.16(b)). It is considered that particle crushing of the residual soil would be one of the components of the time-dependent settlement.

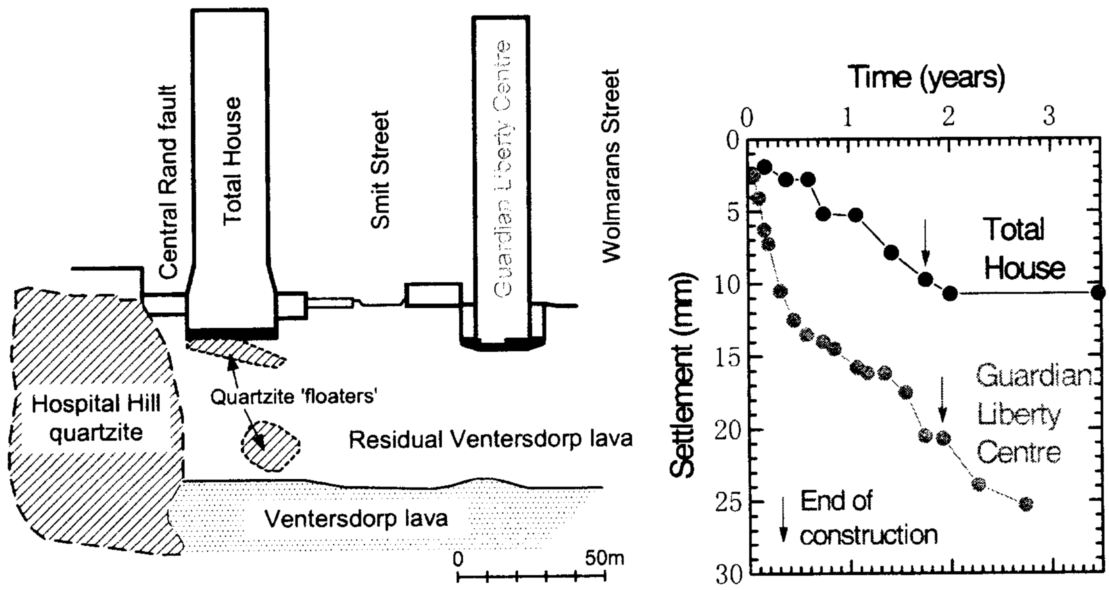


(a) Buildings and ground (b) Time-settlement curves

**Figure 1.16 Settlement of buildings founded on weathered andesite laba (Jaros, 1978, Barksdale and Blight, 1997)**

Mukai et al. (1999) reported an observation of progressive settlement on a 100m high airport embankment fill of granite in Hiroshima for the period of 7 years after completion (Figure 1.17). High embankments were fully compacted. However, at the embankment of 80 – 100m high, time-dependent settlement of 10 – 20 mm per year occurred after several years elapsed. Occurring of particle crushing in the embankments would be one of the reasons for the time-dependent settlement.

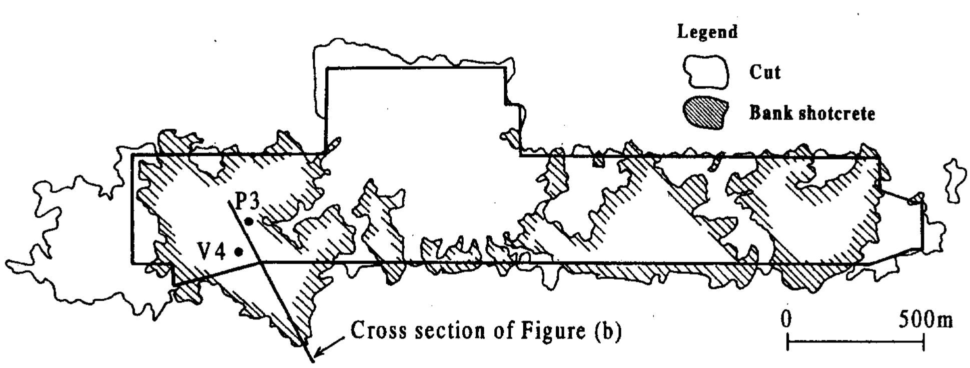


(a) Outline of embankment (horizontal projection)

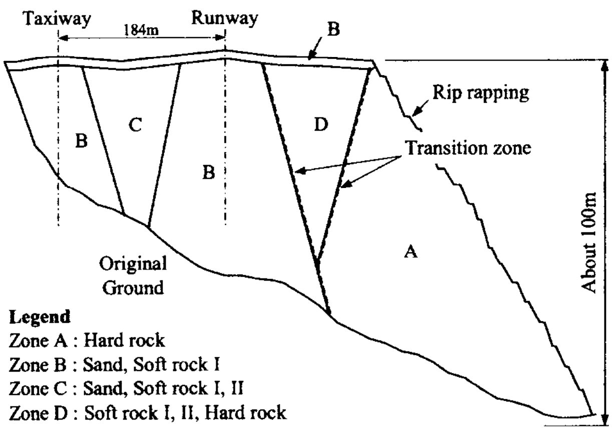


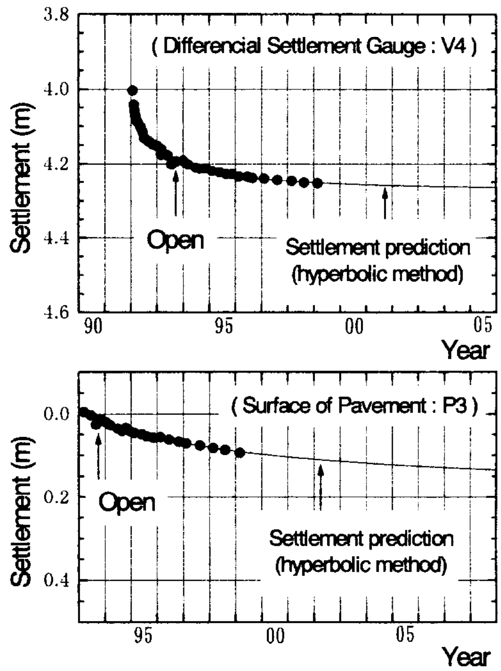


**(b) Outline of embankment(cross section)** **(c) Settlement – time curves**

**Figure 1.17 Progressive settlement on a high airport embankment (Mukai et al.,1999)**

Hirano et al.(2000) also reported time-dependent settlements of 90m high embankment made of weathered granite soil for improvement of a site for housing, industry and commerce. They conducted compression settlement tests using the apparatus shown in Figure 1.18(a) for determining the degree of compaction for the embankment. The specimens of the tests were made from the in-situ weathered granite soil. The specimens were subjected to stress controlled loading, each load was sustained over 14days. Figure 1.18(b) shows an example of the relationships between settlement and elapsed time. In this test, the specimen was subjected to seepage of water at 7days after loading. Time-dependent settlement was also observed in this test during the loading term. The gradient of settlement – elapsed time curve after the seepage was greater than the gradient of the curve before the seepage. It is considered that the time-dependent settlement would be due to particle crushing and that the progress of particle crushing would be influenced from the seepage of water.

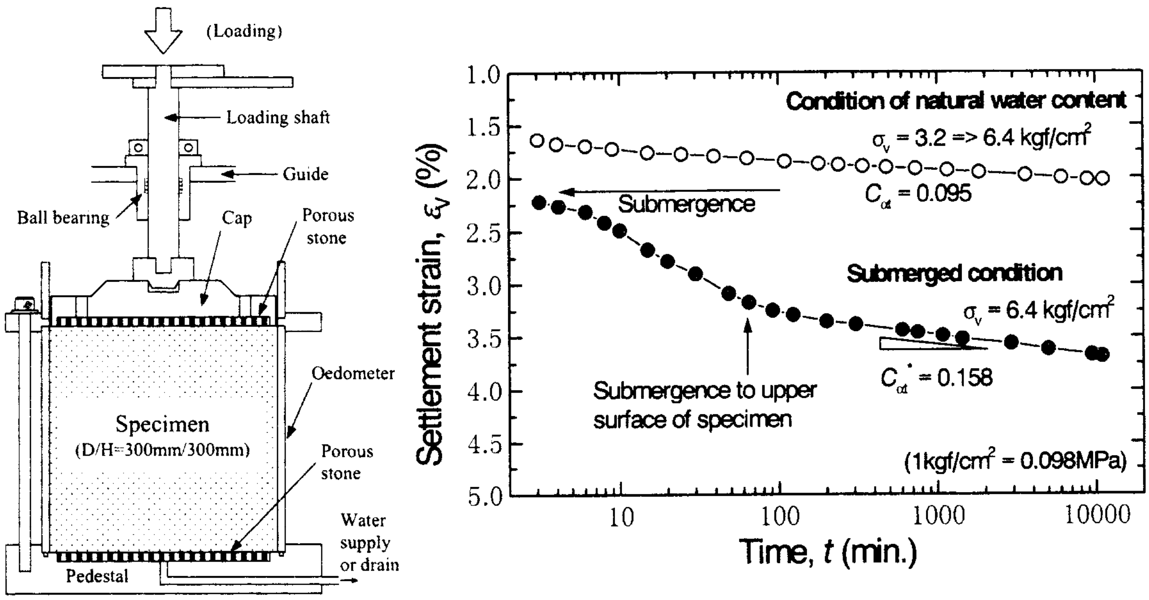


**(a) Test apparatus** **(b) an example of settlement – elapsed time curves**

**Figure 1.18 Long-term compression settlement test (Hirano et al., 2000)**

Kojima(1993) conducted consolidation tests of dried Kaorine powder to investigate the influence of adsorbed water on time-dependent compression. Figure 1.19(a) shows the data of density for three Kaorine specimens plotted against elapsed time in a logarithmic scale over the test period of 10 days. The sustained pressures were 313.6kPa, 627.2kPa and 1254.4kPa, respectively. The figure clearly shows time-dependent behavior, similar to the secondary consolidation process for saturated clays. Since there existed no water in the clay powder, the time-dependent behavior observed must be attributed to time-dependent frictional behavior at contact points of clay particles, leading to rearrangement of particle orientation. The overall compression strain of the dry Kaorine powder can be classified into three stages; instantaneous settlement, primary creep, secondary creep and the rest, as shown in Figure 1.19(b). Figure 1.19(c) shows a comparison of the primary creep behavior between the dry and the saturated Kaorine specimen, of which stress histories were identical. It is observed that the creep rate of the dry specimen is slightly larger than that of the saturated. Kojima(1993) presumed that the viscosity of adsorbed water influenced the creep rate. The author presumed that particle crushing of the Kaorine powder influenced the creep rate. The dry clay powder is time-dependently compressed due to frictional behavior at contact points of particles, accompanying with breakage at the edges of the particle. On the other hand, the saturated clay particle holds bonding water, tightly attached to the surface of the particle, and the clay particle does not directly contact with the neighboring particle. Thus breakage of particles is unlikely to occur in the saturated specimen. This difference might be the reason.

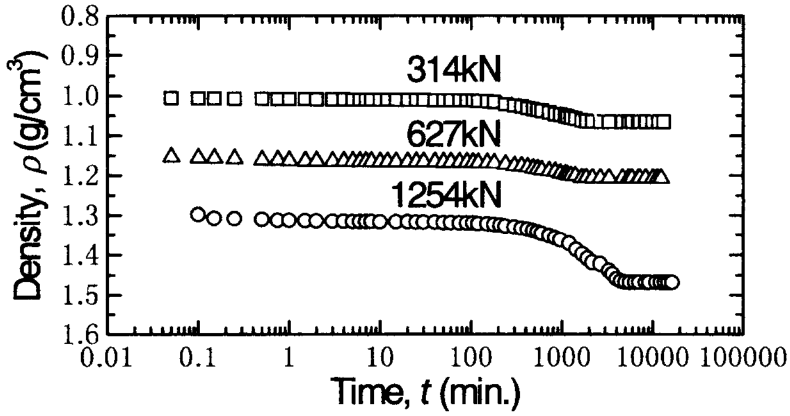


(a) Time-dependent compression of Kaoline powder

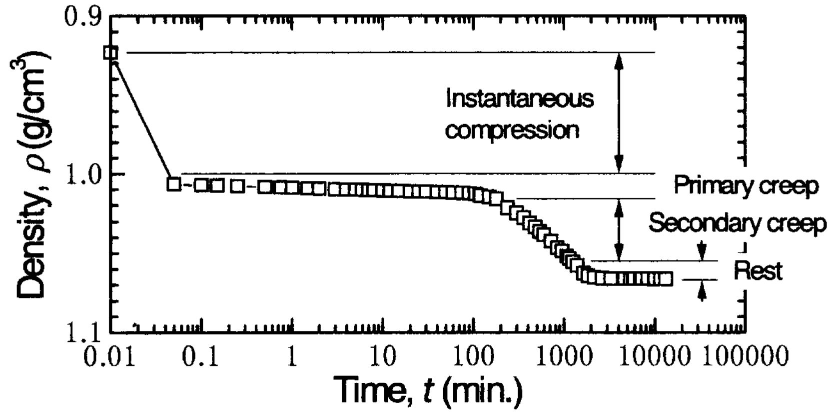


(b) Classification of compression stages of Kaoline powder

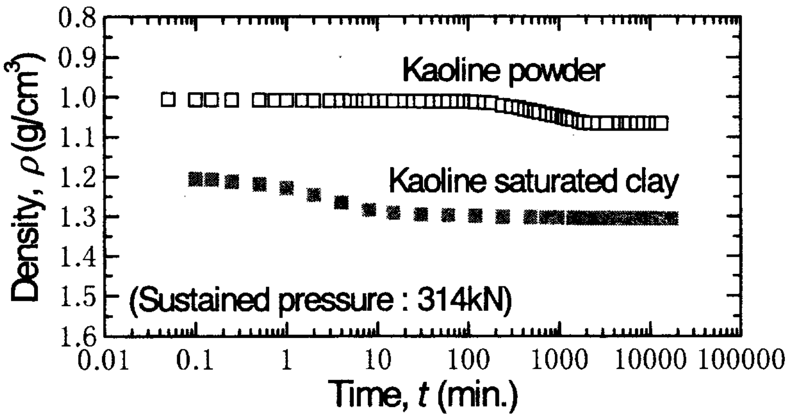


(c) Comparison between Kaoline powder and saturated Kaoline clay

**Figure 1.19 Results of consolidation tests of dry Kaorine powder (Kojima, 1993)**

Galer et al.(1999) investigated time-dependent compressibility of some decomposed granites, in the light of particle crushing. A series of triaxial compression tests was conducted on some decomposed granite soils. In the isotropic compression stages of the triaxial tests, after applying an isotropic stress increment, the progressive increase of volume change was observed though dissipation curves of pore water pressure were stabilized (Figure 1.20). They concluded that this volume change progress is due to particle crushing.

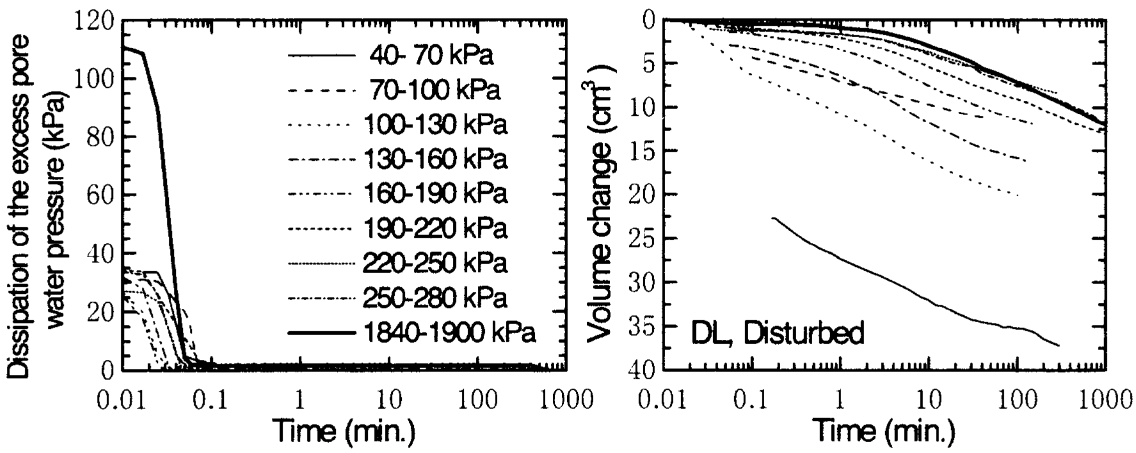


**(a) Dissipation of the excess pore water pressure** **(b) Volume change**

**Figure 1.20 Time-dependency of the volume change in constant isotropic conditions of a decomposed granite (Galer et al., 1999)**

Galer et al.(1999) also performed some crushing tests of individual particles in an attempt to investigate the crushing behavior of decomposed granite. In the crushing tests, as shown in Figure 1.21(a), first a particle first crushes, then each fragment of the first crushing crushes, and finally each fragment of the second crushing crushes. The results of these tests(Figure 1.21(b)) showed that the probability of survival decreases for fragments originated from the same particle. But Galer et al. indicated that these results alone could not fully explain the time-dependent behavior of decomposed granite and that further research should be carried out to integrate the stress-strain behavior of individual constitutive particles into the behavior of a whole specimen.

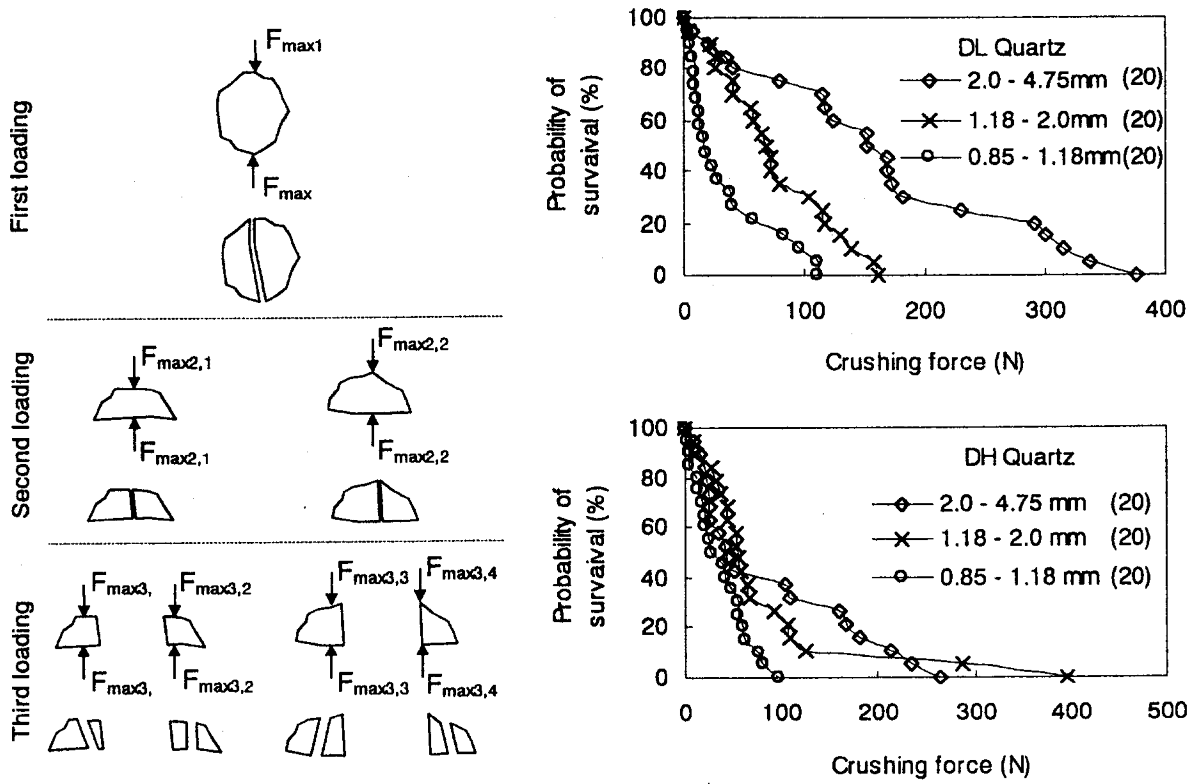


**(a) Sequence of three stage crushing** **(b) Probability of survival vs. crushing force**

**Figure 1.21 Three stage crushing tests of individual particles (Galer et al.,1999)**

Sinjo(2000) carried out creep tests of carbonate sand in coral reefs using oedometer. The creep deformation increased continuously for long time period (Figure 1.22(a)). He measured vertical pressure and lateral pressure during each test, and showed the variation of value of *K*o with time (Figure 1.22(b)). Compression strain gradually increases with time and seems to converge at around 24 hours, but after that it starts increasing again. The value of *K*o exhibits fluctuation after 24 hours. From these measurements, he concluded that creep deformation increased continuously for long time period with an alteration of particle breakage and rearrangement.

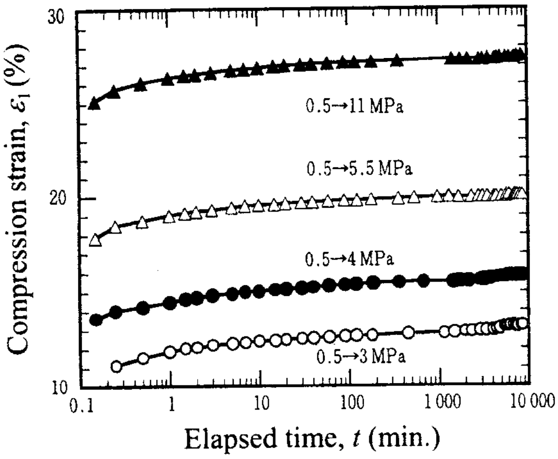


**(a) Compression strain vs. logarithm of time**

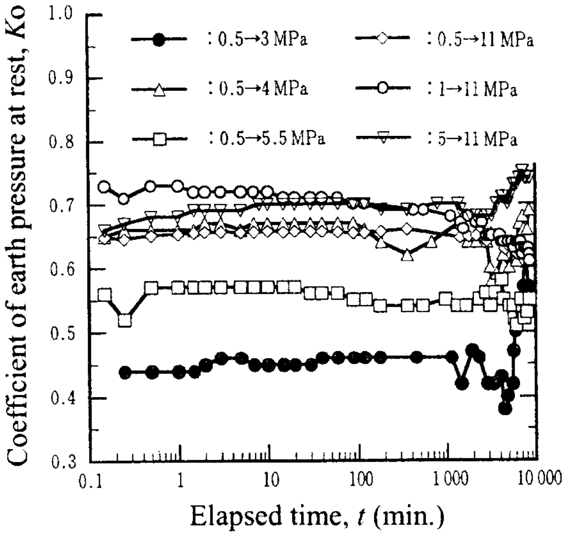


**(b) Value of $Ko$ vs. logarithm of time**

**Figure 1.22 Creep tests of carbonate sand in coral reefs (Sinjo, 2000)**

The summary of the Subsection 1.3.2 is as follows :

- In laboratory soil tests, for example triaxial compression test and one-dimensional compression test, of specimens made of particulate geomaterials under high pressure ranges, time-dependent behavior due to particle crushing have been discussed through the following facts: (a) time required to reach convergence of consolidation increased as confined pressure was increased, (b) changes in particle size distributions were observed and crushed particles were observed by a microscope, (c) volume changes of specimen were observed though dissipation curves of pore water pressure were stabilized, etc..
- In in-situ tests or measurements of settlements of prototype structure, it was supposed based on the component of ground (that is to say, the ground was mainly made of crushable geomaterials) that time-dependent settlement of plate or structure was due to particle crushing. The time-dependent settlement continued for a long time (during about several years). It was considered that water existence would be influenced the time-dependent settlement.
- The experimental studies by Leung et al.(1996) and Yet et al.(1996) verified occurrence of time-dependent behavior due to particle crushing. The mechanism of the behavior has been considered to be an alteration of particle breakage and rearrangement. But there was no study that discussed the process of particle crushing of individual particles during time-dependent behavior.

## 1.4 Objectives of this study

Time-dependent behavior of crushable geomaterials or granular materials subjected to high pressures has been indicated by several researchers through in-situ tests, laboratory model tests and structures in use. The mechanism has been considered to be an alteration of particle breakage and rearrangement. However, the study of the detailed mechanism of the behavior (that is to say, the study from the viewpoint of microstructure of soil) has not been conducted yet.

The main purpose of this study is to clarify the detailed mechanism of time-dependent behavior due to particle crushing. The concept of this study is the flow shown in Figure 1.2. In this study, detailed mechanism of each stage (particle crushing, rearrangement of particles and redistribution of contact stress) will be investigated through three kinds of model tests with careful visual observations and numerical analyses.

The objectives of this study can be summarized as follows :

(a) to reappraise plate loading tests performed on weathered granite grounds in order to confirm the occurrence of time-dependent behavior of natural geomaterials mainly due to particle crushing and clarify the characteristics of the behavior ;

(b) to conduct a series of single particle crushing tests against four crushable materials in order to clarify the crushing behavior of the materials, and to calculate statistical values of characteristic values obtained from the tests in order to grasp the degree of variation of the characteristic values ;

(c) to conduct a series of one-dimensional compression tests with careful visual observations against the four crushable materials for the purpose of clarifying the detailed mechanism of time-dependent compression of a specimen due to particle crushing in one-dimensional compression test, and to conduct a series of creep tests of single particles for separating the strain due to creep from all time-dependent strain, that is to say, separating the strain due to particle crushing ;

(d) to conduct a series of model footing loading tests on a model ground made of a sort of crushable material in order to clarify the detailed mechanism of time-dependent settlement of footing ;

(e) to recommend a method of numerical modeling for particle crushing, and to analyze an one-dimensional compression test taking into account the modeling in order to verify that the modeling represents the time-dependent behavior due to particle crushing.

Figure 1.23 shows the flow of this study.

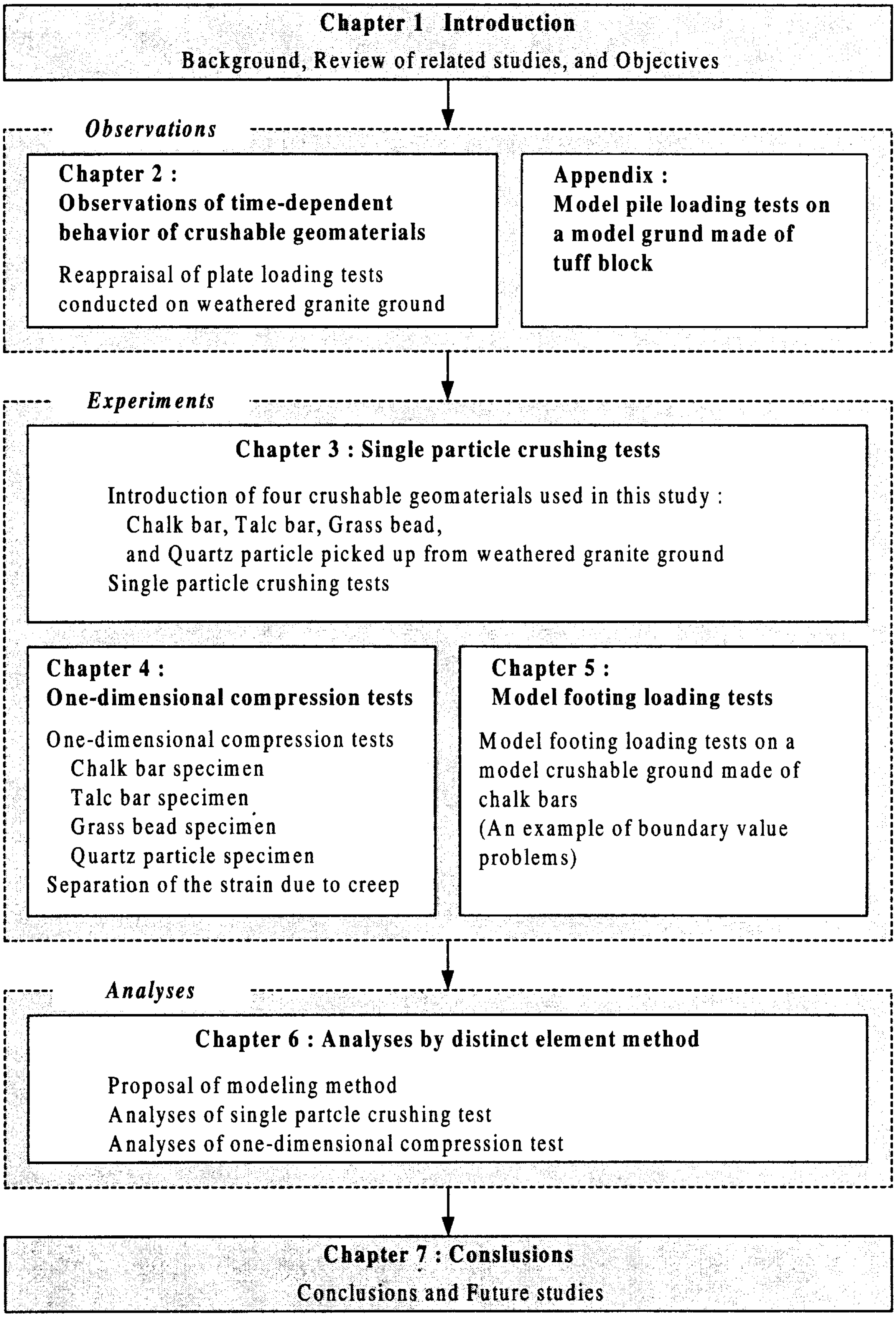


**Figure 1.23 Flow of this study**

# CHAPTER 2

# OBSERVATIONS OF TIME-DEPENDENT SETTLEMENT OF PLATE LOADING TESTS ON WEATHERED GRANITE GROUND

## 2.1 Introduction

In Chapter 2, reappraisal of the data of plate loading tests on crushable geomaterials is made to confirm the time-dependent behavior due to particle crushing. The plate loading tests were conducted on a decomposed granite ground at three different degrees of weathering by Hattori et al.(1998b) and Galer et al.(1998). The progress of settlement is plotted against elapsed time under each loading stage. The characteristics of time-dependent behavior and the relationship between the characteristics of time-dependent behavior and soil parameters are discussed.

## 2.2 Outlines of the weathered granite ground and plate loading tests

The plate loading tests described in this Chapter were carried out at the following three decomposed granites :

- Hiroshima, in Hiroshima prefecture, Japan (Hattori et al., 1998b),
- Ube, in Yamaguchi Prefecture, Japan (Galer et al., 1998 and Galer, 1999), and
- Abukuma, in Fukushima prefecture, Japan (Hattori et al., 1998c).

The general descriptions of these sites are listed in Table 2.1. Table 2.2 shows all the test cases investigated in this Chapter.

The degree of weathering for granite, shown in Table 2.1 and 2.2, were judged based on the rock classification standard for weathered granite provided by Honshu-Shikoku Bridge Authority (Yamagata and Kurino, 1984). The elastic wave velocities $V_p$ and $V_s$ given by the seismic refraction tests were mainly taken into account for the classification of the decomposed granites. The class DL denotes a more advanced state of weathering than the class DH. In Hiroshima site, plate loading tests were performed at two sites with different degrees of weathering, DL and DH. In other two sites, all the tests were conducted on DL class weathered granite. Since the test sites were situated on the hill or hillside, the ground water level of those sites were well below the ground surface.

Each test was conducted in accordance with the standard of JGS1521-1995. The load of each loading stage was kept constant for 15-30 minutes.

After the test in Hiroshima, the ground under the plate was vertically cut, and the vertical section was observed. Hattori et al.(1998b) found the development of horizontal microcracks in the ground below the plate. The record of the ground deformation did not show bulging at the ground surface during the loading. From these results, the failure mechanism of the plate loading tests would be of local shear failure. After a series of the tests, two undisturbed samples were taken; one from the area under the plate and the other from the area far from the plate, and observed by using a polarization-microscope. The photographs by the polarization-microscope are shown in Photograph 2.1. It is obvious that more particle crushing occurred in the specimen of under the plate than that of far from the plate.

The plate loading tests in Ube and Abukuma also revealed a failure mechanism of local shearing type, coupled with particle crushing beneath the footings.

**Table 2.1 Sites of weathered granite ground conducted plate loading tests ( Hattori et al., 1998b, 1998c, Galer et al., 1998 and Galer, 1999 )**

| Site name | Hiroshima | | Ube | | Abukuma | |
|---|---|---|---|---|---|---|
| Location | Western Japan Hiroshima Prefecture | | Western Japan Yamaguchi Prefecture | | Eastern Japan Fukushima Prefecture | |
| Topography | Hills | | Hillside | | Hills | |
| Elevation | 270 m | | 105 m | | 500 – 800 m | |
| Category of granite | Biotite granite | | ( unknown ) | | Grano-diorite | Biotite granite |
| Period | Cretaceous period | | ( Mesozoic ) | | Jurassic period – Cretaceous period | |
| Mineralogical conposition | Quartz (40%)<br>Feldspar (32%)<br>Plagioclase (22%)<br>Biotite (6%) | | Quartz (25%)<br>Feldspar (33%)<br>Plagioclase (28%)<br>Biotite (14%) | | Q. (39%)<br>F. (5%)<br>P. (42%)<br>B. (9%)<br>Amphibole<br>Ortho-pyroxene | Q. (30%)<br>F. (24%)<br>P. (35%)<br>B. (8%) |
| Degree of weathering * | DL | DH | DL (Site A) | DL (Site B) | DL | |
| Moisture content, $w$(%) | 13.1 | 1.71 | 9.63 | 11.17 | Approximately 10% | |
| Total density, $\rho_t$ (kg/m$^3$ ) | 1754 | 2147 | 1836 | 1819 | 1880 | |
| Dry density, $\rho_d$ (kg/m$^3$ ) | 1551 | 2111 | 1675 | 1636 | 1630 | |
| Void ratio, $e$ | 0.710 | 0.260 | 0.554 | 0.602 | 0.64 | |
| Porosity, $n$ (%) | 41.52 | 20.63 | 35.65 | 37.58 | – | |
| Degree of saturation, $S_r$ (%) | 49.10 | 17.64 | 45.25 | 48.63 | – | |
| References | Hattori et al. (1998b) | | Galer et al. (1998)<br>Galer (1999) | | Hattori et al. (1998c) | |

* Classification of weathered granite rocks (after Yamagata and Kurino, 1984)

**Table 2.2 Outline of plate loading tests (Hattori et al., 1998b, Galer et al., 1998 and Galer, 1999)**

| Site | Test Name | Degree of weathering | Configuration of plate | Diameter of plate (mm) | Performed year and month |
|---|---|---|---|---|---|
| Hiroshima | Hiro_DH_C100 | DH | Circular | 100 | November 1995<br>July 1996 |
| | Hiro_DH_C200 | | | 200 | |
| | Hiro_DH_C300 | | | 300 | |
| | Hiro_DL_C100 | DL | Circular | 100 | |
| | Hiro_DL_C200 | | | 200 | |
| | Hiro_DL_C300 | | | 300 | |
| Ube | Ube_A_C200 | DL (Site A) | Circular | 200 | August 1997 |
| | Ube_A_C300 | | | 300 | |
| | Ube_B_C200 | DL (Site B) | Circular | 200 | |
| | Ube_B_C300 | | | 300 | |
| Abukuma | Abu_12 | DL | Circular | 300 | February 1993 |
| | Abu_13 | | | | |
| | Abu_21 | | | | |
| | Abu_25 | | | | |
| | Abu_28 | | | | |
| | Abu_E11 | | | | |
| | Abu_E5 | | | | |
| | Abu_E7 | | | | |

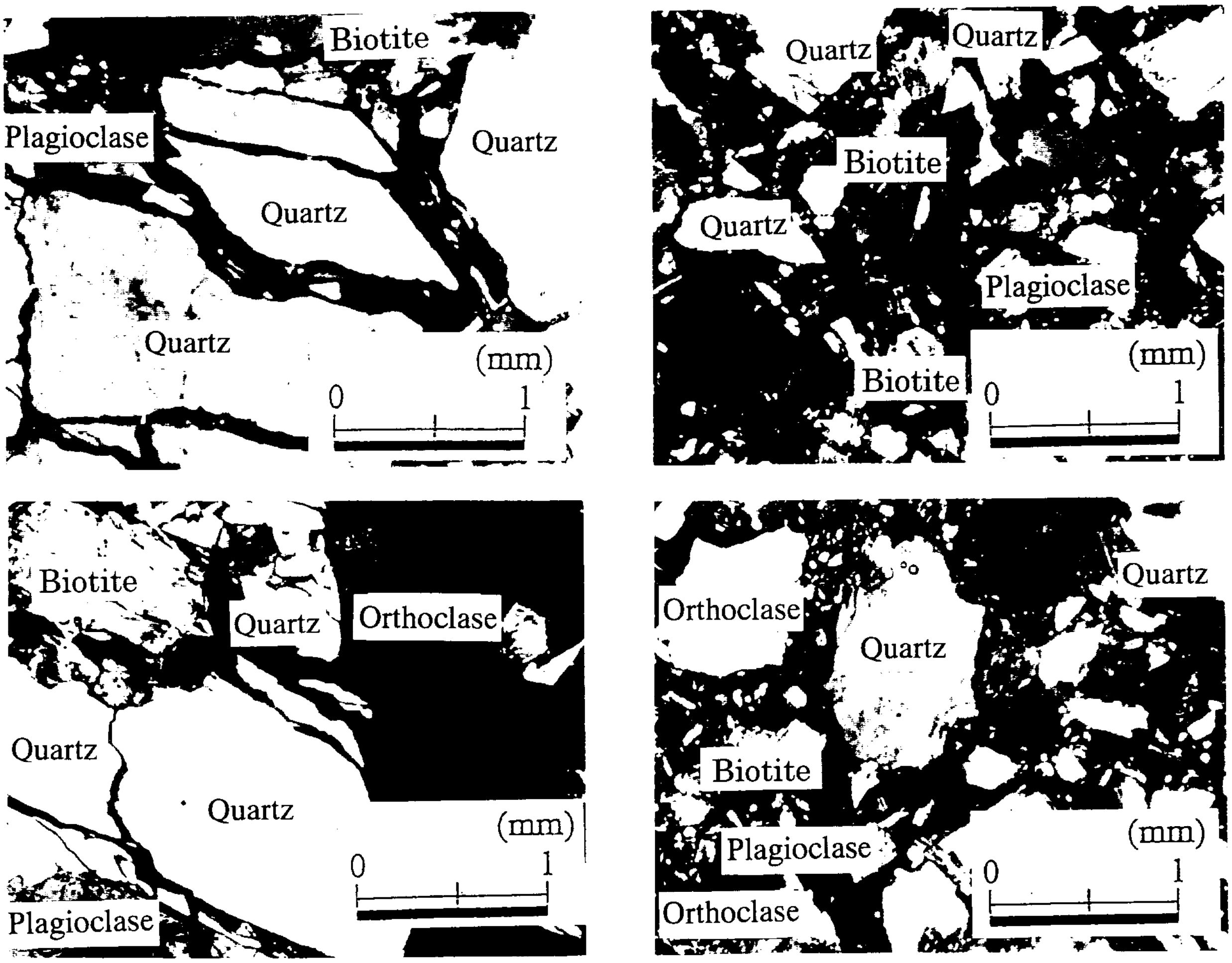


**(a) Specimen far from footing** **(b) Specimen under footing**

**Photo. 2.1 Observation of particle crushing (Hattori et al., 1998b)**

## 2.3 Reappraisal of test results and discussions

In Figure 2.1, the data of average plate pressure($p$) are plotted against the settlement($S$) normalized by the plate diameter($B$). Clearly peak loads are not observed in any of these $p$ – $S/B$ curves.

Figure 2.2 shows examples of the plots of the variation of plate settlement with time under sustained loads. The plate settlement increases linearly with time of logarithmic scale. The larger the sustained load is, the greater the gradient of the settlement-time curve is. The gradient of settlement – time curve is a rate of creep settlement, which is called $C_{\alpha s}$ in this chapter. The gradient was defined as the creep coefficient by Leung et al.(1996) and Yet et al.(1996) who conducted loading tests of piles under the acceleration field in a centrifuge. Since the ground water level of those sites were well below the ground surface, it is considered that the time-dependent settlement of the plate was caused not by dissipation of excess pore water pressure, but by particle crushing phenomena.

Figure 2.3 shows the variation of the rate of creep settlement ($C_{\alpha s}$) versus the average plate pressure($p$) with various degrees of weathering and with various diameters of plate. The $C_{\alpha s}$ is noted to increase roughly linearly with bearing pressure. The magnitudes of $C_{\alpha s}$ of DL are larger than those of DH. In the same degree of weathering, and at the same bearing pressure, the larger the diameter of plate, the larger the rate of creep settlement. It is considered that this tendency is stemmed from the size effect. It is considered that this size effect would be a reflection of crushing phenomena of soil particles (or failure of ground in the case of intact ground material) : The stress bulb having a intensity under a large plate is larger than that of a small plate. When the intensity of the stress bulb is comparable to the crushing strength of particles in the bulb, the number of crushed particles in the bulb of the large plate would be more than the corresponding number of the small plate. It is considered that the settlement and the rate of creep settlement of the large plate would be larger than those of small plate, according to the number of crushed particles.

From Figure 2.3, it was clear that $C_{\alpha s}$ was related to the degree of weathering. Thus it is considered that $C_{\alpha s}$ is related to the elastic wave velocity of ground which is mainly referred for determination of the degree of weathering. Figure 2.4 presents the relationships between the rate of creep settlement $C_{\alpha s}$ and elastic wave velocities $V_p$ and $V_s$ obtained from seismic prospecting at the test locations. Each figure is plotted under a plate pressure and a plate diameter. The $C_{\alpha s}$ decreases with increasing of $V_p$ or $V_s$. However, it is observed that variability in $C_{\alpha s}$ increases with decreasing of $V_p$ or $V_s$. It is obvious that some other factors influencing the value of $C_{\alpha s}$ would exist.

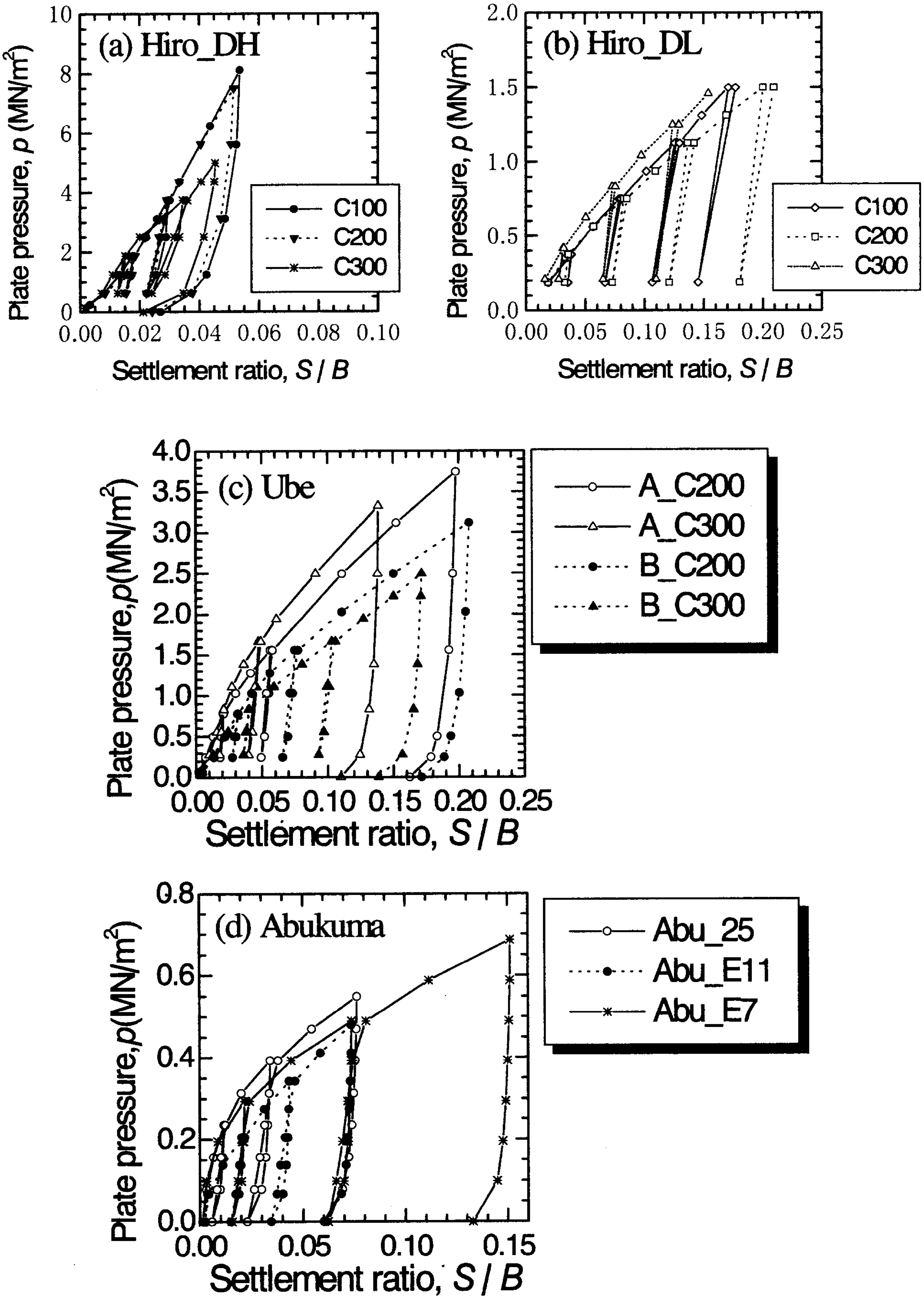


**Figure 2.1 Load-settlement curves of plate loading tests ( Hattori et al., 1998b and Galer et al., 1998)**

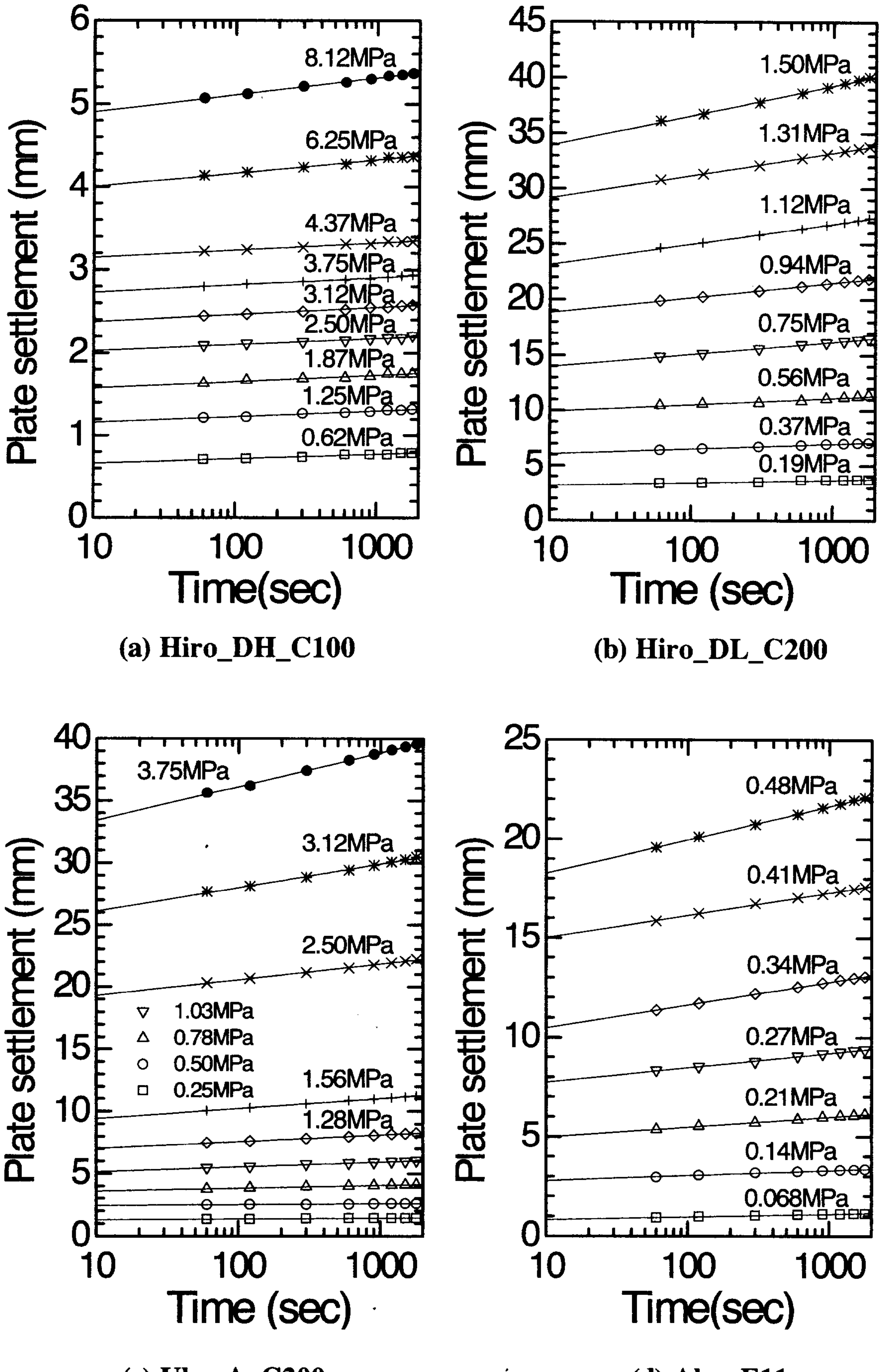


**(a) Hiro_DH_C100** **(b) Hiro_DL_C200**

**(c) Ube_A_C200** **(d) Abu_E11**

**Figure 2.2 Plate settlement - time curves**

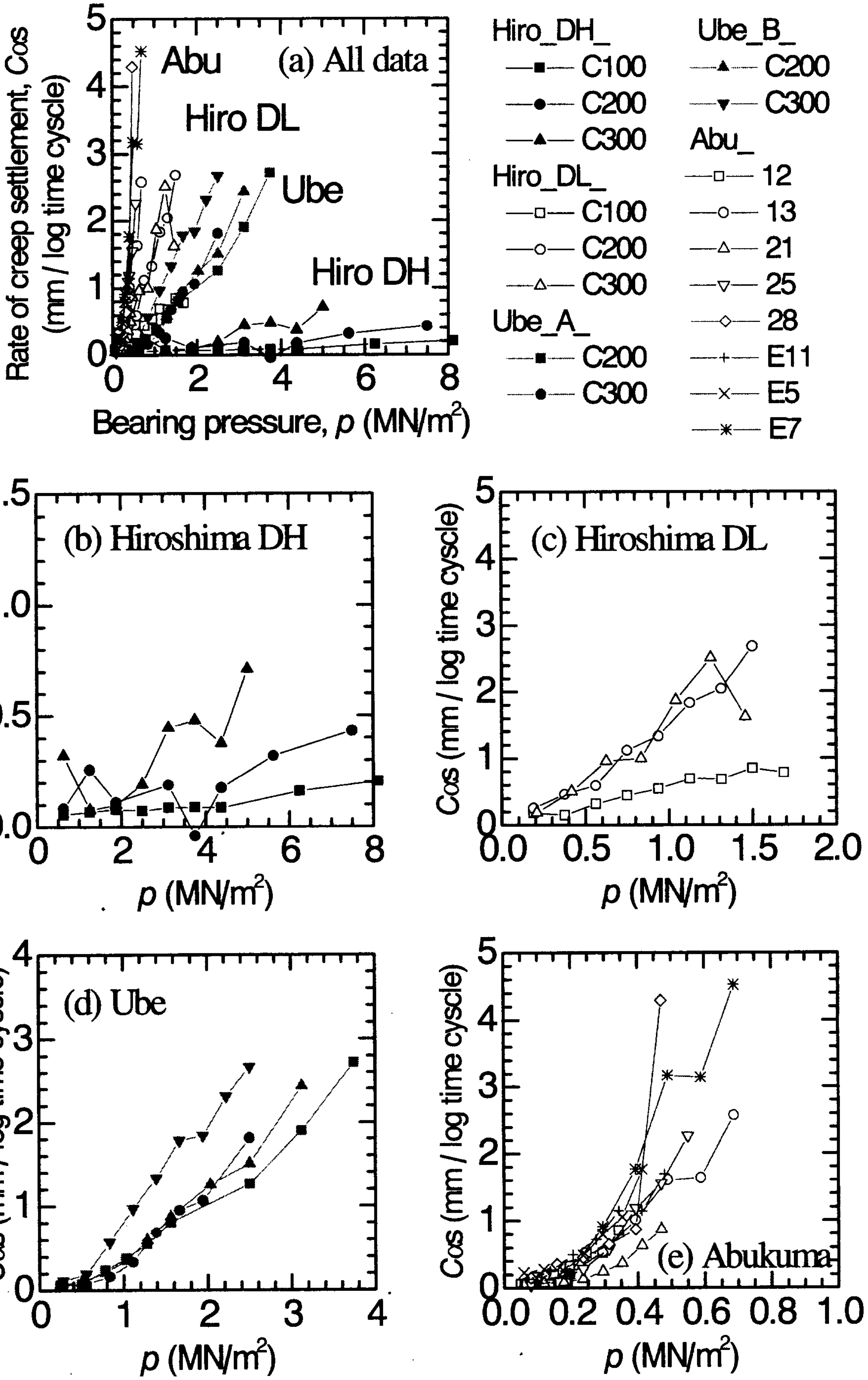


**Figure 2.3 Rate of creep settlement($C_{\alpha s}$) versus bearing pressure**

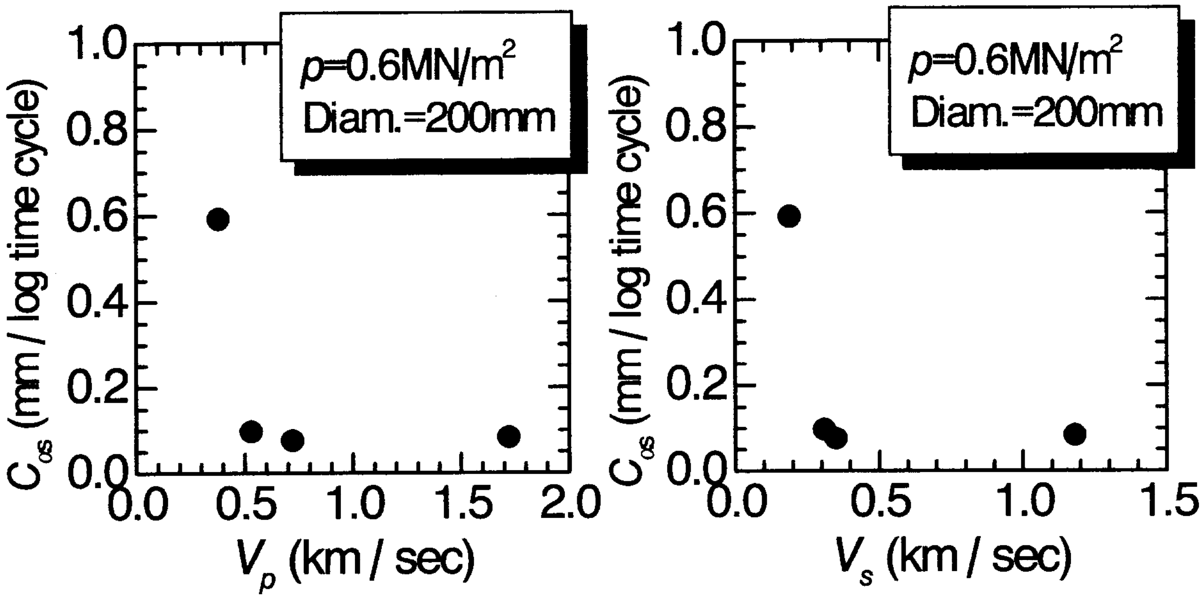


(a) $p = 0.6\mathrm{MN/m^2}$, Plate diameter : 200mm

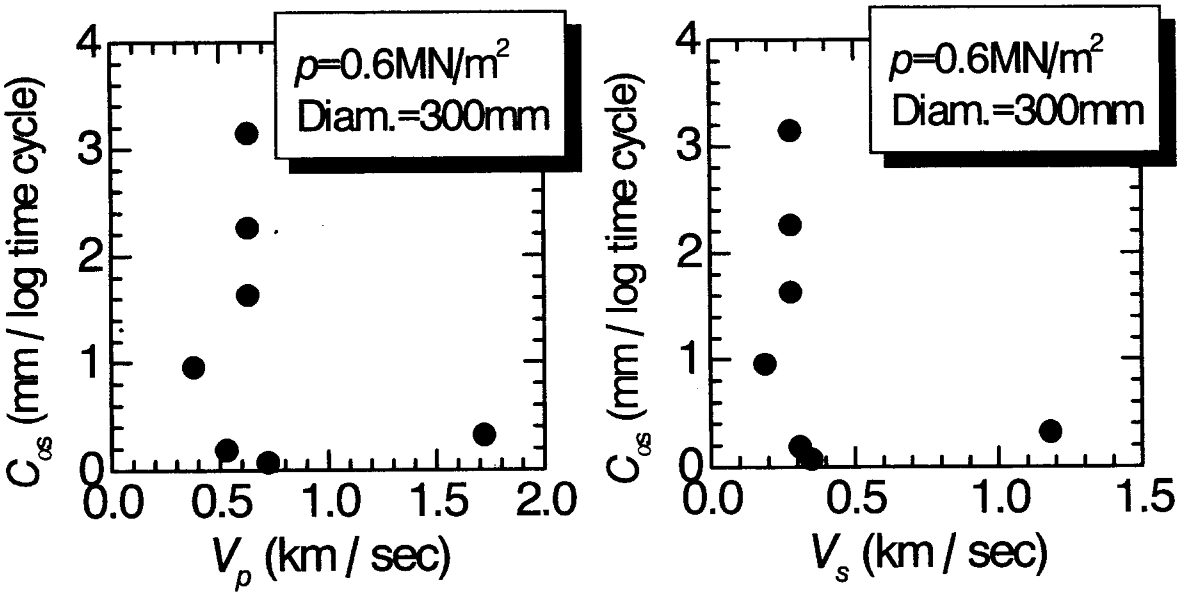


(b) $p = 0.6\mathrm{MN/m^2}$, Plate diameter : 300mm

**Figure 2.4 Rate of creep settlement($C_{\alpha s}$) versus elastic wave velocity**

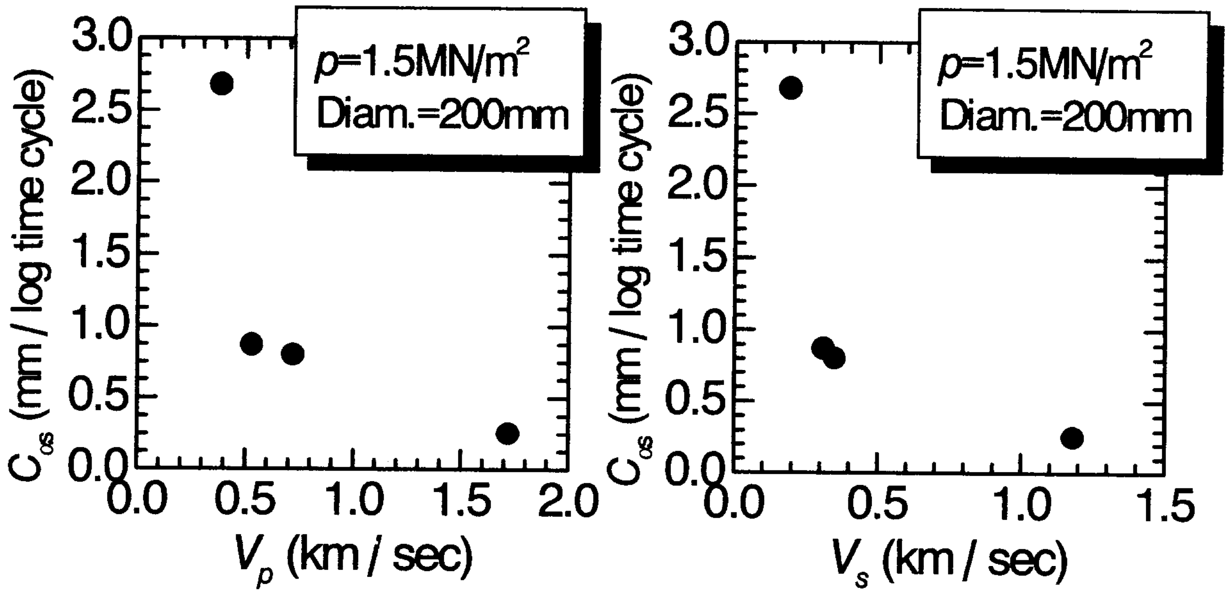


(c) $p$ = 1.5MN/m$^2$, Plate diameter : 200mm

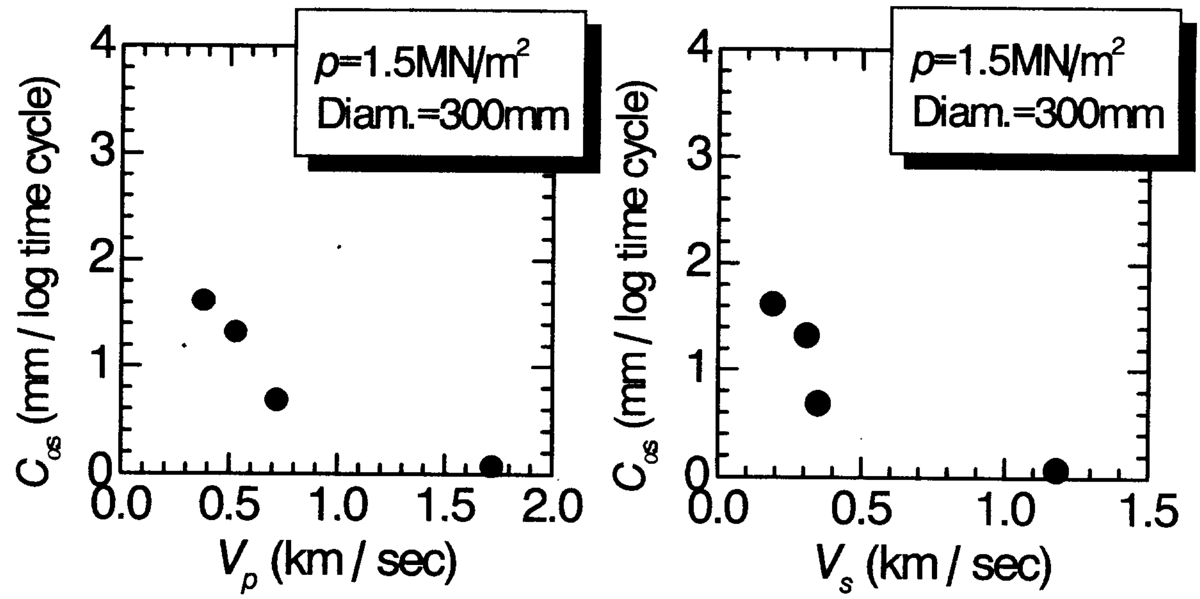


(d) $p$ = 1.5MN/m$^2$, Plate diameter : 300mm

**Figure 2.4 Rate of creep settlement($C_{\alpha s}$) versus elastic wave velocity**

## 2.4 Conclusions

In Chapter 2, reappraisal of plate loading tests conducted on a weathered granite ground, where crushing phenomena had been observed beneath the plate after a test, were performed. The following conclusions are drawn.

- Time-dependent settlement of plate was occurred even on the dry ground. The settlement of plate increased almost linearly with time of logarithmic scale.
- The gradient of settlement – elapsed time curve (called rate of creep settlement) increased with increasing of plate pressure, degree of weathering and area of plate.
- The size effect of the rate of creep settlement is considered to be a reflection of crushing phenomena in the ground.
- The rate of creep settlement was related to elastic wave velocity of ground, but there would exist some other factors that affect the rate of creep settlement.

# CHAPTER 3

# PROPERTIES OF CRUSHABLE MATERIALS AND SINGLE PARTICLE CRUSHING TESTS

## 3.1 Introduction

In the last chapter, time-dependent settlement of plate loading tests on a ground made of crushable geomaterials was discussed. In the following chapters, Chapters 4 and 5, this phenomenon will be verified and discussed by laboratory model tests. Ground condition will be simplified for the laboratory tests. Specimen or model ground will be made of particulate and cohesionless crushable materials. Configuration of particles of these materials will be cylindrical or spherical. The cylindrical particles will be packed in a steel box two-dimensionally by hexagonal or simple cubic packing.

In Chapter 3, four crushable particulate materials used in the model tests of Chapters 4 and 5 will be introduced. Main properties of the four particulate materials will be explained in Section 3.2. Single particle crushing tests will be performed against the four materials. The results and discussion of these tests will be also described in Section 3.3.

As mentioned in Chapter 1, time-dependent behavior due to particle crushing may be considered to progress by occurring "particle crushing" and subsequent "rearrangement of fragments" and "stress redistribution". Single particle crushing tests will give us basic information about "particle crushing" and "rearrangement".

## 3.2 Crushable particulate materials used in experiments and the reasons for choosing these materials

Four different materials were selected for this study. They are

- Chalk bar,
- Talc bar,
- Glass bead,

and

- Quartz particle from weathered granite ground.

The main characteristics of the four particles are shown in Table 3.1. It is considered that the time-dependent behavior of a brittle material would be different from that of a ductile material. Thus glass bead was selected as the brittle material, while chalk bar was chosen as the ductile material. Quartz particle was also tested as a natural and crushable material. Talc bar was also selected as the ductile material, but as after-mentioned, the brittleness of the talc bar is about three times larger than that of the chalk bar (see Table 3.2). Another reason for selecting the talc bar is to investigate the influence of the existence of water on the time dependency.

The chalk bar, talc bar, and glass beads used were commercially available industrial materials. The chalk bars and the glass beads are artificial materials, while talc bars are natural materials. They are cored from natural talc. Quartz particles were obtained from the Hiroshima DL weathered granite (Hattori et al., 1998a).

The chalk bars and the talc bars were in a cylindrical. In the experiments of this study, they were laid down, and were piled up two-dimensionally for visualization of crushing phenomena.

The results of unconfined compression tests of chalk bars and talc bars are shown in Table 3.2. From these tests and the single particle crushing tests mentioned after, the brittleness were obtained. The brittleness of the talc bar is about three times larger than that of the chalk bar.

The outside appearance of the four particulate materials are shown in Photograph 3.1.

**Table 3.1 Main characteristics of particles**

| | Chalk bar | Talc bar | Glass bead | Quartz particle |
|---|---|---|---|---|
| Natural or artificial | Artificial | Natural (trimmed rock) | Artificial | Natural |
| Main component | $CaCO_3$ | Natural talc | (Glass) | Origin ground : Weathered granite ground of Hiroshima<br>Class : DL ‡ |
| Shape | Cylindrical | Cylindrical | Sphere | (Angular) |
| Size | Diam. : 9.3 – 9.7 mm<br>Length : 30 mm † | Diam. : 6.3 – 6.4 mm<br>Length : 20 mm † | Nominal diameter : 1 mm | Grain size :<br>1) 0.85 mm – 2.0 mm<br>2) 2.0 mm – 4.75 mm |
| Density | 1.64 $Mg/m^3$ | 2.81 $Mg/m^3$ | 2.5 $Mg/m^3$ | 1.64 $Mg/m^3$<br>(Hattori et al.,1998a) |

† Chalk bars and talc bars were cut by wire saw and those cross sections were sandpapered.
‡ Classification of weathered granite rocks (after Yamagata and Kurino, 1984)

**Table 3.2 Unconfined compression strength and brittleness of chalk bar and talc bar**

| | Chalk bar ‡ | Talc bar ( Dry ‡ ) | Talc bar (Saturated) |
|---|---|---|---|
| Diameter of specimen | 9.3mm – 9.7 mm | 6.3mm – 6.4 mm | 6.3mm – 6.4 mm |
| Length of specimen | 20 mm | 13 mm | 13 mm |
| The number of tests | 5 | 6 | 6 |
| Unconfined compression strength (Mean value) | 3.60 $MN/m^2$ | 17.4 $MN/m^2$ | 13.1 $MN/m^2$ |
| Coefficient of variation | 0.220 | 0.407 | 0.472 |
| Tensile strength ( from Table 3.3) | 0.667 $MN/m^2$ | 0.983 $MN/m^2$ | 0.691 $MN/m^2$ |
| Brittleness † | 5.4 | 17.7 | 19.0 |

† Brittleness = Unconfined compression strength / Tensile strength
‡ Chalk bars and talc bars(Dry) were tested in oven-dry condition.
( They dried in an oven at a controlled temperature of 110°C for 24 hours. )

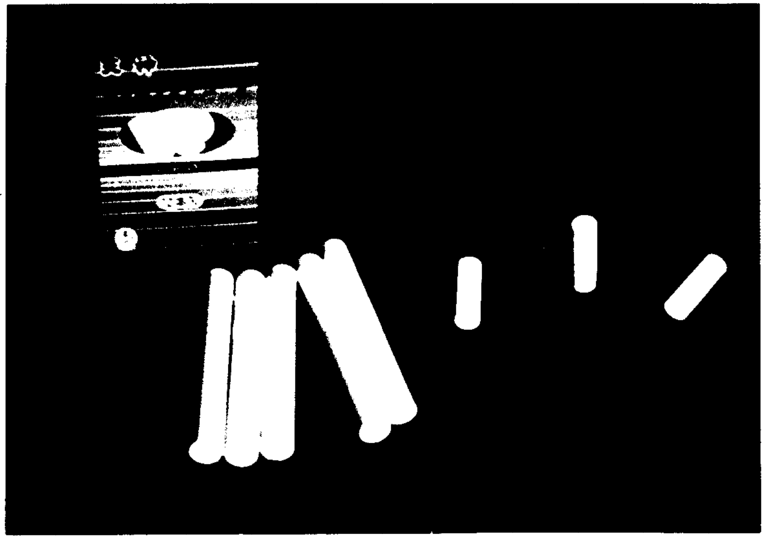

(a) Chalk bars

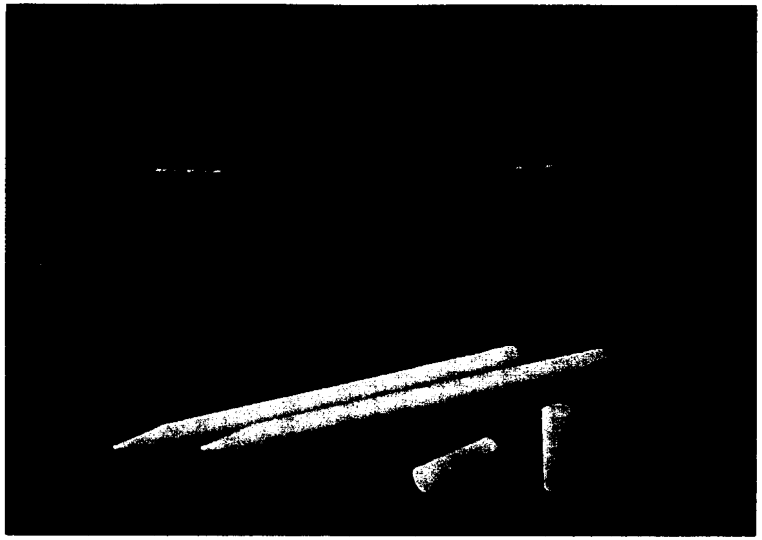

(b) Talc bars

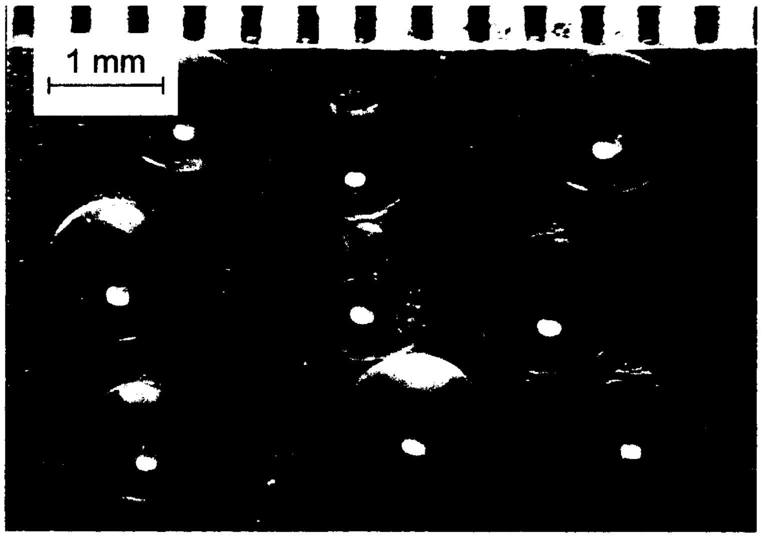


(c) Glass beads

(d) Quartz particles

Photo. 3.1 Crushable granular materials used in this study

### 3.3 Single particle crushing tests

#### 3.3.1 Purposes of this test

Single particle crushing tests have been conducted by many research workers and the methods of these tests are almost the same : a soil particle placed between flat platens was crushed only by vertical diametral compression forces to mainly obtain tensile strength of the particles. Based on the mechanism of time-dependent behavior previously explained in Chapter 1, the purposes of single particle crushing tests in the present study is to obtain the following information ;

(1) force – displacement curve,

(2) crushing behavior of each particle during loading,

(3) crushing strength,

(4) characteristic initial stiffness ( initial gradient of characteristic stress – characteristic strain curve),

(5) number of fragments after crushing, and

(6) shape of each fragment after crushing.

#### 3.3.2 Test procedures

Figure 3.1 illustrates the single particle crushing test set up, using a loading frame of conventional triaxial test apparatus. Photograph 3.2(a) shows the test apparatus.

Each particle was placed in the steadiest possible condition. Photographs 3.2(b) – (e) shows the setting of each particle. The chalk bar and the talc bar were crushed like the Brazilian test. The particle was then loaded under a constant deformation rate of 0.625mm/min. for chalk bar specimens, 0.175mm/min. for talc bars, and 0.088mm/min. for glass beads and quartz particles. Loading was continued until the particle crushed entirely, indicating that the particle cannot sustain the load applied. If the particle did not crush completely, the test was terminated after 3 minutes.

A load was used to monitor the loading force, while two gap sensors measured the displacement of the pedestal shown in Figure 3.1. Main performance of load cell, gap sensor and A/D converter were as follows ;

- Load cell with its pre-amplifier :

  Capacity : 1kN,

  Output volt set : 4V / 800N,

- Gap sensors with its exclusive converter :

  Capacity : 4 mm,

  Output volt : ±5V / ±2mm,

- A/D converter :

  Resolution : ±5 V / 14 bit.

From the above-mentioned performance, the accuracy of load cell is 0.12N, and that of gap sensor is 0.00025mm.

Use of a digital microscope with maximum magnification of 175 permitted us to make visual observation of particle behavior under compression and crushing. A video deck was used for recording.

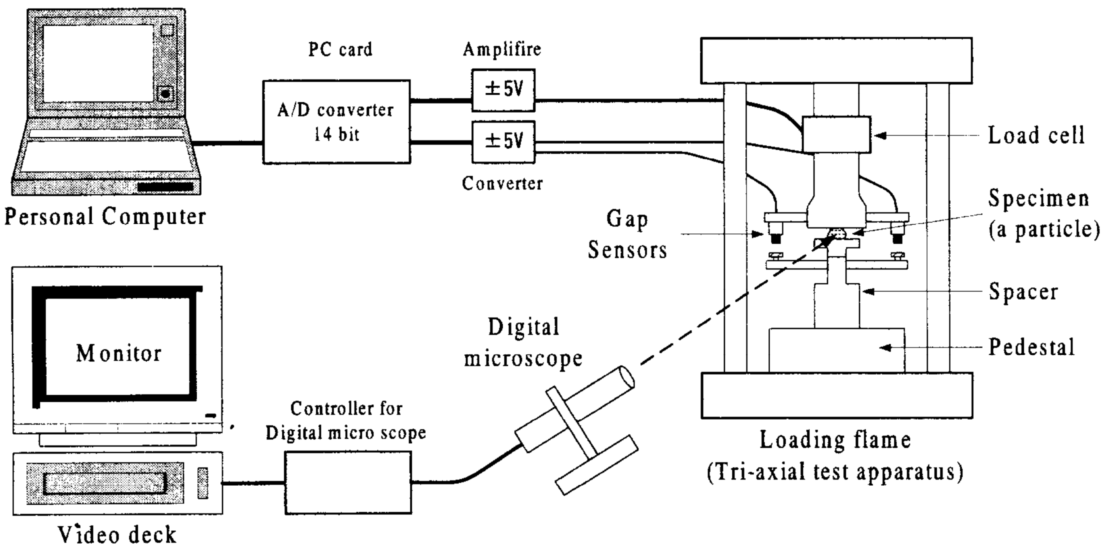


**Figure 3.1 Test apparatus and measurement system for single particle crushing test**

Chalk bars were tested in oven-dry conditions; chalk bars were dried in an oven at a controlled temperature of 110°C for 24 hours. Talc bars were tested in the oven-dry condition and saturated condition. For the saturated condition, talc bars were submerged under water and a vacuum of 100kPa was applied to them for 12 hours. But change in mass was negligible. Glass beads and quartz particles were tested under room-dry conditions. All tests were performed under a room temperature.

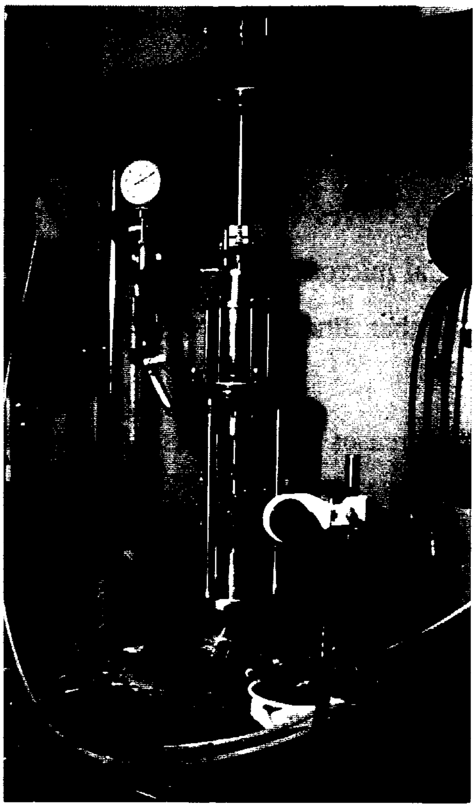

(a) Test apparatus

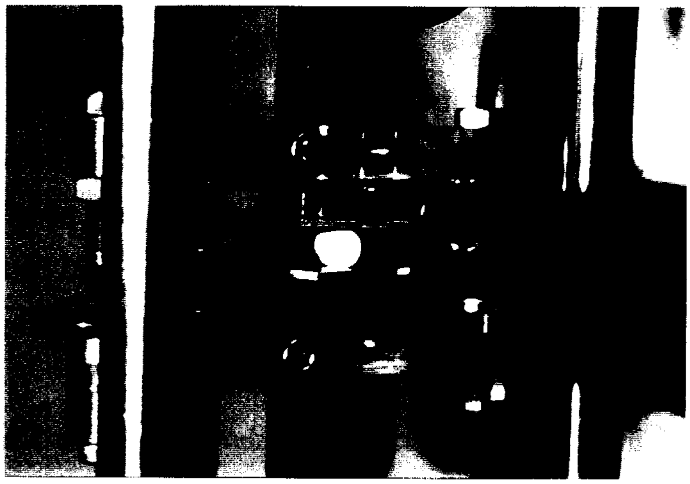

(b) Chalk bar

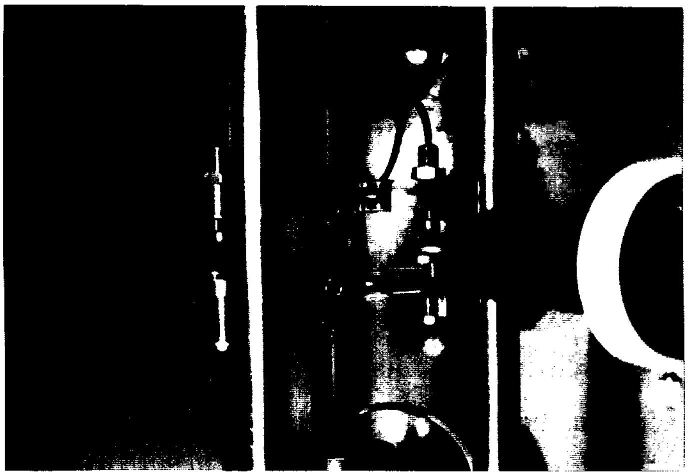

(c) Talc bar (dry)

(d) Talc bar (saturated)

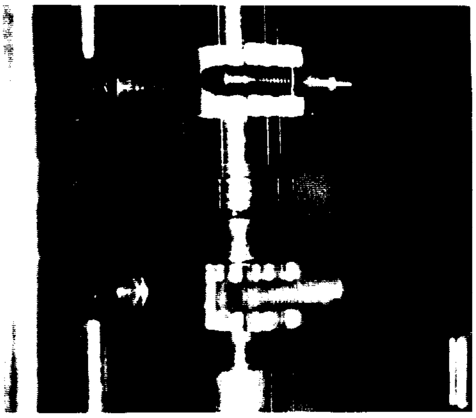

(e) Glass bead

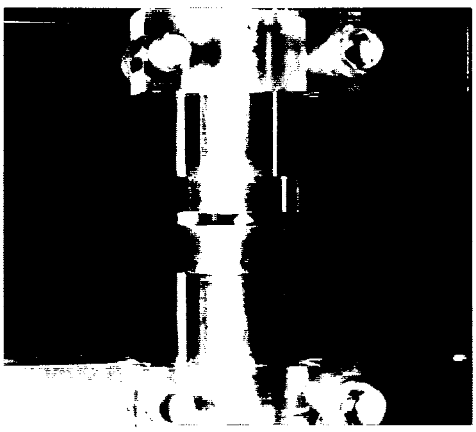

(f) Quartz particle

**Photo. 3.2 Single particle crushing test**

### 3.3.3 Test results and discussions

**(1) Force – displacement curve and crushing behavior of each particle**

Figure 3.2 shows typical force – displacement ($F$ – $w$) curves for the four materials together with the progress of crushing observed by the digital microscope. Pictures taken by the digital microscope are shown in Photograph 3.3 for chalk bar, Photograph 3.4 for talc bar and Photograph 3.5 for quartz particles.

In the case of the chalk bars shown in Figure 3.2(a), $F$ increases with increase in $w$ up to around 0.2mm until the first peak force appears. At the first peak force, a vertical initial crack suddenly occurs and the chalk bar splits in two pieces. After the peak force, $F$ reduces rapidly to about 60 – 70% of the peak force, but after that again continues to increase up to more than 1mm of displacement with some occasional small drops. During this process, the initial crack gradually opens wider and new cracks develop one after another along the initial crack ; finally the upper and lower edges of crushed particle collapse and, consequently, the top and bottom areas in contact with the loading platens widen.

In the case of the talc bars shown in Figure 3.2(b), $F$ increases with $w$ up to the first distinct peak force, although there are some small drops on the way. At each peak of these small drops, the talc bar is partially broken ; that is to say, a splitting crack partially develops. At the distinct peak force, $F_c$, the splitting crack runs through the body of the talc bar. In addition, the crack is generally neither straight nor vertical. One reason for these phenomena may be that the talc is a natural material and not entirely uniform. After the peak force, $F$ reduces rapidly to about 60 - 70% of the peak value, and then becomes almost constant for a while, before finally gradually decreasing. During this process, The crushed talc bar gradually rotates. This is because the splitting crack of the talc bar is neither straight nor vertical.

In the case of the glass beads shown in Figure 3.2(c), $F$ increases almost proportionally with $w$ up to around 0.1mm until peak force $F_c$. At the peak force, the particle burst sideways and is instantly broken into 30 – 50 pieces. After the peak force, $F$ rapidly decreases to zero, showing that once particle is crushed, glass bead can no longer withstand any applied force.

In the case of the quartz particles presented in Figure 3.2(d), $F$ increases with increase in $w$ until the first distinct peak force $F_c$, although there are again some small drops on the way. At each peak of small drops, the quartz particle is broken on the edges which are in contact with the loading plates. At the distinct first peak, they are crushed typically along the visible discontinuities of crystal structure, catastrophically into a number of pieces. After that, only a limited number of crushed fragments sustain the load. Thus after the first distinct peak, the $F-w$ curve shows quite different behavior for each test.

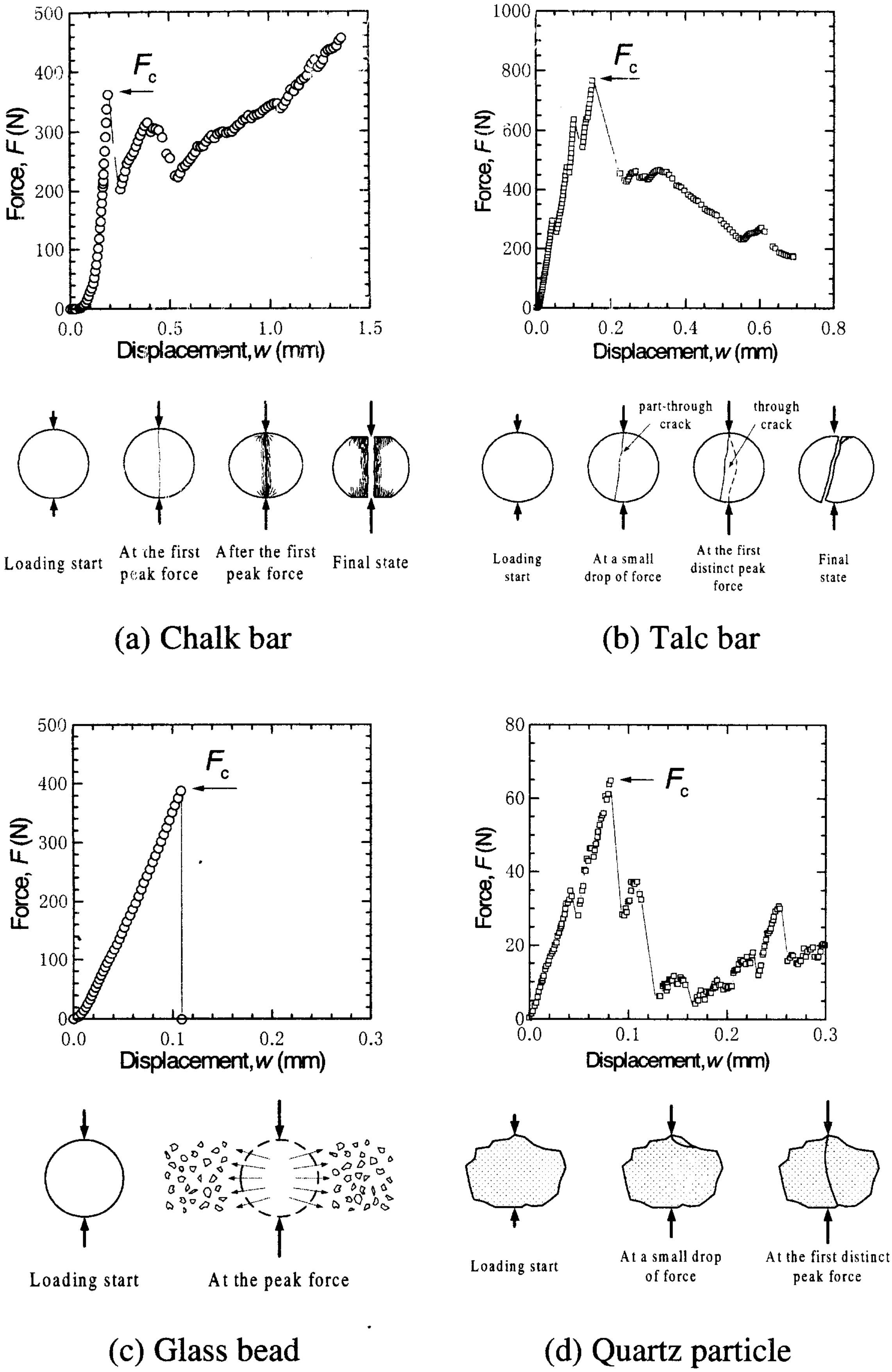


Figure 3.2 Typical load - displacement relationships of single particle crushing tests and illustrations of particles during the tests

(a) Loading start

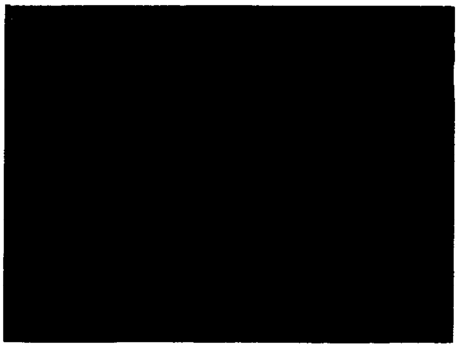

(b) At the first peak force

(c) After the first peak force

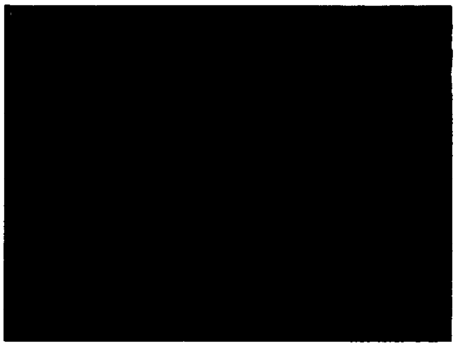

(d) Final state

Photo. 3.3 Chalk bar under the single particle crushing test

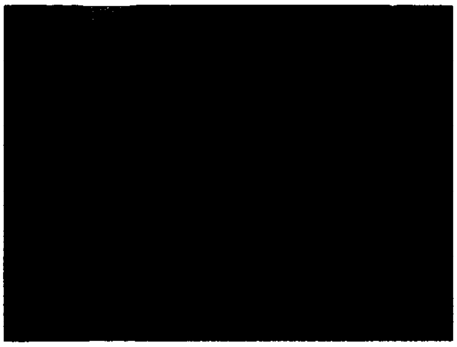

(a) Loading start

(b) Crack occurs

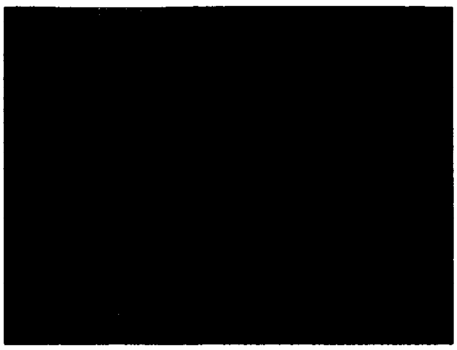

(c) Crack opens

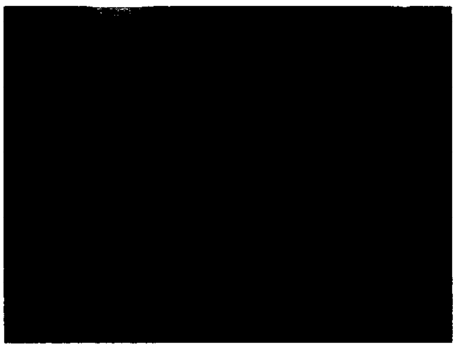

(d) Final state

Photo. 3.4 Talc bar under the single particle crushing test

(a) Example 1 : Loading start

(b) Example 1 : At a small drop of force

(c) Example 1 : After the first distinct peak force

(d) Example 2 : Loading start

(e) Example 2 : At a small drop of force

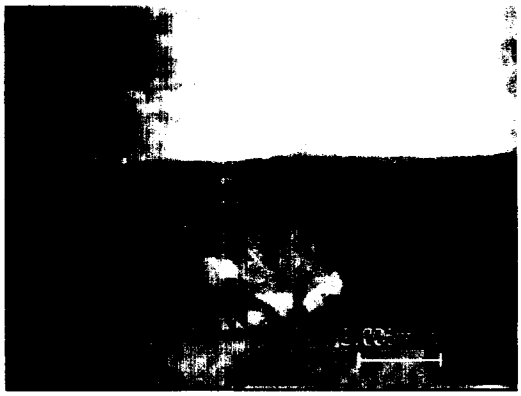

(f) Example 2 : After the first distinct peak force

Photo. 3.5 Quartz particles under the single particle crushing test

**(2) Crushing strength and initial stiffness of single particle crushing test**

For comparison of characteristics of single particle crushing test among the four types of particles, a crushing strength (which means tensile strength) and a characteristic initial stiffness are defined here.

The single particle crushing test of the chalk and the talc bars is identical with the Brazilian test. Thus a tensile strength $\sigma_c$ or a tensile stress $\sigma$ distributed along a vertical diametral axis are given as follows :

$$\sigma_c = \frac{2F_c}{\pi DL} \tag{3.1}$$

$$\sigma = \frac{2F}{\pi DL} \tag{3.2}$$

where $D$ is the diameter of a cylindrical bar, and $L$ is its length. $F_c$ is the first distinct peak force. From now on, the tensile strength defined above is called as crushing strength.

For glass beads and quartz particles, the following tensile strength specified in the ISO/DIS 11273-1(1996) is adopted as the crushing strength in this study.

$$\sigma_c = \frac{F_c}{A_m} = \frac{F_c}{\left(\frac{\pi}{4} \cdot d_m^{\ 2}\right)} \tag{3.3}$$

where

$$d_m = \frac{d_1 + d_2 + d_3}{3} \tag{3.4}$$

in which $A_m$ is the mean area of the particle, $d_1$, $d_2$, $d_3$ are the maximum, intermediate and minimum principal axis of the particle, respectively (i.e. $d_1 > d_2 > d_3$), $d_m$ is the mean diameter of the particle which is calculated by Equation (3.4).

After the crushing strength defined by Equation (3.3), the characteristic tensile stress for the glass beads and the quartz particles is defined as follows :

$$\sigma = \frac{F}{A_m} \tag{3.5}$$

McDowell and Bolton (1998) used the definition of a characteristic tensile stress as $\sigma = F/d_m^{\ 2}$ following Jaeger(1967). Equation (3.5) gives 27% larger values compared to the stress defined by McDowell and Bolton(1998) and Jaeger(1967).

For definition of a characteristic initial stiffness, the characteristic strain of a particle is defined as follows :

$$\varepsilon = \frac{\Delta d_h}{d_h} = \frac{d_h - w}{d_h} \tag{3.6}$$

where $\varepsilon$ is a characteristic strain of the particle, $d_h$ a particle height in the compression direction, $\Delta d_h$ the change of $d_h$, and $w$ the displacement measured by the gap sensors.

The characteristic initial stiffness is defined as the most representative slope of the initial part of the $\sigma - \varepsilon$ curve.

**Table 3.3 Statistical values of single particle crushing tests**

| | The number of test | Mean crushing force (N) | Crushing strength : $\sigma_c$ | | |
|---|---|---|---|---|---|
| | | | Mean value (MN/m$^2$) | Standard deviation (MN/m$^2$) | Coefficient of variation |
| Chalk bars | 25 | 299 | 0.667 | 0.114 | 0.17 |
| Talc bars (Dry) | 30 | 196 | 0.983 | 0.400 | 0.41 |
| Talc bars (Sat.) | 20 | 138 | 0.691 | 0.326 | 0.47 |
| Glass beads | 10 | 415 | 324 | 45.6 | 0.14 |
| Quartz particles | 20† | 67.0 | 38.1 | 31.3 | 0.82 |

| | Characteristic initial stiffness | | |
|---|---|---|---|
| | Mean value (MN/m$^2$) | Standard deviation (MN/m$^2$) | Coefficient of variation |
| Chalk bars | 95.8 | 26.2 | 0.27 |
| Talc bars (Dry) | 233 | 53.4 | 0.23 |
| Talc bars (Sat.) | 121 | 55.0 | 0.46 |
| Glass beads | 4035 | 808 | 0.20 |
| Quartz particles | 1230 | 551 | 0.48 |

† The particles that have the diameter $d$ = 0.85mm – 2.0mm were selected.

Table 3.3 summarizes the statistical values of the crushing strength and the characteristic initial stiffness. Mean crushing strength widely varies from 324 MN/m$^2$ for the glass bead to 0.667 MN/m$^2$ for the chalk bar. This is also the case of the mean characteristic initial stiffness. Industrial materials like the chalk bars and the glass beads show, as expected, a small coefficient of variations in the range of 0.10 to 0.30 for both the mean crushing strength and the mean characteristic initial stiffness. The natural quartz particle, however, shows a significantly large coefficient of variations of more than 0.8 for the crushing strength and nearly 0.5 for the characteristic initial stiffness. The shape of each particle and the direction of potential crystal imperfection relative to the loading direction may be also responsible for these large values of the coefficient of variation. Although the swelling of the talc bar was not observed, the crushing strength of the saturated talc bar is smaller than that of the dry talc bar. The same thing is found in the chracteristic initial stiffness of the saturated talc bar. The reason is not clear, but it is considered that the talc bars might swell a very small amount of water which affects the crushing strength and the characteristic initial stiffness of the talc bars.

McDowell and Bolton(1998) reported that the data of crushing strength can be well interpreted by the Weibull statistics such as fracture of brittle ceramics. McDowell and Amon(2000) clarified assumptions that are needed for well application for Weibull statistics to tensile failure of soil grains : the use of Weibull requires an assumption of geometric similarity to be made, and an assumption of very small contact area. In addition, they validated that the use of Weibull as a tool in the analysis of particle crushing : the average crushing force is not a strong function of particle size, and the force required to break a small particle asperity is also shown not to be a strong function of the asperity size. Weibull(1951) stated that for a volume $V$, under an applied tensile stress $\sigma$, the 'survival probability' $P_s(V)$ of a block of a material is given by

$$P_s(V) = \exp\left[-\frac{V}{V_0}\left(\frac{\sigma}{\sigma_0}\right)^m\right] \qquad (3.7)$$

where $V_0$ is a reference volume of material such that

$$P_s(V_0) = \exp\left[-\left(\frac{\sigma}{\sigma_0}\right)^m\right] \qquad (3.8)$$

and the parameter $\sigma_0$ is the value of tensile stress $\sigma$ such that 37% (i.e. 100exp(-1)%) of the total number of tested blocks survive, and $m$ is the Weibull modulus that is an index of variability. McDowell and Bolton(1998) expected that the values of $m$ for soils to be in the range of 5 to 10.

Nakata et al.(1999) conducted single particle crushing tests of quartz particles and feldspar particles of Aio sand, a beach sand from Yamaguchi prefecture. They applied the Weibull statistics to crushing strength derived from the tests, the definition of crushing strength was the same as McDowell and Bolton(1998), and found $m$ to be 4.2 for quartz particle.

McDowell and Amon(2000) applied the Weibull statistics to crushing strength of Quiou sand, a very weak limestone material from Northern France, and found $m$ to be 1.5 for Quiou sand. According to them, the reason for the small value of $m$ is that there is no strong correlation between force at failure and particle size for Quiou sand.

Application of the Weibull statistics to the crushing strength of the four materials in this study is shown in Figure 3.3. Although the number of data is limited, the crushing strength of these materials can be well explained by Weibull distribution for the cases of the chalk bar and the glass bead as shown in Figures 3.3(a) and (d). The values of parameter $m$ of these materials are 7.5 and 8 within the range that McDowell and Bolton(1998) expected for soils. The Weibull distributions for the case of the talc bar show some deviations between theoretical curves of $m$=4.5 or 6.5 and data curves from 1.0 of $\sigma_c/\sigma_0$ (see Figures 3.3(b) and (c)). It is thought that this deviation could be caused by elimination of low quality talc in the manufacturing process. A similar deviation is shown in the Weibull distribution of chalk bar, though the deviation is very small (see Figure 3.3(a)). As shown in Figures 3.3(e) and (f), the natural quartz particle does not fit in the Weibull distribution as good as the glass bead or the chalk bar. Although there are some deviations from the Weibull distribution, it generally explains the overall trend with the parameter $m$ value of 2 or 3, which is much smaller than previously reported for other materials. This small $m$ value implies that natural quartz particles tested in the present study have a larger dependency of crushing strength on particle size, according to McDowell and Bolton(1998)'s equation of $\sigma_0 \propto d^{-3/m}$ and to McDowell and Amon(2000). However, it was not positively confirmed from the test data of the present study, mainly because of the large variation, as has been afore-mentioned.

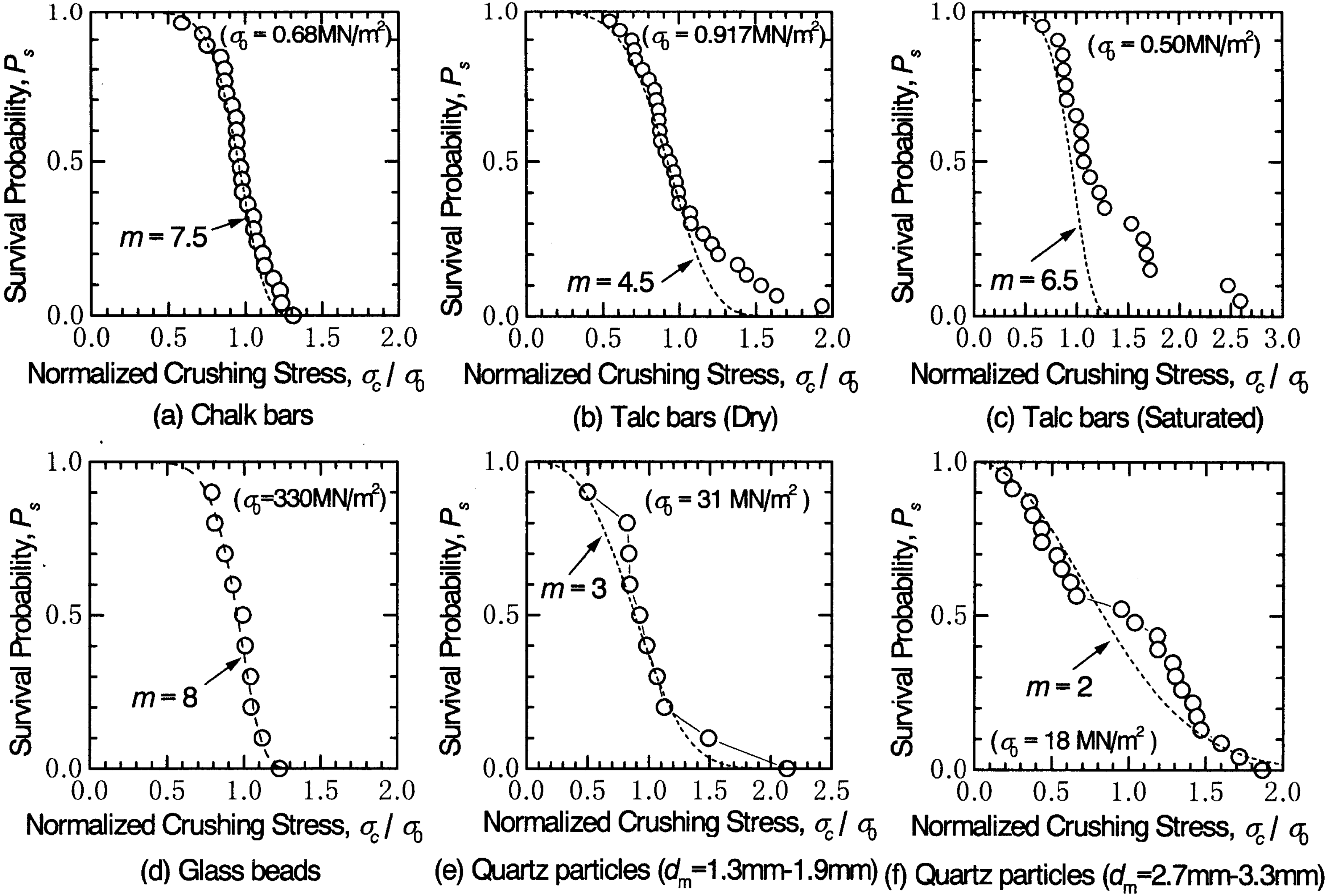


**Figure 3.3 Normalized survival crushing curves**

### (3) Number and shape of fragments after crushing

Chalk bars and talc bars were always split in half (two fragments) and glass beads were always crushed to small fragments of about 30-50 pieces. But the crushing pattern of the quartz particles seems to be different in every particle depending on particle shape and potential crystal imperfections. Figure 3.4 shows the frequency of the numbers of pieces of quartz particles after crushing. The frequency($P(n_p)$) decreases exponentially with the increase in fragment numbers($n_p$) with a regression curve of

$$P(n_p) = 0.22\exp\left(\frac{n_p - 2}{4.5}\right). \tag{3.9}$$

The relative frequency in which a particle is split in two pieces is 25%.

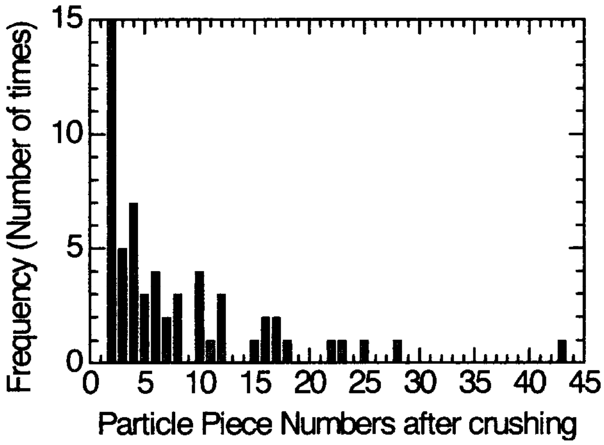


(a) Frequency

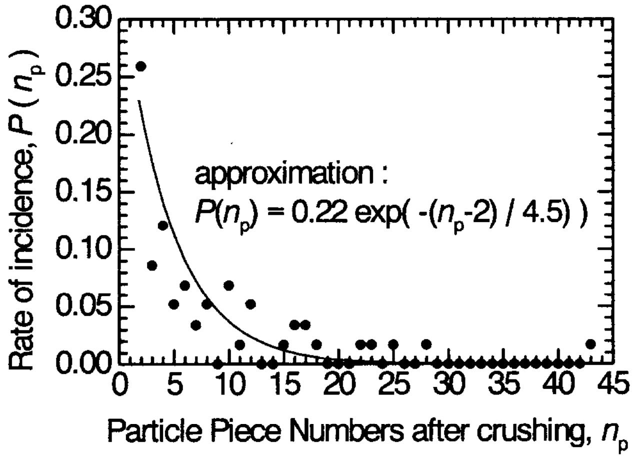


(b) Relative frequency

**Figure 3.4 Frequency of particles after crushing**

Figure 3.5 shows the changes in shape of particle before and after crushing in terms of flatness ratio ($d_3/d_2$) and elongation ratio ($d_2/d_1$). The dispersions of these values after crushing become larger than the values before crushing. But the differences of these two parameters between before and after crushing are small. The mean values of these ratios after crushing become slightly larger than those values before crushing, indicating that the particles after crushing become more spherical than the particles before crushing, partly due to bearing failures at edged contact points. Nonami et al.(1998) compared the flatness ratio and elongation ratio of rhyolite particles before triaxial test with those afterwards. It is interesting that those ratios after the test become larger than those values before the test in the case of triaxial compression tests.

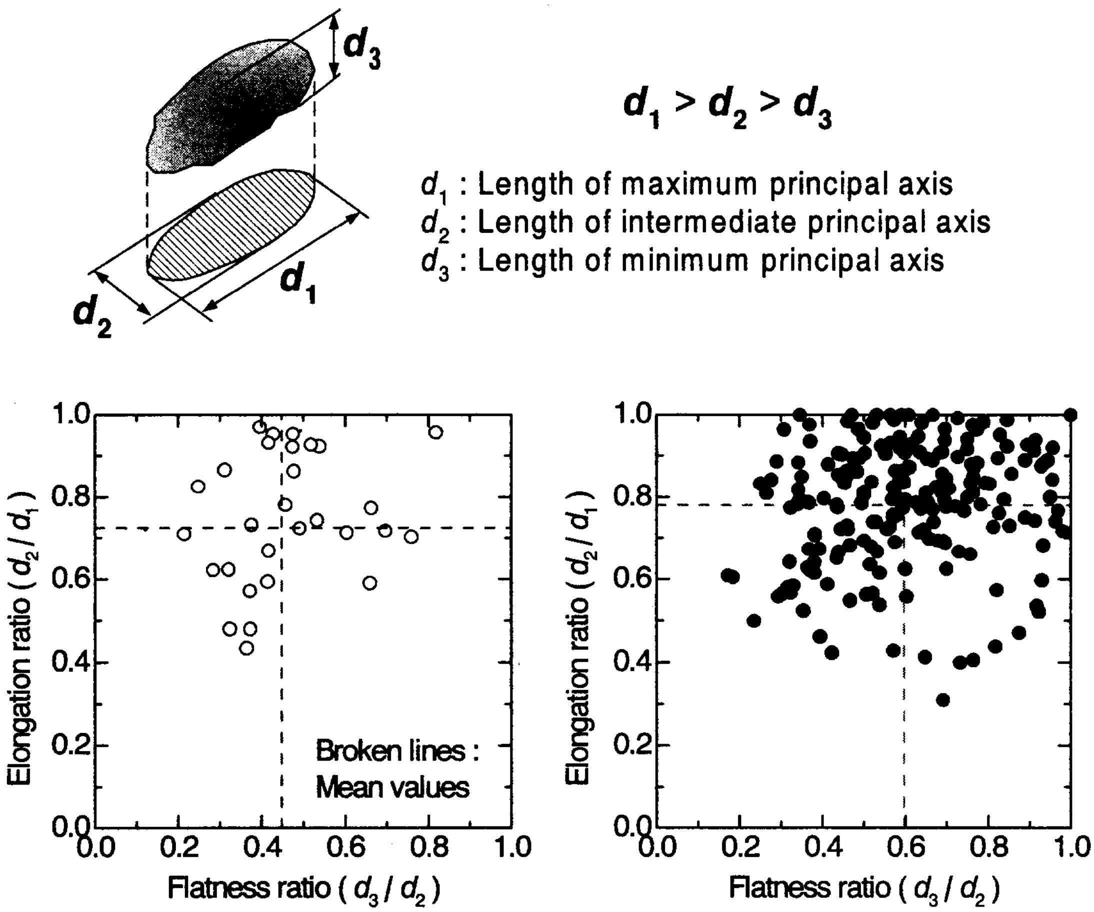


(a) Before crushing ( $n$ = 29 )

(b) After crushing ( $n$ = 204 )

**Figure 3.5 Distribution of flatness ratio and elongation ratio**

### (4) Crack opening of chalk bar under the single particle crushing test

In the case of chalk bar crushing test, it was observed that the initial crack gradually opened wider during loading (refer to Photograph 3.3). The crack opening means increasing of the width of chalk bar during loading. Figure 3.6 shows the changes of the height($D_v$) and width($D_h$) of a chalk bar during loading. $D_v$ and $D_h$ are plotted against load($F$). The width of chalk bar was measured from the pictures taken by the digital microscope. Before the load reaches the crushing force $F_c$, that is to say, before the initial crack runs through the body of chalk bar, $D_v$ decreases to 8.9mm, but the magnitude of $D_h$ remains the same. On the other hand, after the load reaches the $F_c$, $D_v$ decreases and $D_h$ increases. The magnitude of increase of $D_h$ is larger than the magnitude of decrease of $D_v$. It is confirmed that the width of chalk bar which is under the unconfined condition increases after the initial crack occurs, and the magnitude of the increment of the width is significant.

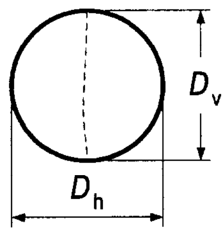


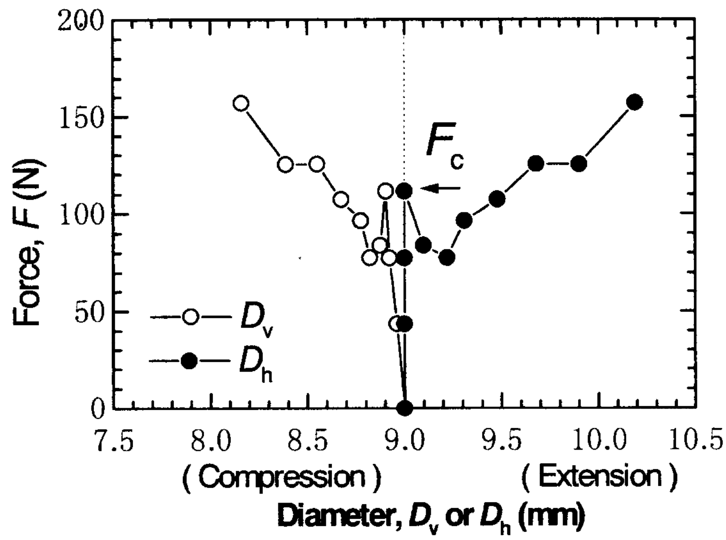


**Figure 3.6 Change of vertical diameter and horizontal diameter (Chalk bar : an example)**

**(5) Direction and configuration of splitting crack in the case of talc bar**

In the case of talc bar, the splitting crack is generally neither straight nor vertical as shown in Figure 3.2(b) and Photograph 3.4. The reasons for this is considered to be that the distribution of defects is random in a talc bar and that the size of a defect is large compared to the diameter of a talc bar. In these conditions, the angle of inclination of the splitting crack must be scattered. The configuration and the inclination of the splitting crack will be discussed here.

Figure 3.7 illustrates observed splitting crack patterns. The solid lines denote cracks on one side, the dotted lines denote cracks on the other side. In Pattern (a), the splitting crack is almost straight and vertical. In Patterns (b),(c),(d),(e),(f) and (g), the splitting cracks curves or runs diagonally. In Pattern (h), a talc bar does not split in two pieces, but crushed in three pieces as shown in Figure 3.7. Table 3.4 shows the frequency of each crack pattern shown in Figure 3.7. 50 single particle crushing tests were conducted against talc bars as shown in Table 3.3. In the 50 tests, the number of Pattern (a) was about 10% of the total number of talc bar tests. The number of Pattern (h) was also about 10% of the total number of the tests. In about 80% of the tests, the splitting crack curved or run diagonally. Table 3.4 also shows the magnitude of angle $\theta$ indicated in Figure 3.7(e). The magnitude of angle $\theta$ was scattered from $10^\circ$ to $50^\circ$. Thus, it was verified that the inclinations of the splitting cracks were scattered.

Even if the splitting crack run through the body of talc bar almost straightly and vertically, the semi-circular fragments of a talc bar gradually rotated. After the splitting crack run through the body of a talc bar, either of the two semi-circular fragments would support the load. The semi-circular fragment that supported the load would be slightly larger than another fragment in volume, and it would be in an unsteady state after the cracking. To cancel the unsteady state, the lager semi-circular fragment would rotate, not collapse in its edges. In the case of the chalk bar, semi-circular fragments collapsed in their edges, not rotated. The difference in behavior between the talc bar and the chalk bar may be due to the differences of the crushing strength, the characteristic initial stiffness, and friction of the surface of the cylindrical particles.

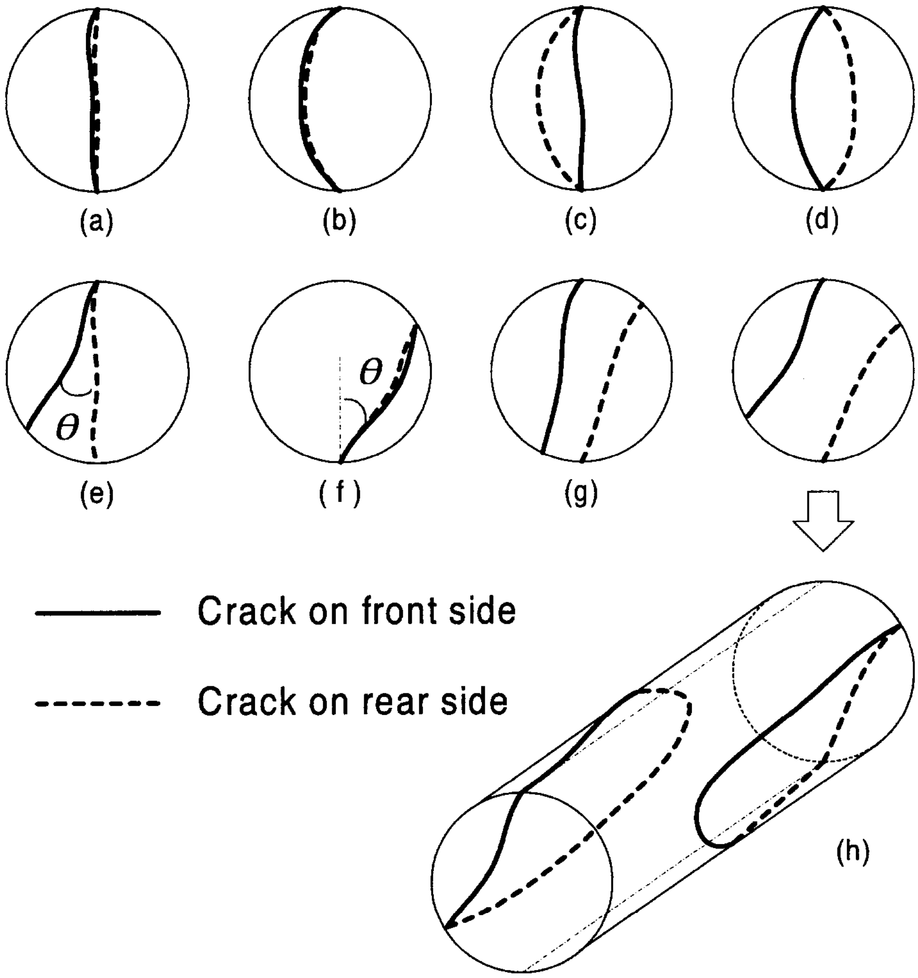


**Figure 3.7 Illustration of cracks occurred on talc bar**

**Table 3.4 Frequency of crack patterns illustrated in Figure 3.7**

| Crack pattern | Frequency |
|---|---|
| (a) | 5 |
| (b) | 3 |
| (c) | 8 |
| (d) | 2 |
| (e) | 11 |
| (f) | 1 |
| (g) | 12 |
| (h) | 6 |
| Other patterns | 2 |

| $\theta$ ( pattern (e) ) | Frequency |
|---|---|
| 10° | 2 |
| 20° | 5 |
| 30° | 1 |
| 40° | 1 |
| 50° | 2 |

### (6) Influence of friction of platens on crushing strength and $F-w$ curve

If the friction between the platens and particles influences the crushing strength and the characteristic initial stiffness, the degree of influence must be estimated.

Single particle crushing tests of chalk bars were newly carried out to investigate the influence of friction of the platens. A 4cm square aluminum plate with different roughness was placed on the upper and the lower platen. A chalk bar was loaded by the platens through these aluminum plates(see Photograph 3.2(b)). The following three types of aluminum platens were used for the crushing tests.

- Plane aluminum plates (after called "PA")
- Aluminum plates with glued chalk powder on the surface (CP)
- Aluminum plates with glued Toyoura sand on the surface (TS)

Chalk powder or Toyoura sand were put on the aluminum plates by the following method : paste was applied to the aluminum plates uniformly as much as possible, then the powder or sand were sieved and rained on the aluminum plates by a sieve of 0.105mm. The friction (i.e. frictional coefficient) of the plates may be compared as follows : PA$<$CP$<$TS.

The test procedure of the single particle crushing test was the same as the method mentioned before. Five tests were performed for each type of plates.

The results of the crushing strength and the characteristic initial stiffness are summarized in Table 3.5. First of all, it must be mentioned about the magnitude of the crushing strength : the mean value of crushing strength of PA is 40% smaller than the value of chalk bar in Table 3.3(a), and the coefficient of variation of crushing strength of PA is 80% larger than the value of chalk bar in Table 3.3(a) though all tests were conducted in the same test method. This difference in the strength and stiffness may be stemmed from deterioration about time : The tests shown in Table 3.5 were performed about two years after the tests shown in Table 3.3. The tests of Table 3.3 were performed in October, 1998, and the tests shown in Table 3.5 were conducted in October, 2000.

Thus, the results in Table 3.5 will be discussed separately after this.

**Table 3.5 Crushing strength and characteristic initial stiffness of single particle crushing tests with different frictional conditions**

| | | Crushing strength ($MN/m^2$) | | Characteristic initial stiffness ($MN/m^2$) | |
|---|---|---|---|---|---|
| PA | 1 | 0.354 | Mean value : 0.395 ( COV : 0.313 ) | 102.6 | Mean value : 121.3 ( COV : 0.344 ) |
| | 2 | 0.354 | | 63.3 | |
| | 3 | 0.415 | | 138.9 | |
| | 4 | 0.592 | | 175.3 | |
| | 5 | 0.259 | | 126.5 | |
| CP | 1 | 0.578 | Mean value : 0.430 ( COV : 0.351 ) | 98.3 | Mean value : 76.2 ( COV : 0.332 ) |
| | 2 | 0.265 | | 51.2 | |
| | 3 | 0.500 | | 65.7 | |
| | 4 | 0.537 | | 107.9 | |
| | 5 | 0.270 | | 57.8 | |
| TS | 1 | 0.249 | Mean value : 0.257 ( COV : 0.171 ) | 32.9 | Mean value : 29.8 ( COV : 0.202 ) |
| | 2 | 0.185 | | 19.4 | |
| | 3 | 0.290 | | 29.9 | |
| | 4 | 0.270 | | 32.7 | |
| | 5 | 0.291 | | 34.0 | |

PA : Plane aluminum platens
CP : Aluminum platens with chalk powder
TS : Aluminum platens with Toyoura sand

The mean crushing strength in CP is roughly as large as that in PA, while the crushing strength of TS is 40% smaller than that of PA. From the results, it is considered that the crushing strength would not be affected by the friction of the platens, if the friction of a platen is smaller than that of surface of particle. But it is considered that the strength would be affected, if the friction is larger than that of surface of chalk bar. This lower crushing strength would be explained by the following behavior : sand particles fixed on the platens may penetrate the surface of chalk bar, then the notches made by the sand particles would be apt to become crack initiation sites.

The data of the characteristic initial stiffness presented in Table 3.5 suggest that the characteristic initial stiffness decreases with increasing of friction. This tendency would be originated from the following microscopic contact behavior between chalk bar and platen (aluminum plate) : powder of chalk or sand particle fixed on the upper platen would be touched the surface of chalk bar with lower side of itself, then a real contact area of surface of chalk bar with the upper platen would gradually widen, accompanying the penetration of asperities of platen to chalk or collapse of asperities. It takes more time (i.e. more displacement of platen) to widen the real contact area in the case of large friction platen that have steep bumps than in the case of small frictional platen that have gentle bumps.

There were no difference in crushing pattern of chalk among the three types of platen : all chalk bars were split as shown in Figure 3.2(a).

The summary of these tests is as follows : it is considered that the crushing strength would not be influenced by the friction of platen, if the friction of platen is smaller than that of the surface of particle, and that the characteristic initial stiffness would be affected by the friction of platen.

## 3.4 Conclusions

In Chapter 3, the main properties of four different types of crushable particles adopted for the experiments described in Chapters 4 and 5 were shown, and single particle crushing tests were performed to investigate properties of single particle crushing. The summary of Chapter 3 is as follows :

- The crushing behavior during the single particle crushing test was different according to the difference of material properties.
- The crushing strength of the four crushable materials could be explained by the Weibull distribution.
- The distribution of numbers of fragments after single particle crushing tests of quartz particles from weathered granite ground was approximated with an exponential function. The variability of flatness ratio and elongation ratio of fragments after single particle crushing tests became larger than before the crushing tests, and the change of mean values of these ratios indicated that the shape of fragments tend to be rounded.
- The crushing strength would not be influenced by the friction of platen, if the friction of platen is smaller than that of the surface of particle, while the initial stiffness would be affected by the friction of platen.

# CHAPTER 4

# TIME-DEPENDENT BEHAVIOR OF FOUR CRUSHABLE MATERIALS IN ONE-DIMENSIONAL COMPRESSION TESTS

## 4.1 Introduction

One-dimensional compression tests on aggregates of four crushable materials, used in the single particle crushing tests described in Chapter 3, were conducted to examine the time-dependent behavior due to particle crushing with careful visual observations.

Time-dependent compression was observed in all of the tests. The aspects of time-dependent compression of the four materials were different.

Creep tests of a single particle (chalk bar) were carried out to obtain characteristics of creep deformation of material itself. The obtained creep characteristics were used for separating the compression strain into the following three components: instantaneous strain, creep strain of material, and other strain that means the strain due to particle crushing. The separation of strain was performed to clarify the amount of component of particle crushing.

Mechanism of time-dependent compression of each material was discussed based on the visual observations.

Finally, relationships between a rate of creep strain and loading pressure were discussed.

## 4.2 Test procedures

Figure 4.1 illustrates the test apparatus of one-dimensional compression tests under plane strain conditions. A pneumatic actuator of 20kN capacity was used for loading. A load cell with a capacity of 20kN was used to monitor the loading force, while two gap sensors with an accuracy of 0.001mm measured the displacement of loading plate. Either a video camera or a digital microscope was used for the observation of particle behavior under crushing. The details of a test box and specimen are illustrated in Figure 4.2. The test box is made of stainless steel and has a width of 100mm, a height of 100mm and a depth of 30mm. There is a glass window on the front side wall, through which visual observation can be made. Four crushable materials, that are chalk bar, talc bar, grass bead, and quartz particle, are used for the tests.

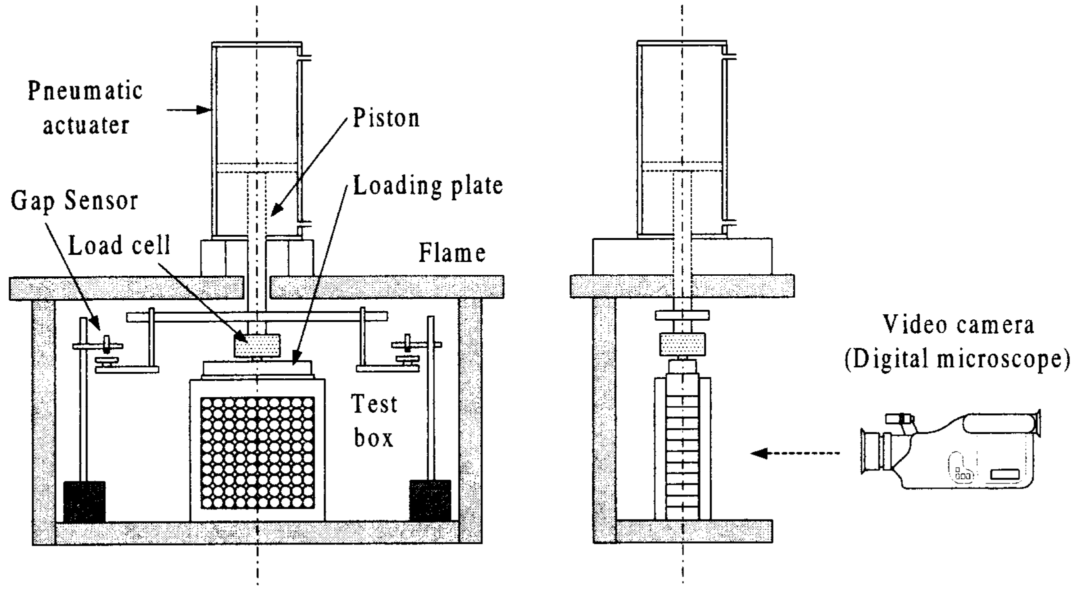


**Figure 4.1 Test apparatus of one-dimensional compression test**

In the case of chalk bar specimen, the chalk bars were carefully piled up in the stainless steel box two-dimensionally. The two packing patterns were adopted : cubic packing in which each chalk bar has 4 contact points and hexagonal packing where each chalk bar has 6 contact points as are also illustrated in Figure 4.2(a). These regular packing patterns were adopted for the following reasons :

1) In these experiments, the author pays attention to the behavior of individual particle that contacts with neighbor particles. It is considered that the behavior of a specimen made of regular-packed particles is different from the behavior of a specimen made of random-packed particles. However, the following matter is common to both packing patterns: each particle in specimen contacts with surrounding particles through some contact points. In the regular packing patterns, only one packing pattern exists in the specimen, but in the random packing patterns, a large number of packing patterns exists in the specimen to the contrary. In the experiments of chalk bar specimen and below-mentioned talc bar specimen, the most basic contact patterns —— cubic packing pattern and hexagonal packing pattern —— will be discussed.
2) It is one of the reasons for adopting the regular packing patterns to ensure the repeatability of the experiments. If one had ensured the repeatability of the experiments adopting the regular packing, one must have prepared a large test box compared to the diameter of the

chalk bar or the talc bar. Under a restriction of the loading capacity of 20MN, it is considered that the adapting of regular packing patterns would ensure the repeatability of the experiments.

3) It is easy to observe the cracks appeared on the cross sections of chalk bars or talc bars under the regular packing patterns.

In the case of talc bar specimen, square aluminum bars were used to fill up the extra spaces in the steel box. The number of talc bars of a talc bar specimen is nearly equal to that of a chalk bar specimen. Only simple cubic packing was adopted. Dry and saturated specimens were tested. A pressure of -100kPa was applied to the talc bars in water for 12 hours for saturation. Then they were packed in water. Pore water could drain from the gap between the loading plate and the steel box.

In the case of specimen made of glass beads or quartz particles, the aluminum bars were used to fill up the extra spaces in the steel box. So the shape of specimen is a cube with sides of 15mm or 20mm long. The specimen was made as follows : Particles were poured into the space, and were compacted by manually shaking the box for about 20 seconds to control the density of the specimen.

Photograph 4.1 shows the general views of the test apparatus and the test box.

Table 4.1 summarizes the information about the test materials and specimens for all the 16 cases of one-dimensional compression test. All the tests were conducted with several loading stages with maintaining the load for about 24 hours at each loading step. In Case C5, C6 and C7, that had larger loading stages than other cases of chalk bar specimen, the load of each loading stage was maintained for about 12 hours.

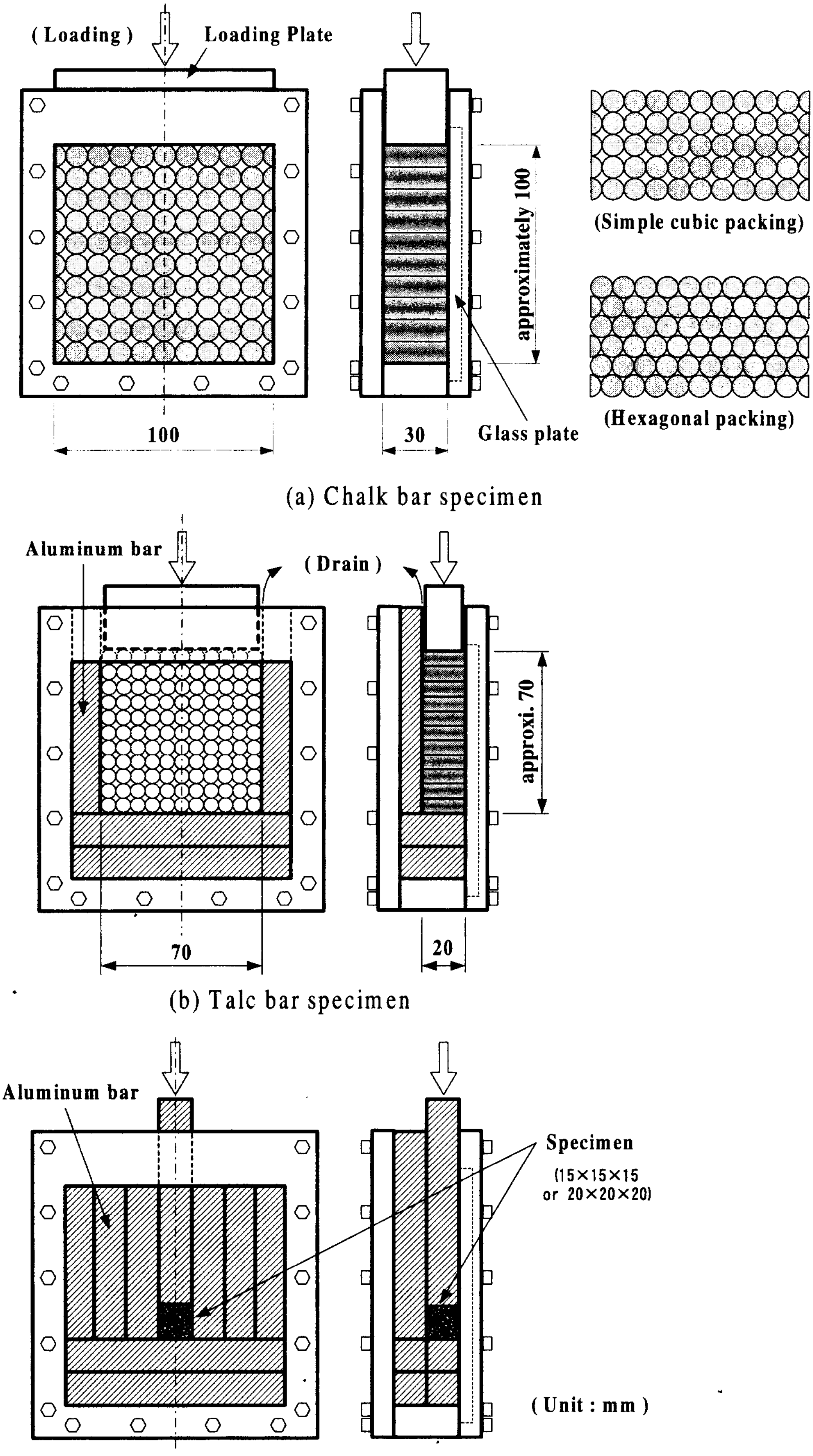


(a) Chalk bar specimen

(b) Talc bar specimen

(c) Glass beads specimen and quartz particle specimen

**Figure 4.2 Specimen in test box**

**(a) Test apparatus and measurement system**

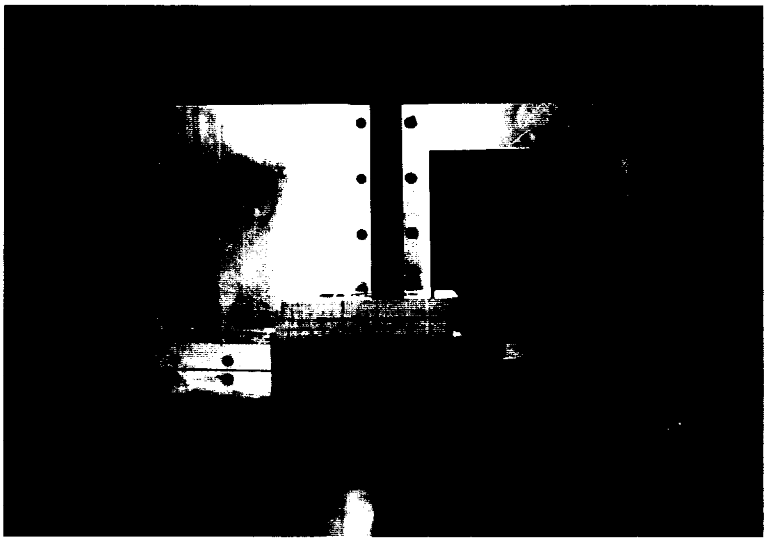

**(b) Test box and loading plate**

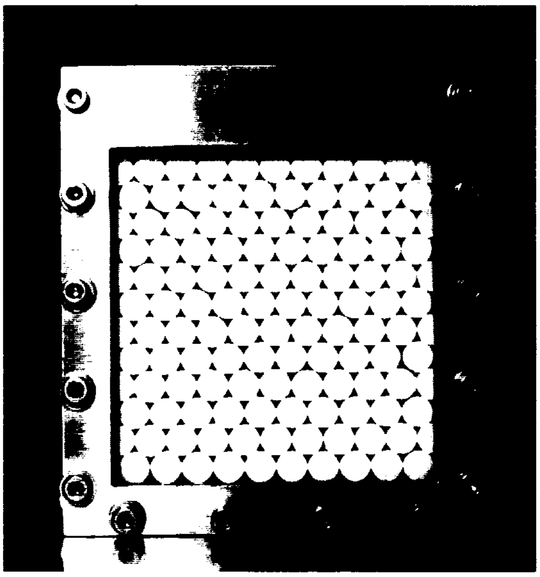

**(c) Chalk bar specimen**


**(d) Quartz particle specimen**

**Photo. 4.1 One-dimensional compression test**

## Table 4.1 Outline of specimen and test cases of one-dimensional compression tests

| Test Name | Particle | | Specimen | | | | Test Results | |
|---|---|---|---|---|---|---|---|---|
| | Material | Size | Size (mm) | The number of particles | Mass (kg) | $e_0$ ‡ | Yield stress (MN/m$^2$) | $\lambda$** |
| Case C1 | Chalk bar | Diameter : 9.3～9.7mm Length : 30mm | $W$ (Width) : 100 $H$ (Height) : 105† $D$ (Depth) : 30 | 110 (Simple cubic packing) | 0.4 | 0.344 | 1.00 | 0.114 |
| Case C2 | | | | | | 0.355 | 1.15 | 0.120 |
| Case C3 | | | | | | 0.364 | 1.40 | 0.139 |
| Case C4 | | | | | | 0.362 | 1.22 | 0.119 |
| Case C5 | | | | | | 0.357 | 1.10 | 0.107 |
| Case C6 | | | | | | 0.362 | 1.18 | 0.121 |
| Case C7 | | | | 120 (Hexagonal packing) | 0.45 | 0.200 | 1.80 | 0.063 |
| Case T1 | Talc bar | Diameter : 6.3～6.4mm Length : 20mm | $W$ (Width) : 70 $H$ (Height) : 70† $D$ (Depth) : 20 | 121 (Simple cubic packing) | 0.21 (Dry) | 0.284 | 4.33 | – |
| Case T2 | | | | | | 0.285 | 5.00 | – |
| Case T3 | | | | | 0.25 (Sat.*) | 0.282 | 3.35 | – |
| Case G1 | Glass bead | Nominal diameter : 1mm | $W15 \times H15^{\dagger} \times D15$ | Approximately 1800 | 0.005 | 0.70 | 14.7 | 0.373 |
| Case G2 | | | | | | 0.63 | 17.0 | 0.424 |
| Case G3 | | | | | | 0.61 | 21.2 | 0.632 |
| Case Q1 | Quartz particle | Grain size : 0.85mm～2.0mm | $W15 \times H15^{\dagger} \times D15$ | Approximately 600 | 0.005 | 1.06 | 2.30 | 0.239 |
| Case Q2 | | | $W20 \times H20^{\dagger} \times D20$ | Approximately 1400 | 0.012 | 0.82 | 4.00 | 0.193 |
| Case Q3 | | | | | | 0.84 | 3.80 | 0.178 |

† Approximate value ‡ $e_0$ : Initial void ratio * Saturated specimen

** $\lambda$ : Compression index ( the slope of $e - \log p$ ( $\ln p$) curve in the region after yield stress )

## 4.3 Test results and discussions

### 4.3.1 $e - \log p$ curves

Figure 4.3 shows $e - \log p$ curves of one-dimensional compression tests of each test. Each curve is a plot of the final void ratios at each loading step, and the shape of the curve is similar to that of a typical $e - \log p$ curve of clay. In this study, yield stress of each test on the compression curve( $p_y$ ) was obtained by an intersection point of the following two lines : one is the tangent of the initial part of $e - \log p$ curves, the other is the normal compression line.

As is presented in Figure 4.3(a) for the chalk bar specimen, Case C1 to C6 of cubic packing consistently show the similar curves, giving the average yield stress of 1.18 MN/m$^2$. Case C7 of hexagonal packing has a smaller void ratio and gives a larger yield stress of 1.80 MN/m$^2$, almost one and a half times larger than the corresponding value of cubic packing. But the compression curves of the two packing patterns seem to converge at the stress level around 10 MN/m$^2$, indicating that the compressibility index increases with increasing of initial void ratio. In the cases of the talc bar specimens(T1, T2 and T3) shown in Figure 4.3(b), the gradient of $e - \log p$ curves changes sharply at the last loading stage. The curve of the saturated specimen(T3) has a smaller gradient than the dry specimens(T1 and T2) before the last loading stages. The predicted yield stress of Case T3 is also smaller than the corresponding values of the dry specimens. In the cases of the glass beads specimens(G1, G2 and G3) shown in Figure 4.3(c), the gradient of $e - \log p$ curves changes sharply near the yield stress of around 15 to 20 MN/m$^2$, while in the cases of quartz particles specimens(Q1, Q2 and Q3) shown in Figure 4.3(d), the gradient of the curves changes gradually without showing a clear yield stress point. McDowell and Bolton(1998) indicated that the larger the Weibull modulus of single particle crushing test is, the shaper the change of gradient of $e - \log p$ curve is. This tendency is recognized in the comparison of the chalk bar specimens and the talk bar specimens or the glass bead specimens and the quartz particle specimens.

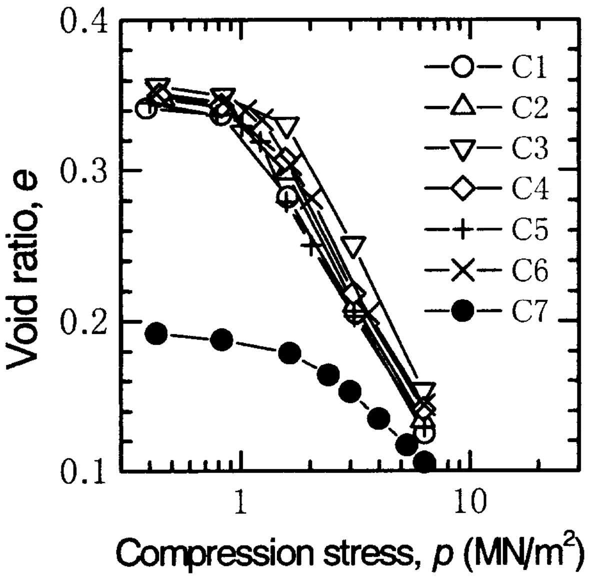


(a) Chalk bar specimen

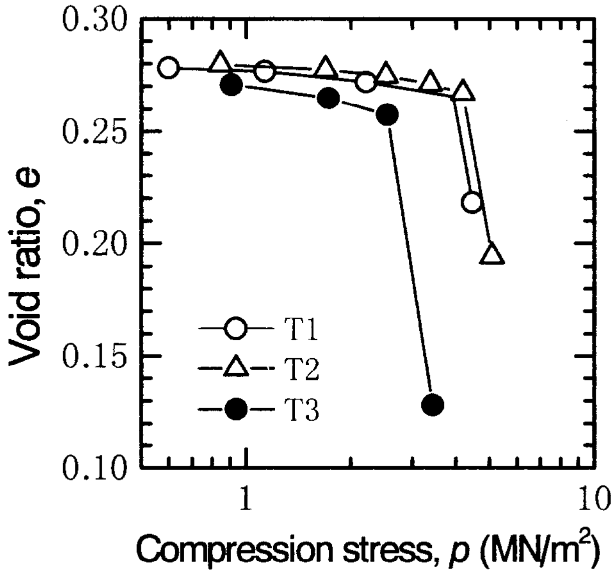


(b) Talc bar specimen

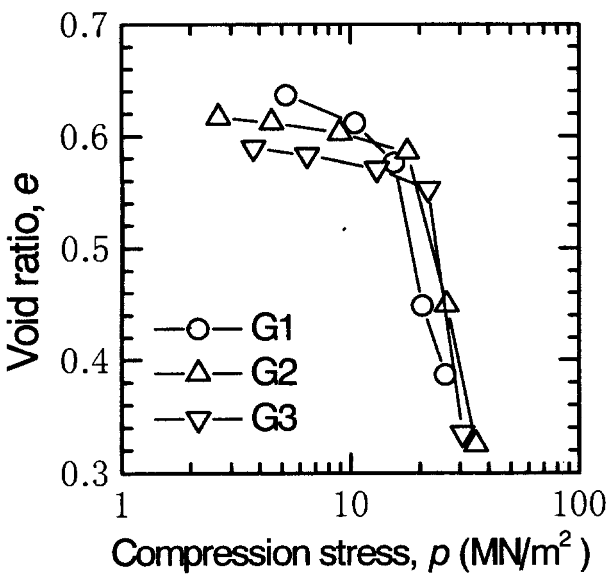


(c) Glass bead specimen

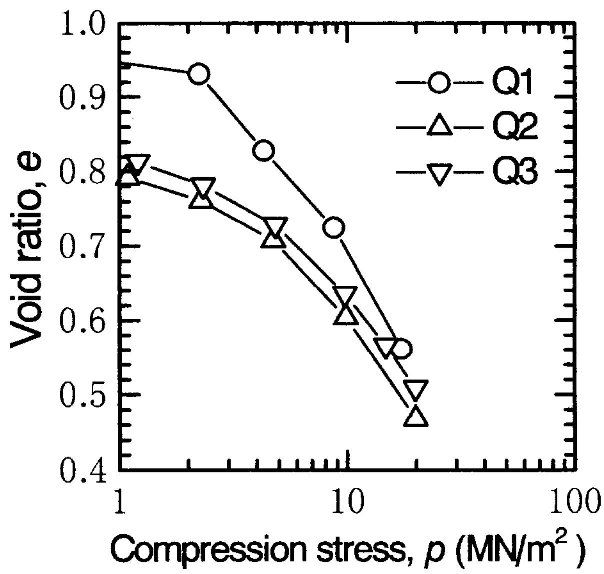


(d) Quartz particle specimen

**Figure 4.3** ***e*** **- log** ***p*** **curves of one-dimensional compression tests**

Table 4.1 shows the slope of the $e - \log p$ ( $\ln p$ ) curve in the region after yield stress, termed " $\lambda$ " by Roscoe et al.(1963). The $e - \log p$ curves of each material seem to converge to a constant value of $\lambda$. Before convergence, $\lambda$ will be influenced by the initial void ratio. In the case of the chalk bar specimen and the quartz particle specimen, the larger the initial void ratio is, the lager the $\lambda$ is. In the case of the glass beads specimen, the larger the initial void ratio is, the smaller the $\lambda$ is. McDowell and Bolton(1998) indicated that the index $\lambda$ is in the range of 0.1 – 0.4 for a wide range of granular materials. The values of $\lambda$ in the present tests almost fall in this range. In the case of talc bar specimen, it is impossible to estimate $\lambda$ since there was only one loading beyond the yield stress.

### 4.3.2 Strain vs. elapsed time curves

Figure 4.4 shows the strain vs. elapsed time curves of the chalk bar specimen under sustained loading of each step. Strain was calculated by the following equation :

$$\bar{\varepsilon} = \frac{w_p}{h} \tag{4.1}$$

where $w_p$ is the settlement of loading plate, $h$ is the initial height of specimen of each loading step. The plots of compression stress vs. elapsed time are also shown in Figure 4.4. The present pneumatic loading system generally required about 10 seconds before the load had reached the predetermined load. It is observed from the figures that even after the stress reached the sustained stress, the strain rather smoothly continued to increase with time, in particular for the applied loading pressure of 1.56 – 1.57MN/m$^2$, demonstrating the phenomenon of the time-dependent behavior.

Figure 4.5 presents the strain – time curves of the talc bar specimens(T1, T2, T3). The plots of compression stress vs. elapsed time are also shown in Figure 4.5. The applied load can effectively be regarded constant at about 10 seconds. Except the last loading stage of each test, the strain at each stage nearly smoothly continued to increase with time after about 10seconds in Case T1, after about 70seconds in Case T2 and after about 400seconds in Case T3. In the last loading stage of each test, a large jump suddenly occurs at 2000seconds in Case T1, 7000seconds in Case T2 and at 300seconds in Case T3. The magnitude of the strain after the jump is three to ten times larger than that before the jump. The mechanism of these jumps will be discussed later.

Figure 4.6 shows the strain - time curves of glass bead specimens (G1, G2, G3). The plots of compression stress versus elapsed time are also shown in Figure 4.5. Each specimen has a different initial void ratio. Some curves have several sudden jumps even during the sustained loading period. When these sudden jumps appeared, one or a few glass beads must have burst. The sounds of crushing were heard at the time. The jumping during the sustained loading step means that the crack can grow even under a sustained load condition. In Case G1, two loading stages of 15.5MN/$m^2$ and 20.6MN/$m^2$ have some sudden jumps during the sustained loading, in Case G2, the curves of the last two steps of 26.3MN/$m^2$ and 35.5MN/$m^2$ have some jumps, other curves indicate only small strain. In Case G3, only one curve of the last loading stage(30.7MN/$m^2$) has some jumps. It is noticed that the larger the initial void ratio is, the more jumps appeared in the strain curves, suggesting that the smaller the coordination number is, the stronger the time-dependency is.

The strain-time curves with stress-time curve of quartz particle specimens are shown in Figure 4.7. The configuration of strain-time curve is similar to that of the chalk bar specimen, without any jumping phenomenon.

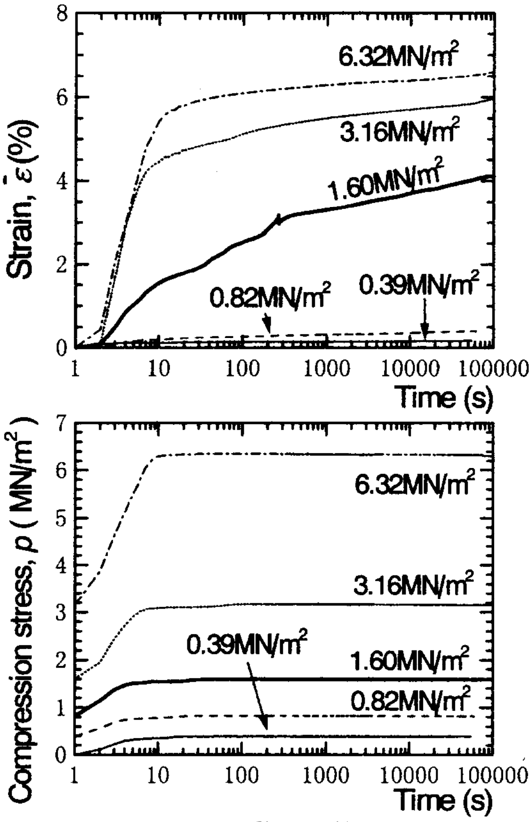


(a) Case C1

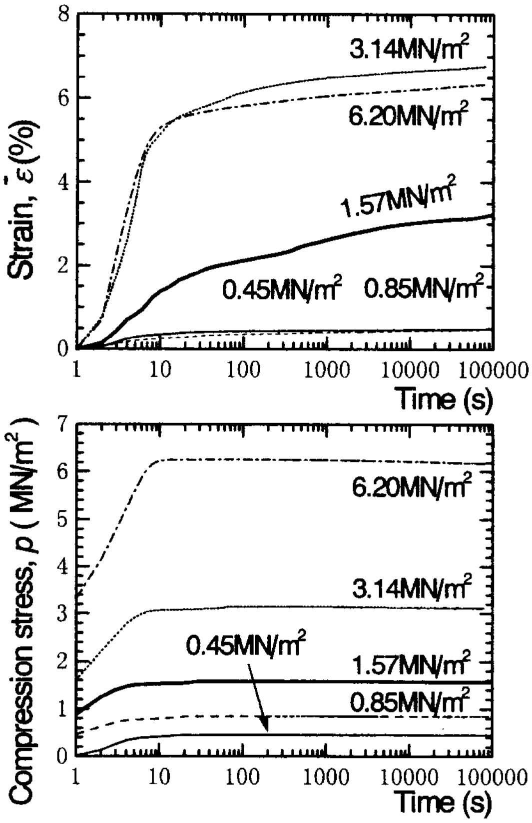


(b) Case C2

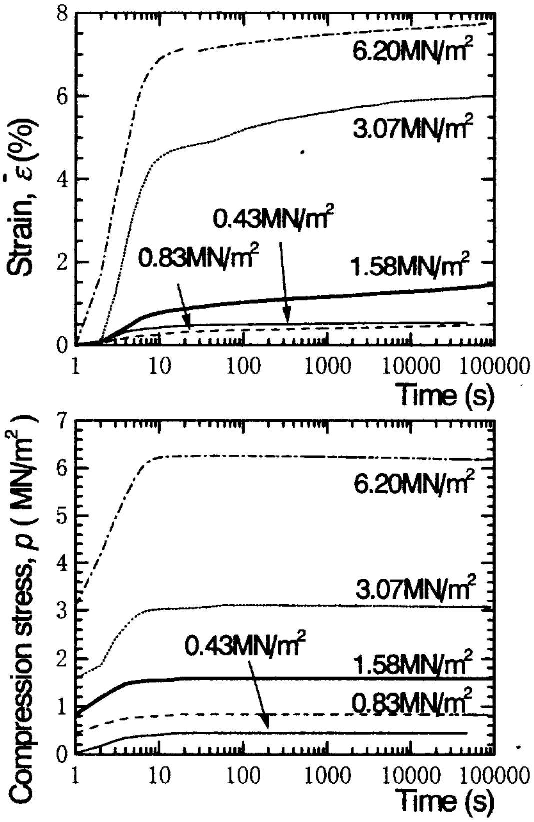


(c) Case C3

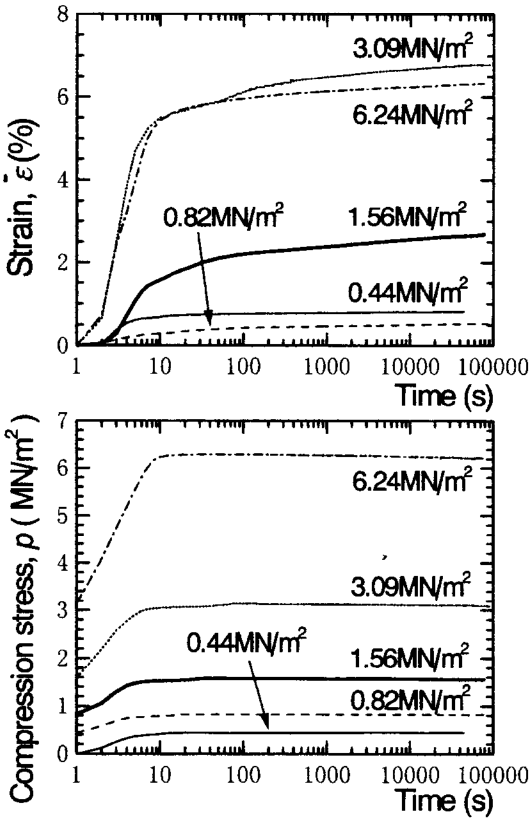


(d) Case C4

Figure 4.4 Strain or stress vs. elapsed time curves of one-dimensional compression tests (Chalk bar specimens)

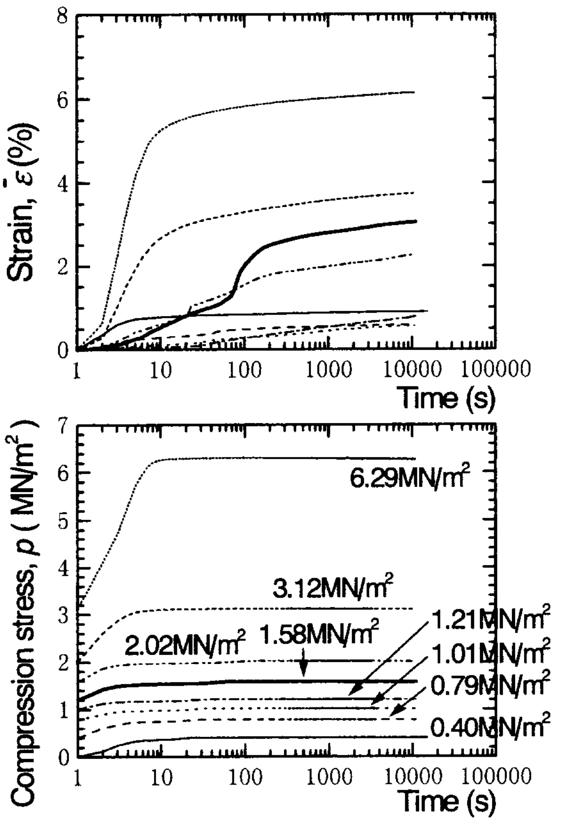


(e) Case C5

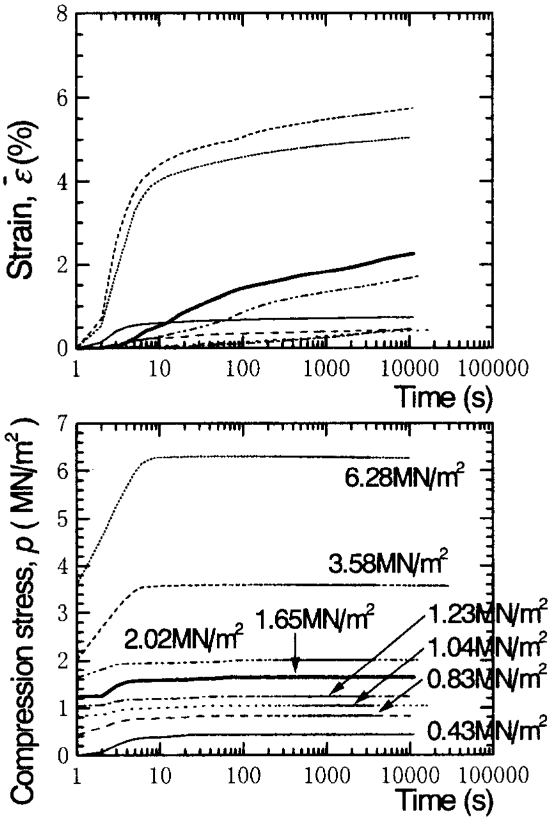


(f) Case C6

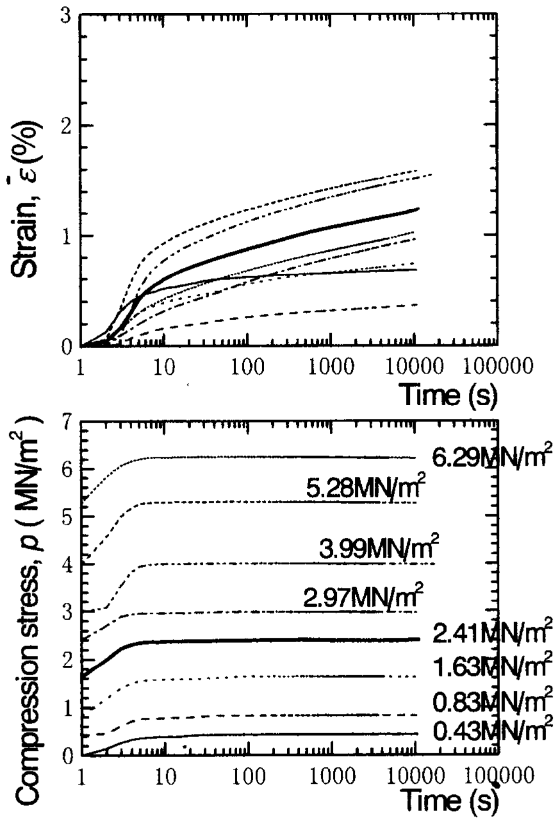


(g) Case C7

Figure 4.4 Strain or stress vs. elapsed time curves of one-dimensional compression tests (Chalk bar specimens)

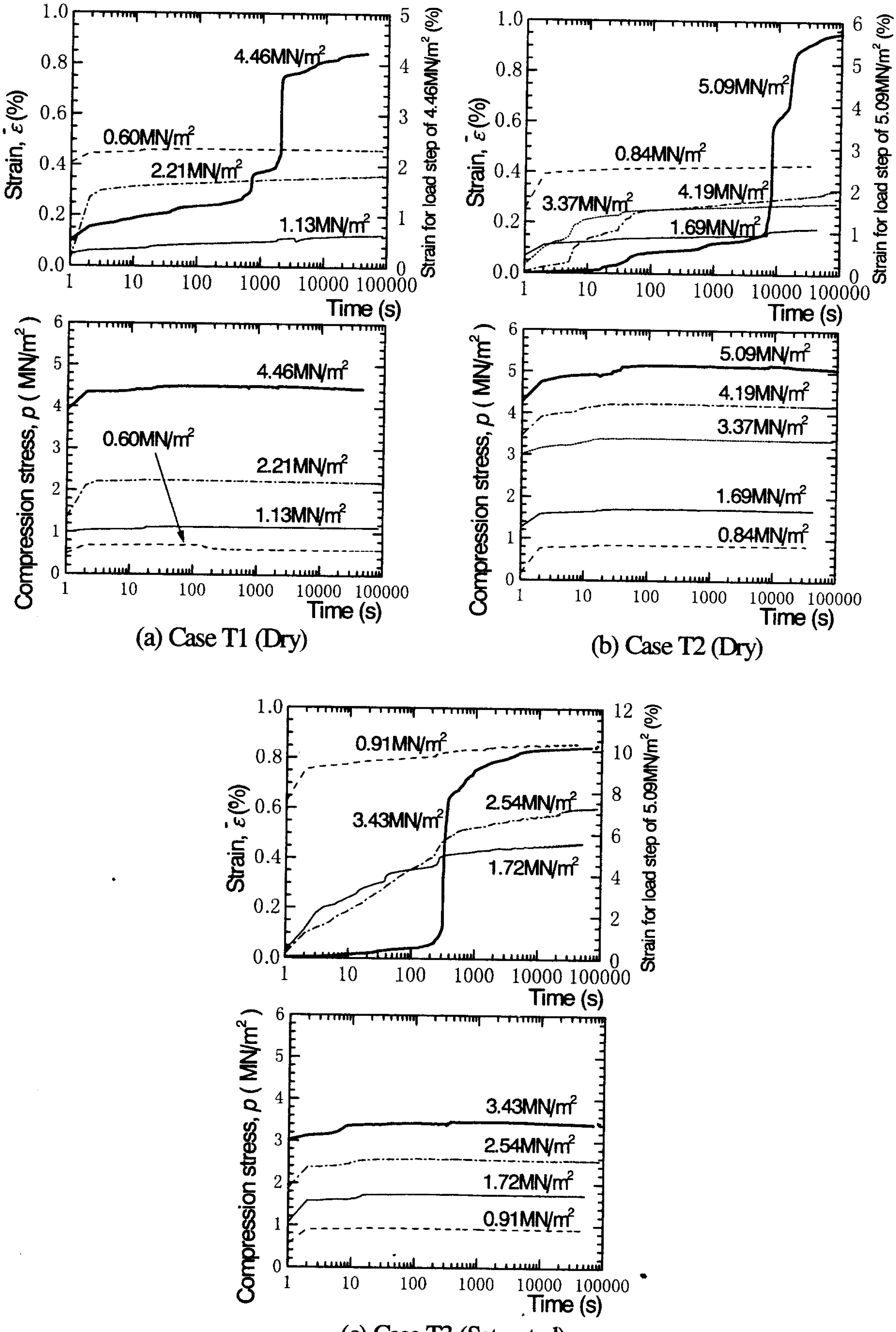


Figure 4.5 Strain or stress vs. elapsed time curves of one-dimensional compression tests (Talc bar specimens)

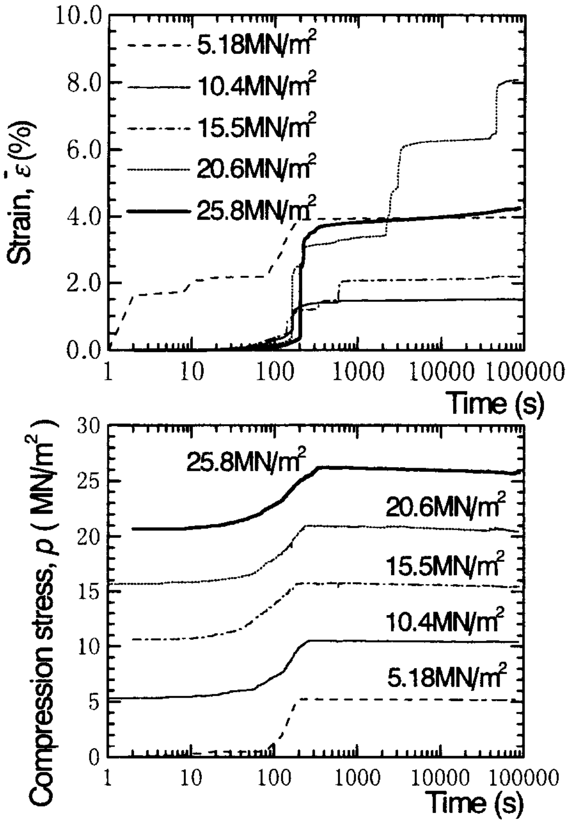


(a) Case G1 ($e_0$=0.70)

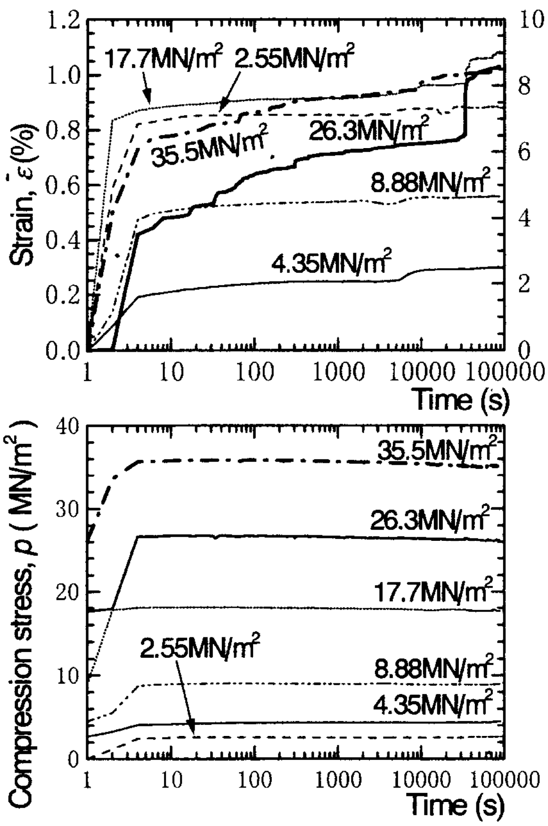


(b) Case G2 ( $e_0$=0.63 )

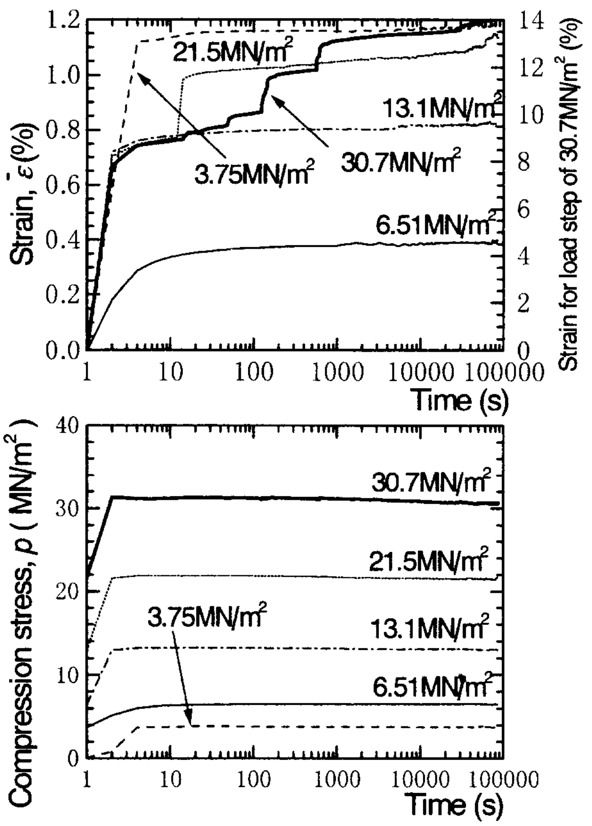


(c) Case G3 ( $e_0$=0.61 )

Figure 4.6 Strain or stress vs. elapsed time curves of one-dimensional compression tests (Glass bead specimens)

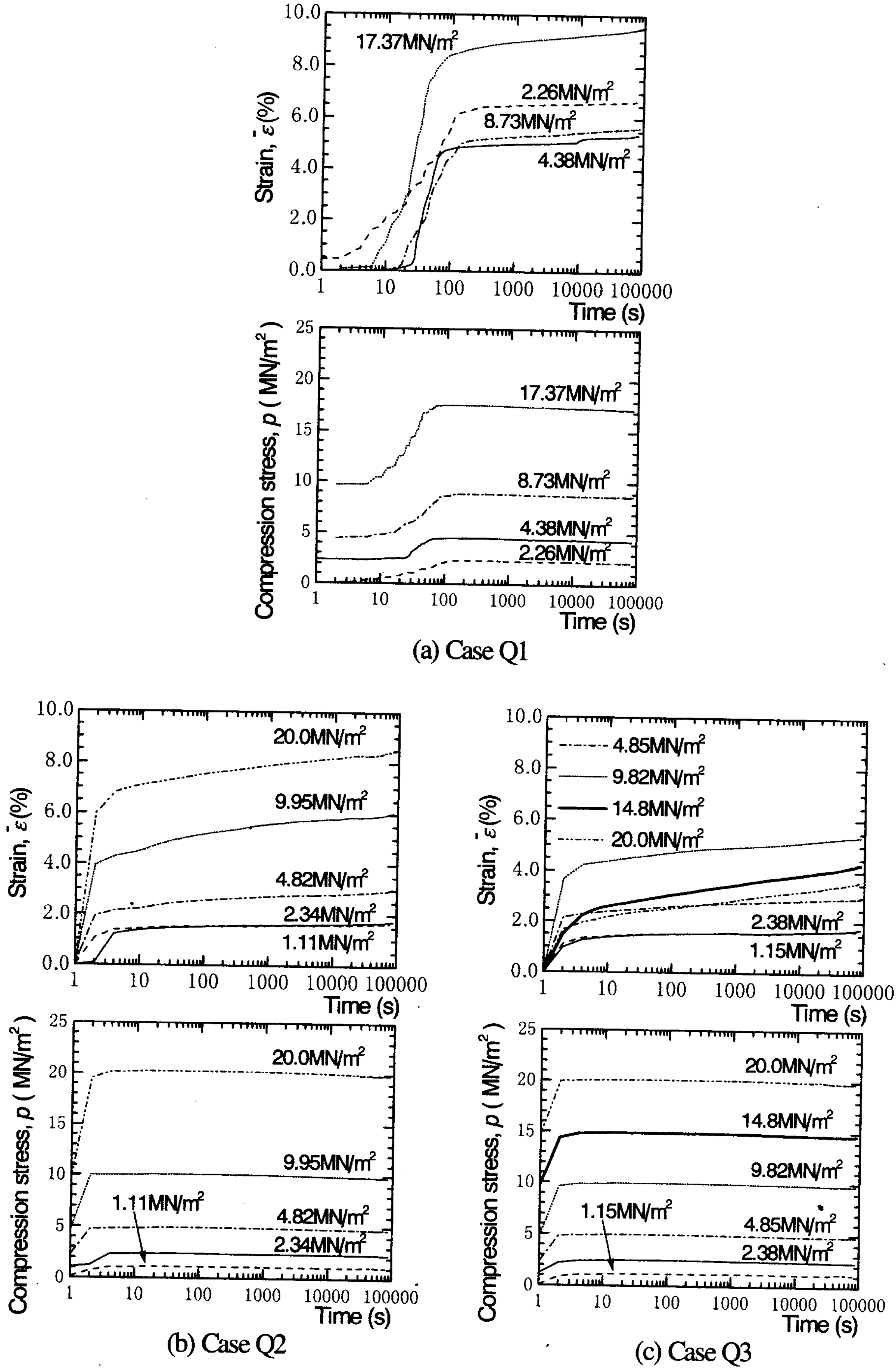


Figure 4.7 Strain or stress vs. elapsed time curves of one-dimensional compression tests (Quartz particle specimens)

### 4.3.3 Mechanism of time-dependent compression

#### (1) Chalk bar specimen

Table 4.2 lists the loading pressure and the data of cumulative crushing ratio of each loading step. Cumulative crushing ratio, $R_{CC}$, is defined as follows :

$$R_{CC} = \frac{n_{CC}}{n_{ALL}} \tag{4.2}$$

where $n_{CC}$ is the cumulative number of crushed bars at each loading stage, and $n_{ALL}$ is the number of all the chalk bars composing a specimen. The numbers of crushed chalk at the end of each load step were visually counted by the recorded visual data.

In order to accurately define the yield stress and its corresponding cumulative crushing ratio, Case C5, C6 and C7 were tested with small loading increments. It was found that the cumulative crushing ratio at the yield stress is about 40%. It is interesting to notice that the cumulative crushing ratio of 40% is close to the 37% of the survival probability $\sigma_0$ of single particle crushing test. McDowell and Bolton(1998) called the behavior near the yield stress 'clastic' yielding. They defined a clastic yield stress as the value of macroscopic stress which causes the maximum rate of grain fracture under increasing stress, for particle loaded in one-dimensional compression.

**Table 4.2 Loading pressure and cumulative crushing ratio(Chalk bar specimen)**

| Test Name | Loading pressure ($MN/m^2$ ) and cumulative crushing ratio (%) | | | | | | | |
|---|---|---|---|---|---|---|---|---|
| | Step1 | Step2 | Step3 | Step4 | Step5 | Step6 | Step7 | Step8 |
| Case C1 | 0.39 (1%) | 0.82 (12%) | 1.60 (67%) | 3.16 (84%) | 6.32 (86%) | | | |
| Case C2 | 0.45 (5%) | 0.85 (7%) | 1.57 (56%) | 3.14 (78%) | 6.20 (85%) | | | |
| Case C3 | 0.43 (0%) | 0.83 (5%) | 1.58 (40%) | 3.07 (83%) | 6.20 (92%) | | | |
| Case C4 | 0.44 (0%) | 0.82 (6%) | 1.56 (51%) | 3.09 (82%) | 6.24 (89%) | | | |
| Case C5 | 0.40 (0%) | 0.79 (17%) | 1.01 (35%) | 1.21 (47%) | 1.58 (67%) | 2.02 (69%) | 3.12 (74%) | 6.29 (80%) |
| Case C6 | 0.43 (4%) | 0.83 (18%) | 1.04 (32%) | 1.23 (45%) | 1.65 (66%) | 2.02 (73%) | 3.58 (86%) | 6.28 (87%) |
| Case C7 | 0.43 (0%) | 0.83 (4%) | 1.63 (37%) | 2.41 (71%) | 2.97 (83%) | 3.99 (91%) | 5.28 (94%) | 6.28 (94%) |

Note ) Loading pressure in the shade cell : Loading pressure that is the nearest step to yield stress and also beyond the yield stress

Figure 4.8 shows the progress of crushing patterns during loading process observed in a cubic packing tests. Two crushing modes were observed as illustrated in Figure 4.9. Mode A is the same as the single particle crushing test, "vertical splitting mode", where not very large horizontal forces seem to be applied to both sides of the chalk bar. Although it might have been caused partly by experimental variations due to manual packing and also due to dimensional variation of the chalk bars, it seems that this is a natural occurrence under the condition that no initial lock in horizontal forces between particles. Mode B is "sideways splitting mode", occurring between the nearest two contact points. Mode B must have appeared when the confining forces from both sides of chalk bars were sufficiently large. As is seen in Figure 4.8, the observed mode is almost Mode B after the loading stage closest to the yield stress. By that loading stage, it is expected that horizontal forces between particles become large enough to cause "sideways splitting mode".

Figure 4.10 shows the development of particle crushing under a sustained load of $1.57MN/m^2$ of Case C2 at six different time stages. When a crack was observed in a cross section of a chalk bar, it was regarded as crush. The increase in the number of crushed chalk bar occurred only in the first 45 seconds.

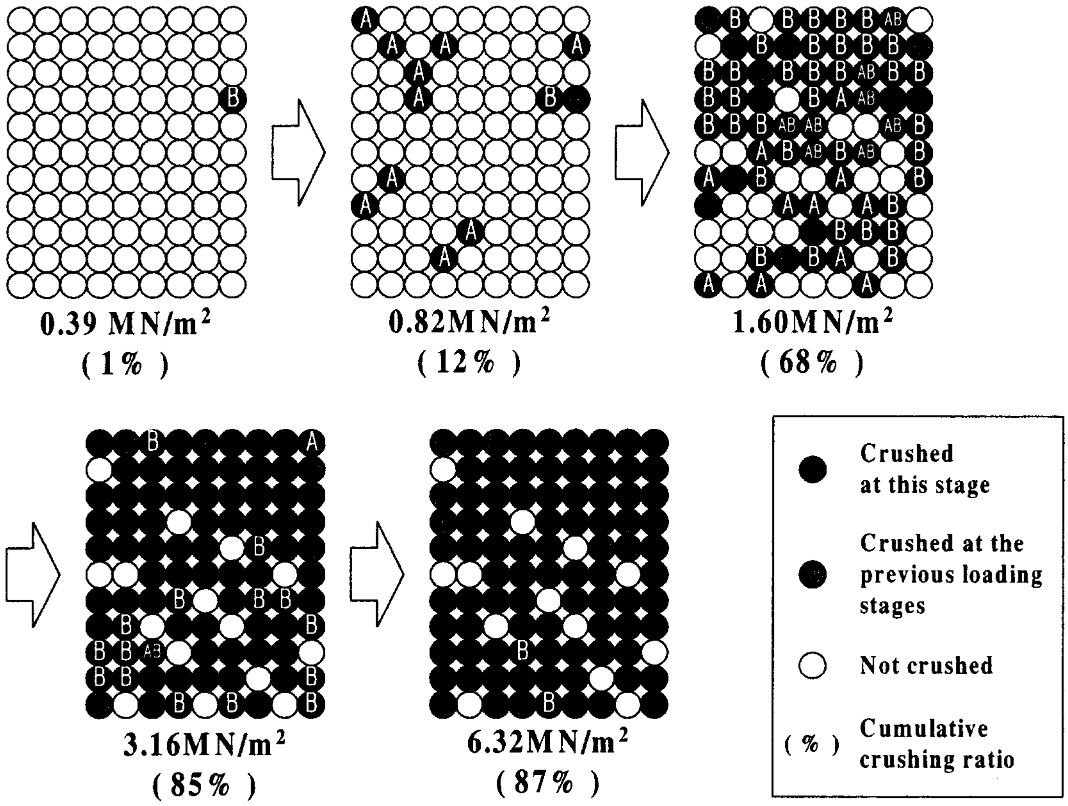


Figure 4.8(a) Macroscopic crushing progress and crushing patterns
( Case C1 : Simple cubic packing )

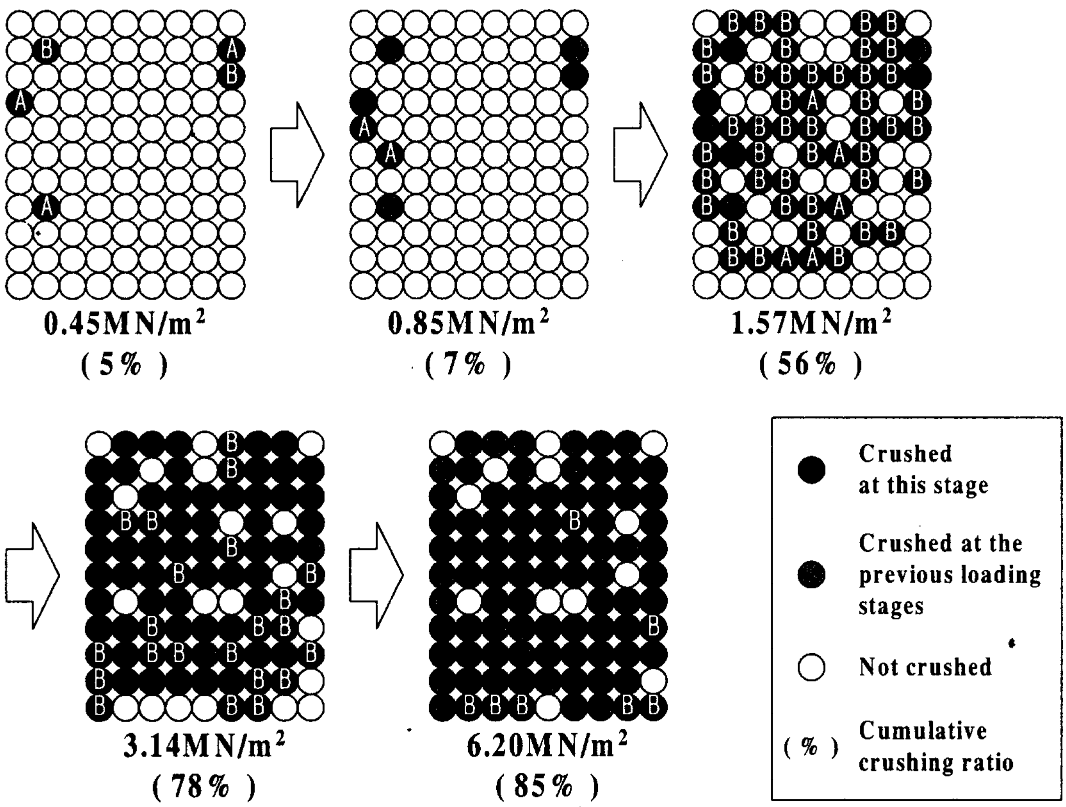


Figure 4.8(b) Macroscopic crushing progress and crushing patterns
( Case C2 : Simple cubic packing )

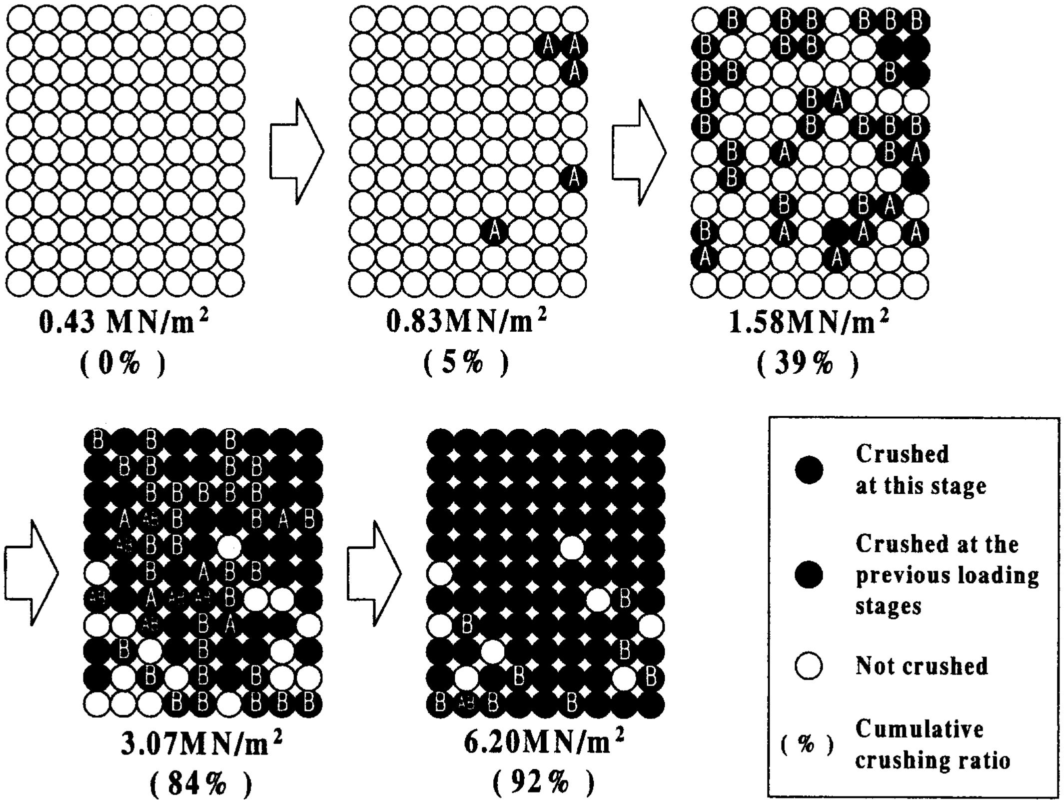


Figure 4.8(c) Macroscopic crushing progress and crushing patterns ( Case C3 : Simple cubic packing )

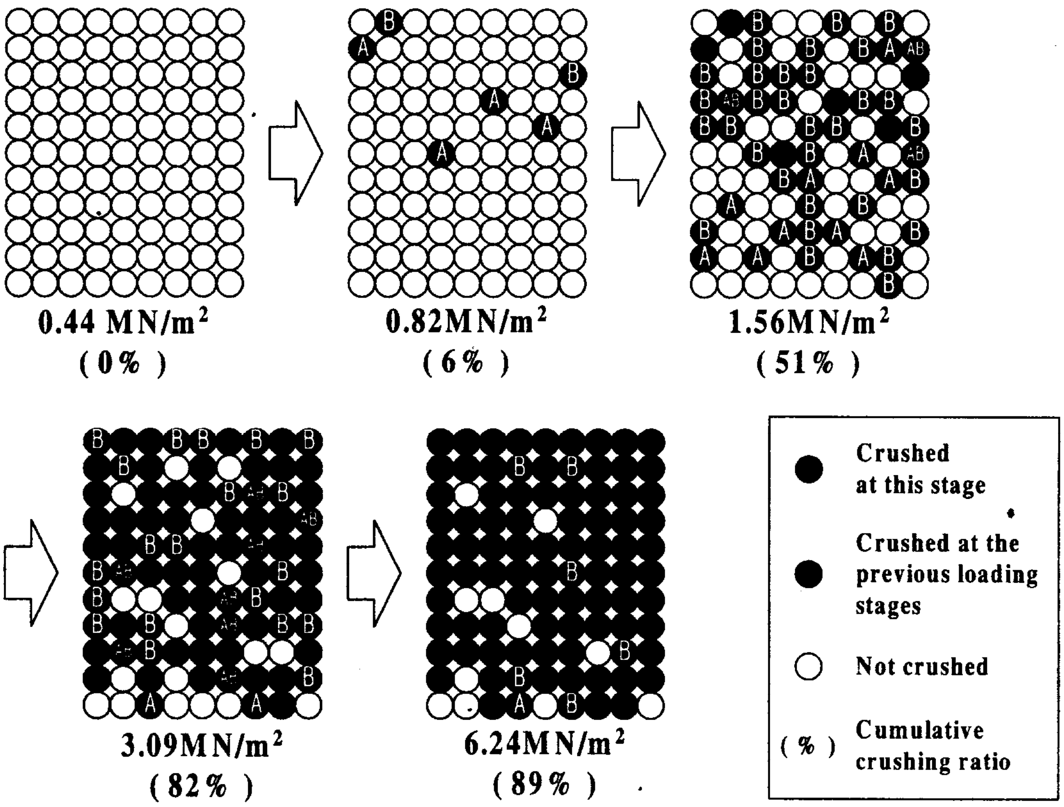


Figure 4.8(d) Macroscopic crushing progress and crushing patterns ( Case C4 : Simple cubic packing )

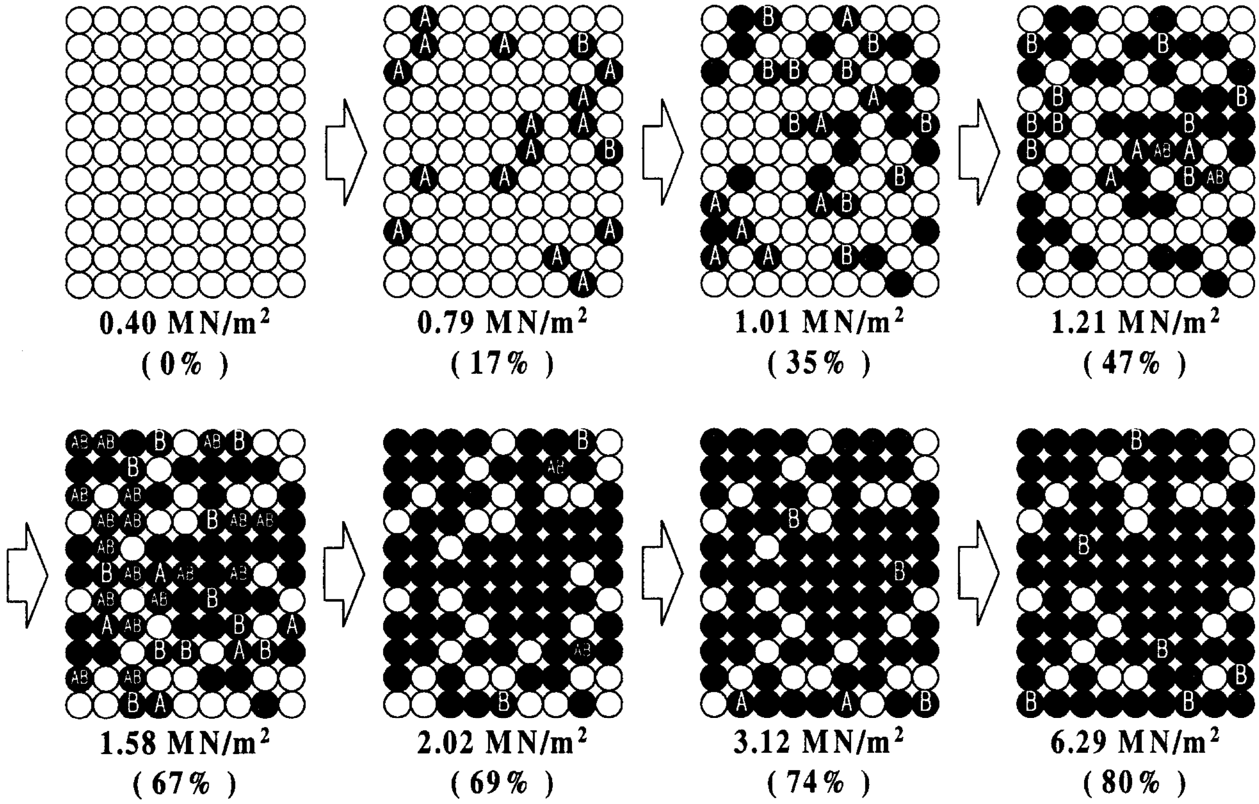


**Figure 4.8(e)** **Macroscopic crushing progress and crushing patterns**
**( Case C5 : Simple cubic packing )**

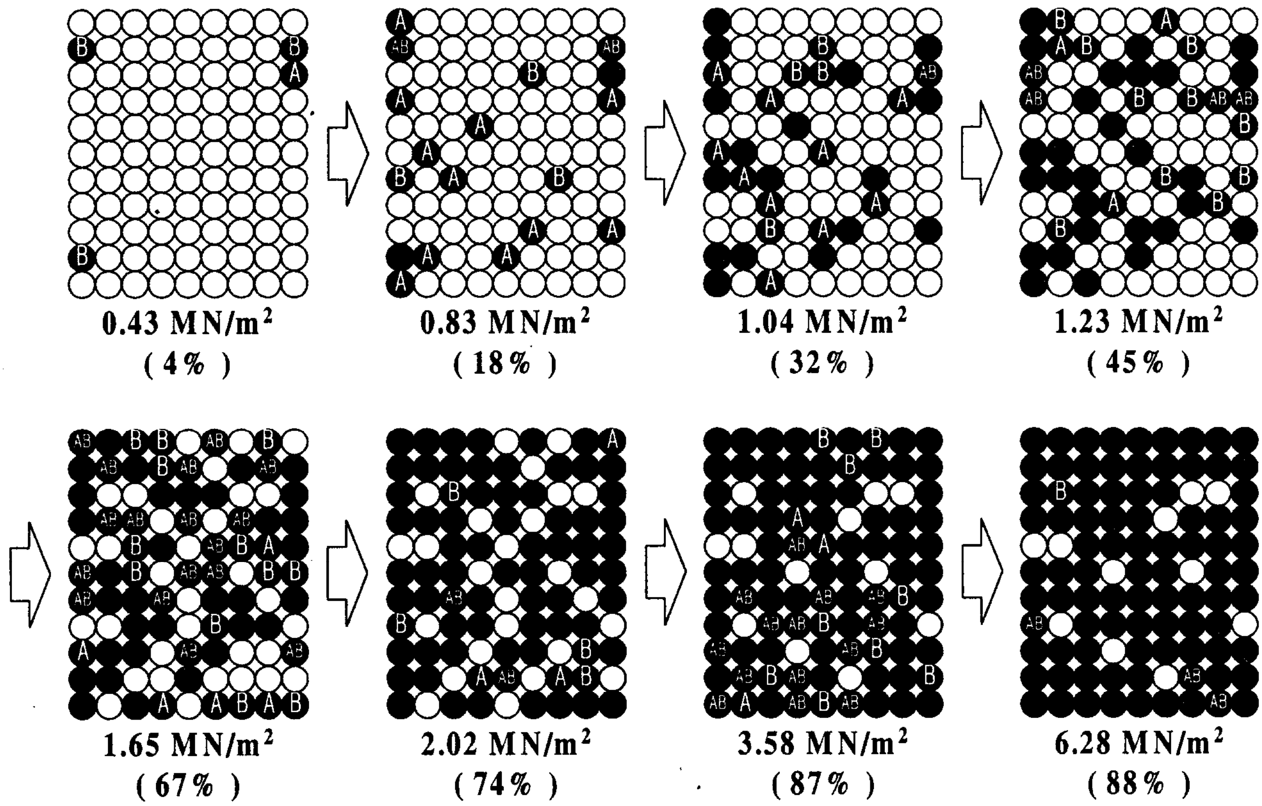


**Figure 4.8( f )** **Macroscopic crushing progress and crushing patterns**
**( Case C6 : Simple cubic packing )**

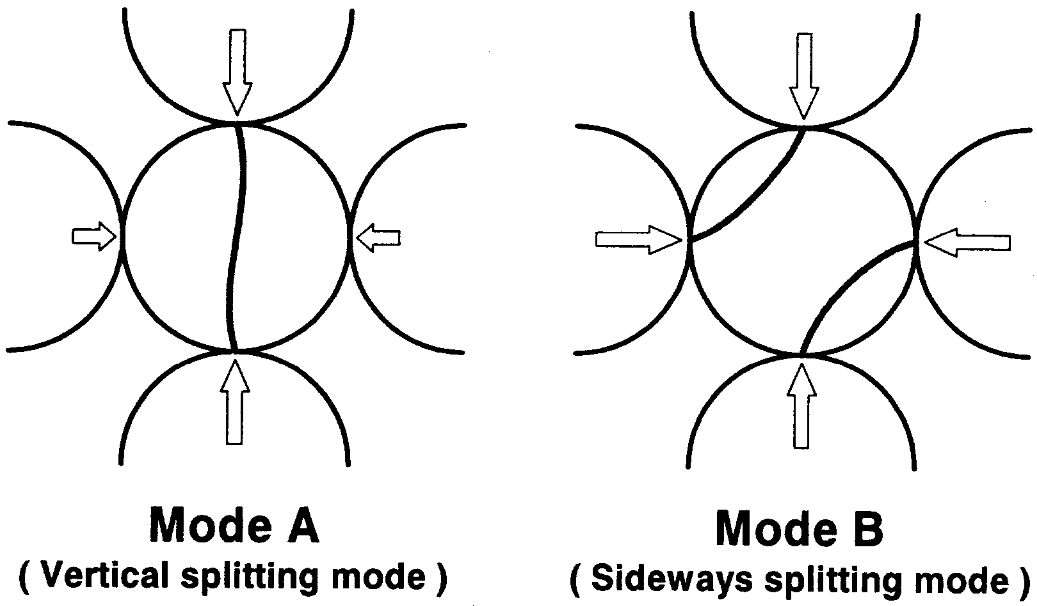


Figure 4.9 Crushing modes (Sinple cubic packing case)

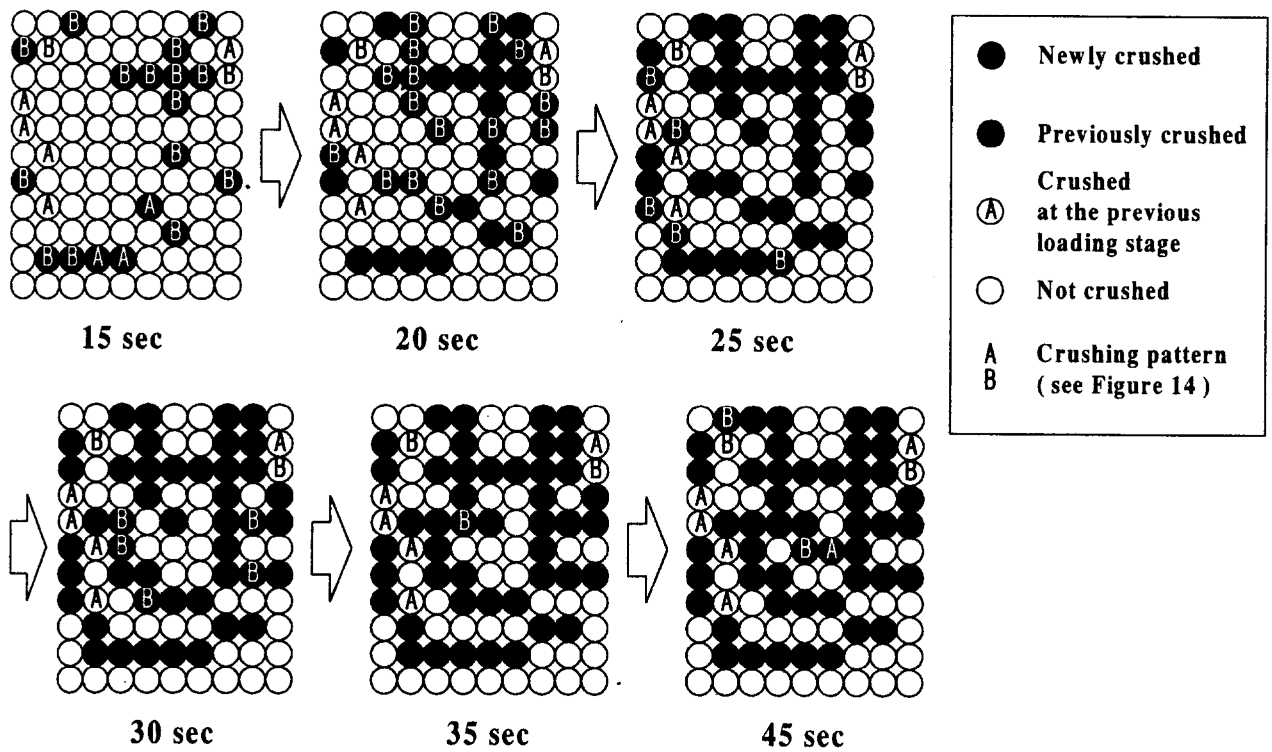


Figure 4.10 Development of particle crushing under a loading pressure ( Case C2 ;Loading pressure : 1.57MN/m$^2$ )

Photograph 4.2 shows the progress of the chalk bar crushing under an one-dimensional compression test. Photographs 4.2(a) and (c) were taken two hours after the application of loading pressure closest to the yield stress. Photographs 4.2(b) and (d) were taken 24 hours after the loading pressure was applied. (a) and (b) are the vertical splitting mode(Mode A). The width of the vertical crack slightly increased as time went on. Local crushing progress was observed at the upper part of fragmented chalk during the elapsed time. (c) and (d) are the sideways splitting mode(Mode B). The fragments were separated from the original body and went into surrounding voids. After that, the local crushing progressed with time at the edges of the remaining original particle.

Photograph 4.3 shows the chalk bar specimen after test. Almost all the chalk bars were crushed, but the array of the crushed chalk bar remains its original pattern. And almost all the chalk bars in the specimen were crushed in Mode B as mentioned before. In crushing Mode B, the remaining parts of the crushed chalk bars would settle predominantly associated with the progress of the local crushing at contact points. This mechanism does not involve horizontal movement and rotation of the particle. Thus it was considered that the horizontal displacement and the rotation of each chalk bar did not play a significant role in causing compression.

Accordingly, the major source of the time-dependent strain development must have been the local crushing progress at contact areas. Any occurrence of particle splitting must have accelerated the local crushing speed because of the increase in stress at the contact areas due to decreasing cross sectional area of the particles.

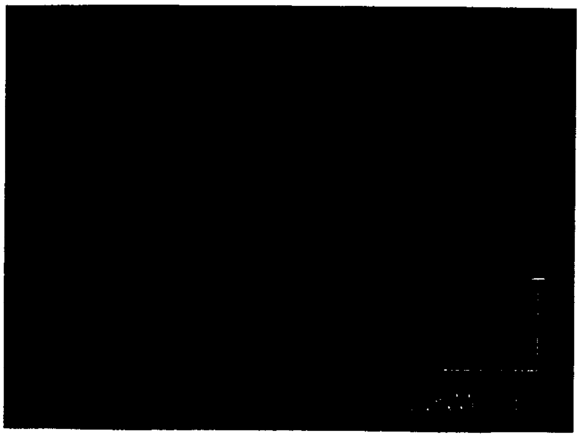

(a) Mode A : 2 hours after loading

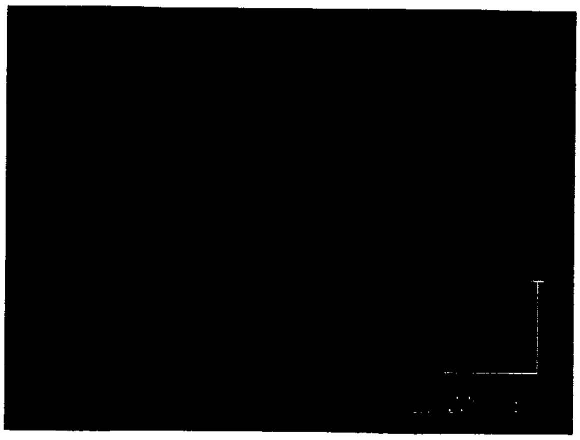

(b) Mode A : 24 hours after loading

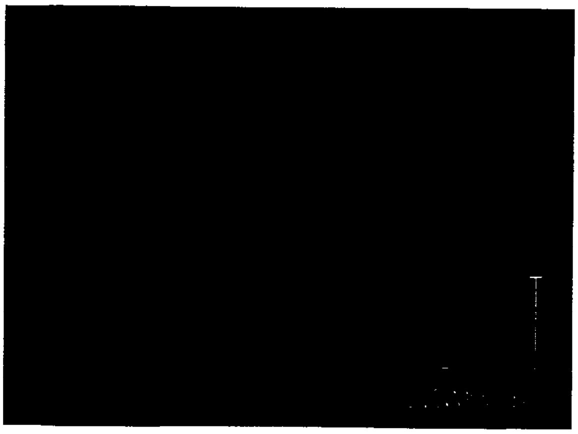

(c) Mode B : 2 hours after loading

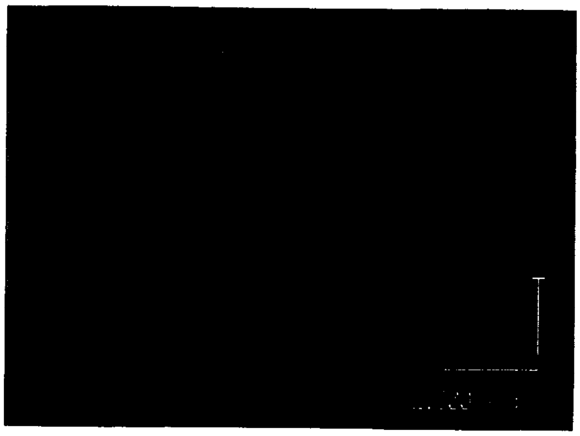

(d) Mode B : 24 hours after loading

Photo. 4.2 Progress of crushing of chalk bar under one-dimensional compression test

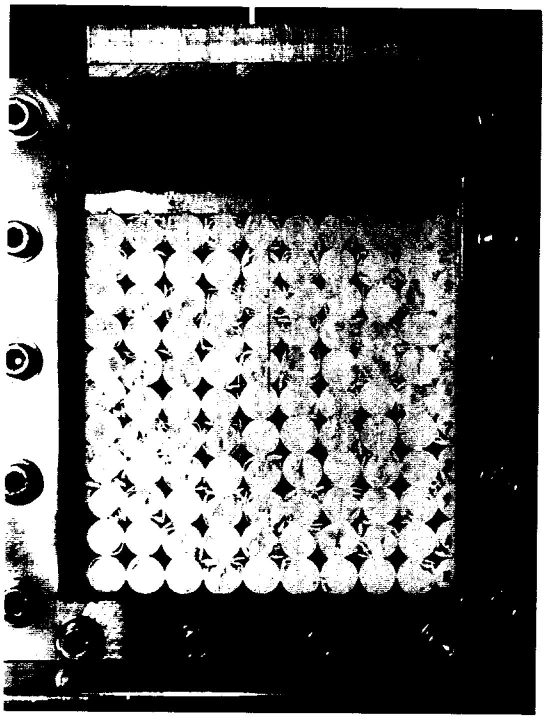

Photo. 4.3 Chalk bar specimen after one-dimensional compression test

Figure 4.11 illustrates crushing modes and the crushing progress of hexagonal packing case (Case C7). Three crushing modes Mode C, D and E as shown in Figure 4.12 were observed. Mode C is effectively identical to Mode A of "vertical splitting mode" while, Mode D and E are classified into a family of Mode B, "sideways splitting mode". The dominant modes are Mode D and Mode E. At the final loading stage, 95% of all the crushed chalk bars belong to Mode D and Mode E, showing that the chalk bars of hexagonal packing were confined more rigidly compared to cubic packing cases. From Step 2 to Step 4, Mode D is more marked than Mode E, while from Step 5 to Step 8, Mode E is more noticeable than Mode D. It is also noticed that almost every chalk bar had two to four cracks, and these cracks did not occur at the same step, but occurred progressively step by step. The mechanism of time-dependent compression of the hexagonal packing case would be fundamentally the same as that of the cubic packing case.

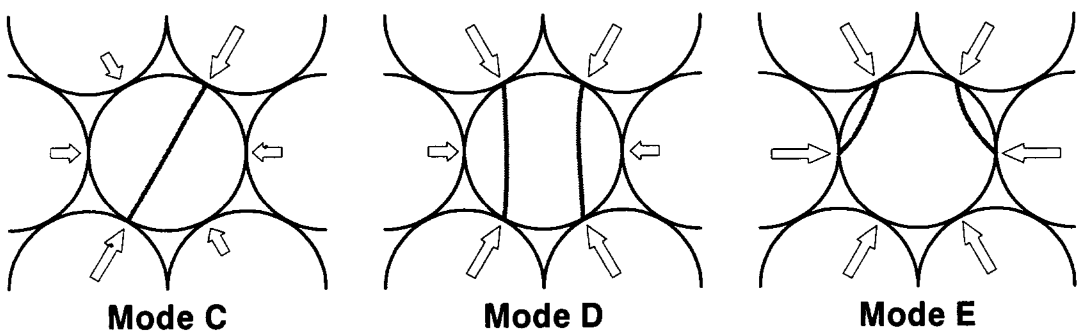


**Figure 4.12 Crushing Modes (Hexagonal packing case)**

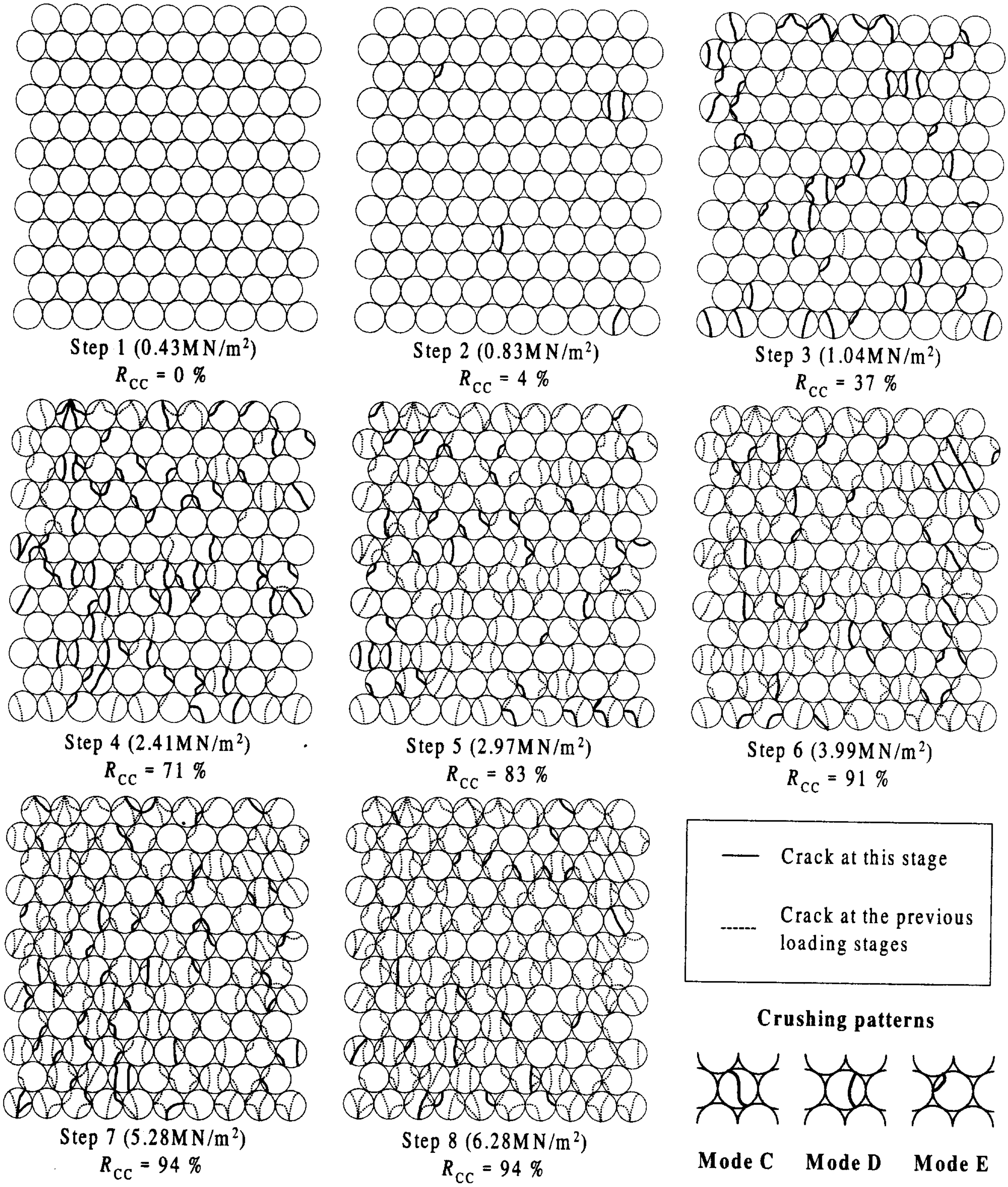


**Figure 4.11 Crushing patterns and macroscopic crushing progress ( Chalk bar specimen : Case C7 : Hexagonal packing )**

### (2) Talc bar specimen

There are two aspects of time-dependent behavior due to particle crushing for the talc bar specimen : smooth increase of strain that appears under sustained loads and the sudden increase of strain at the final loading stage (see Figure 4.5).

Photograph 4.4 shows the progress of a talc bar crushing under an one-dimensional compression test. Photo. 4.4(a) was taken 6 hours after the final loading started. Photo. 4.4(b) was taken 24 hours after the load was applied. It is observed that the contacting length(area) at the lower part increased from 3.2mm to 3.6mm and that new crack occurred at the lower left part of the talc bar during the elapsed time. It is considered that the mechanism of gradual compression is the same as that of the chalk bar specimens.

Table 4.3 lists the sustained stress values and data of cumulative crushing ratio of each loading step. In all of the three cases, the cumulative crushing ratio exceeded 40% at the final loading stage. By referring to the $e$ – log $p$ curves shown in Figure 4.3(b), large compression occurred at the last loading stage. Thus, it is considered that the specimen that the cumulative crushing ratio exceeds 40% would be capable of causing a large compression.

**Table 4.3 Loading pressure and cumulative crushing ratio(Talc bar specimen)**

| Test Name | Loading pressure (MN/m$^2$ ) and cumulative crushing ratio (%) | | | | | |
|---|---|---|---|---|---|---|
| | Step1 | Step2 | Step3 | Step4 | Step5 | Step6 |
| Case T1 | 0.60 (0%) | 1.13 (2%) | 2.21 (9%) | 4.46 (50%) | | |
| Case T2 | 0.84 (0%) | 1.69 (1%) | 2.52 (7%) | 3.37 (14%) | 4.19 (24%) | 5.09 (51%) |
| Case T3 | 0.91 (2%) | 1.72 (11%) | 2.54 (23%) | 3.43 (64%) | | |

Note ) Loading pressure in the shade cell : Loading pressure that is the nearest step to yield stress and also beyond the yield stress

Figure 4.13 shows the progress of crushing patterns during loading process observed in each test. The two crushing modes, Mode A and Mode B, were also observed. In contrast to the chalk bar specimen, about 70% of all the crushed talc bars belonged to the Mode A in the final loading stage. Possible reasons why many talc bars crushed in Mode A would be that the horizontal forces between talc bars were small because of the manual packing and the dimensional variation of the talc bars, and that the strain at the first peak force($F_c$) of talc bar is much smaller than chalk bar.

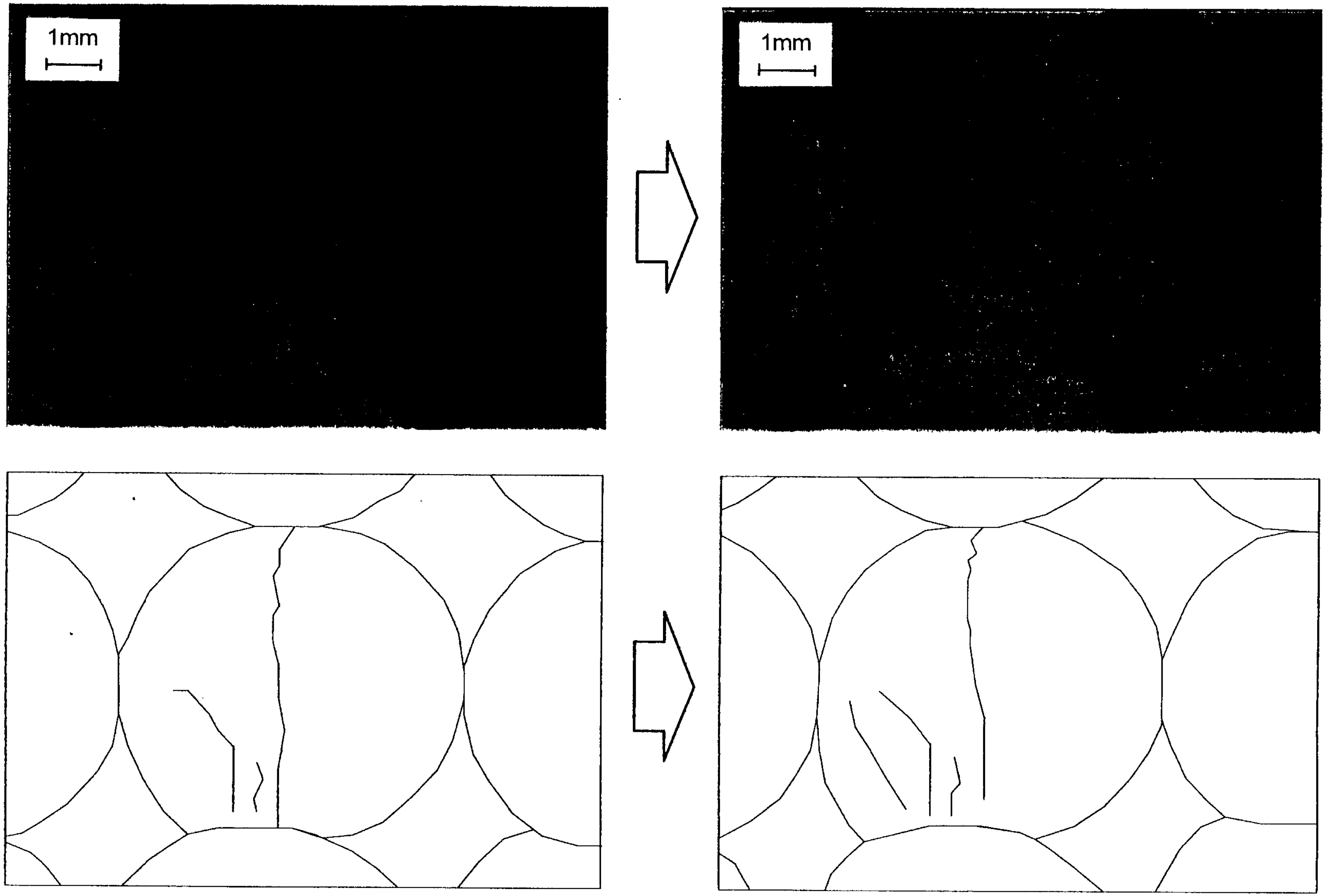


(a) 6 hours after loading

(b) 24 hours after loading

Photo. 4.4 Progress of talc bar crushing under one-dimensional compression test (Final loading stage)

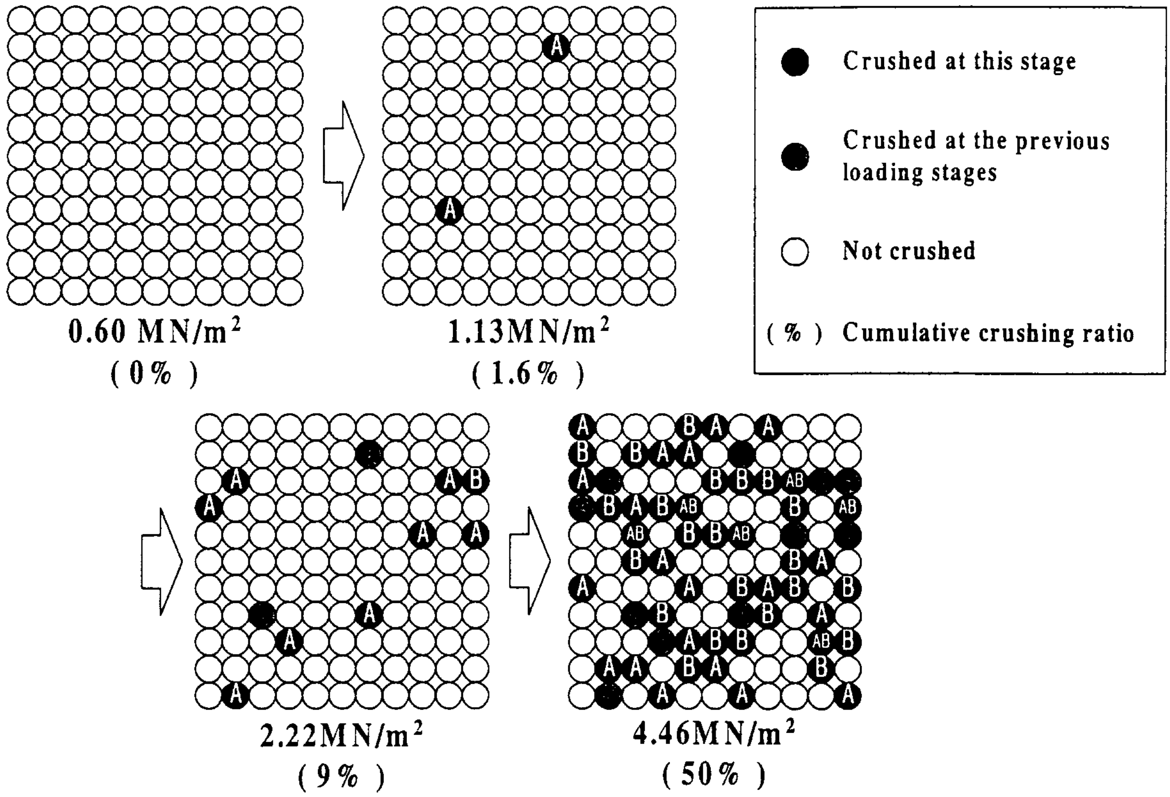


Figure 4.13(a) Macroscopic crushing progress and crushing patterns
( Talc bar specimen : Case T1 )

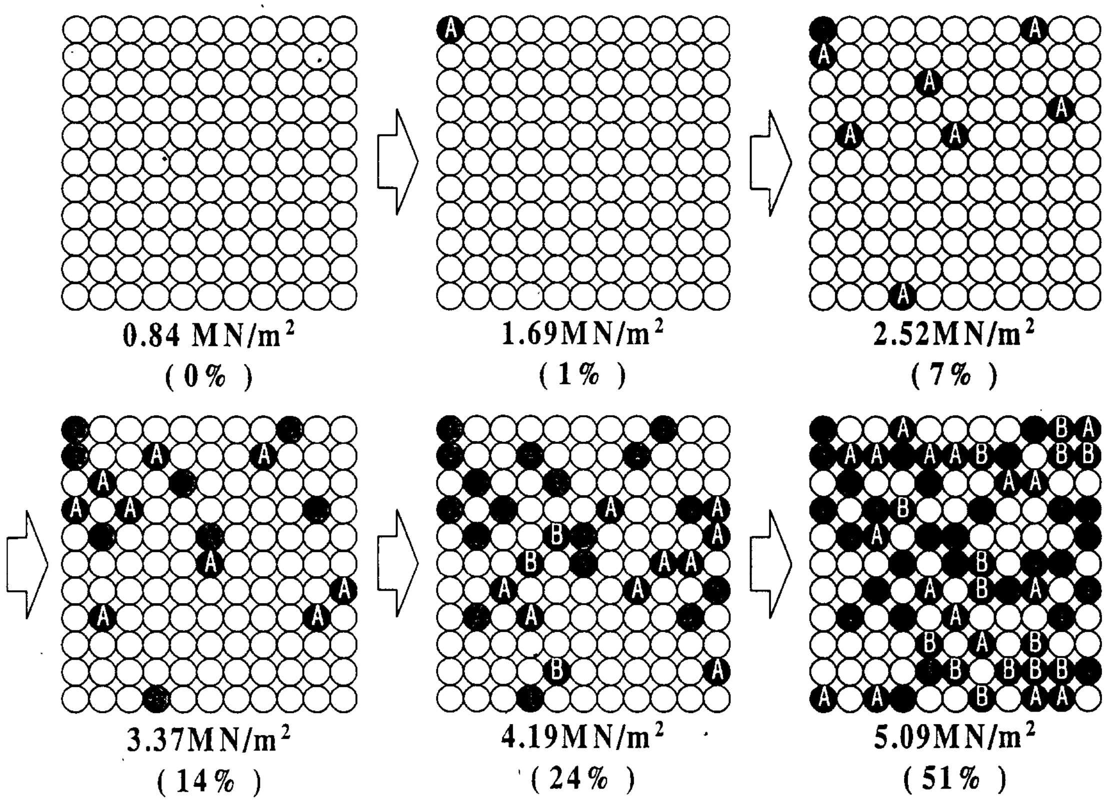


Figure 4.13(b) Macroscopic crushing progress and crushing patterns
( Talc bar specimen : Case T2 )

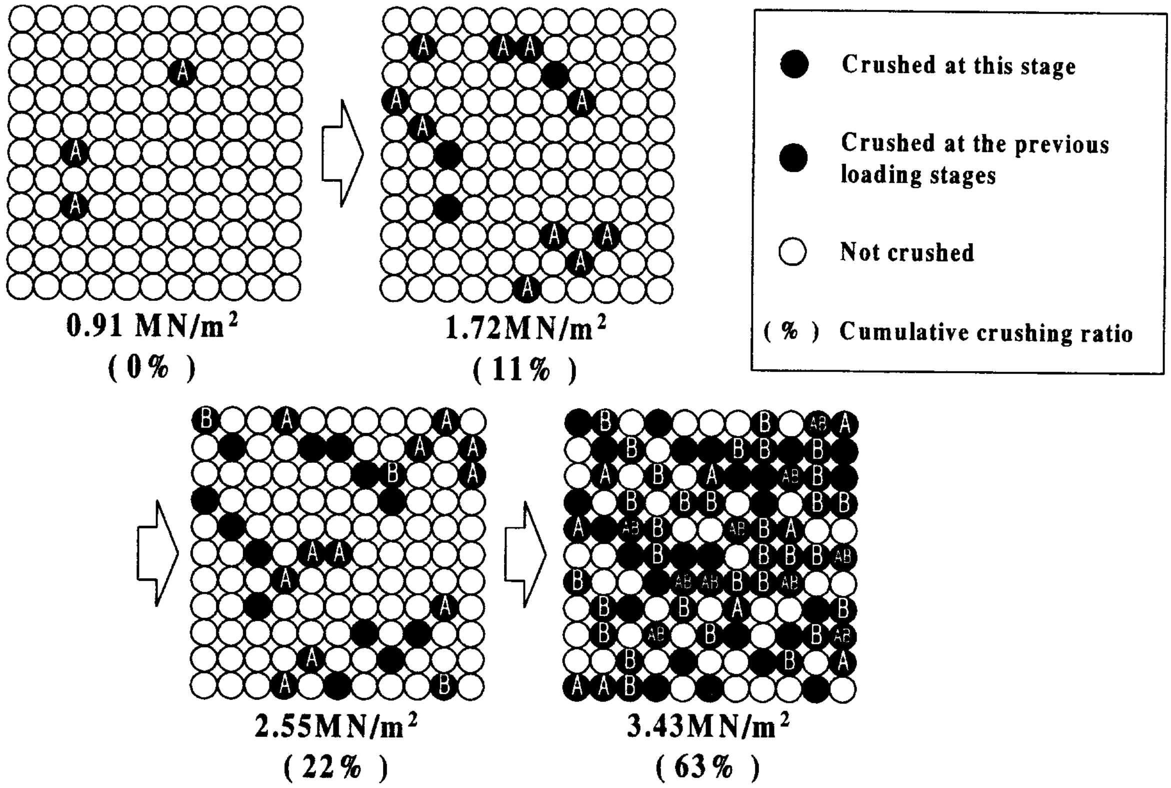


**Figure 4.13(c) Crushing patterns and macroscopic crushing progress (Talc bar specimen : Case T3)**

Figure 4.14 shows an example of sketches of cracks appeared on the talc bars in a loading stage. Also in the one-dimensional compression tests, many cracks of Mode A were neither straight nor vertical as well as the single particle crushing tests of talc bars. Such a crack configuration would contribute to occurrence of the rapid compression mentioned below.

Figure 4.15 shows the development of particle crushing under a sustained loading pressure of 5.09MN/m$^2$ of Case T2 at four different time stages. There were about ten talc bars that were newly crushed in the interval from 30minutes to 6hours. The sudden increase of strain occurred at about 2hours (see Figure 4.5). There must have been a relationship between the new crush of talc bars in that interval and the sudden increase of strain.

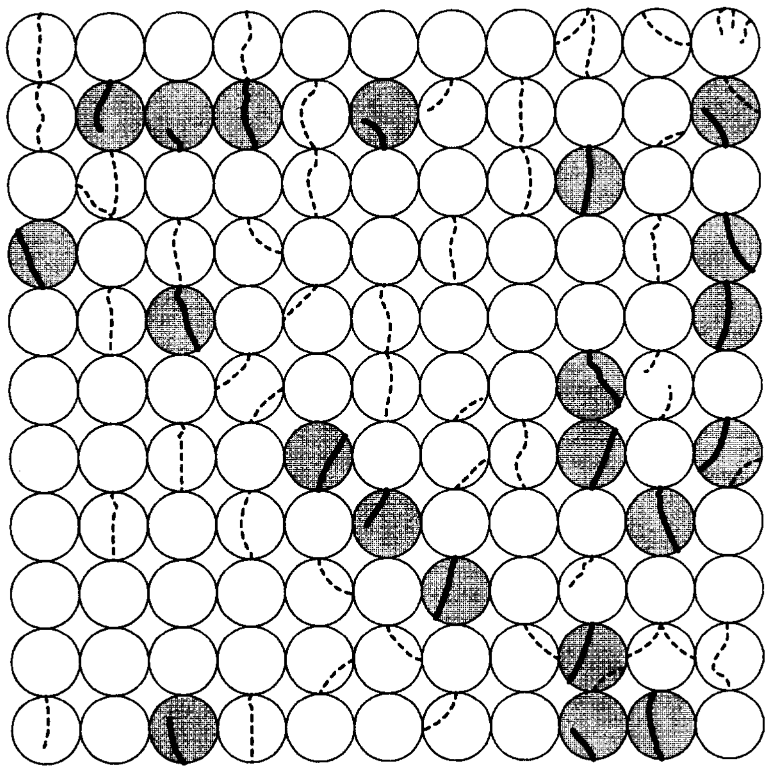

**Figure 4.14 Sketch of cracks (Case T2 ; 5.09MN/m$^2$ )**

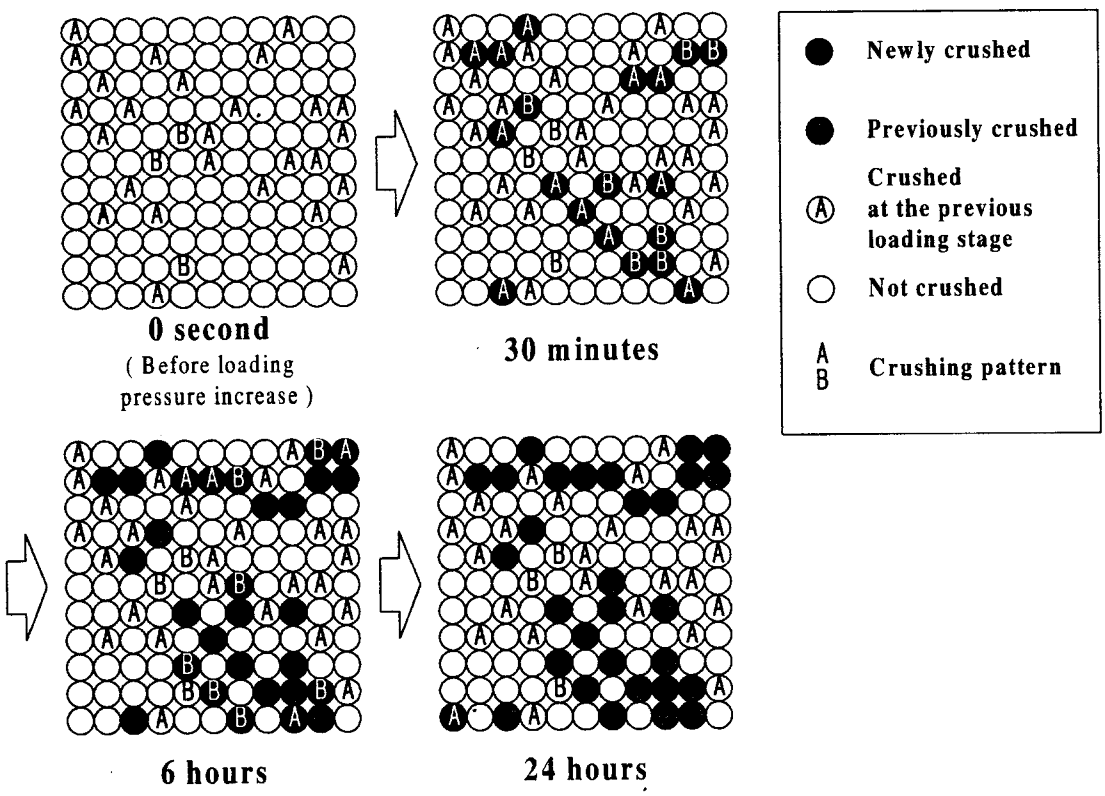


**Figure 4.15 Development of particle crushing under a loading pressure ( Talc bar specimen : Case T2 ; Loading pressure : 5.09MN/m$^2$ )**

Photograph 4.5(a) shows the talc bar specimen of Case T3 under the final loading stage after 100seconds from the onset of loading, and Photograph 4.5(b) shows the same specimen after 1000seconds. The sudden strain increment occurred at about 300seconds (see Figure 4.5(c)). It is observed that the array of the crushed talc bars shown in Photo.4.5(a) was noticeably changed. It is also seen that there were some talc bars smashed severely during that elapsed time, on the other hand, there were some talc bars being not crushed.

Photograph 4.6 shows a talc bar crushed in Mode A after the sudden compression shown in Figure 4.5(c). It is seen in the photograph that the severe local crushing at the upper and lower contact areas progressed. It is also noted that the crack initially developed in the vertical direction and curved from the upper right to the lower left direction. Photo.4.5(b) shows several talc bars showing the crack pattern, similar to that of Photo.4.6.

Figure 4.16 illustrates the mechanism of the smashing pattern appeared in Photo.4.6. Firstly, a crack fully develops through the bar and the local crushing then progresses at the contact areas, widening the contact areas. Then slips on the contact areas suddenly occur and the two fragmented talc bars move and rotate downward as shown in the right side illustrations of Figure 4.16. This movement results in sudden settlement of the upper talc bars. Once a slippage of one contact area occurs, it triggers other slippage and accelerates the chained-event of the rearrangement of the talc bars throughout the specimen. The sudden rearrangement of the talc bars finally causes the sudden compression of the specimen shown in Figure 4.5.

The inclined cracks mentioned before would encourage the behavior shown in Figure 4.16. As shown in Chapter 3, a talc bar that split with an inclined crack tended to rotate under vertical loading.

Existence of water may affect the magnitude and occurrence time of the sudden jump of strain: as shown in Figure 4.5, the magnitude of the sudden jump of strain in the saturated specimen (Case T3) is larger than that of the dry specimens (Case T1,T2), and the jump of the saturated specimen occurred much earlier than those of the dry one. However, further studies are necessary on the effects of water existence to the sudden jump of strain.

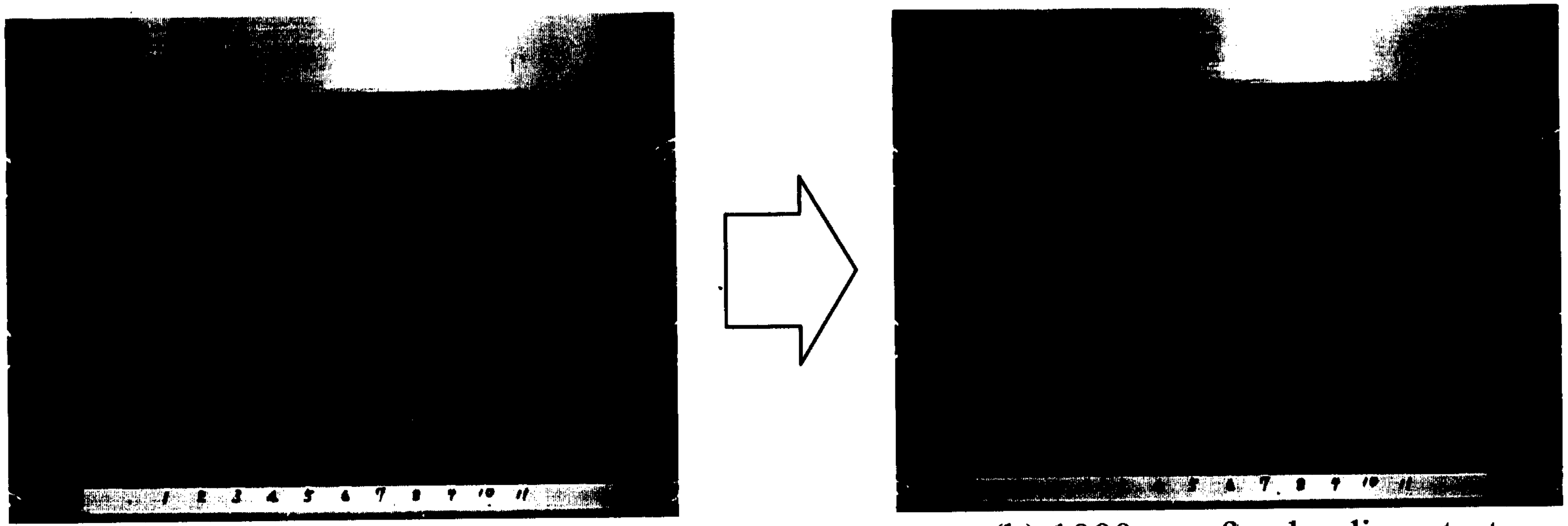

(a) 100sec after loading starts
( before sudden strain increment )

(b) 1000sec after loading starts
( after sudden strain increment )

**Photo. 4.5 Talc bar specimen before and after sudden strain increment (Case T3)**

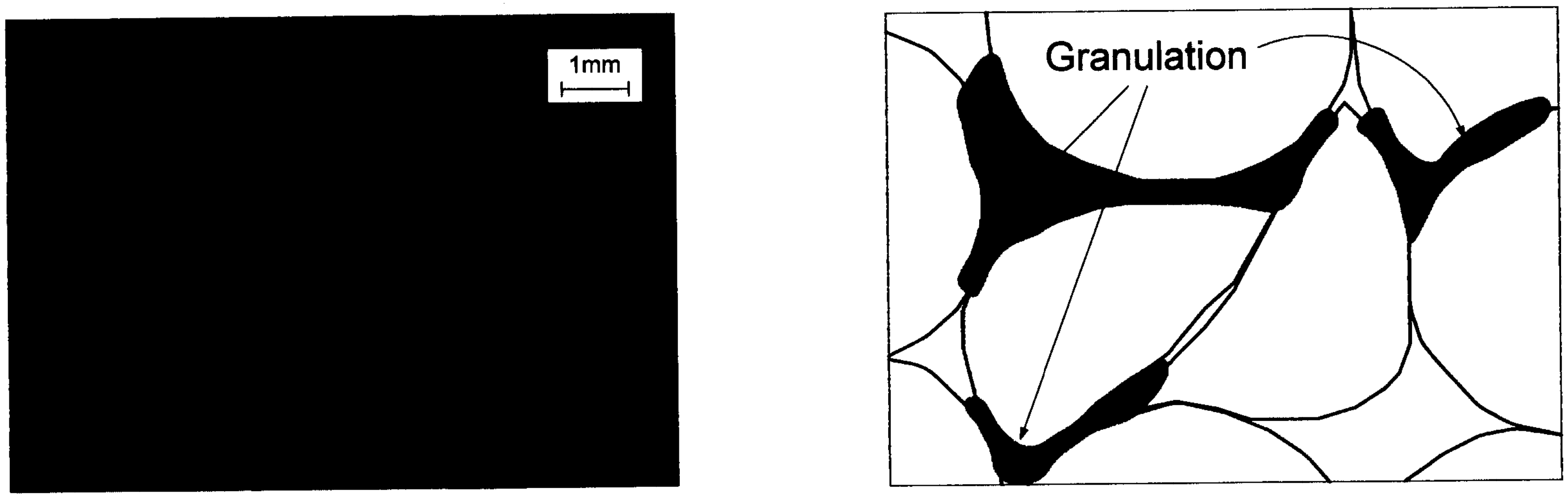


**Photo. 4.6 Final state of talc bar crushed in Mode A**

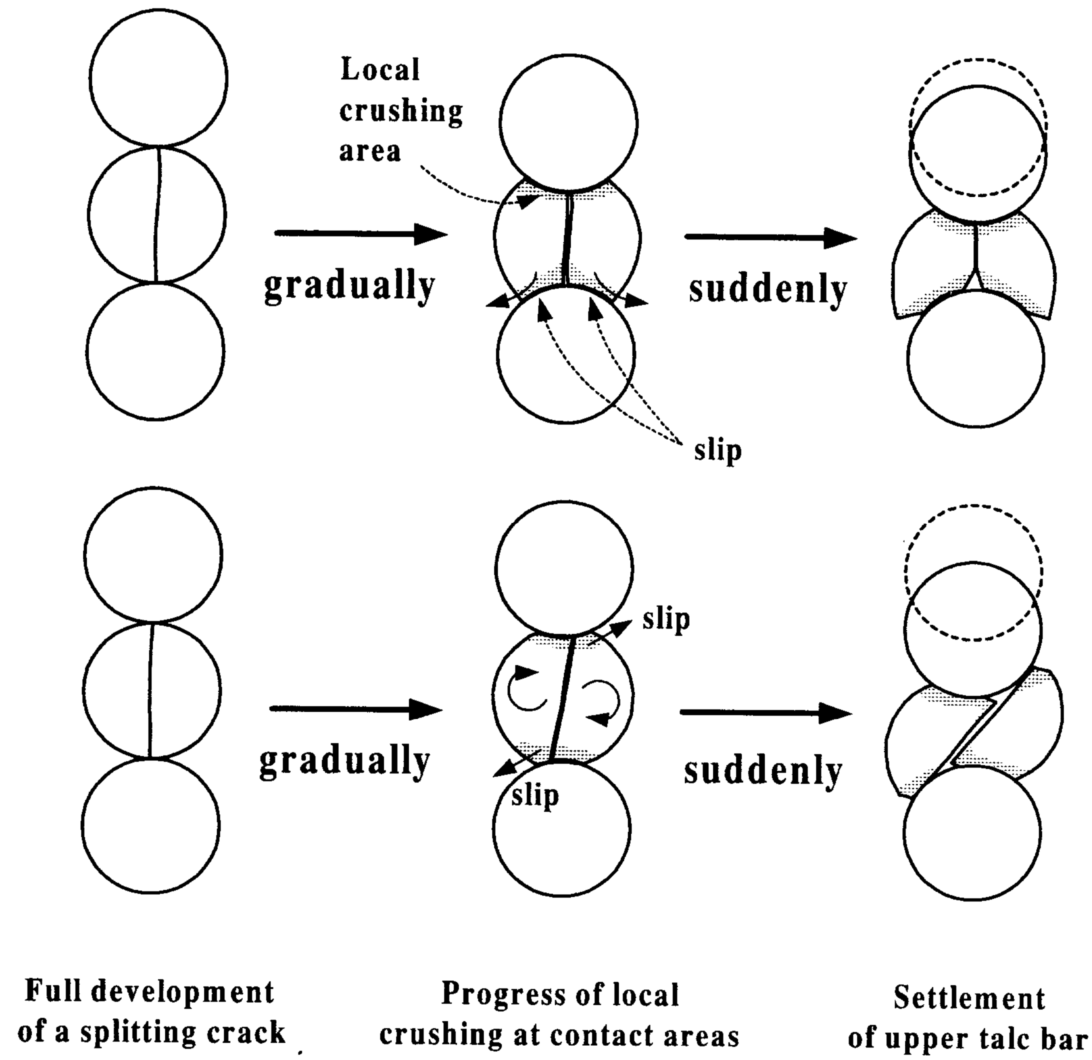


**Figure 4.16 Mechanism of compression due to crushing (Talc bar specimen)**

When contact forces between the particles are redistributed by this sudden particle rearrangement, further particle crushing will take place in the newly established particle structure. It is considered that the crush of the talc bars observed between the period of 30 minutes and 6 hours shown in Figure 4.15 would have occurred under the chain mechanism described above.

### (3) Glass beads specimen

In the cases of glass beads specimens, visual observation was only possible for the particles nearest to the front glass wall, of which behavior is considered to be affected by side wall friction. Figure 4.17 shows the grain size distribution curves before and after the test for the two glass beads specimens. The percentage of fine particles passing through the 0.4mm sieve increases after the test. Photograph 4.7 shows the glass beads whose diameter ranges from 0.85mm to 1.2mm after the test. It was observed that the angular glass beads were crushed only at the surface. And the crushing sound was heard during the loading tests. Based on these facts, the mechanism of settlement is deduced as is illustrated in Figure 4.18. The upper type of crushing(Figure 4.18(a)), which is similar to the manner observed in the single particle crushing tests, may occur for the particles that have little contact points. When a particle instantly crushes, the crushed fragments are captured by the surrounding particles, creating a void, to which the surrounding particles start moving in. On the other hand, the crushing at the surface(Figure 4.18(b)) may occur for the particles having many contact points. However, the contact points still remain in their original position. Further increase in contact forces or even keeping the current contact forces may cause breaking off the edged contact areas.

Thus, it is considered that particle bursting or crushing, rearrangement of particles and breaking off the edged contact areas may concurrently occur in high brittle materials. Obviously more experiments for various materials are need to confirm this observation.

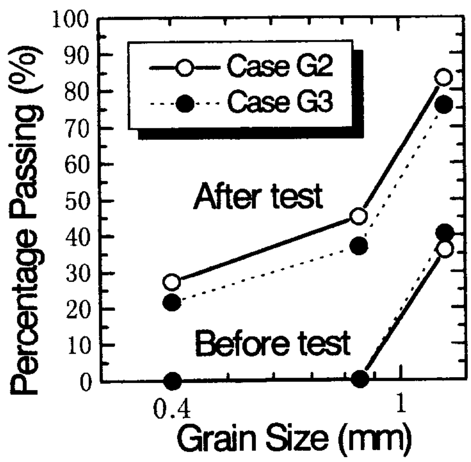


**Figure 4.18 Grain size distribution curves of one-dimensional compression tests (Glass bead specimen)**

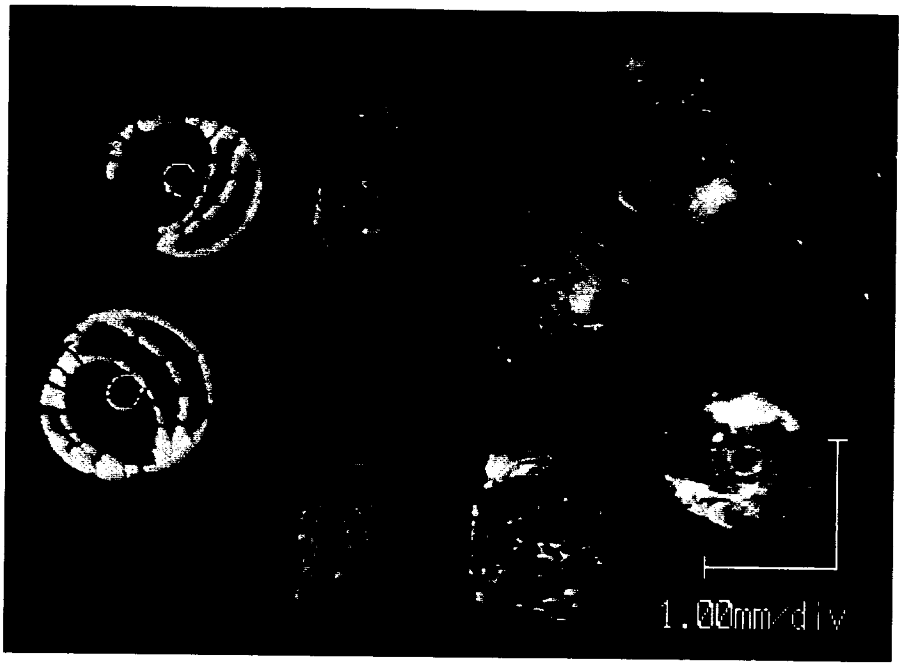


**Photo. 4.7** Glass beads after one-dimensional compression test (0.85mm<$d$<1.2mm, The left two unbroken glass beads were taken for comparison. )

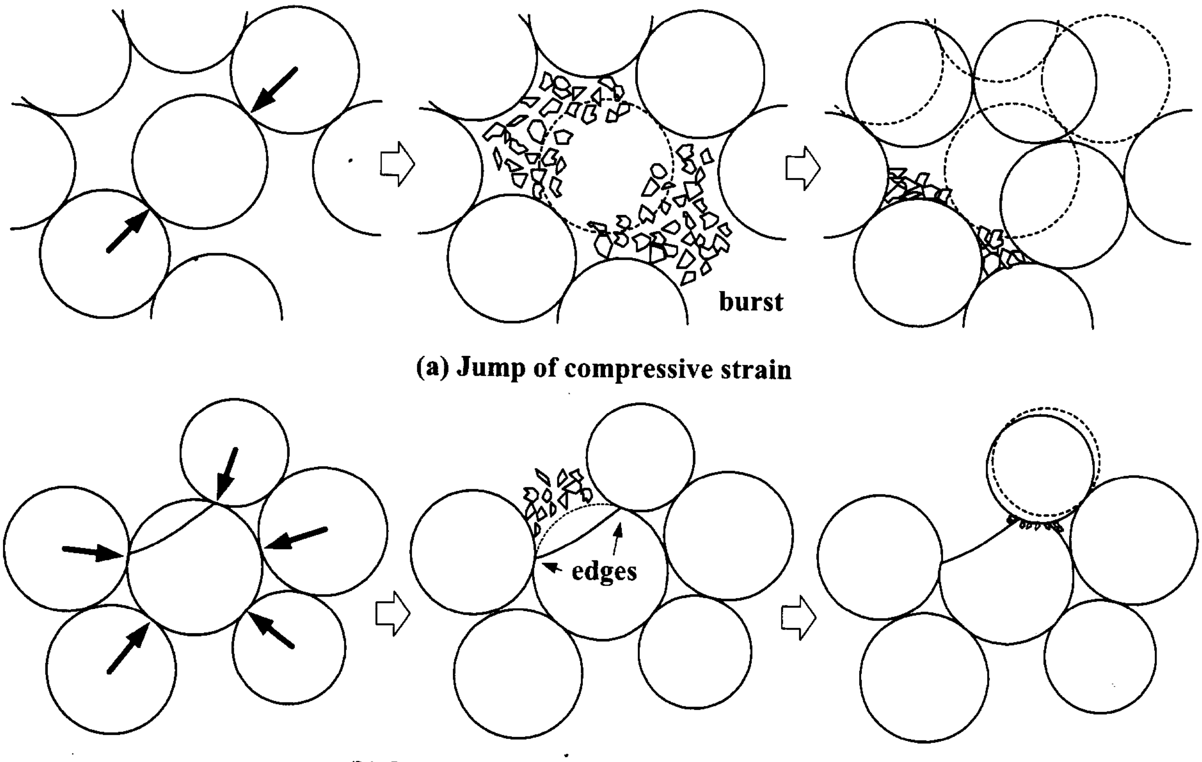


**Figure 4.18 Mechanism of compression due to crushing (Glass beads specimen)**

### (4) Quartz particle specimen

In the cases of the quartz particle specimen, visual observation was only possible for the particles nearest to the front glass wall. Figure 4.19 shows the grain size distribution curves before and after the test for the two quartz particle specimen. The trend of the distribution curves is the same as that of the glass beads specimen. Photograph 4.8 shows the increase of small fragments at the bottom of a quartz particle specimen. These fragments must have been generated by the collapse of angular edges of particles. It was actually observed during the test that these fragment particles were falling down through the skeleton of particles. From these facts, the possible crushing mechanism may be illustrated in Figure 4.20. Edge collapsing may be the dominating mechanism of the settlement of loading plate.

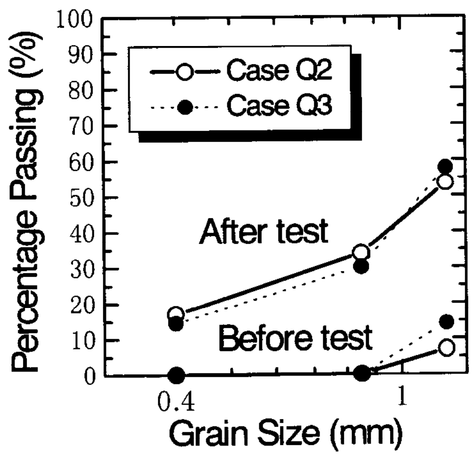


**Figure 4.19 Grain size distribution curves of one-dimensional compression tests (Quartz particle specimen)**

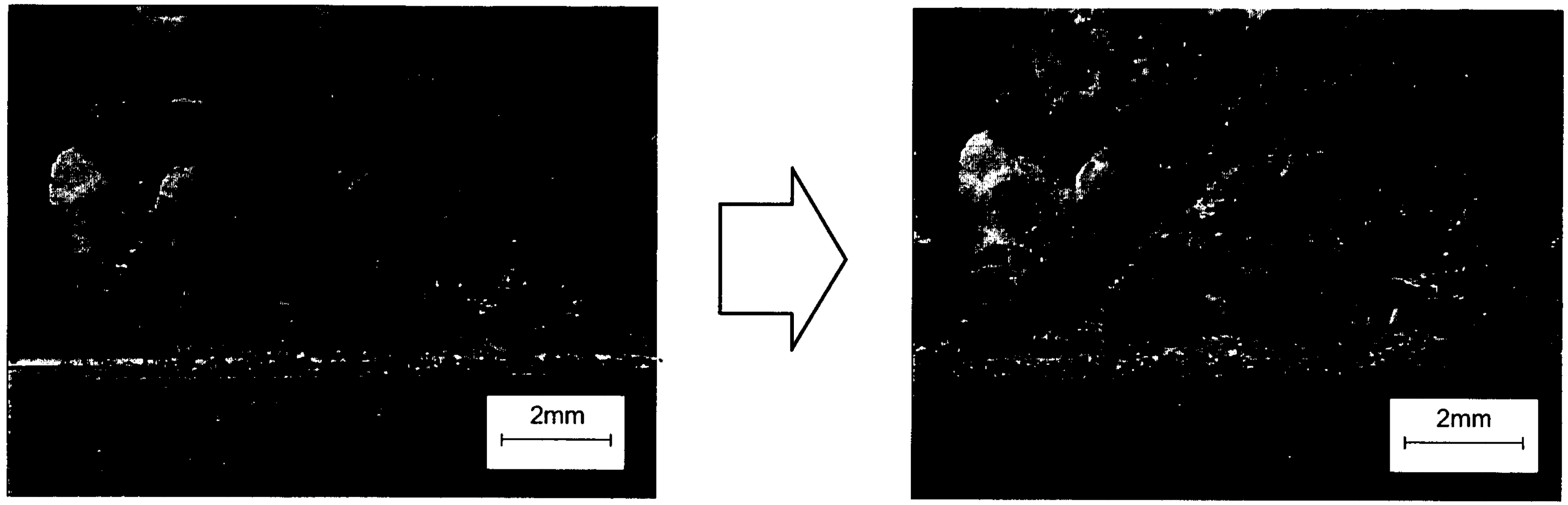


(a) Before test (b) After test

**Photo. 4.8 Bottom area of quartz particle specimen**

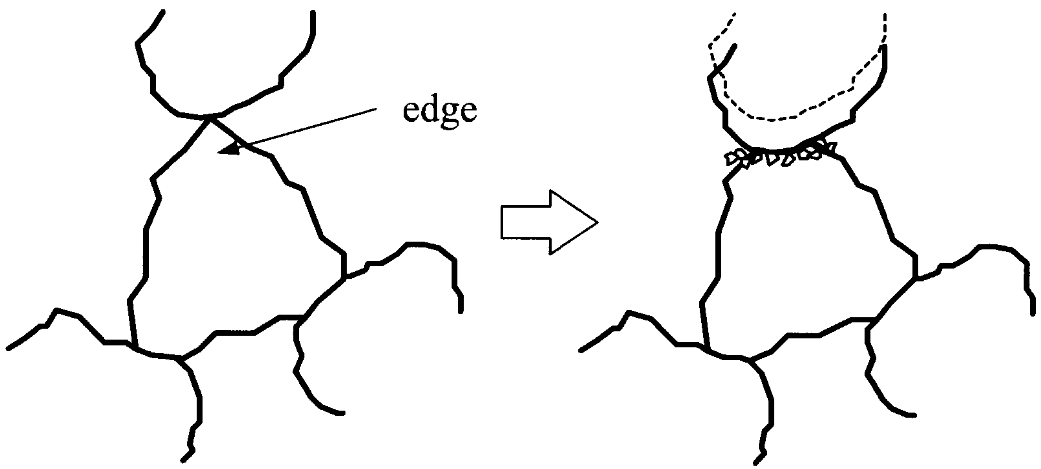


**Figure 4.20 Mechanism of compression due to crushing (Quartz particle specimen)**

### 4.3.4 Separation of compression strain

The compression strain measured in the one-dimensional compression tests would contain the following three components :

1) instantaneous strain,

2) strain due to material creep, and

3) strain due to particle crushing.

In the case of chalk bar specimens, the author attempted to separate these components by creep tests of a single chalk bar.

#### (1) Test procedure of creep test

Figure 4.21 illustrates the test apparatus of the creep test. A test box used was the same as the one-dimensional compression tests. The square aluminum bars were used to fill up the extra spaces in the steel box. An oven-dried chalk bar whose size was 9.5mm in diameter was cut to 20mm in length, and set in a space of the test box. The chalk bar was confined from both sides by two aluminum bars fastened with bolts as shown in the figure. These bolts were fastened with a torque of 0.15Nm. The chalk bar was loaded vertically by weights as shown in Photograph 4.9. Two gap sensors with an accuracy of 0.00025mm measured the vertical displacement of a loading piston.

The creep test was conducted three times. There are three loading stages of 55N, 100N, and 145N in a test. Each load was sustained for 3 – 12 hours. After each test, a check was made by naked eye for cracks or some kind of crushing in the chalk bar.

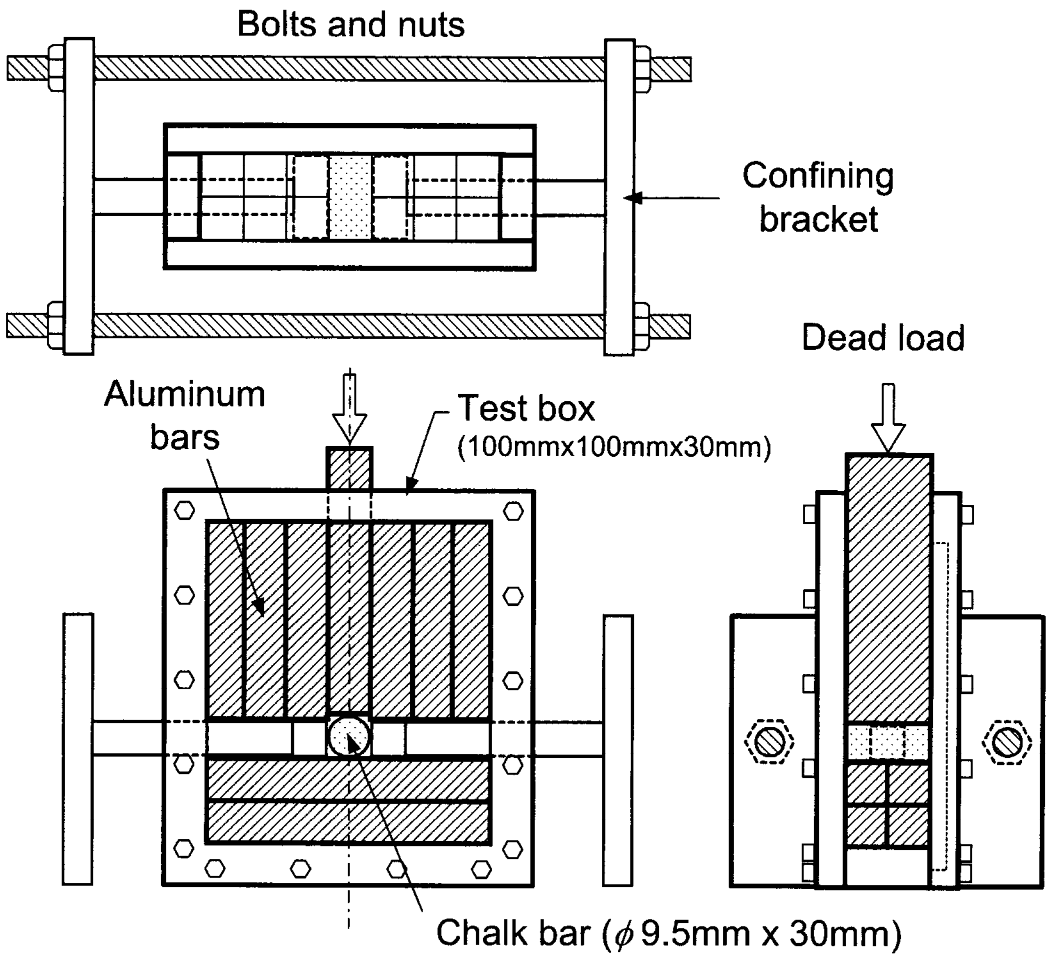


**Figure 4.21 Test apparatus of creep test of single chalk bar**

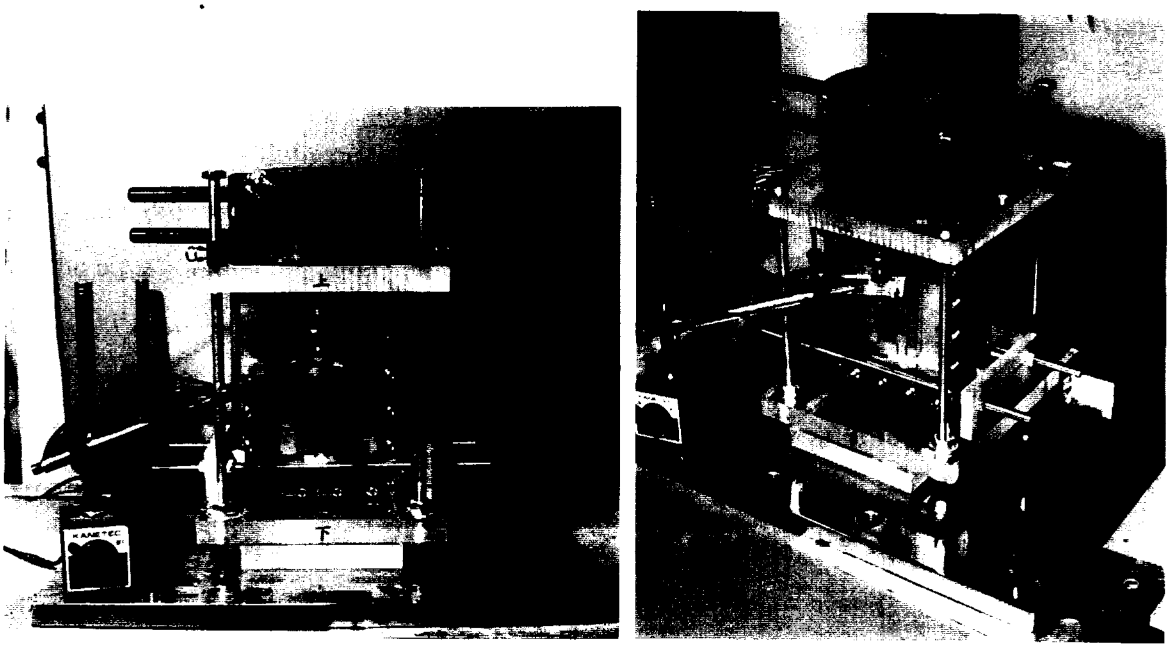

**Photo. 4.9 Creep test of single chalk bar**

## (2) Test results and discussions

Figure 4.22 shows the typical relationships between a creep strain and elapsed time. The creep strain is the characteristic strain defined in Chapter 3. The creep strain was almost proportional to the logarithm of time after about 10 seconds. The rate of creep deformation ($C_{\alpha m}$) was defined as the gradient of the curve. In Figure 4.23, the rate of creep deformation was plotted against the dead load of each loading stage. Although the data is scattered, this figure indicates the general trend that the rate of creep deformation is increasing with increasing of the dead load. This trend was approximated by a straight line represented by the following equation :

$$C_{\alpha m} = 3.5 \times 10^{-6} P_{\mathrm{D}} \tag{4.3}$$

where $C_{\alpha m}$ (unit : 1/log time cycle) is the rate of creep deformation due to material creep, and $P_{\mathrm{D}}$ (unit : N) is dead load of each loading stage. This equation was used for prediction of the creep strain due to material creep in one-dimensional compression test of a chalk bar specimen. A cubic packed chalk bar specimen consists of 10 columns of chalk bars. The strain due to material creep in an one-dimensional compression test is estimated on the assumption that a column in a chalk bar specimen supports one tenth of the load applied to the loading plate of one-dimensional compression test, and that the creep strain occurs according to the $C_{\alpha m}$ obtained from Equation (4.3). The applied load per a column of chalk bar in the specimen was estimated from the following equation:

$$P_{\mathrm{D}} = \frac{P}{10} \tag{4.4}$$

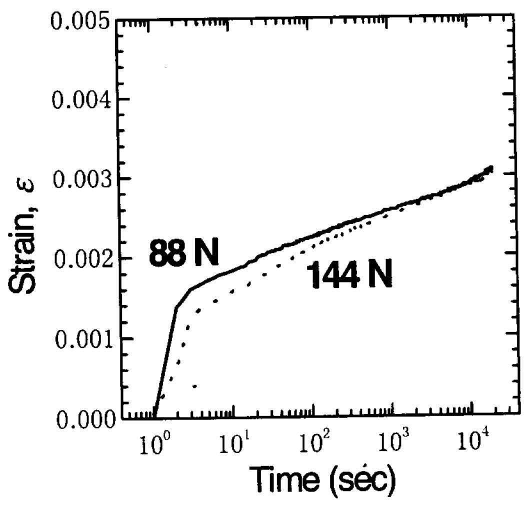


**Figure 4.22 Typical relationships between the creep strain vs. elapsed time**

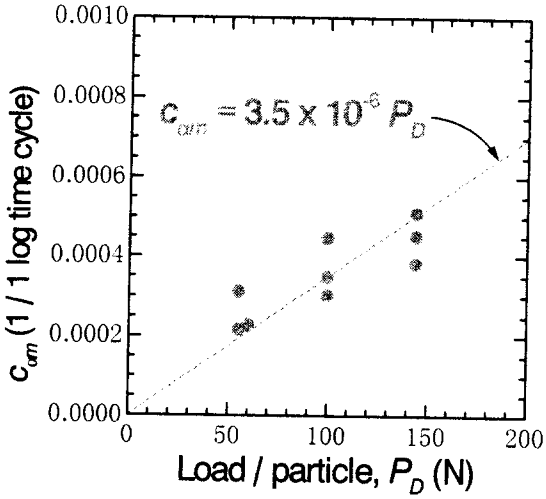


**Figure 4.23 Rate of creep deformation versus dead load**

where $P$ is a sustained load of a loading stage in one-dimensional compression test.

The separation of strain into the three components were conducted as follows:

**1) Instantaneous strain ($\varepsilon_{inst}$)**

The instantaneous strain was estimated as the magnitude of the strain during the first 10 seconds of each loading stage. The first 10 seconds corresponds to the load increasing term.

$$\varepsilon_{inst} = \varepsilon_{all(t=10sec)} \tag{4.5}$$

where $\varepsilon_{all}$ is the compression strain obtained from the one-dimensional compression test. The instantaneous strain is considered to mainly consist of elastic strain and rearrangement of chalk bars resulting from the crushing of chalk bars occurred during the load increasing term.

**2) strain due to material creep ($\varepsilon_{mcreep}$)**

The rate of creep deformation ($C_{\alpha m}$) was estimated from Equation(4.3) and (4.4). The creep strain due to material creep ($\varepsilon_{mcreep}$) at the end of each loading stage was estimated from the equation of

$$\varepsilon_{mcreep} = C_{\alpha m} \times \log t \tag{4.6}$$

where $t$ is elapsed time of each loading stage. In Case C1, C2, C3 and C4, the value of $t$ was set to 86400sec(24hours), in Case C5 and C6, the value of $t$ was set to 43200sec(12hours).

**3) strain due to particle crushing ($\varepsilon_{crush}$)**

The strain due to particle crushing was estimated by the following equation:

$$\varepsilon_{crush} = \varepsilon_{all} - (\varepsilon_{inst} + \varepsilon_{mcreep}). \tag{4.7}$$

That is to say, the strain due to particle crushing ($\varepsilon_{crush}$) was estimated by subtracting the instantaneous strain and the strain due to material creep from the total strain.

Figure 4.24 shows examples of the separation of the compression strain. The separation was attempted in the loading stages that are under the yield stress and the nearest step to the yield stress. The instantaneous strain is shown as area "A", the strain due to material creep is shown as area "B", and the strain due to particle crushing is shown as area "C".

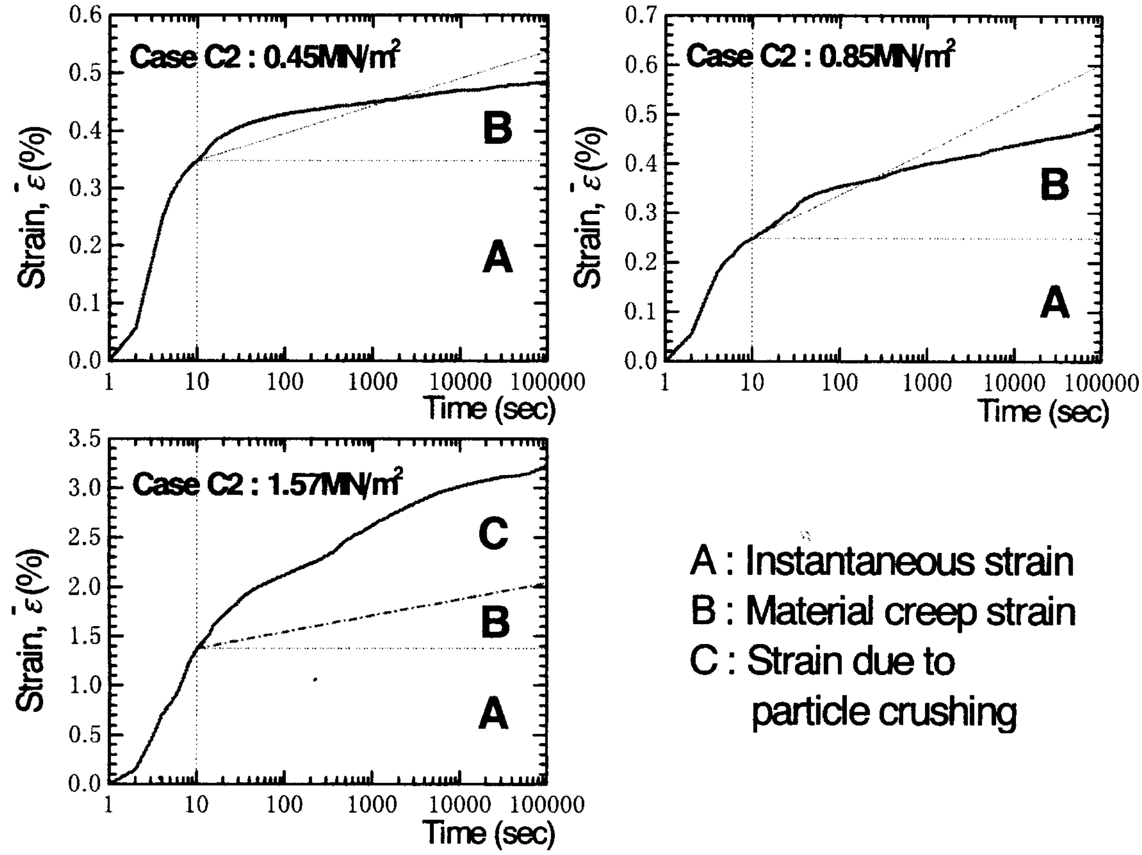


**Figure 4.24 Separation of the compression strain (Case C2)**

In the loading stages of 0.45MN/m$^2$ and 0.85MN/m$^2$, the measured strain($\bar{\varepsilon}$) was approximately in agreement with the summation of the instantaneous strain ($\varepsilon_{inst}$) and the strain due to material creep ($\varepsilon_{mcreep}$). This is attributable to the small numbers of crushed chalk bars in these loading stages shown in Figure 4.8. The reasons why the summation was slightly larger than the measured strain is considered to be as follows:

- The confining forces of the creep tests were slightly smaller than the confining forces in one-dimensional compression tests of chalk bar specimen. The larger the confining forces, the larger the strain due to material creep.

- In the loading stage of $0.85MN/m^2$ in Figure 4.24, one column of chalk bar (,that is to say, one chalk bar,) would share about 240N. From Figure 4.23, it is clear that the load of 240N was greater than the loads of the creep tests. In this study, for simplicity, the trend in Figure 4.23 was approximated a straight line. However, this approximation is likely to overestimate the strain due to material creep in the region of large load over 200N.

In the loading stage of $1.57MN/m^2$, the load was the load nearest to the yield load, the strain due to particle crushing was about 40% of all strain at the end of the loading stage. The cumulative crushing ratio were over 40% in this loading stage. Thus, it is considered that the amount of the time-dependent strain due to particle crushing is significant, provided that the cumulative crushing ratio is over 40%.

The results of separation were summarized in Table 4.4. Case C1, C4, C5 and C6 shows almost the same results as Case C2 of which the results were shown in Figure 4.24. In Case C3, the ratio of the strain due to particle crushing was only about 0.7%. The small ratio of the strain due to particle crushing would be owing to the cumulative crushing ratio of 39% which is not exceeded 40%.

The compression behavior of an aggregate of crushable material would change at the cumulative crushing ratio of 40%. That is to say,

- Under the cumulative crushing ratio below 40%, particle crushing occurred in a specimen would make distribute the load among more particles, thereby the average load support by one particle would become small by crushing. Consequently, time-dependent strain due to particle crushing would be inferior.
- Under the cumulative crushing ratio of about 40%, the load would be distributed to particles in a specimen thoroughly. Under the cumulative crushing ratio above 40%, particle crushing occurred in a specimen would make increase the loads of other crushed or non-crushed particles. Consequently, time-dependent strain due to particle crushing would be superior.

**Table 4.4 Results of strain separation**

| Case | Loading pressure ($MN/m^2$) | Total strain | Instantaneous strain | Strain due to material creep | Strain due to particle crushing |
|---|---|---|---|---|---|
| C1 | 0.39 | 0.0017 | 0.0012 | 0.0015 | --- |
| | 0.82 | 0.0041 | 0.0020 | 0.0033 | --- |
| | 1.60 | 0.0411 (100%) | 0.0155 (38%) | 0.0067 (16%) | 0.0189 (46%) |
| C2 | 0.45 | 0.0049 | 0.0035 | 0.0019 | --- |
| | 0.85 | 0.0047 | 0.0024 | 0.0035 | --- |
| | 1.57 | 0.0325 (100%) | 0.014 (43%) | 0.0065 (20%) | 0.012 (37%) |
| C3 | 0.43 | 0.00534 | 0.0042 | 0.0018 | --- |
| | 0.83 | 0.0050 | 0.0027 | 0.0035 | --- |
| | 1.58 | 0.0144 (100%) | 0.0077 (53%) | 0.0066 (46%) | 0.0001 (0.7%) |
| C4 | 0.44 | 0.0082 | 0.00686 | 0.0017 | --- |
| | 0.82 | 0.0054 | 0.0029 | 0.0034 | --- |
| | 1.56 | 0.0269 (100%) | 0.0157 (58%) | 0.0065 (24%) | 0.0047 (17%) |
| C5 | 0.40 | 0.00893 | 0.00768 | 0.00125 | --- |
| | 0.79 | 0.0059 (100%) | 0.0028 (48%) | 0.0025 (42%) | 0.0006 (10%) |
| | 1.58 | 0.0304 (100%) | 0.0054 (18%) | 0.0050 (16%) | 0.020 (66%) |
| C6 | 0.43 | 0.0073 | 0.0060 | 0.0013 | --- |
| | 0.83 | 0.0044 | 0.0024 | 0.0026 | --- |
| | 1.65 | 0.0224 (100%) | 0.0054 (24%) | 0.0051 (23%) | 0.0119 (53%) |

### 4.3.5 Factors influencing time-dependent behavior

From the above-mentioned results and discussions, the progress of local crushing at contact areas is one of the sources of the time-dependent compressive strain due to particle crushing. Here, some possible factors affecting the local crushing progress are discussed.

A rate of creep strain is introduced for representation of the characteristics of time-dependent behavior as

$$C_\alpha = \frac{\Delta\bar{\varepsilon}}{\Delta t} \tag{4.8}$$

where $C_\alpha$ is a rate of creep strain, $\Delta\bar{\varepsilon}$ is an increment of the strain, and $\Delta t$ is an increment of time (1 logarithmic cycle of time). The rate of creep strain was calculated in the period where the gradient of the strain-time curve was almost constant. If there were some jumping in the curve, $C_\alpha$ was calculated, ignoring these jumps. Thereby, the increment of the strain would contain the three components : instantaneous strain, strain due to material creep and strain due to particle crushing. However, the third one would mainly consist of the local area crushing: the sudden rearrangement of particles would not be included.

The method of least square was used to calculate the rate of creep strain.

Figure 4.25 presents the relationships between the rate of creep strain and the loading pressure normalized by yield stress. In the cases of cubic packing of the chalk bar specimens, the largest $C_\alpha$ appears in the loading step of $p/p_y$ nearly equal to 1.5. In the case of hexagonal packing of the chalk bar specimen, the $C_\alpha$ value is almost constant beyond the yield stress. In the cases of the talc bar specimens, though the rates of creep strain are small, the value of $C_\alpha$ of the saturated specimen(Case T3) is only slightly larger than the values of the dry specimen(Case T1 and T2). Existence of water may not be influential to the local crushing at contact areas. In the cases of the glass beads specimens, the values of $C_\alpha$ are small and constant before the loading pressure reaches the yield stress, after that $C_\alpha$ suddenly increases. In the cases of the quartz particle specimen, the values of $C_\alpha$ increase gradually with increasing of sustained stress. The differences in tendency of $C_\alpha$ among the dry specimens may be stemmed from the shape of edges as well as resistance characteristics of edges against contact forces. Further studies are necessary on the factors influencing the time-dependent behavior.

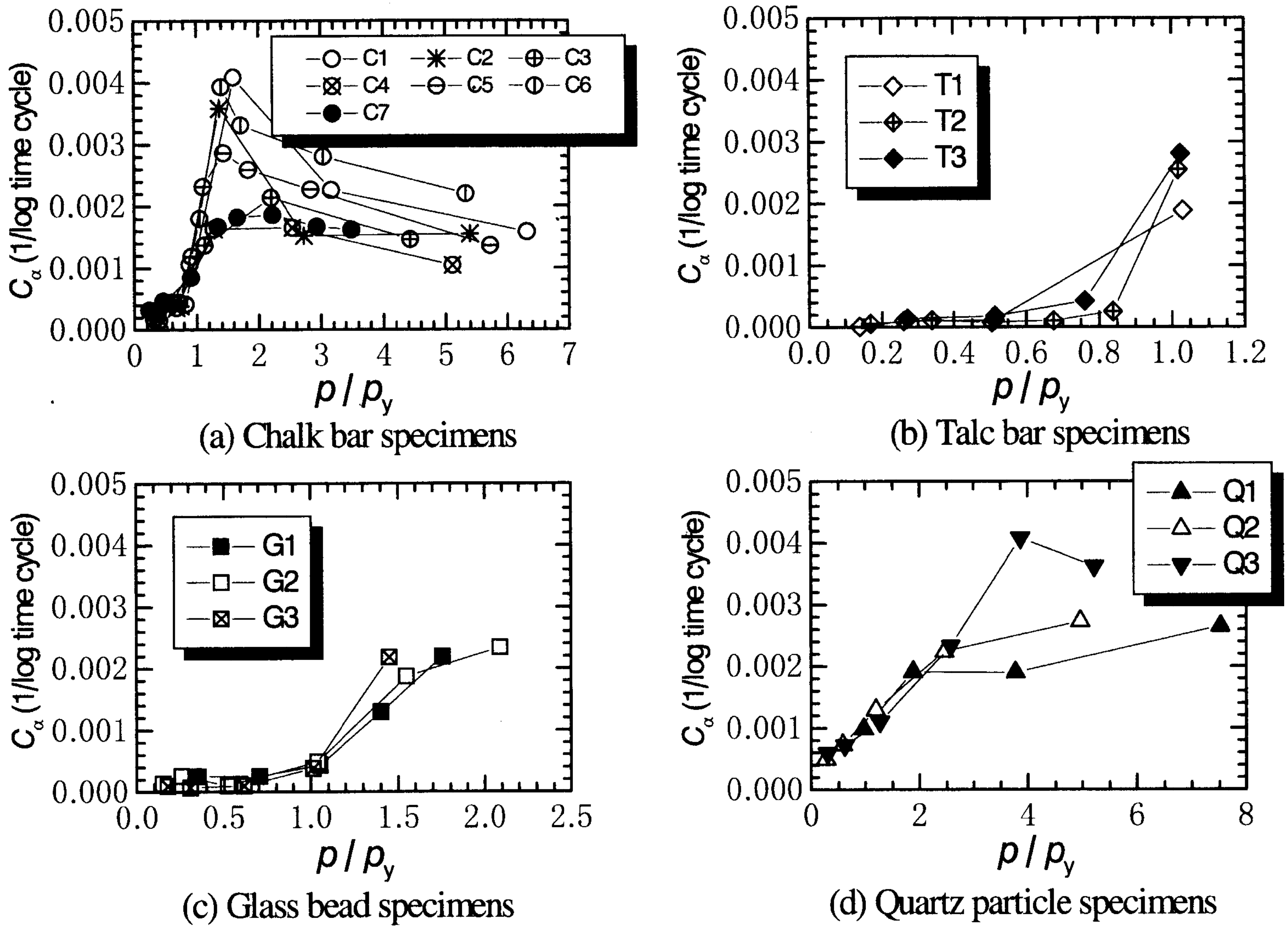


(a) Chalk bar specimens

(b) Talc bar specimens

(c) Glass bead specimens

(d) Quartz particle specimens

**Figure 4.25 Relationships between $C_\alpha$ and loading pressure normalized by yield stress**

## 4.4 Conclusions

In this Chapter, one-dimensional compression tests of four crushable materials were carried out to investigate the time-dependent behavior due to particle crushing. The following conclusions were drawn.

(1) From the observations, it was verified that the time-dependent behavior due to particle crushing is, in general, stemmed from progressive nature of a chained-event of "particle crushing" and subsequent "rearrangement of particles" and "stress redistribution" under the condition of one-dimensional compression. It was found that the detailed mechanism of each event for these four materials is different, depending upon the crushing characteristics of single particle.

(2) The time-dependent behavior of chalk and talc cylindrical bars is initiated by local crushing at contact areas, followed by the formation of continuous crack in the bar either in 'vertical splitting mode' or 'sideways splitting mode'. The formation of continuous crack accelerates further local crushing at the contact areas without noticeable rearrangement of particles for chalk bar. For the case of talc bar, however, slippage occurs along contact areas, triggering other slippage and accelerating the chained-event of the rearrangement of the talc bars.

(3) Glass beads crush instantly into a number of fragments. Movement and rearrangement of particles after crushing mainly cause the time-dependent behavior of specimen of spherical grass beads. In specimens of natural quartz particles, the time-dependent behavior is predominately caused by a combination of the collapse of angular edges of particles and the local crushing at contact areas.

(4) From the results of separation of compression strain into three components: instantaneous strain, strain due to material creep and strain due to particle crushing, the amount of the strain due to particle crushing was significant provided the cumulative crushing ratio is over 40%.

(5) Packing pattern and water existence influenced the rate of creep strain. The difference of packing pattern influenced the loading pressure where the maximum rate of creep strain appeared. Water existence may not be influential to the local crushing at contact areas, but influential to the magnitude and the occurrence time of sudden increment of strain.

# CHAPTER 5

# MODEL FOOTING LOADING TESTS ON CHALK BAR GROUND

## 5.1 Introduction

In Chapter 5, time-dependent behavior due to particle crushing is discussed through an example of boundary value problem. Shallow footing loading tests were conducted on a model ground made of the chalk bars that were also used in the experiments in Chapters 3 and 4. The purpose of the tests is also to clarify the detailed mechanism of the time-dependent behavior due to particle crushing in those tests with careful visual observations. In the shallow footing loading tests, the magnitude of confining contact forces for each chalk bar varies depending on its location in the ground, that is to say, the distribution of contact forces in the ground is not uniform. Thus some chalk bars in the ground can move or rotate if the confining contact forces are small.

## 5.2 Test procedures

Figure 5.1 schematically illustrates a loading system for shallow footing on model ground, composed of the chalk bars in hexagonal packing.

The model container made of steel has dimensions of 500mm wide, 300mm high and 200mm thick. The container was equipped with a clear glass panel on the front wall, but the glass panel was removed for convenience of manual packing of chalk bars and observation.

The chalk bars were employed as the crushable material for the tests to visualize the crushing phenomena. Another reason for employing the chalk bar is its good reproducibility of reaction against loading, which was shown in the one-dimensional compression tests. The chalk bars used in these tests were the same as the chalk bars used in the single particle crushing tests and the one-dimensional compression tests described in Chapters 3 and 4. But in the footing loading tests, chalk bars were used not in the oven-dry condition as the tests in Chapters 3 and 4, but in a room-dry condition. The characteristics of the chalk bars in the room-dry condition are as follows : Density = $1.64 Mg/m^3$ ; the mean crushing strength = $0.562 MN/m^2$ ; and the mean characteristic initial stiffness = $90.0 MN/m^2$. The chalk bars were carefully piled up in the container two-dimensionally. The hexagonal packing was adopted: it is difficult to pile up the chalk bars in the container with the simple cubic packing because of the large space of the container. About 1500 pieces of chalk bars were piled up in all. The reasons that the regular packing pattern was adopted are the same as those of the one-dimensional compression tests described in Chapter 4.

Two acrylic plates of 500mm wide, 300mm high and 20mm thick were loosely placed on the front side and rear side of the piled chalk bars for prevention of collapsing the chalk bars to the front side or rear side. These plates were fixed holding the interval of 32mm. This interval is larger than the length of a chalk bar (30mm). Thus, the boundary condition of the model ground was close to the condition of plane stress.

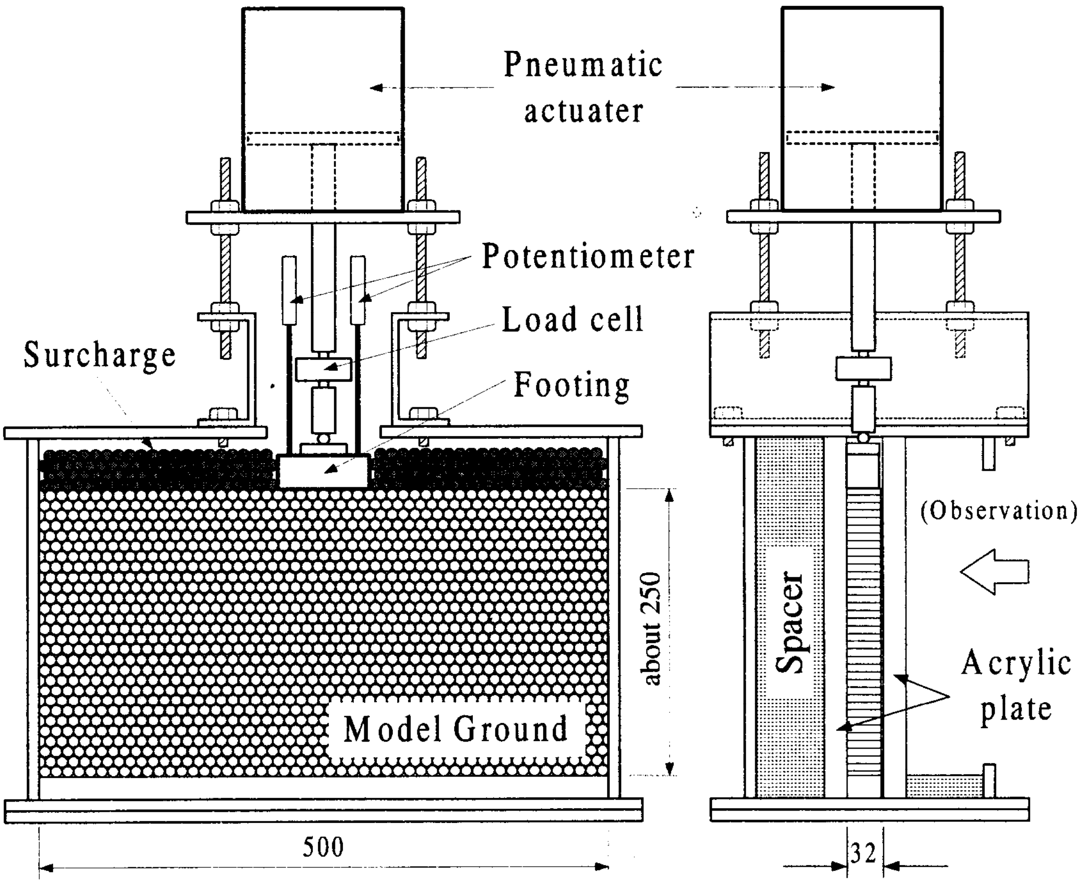


**Figure 5.1 Loading system of shallow footing on model ground made of chalk bars**

**Model Footing :**

The model footing was a steel block of 80mm width, 30mm high and 30mm thick. The ratio of footing width to particle diameter was about 8.5, since the diameter of each chalk bar was about 9.5mm. The model footing was set at the center of the model ground. The base of the footing was roughed by gluing Toyoura sand particles. The footing was loaded through a steel ball in such a way that any rotational movements were allowed during loading.

**Surcharge :**

The surcharge was added to cause particle crushing for a certainty. Before the productive tests that discussed later in this chapter, some preliminary tests were performed to search the suitable magnitude of surcharge. In the preliminary test with no surcharge, particle crushing did not occur: the model ground failed at an ultimate load without particle crushing, only with movements and rotations of chalk bars. In the preliminary test with the surcharge of 0.8MN/m$^2$, particle crushing occurred even in the loading stages that were below the ultimate load. Aluminum bars whose size was 10mm in diameter and 30mm in length were used for surcharge; they were piled up with 4-layered hexagonal packing as shown in Figure 5.1. As the mass of an aluminum bar was about 6.35g and 164 aluminum bars were used in all, the overburden pressure at the level of footing base was about 0.8kN/m$^2$ .

**Loading system and measurement system :**

Vertical load was applied using an air actuator and measured through a load cell. Vertical displacement was recorded by two potentiometers symmetrically placed on the model footing. The main performance of the load cell, the potentiometers, and the A/D converter were as follows;

- Load cell with its pre-amplifier
  - Capacity : 20kN
  - Output volt set : 5V / 6100N
- Potentiometers
  - Capacity : 23mm
  - Output volt : 10V / 23mm
- A/D converter
  - Resolution for load cell : 5V / 14bit
  - Resolution for potentiometers : 10V / 14bit

Thus the accuracy of the load cell was 0.37N, and that of the potentiometers were 0.0014mm.

**Observation :**

Either a video camera or a digital microscope was used for observation of chalk bars. Cross wires were drawn as a target on the cross section of each chalk bar for convenience of observation. The occurrence of cracking of chalk bar was observed by naked eye.

**Room temperature :**

The footing loading tests were conducted in a laboratory where the room temperature was kept at 22°C by an air conditioner.

Photograph 5.1 shows the general view of the test apparatus.

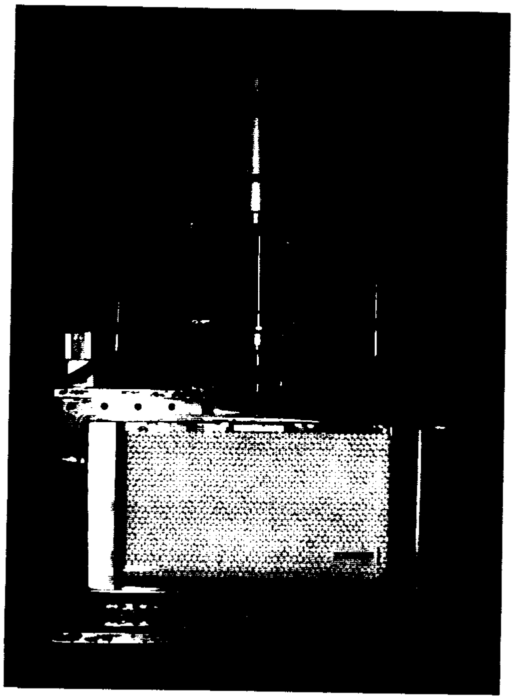
(a) Test apparatus


(b) Digital video camera

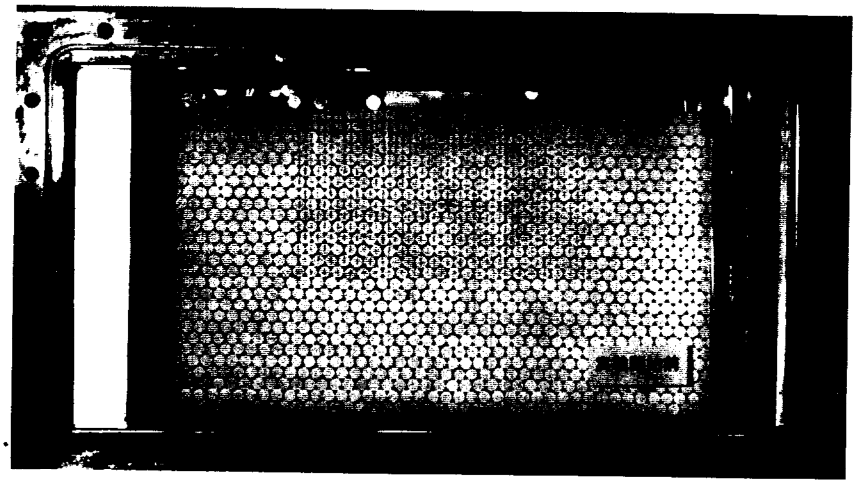
(c) Model ground (front view)

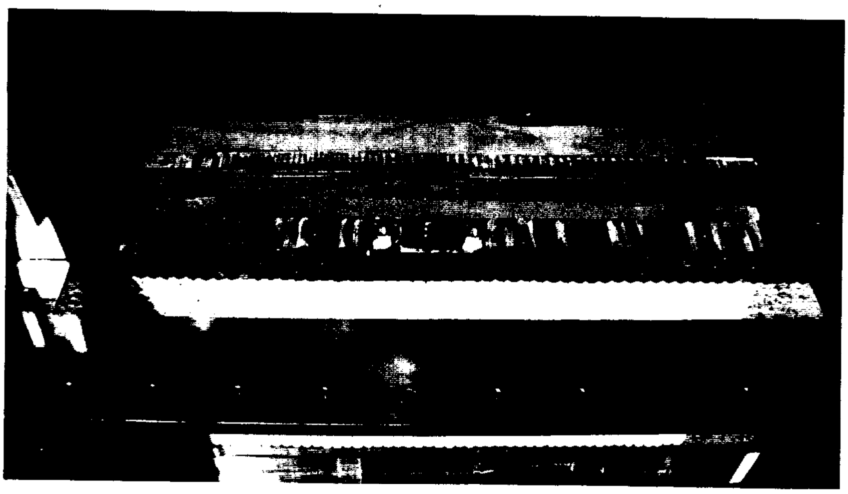
(d) Footing and aluminum bars for surcharge

**Photo. 5.1 Model footing loading test**

**Loading histories of the tests :**

Table 5.1 summarizes loading histories of the footing loading tests. Two monotonic loading tests and four multi-step loading tests (sustained loading tests) were performed. The monotonic loading tests were conducted mainly to obtain the ultimate bearing capacity of the footing, and the load was applied to the footing monotonically at the rate of 50N/minute until the sudden settlement of footing (i.e. failure of ground) was observed. The multi-step loading tests were performed to measure time-dependent settlement of the footing and observe the crushing progress under a sustained loading stage, and the load was increased to a predetermined load at the rate of about 50N/minute and sustained for about 24 hours on the average. The loading term of each loading stage of each test was also presented in Table 5.1.

**Table 5.1 Loading history and ultimate bearing capacity of each footing loading test**

| Test name | Method of loading | Load value and holding times for loads | | Ultimate bearing capacity (N) |
|---|---|---|---|---|
| Test M1 | Monotonic loading | --- | | 776 |
| Test M2 | Monotonic loading | --- | | 1230 |
| Test S1 | Multi-step loading | 390N | 4 hours | 1570 |
| | | 780N | 21 hours | |
| | | 1180N | 27 hours | |
| | | 1570N | --- | |
| Test S2 | Multi-step loading | 390N | 22 hours | 1180 |
| | | 780N | 44 hours | |
| | | 980N | 28 hours | |
| | | 1180N | --- | |
| Test S3 | Multi-step loading | 390N | 24 hours | 1180 |
| | | 590N | 24 hours | |
| | | 780N | 24 hours | |
| | | 980N | 24 hours | |
| | | 1180N | --- | |
| Test S4 | Multi-step loading | 390N | 24 hours | 1960 |
| | | 780N | 24 hours | |
| | | 1180N | 24 hours | |
| | | 1570N | 24 hours | |
| | | 1960N | --- | |

## 5.3 Test results and discussions

### 5.3.1 Load – settlement curves

The loading histories are given in Figure 5.2, in terms of footing settlement and applied load. The straight portions of each curve that are parallel to the axis of settlement mean the time-dependent settlements of the footing under sustained loads.

Although all the tests must have been performed in the same ground condition, there were large differences of ultimate bearing capacity of footing (from 776N of Test M1 to 1980N of Test S4, as shown in Table 5.1) and initial stiffness of load – settlement curve (from 100N/mm of Test M2 to 500N/mm of Test S4) among the tests. Such scattering for the ultimate bearing capacity and the initial stiffness may be originated from small difference of initial array of chalk bars. Photograph 5.2 shows initial packing of each test. Although the chalk bars were packed in hexagonal packing, many chalk bars did not have six contact points with adjacent chalk bars: there were many initial gaps between neighboring chalk bars. Such gaps might have been caused partly by experimental variations due to manual packing and also due to dimensional variation of the chalk bars. Figure 5.3 shows the distribution of clearly identified gaps in each ground beneath the footing. As a qualitative estimation, the gaps were counted in the region of $2.1B$ (in width) × and $1.4B$(in depth) where $B$ is the width of the footing (80mm), and represented by I-shaped marks in the figure. Figure 5.4 presents the relationships between the ultimate bearing capacity and the number of the gaps, and between the initial stiffness and the number of the gap. The ultimate bearing capacity increases with decreasing of the number of the gap. The same tendency is seen in the figure of initial stiffness. The load of the footing would be transmitted to depth of ground through the chalk bars contacted each other. The number of the gaps and the way in which the gaps were scattered would influence the load transmission. The gaps would not be able to bear the transmitted forces. These forces would be shared among the contact points around the gaps. Thus the enlarged contact forces would cause the slip between particles and the particle crushing, and these phenomena would result in the reductions of the ultimate bearing capacity and the initial stiffness.

The following facts may also influence.to the scattering of ultimate bearing capacity and initial stiffness. Firstly, the diameter of a chalk bar was significantly large compared to the footing width or the width of model ground (steel container). The ratio of footing width to the diameter was about 8.5 (80mm/9.5mm), the ratio of model ground width to the diameter was about 53 (500mm/9.5mm). Secondly the number of contacted chalk bars to the footing was different between Test S4 and other tests: in Test S4, nine chalk bars contacted to the footing, while eight chalk bars contacted to the footing in other tests. Consequently, the load carried by one chalk bar in Test S4 is smaller than that of other tests. The largest ultimate bearing capacity and the largest initial stiffness in Test S4 would be stemmed from the smaller load to one particle and the smaller number of the gaps as shown in Figure 5.4.

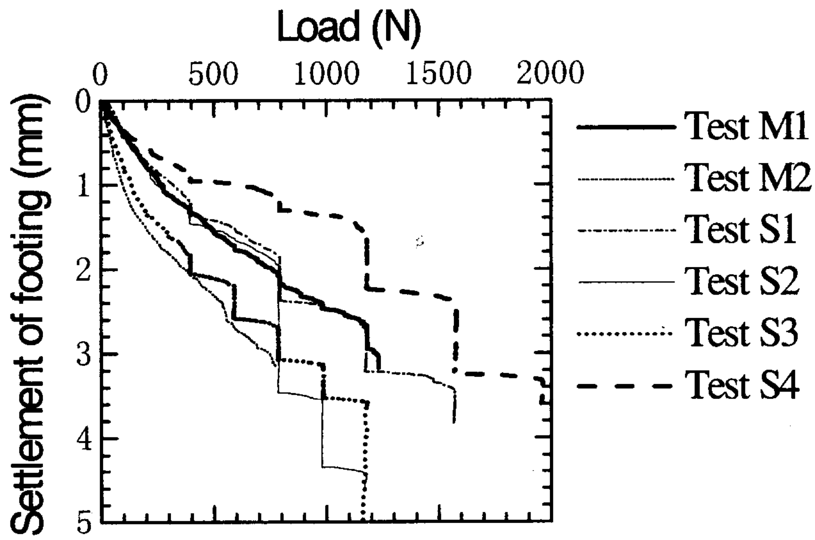


**Figure 5.2 Load – settlement curves**

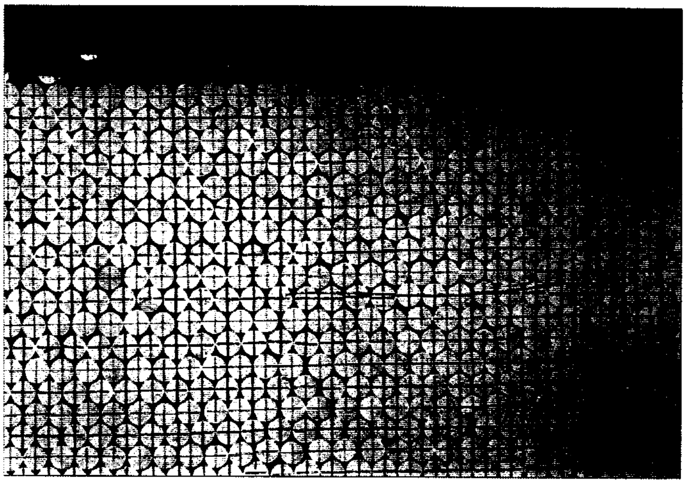

(a) Test M1

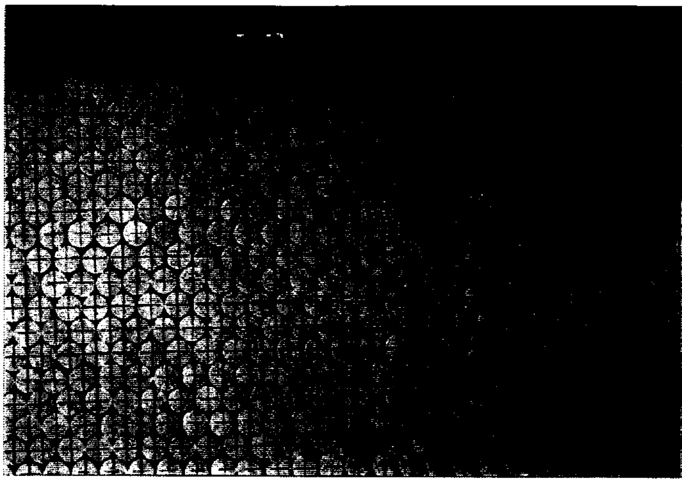

(b) Test M2

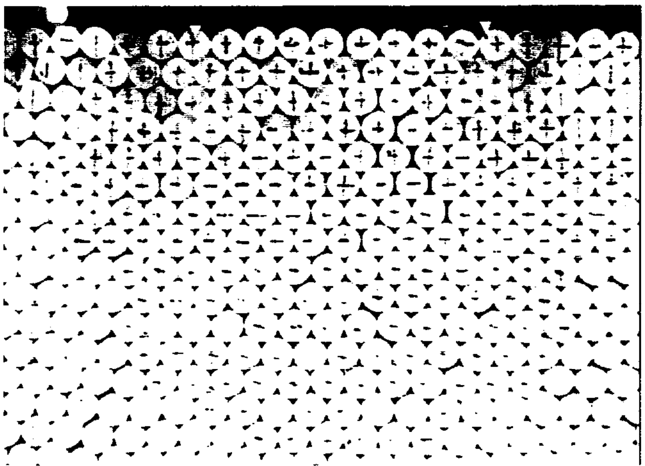

(c) Test S1

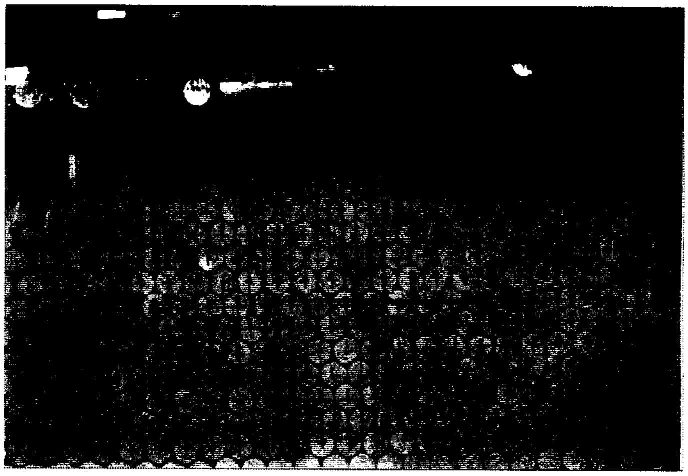

(d) Test S2

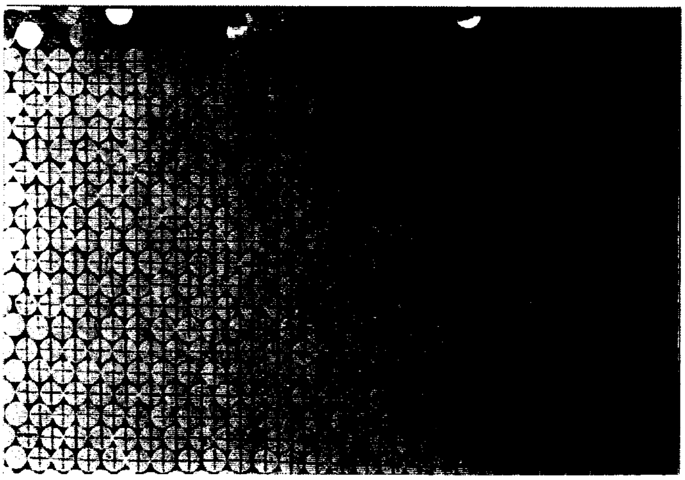

(e) Test S3

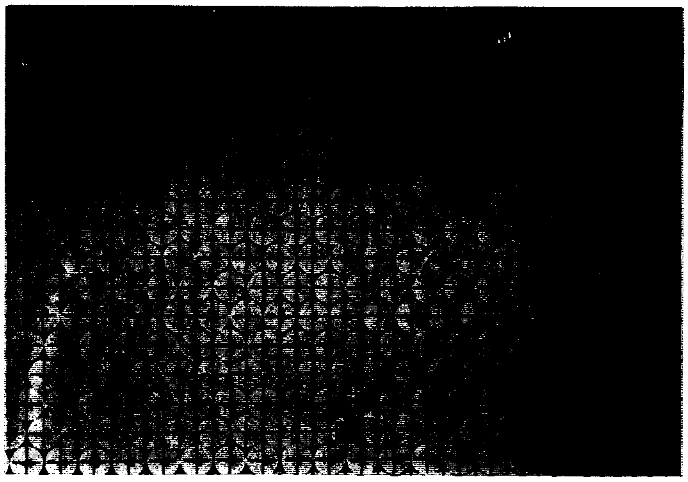

(f) Test S4

**Photo. 5.2 Initial condition of model ground**

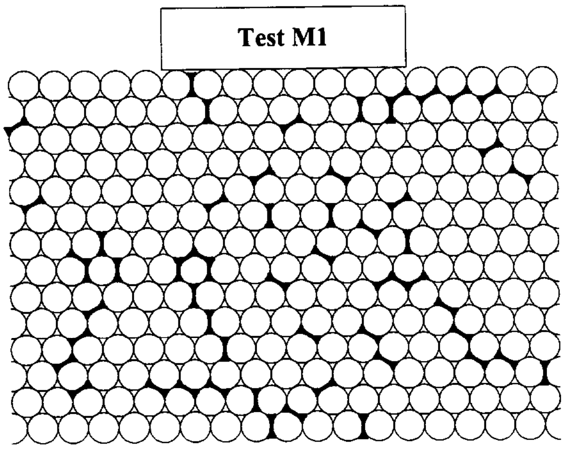


(a) Test M1

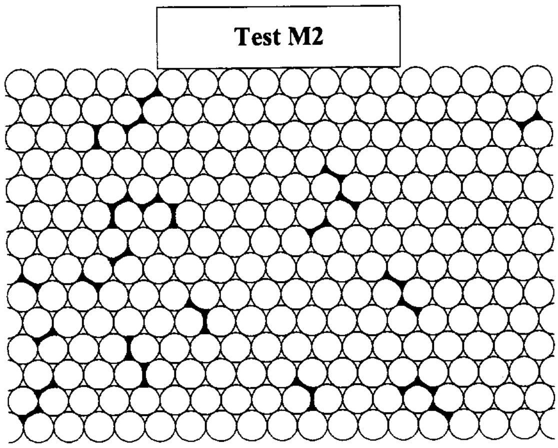


(b) Test M2

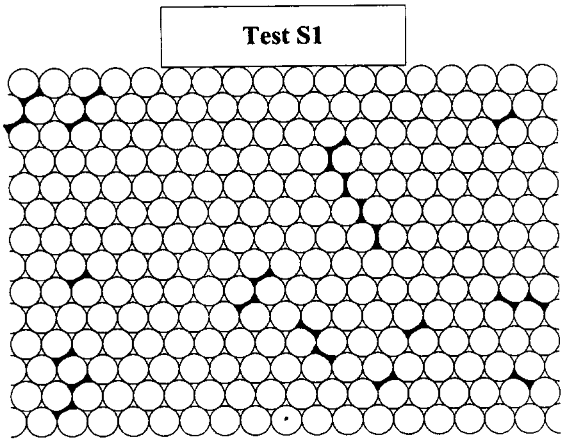


(c) Test S1

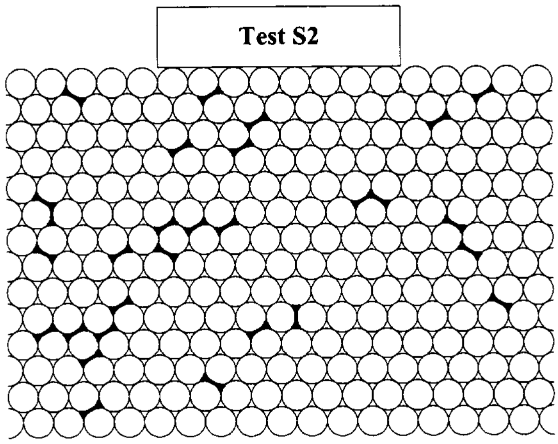


(d) Test S2

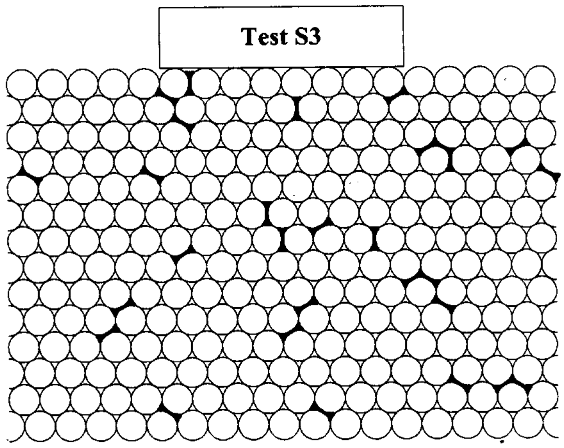


(e) Test S3

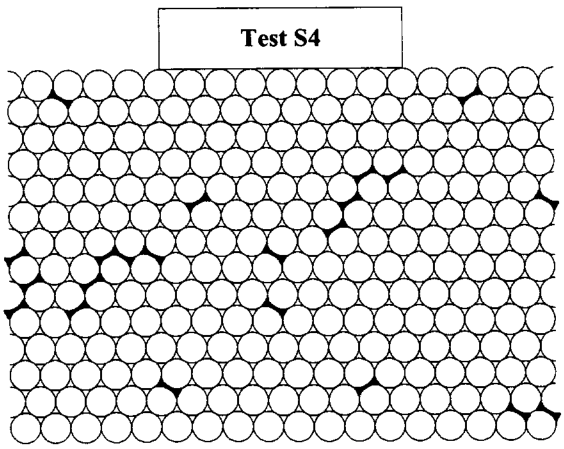


(f) Test S4

**Figure 5.3 Distribution of gaps between two adjacent chalk bars**

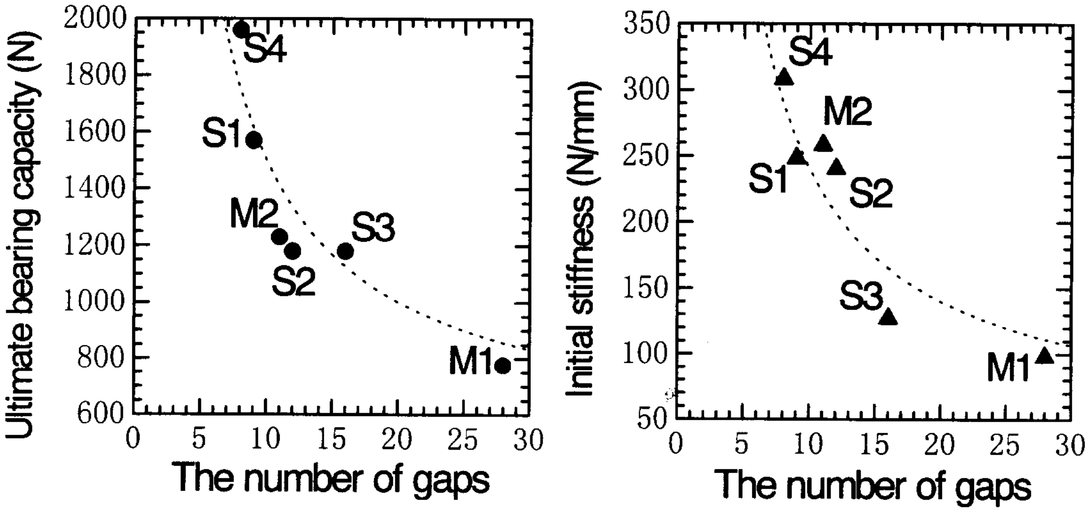


(a) Ultimate bearing capacity
vs. the number of gaps

(b) Initial stiffness of L – s curve
vs. the number of gaps

**Figure 5.4 Relationships between the characteristics of load-settlement curve and the number of gaps**

Photograph 5.3(a) shows a moment of a ground failure, and Photograph 5.3(b) shows the state of the ground after the failure. It was observed that a rapid slipping occurred in the ground and that there was a clear sliding surface in the ground. From the observation, it is obvious that the model ground failed in general shear failure which is one of the failure patterns observed in dense sand ground. Thereby it is considered that the active zone, the zones of radial shear, and the passive zones would be formed in the ground.

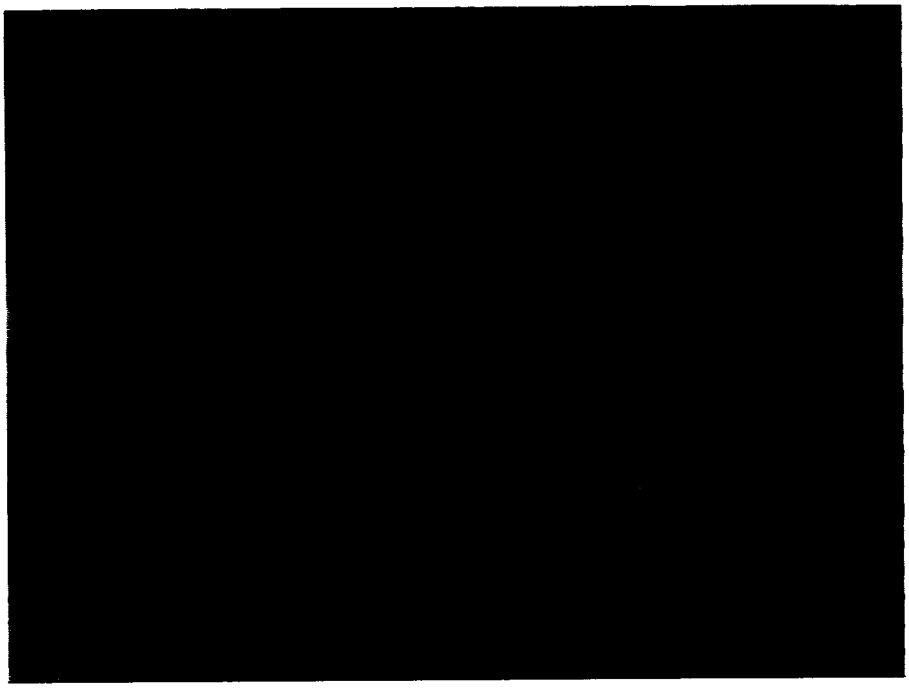

(a) Moment of ground failure

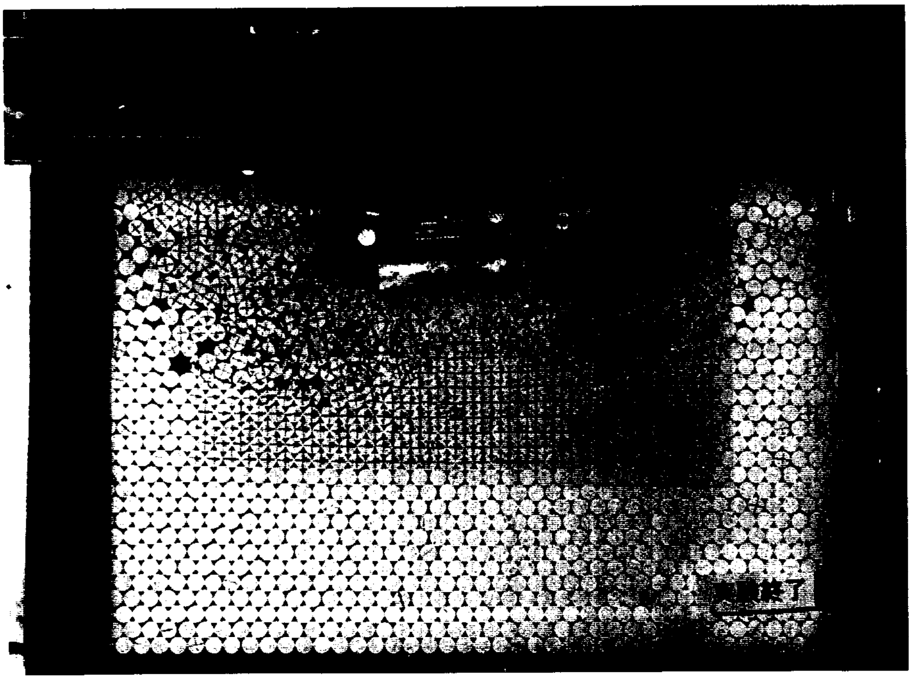

(b) Model ground after ground failure

**Photo. 5.3 Failure of model ground**

### 5.3.2 Time-dependent settlement of footing

The applied load and the settlement were plotted against elapsed time in Figures 5.5 – 5.8, showing that even the load was maintained constant, the settlement is steady increasing. Time-dependent behavior was also observed in the footing loading tests. In the case of the load of 780N in Test S2, there are a few abrupt increases in settlement, which may be compared with the smooth increase trend observed in the one-dimensional compression tests shown in Figure 4.4. This irregular increase may be partly due to the large value of particle diameter-footing width ratio.

The settlements of footing plotted in Figure 5.5 – 5.8 were separated into the left side settlement of footing and the right side settlement of footing. The difference of settlement between the left side and the right side generally occurred in the load increasing stage. But in the case of 980N in Test S3, 780N in Test S4, and 1570N in Test S4, the difference in the gradient of settlement – elapsed time curve between the left side and the right side occurred in the sustained loading stage. The reason will be discussed in Subsection 5.3.3.

The gradient of settlement – elapsed time curve was defined as the rate of creep settlement as shown in Chapter 2. The rates of creep settlement were calculated in the period where the gradients of the settlement – time curves are almost constant. If there were some jumps in a curve, the rate of creep settlement was calculated ignoring these jumps. If the gradient of the curve increased in the course of a sustained loading term, the rate of creep settlement was calculated in the term before and after the increasing. Thus there were some cases that were obtained a few rates of creep settlement in a loading stage. Figure 5.9 presents the relationships between the rate of creep settlement and the sustained load. It is seen that the rate of creep settlement increases with increasing of sustained load. But the variation of the gradient is large. In a sense, there is an upper limit of the rate of creep settlement in a loading stage. It is considered that the rate of creep settlement would be determined depending on some other factors in addition to the magnitude of load.

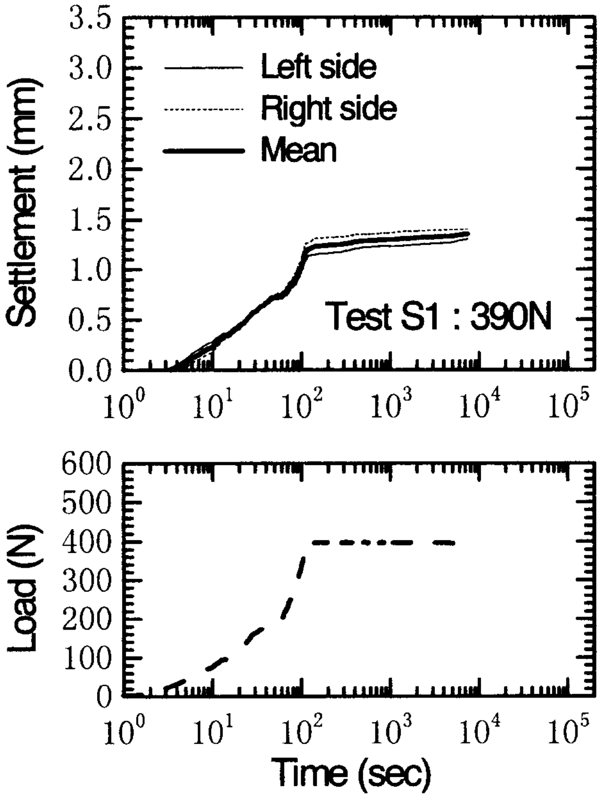


(a) 390N

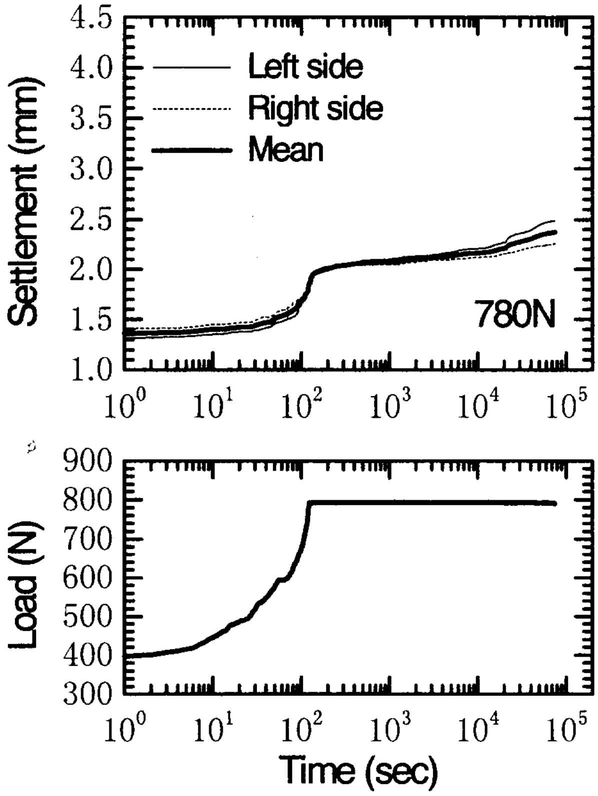


(b) 780N

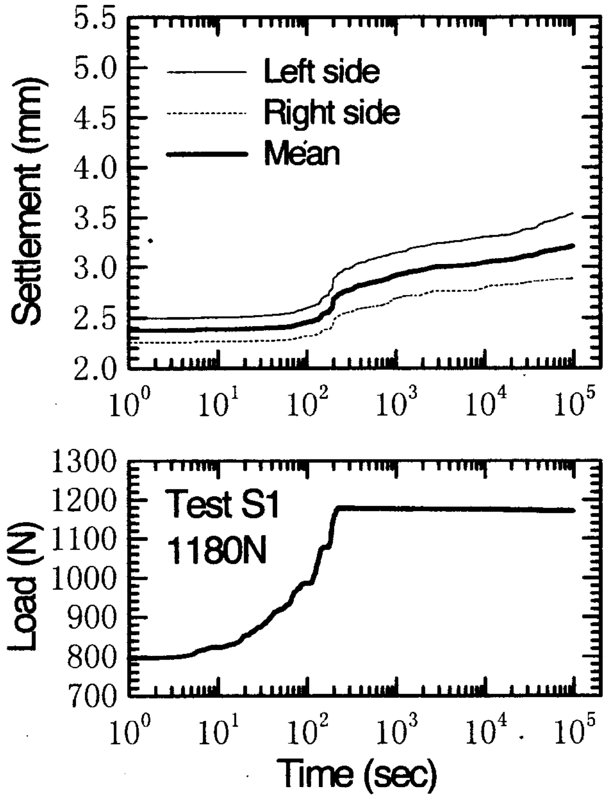


(c) 1180N

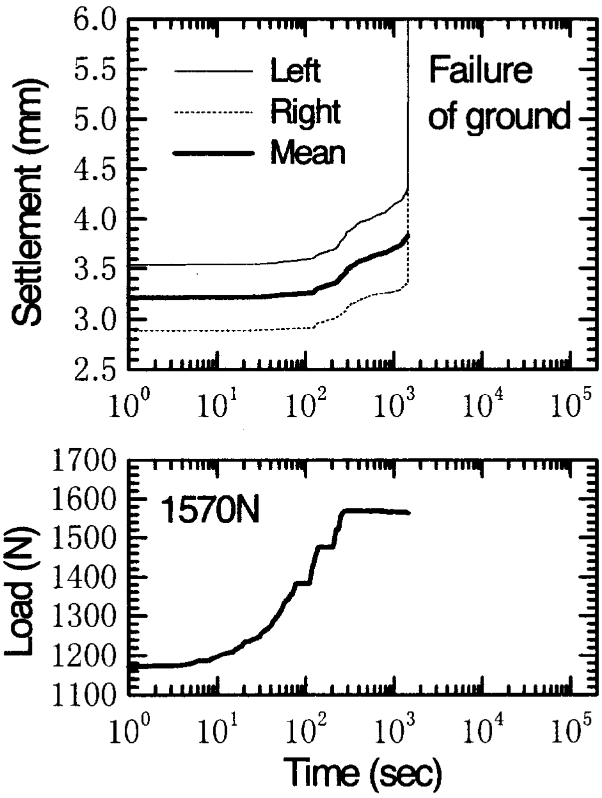


(d) 1570N

**Figure 5.5 Settlement or load vs. elapsed time curves (Test S1)**

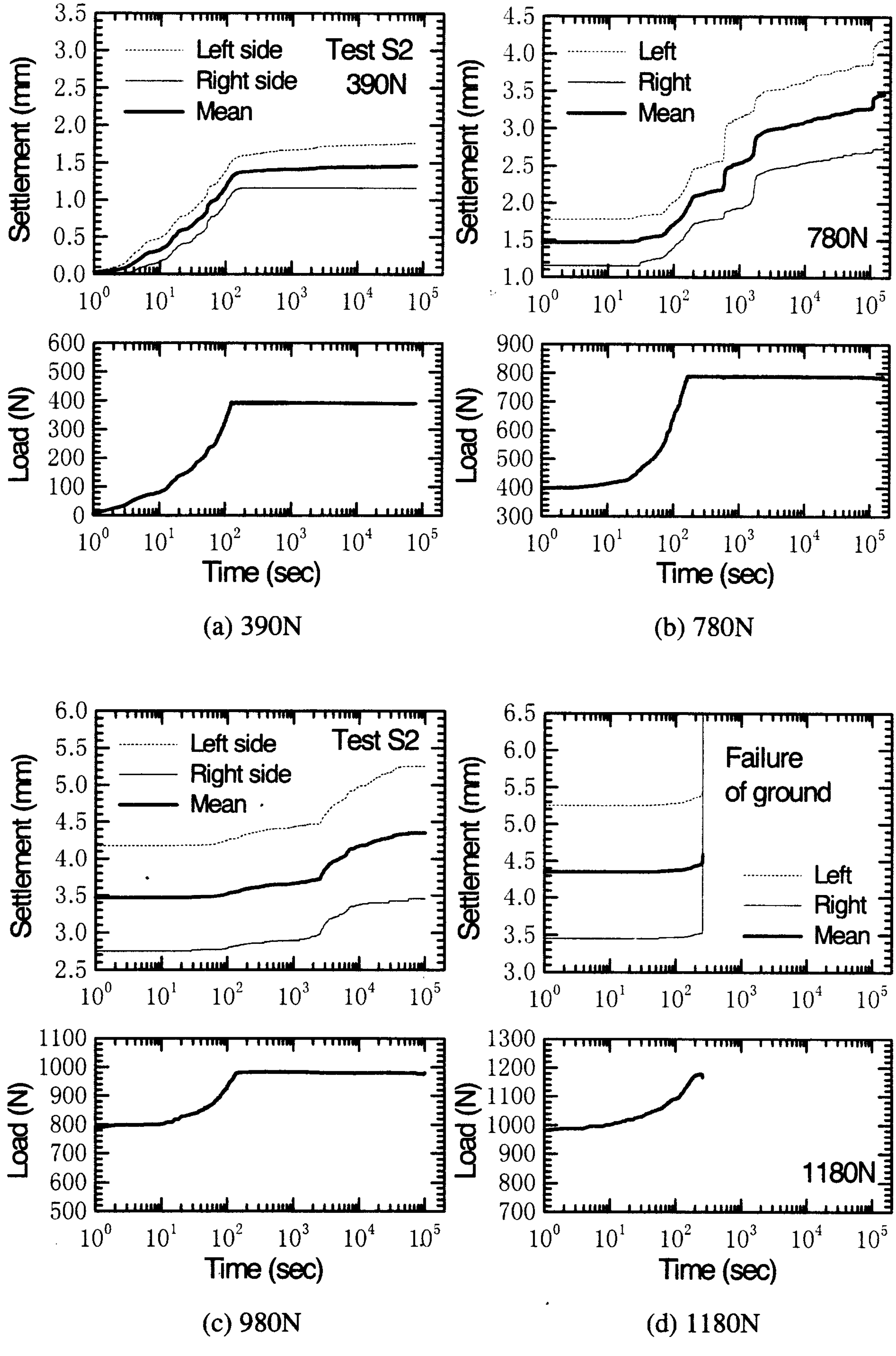


**Figure 5.6 Settlement or load vs. elapsed time curves (Test S2)**

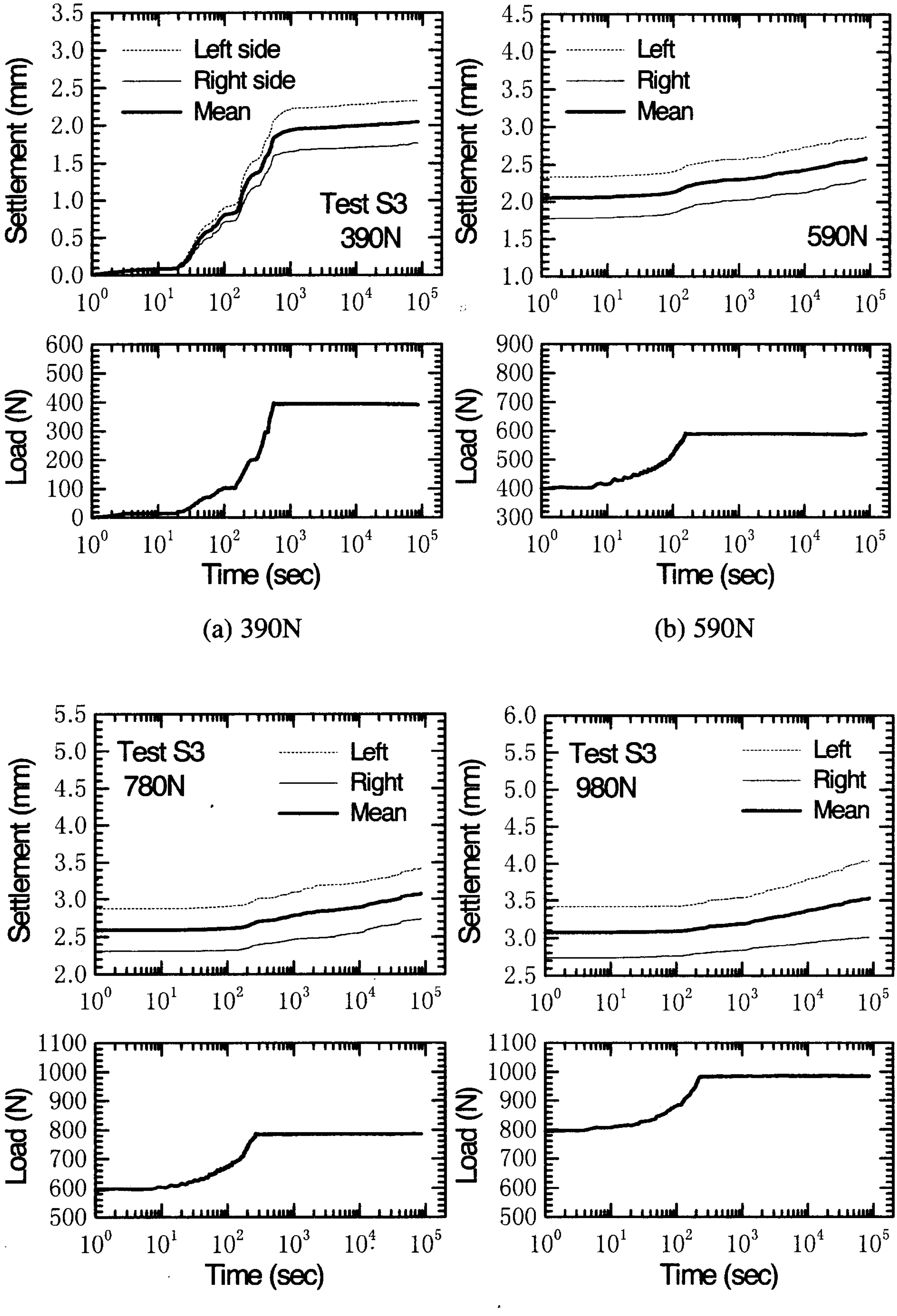


(a) 390N (b) 590N

(c) 780N (d) 980N

**Figure 5.7 Settlement or load vs. elapsed time curves (Test S3)**

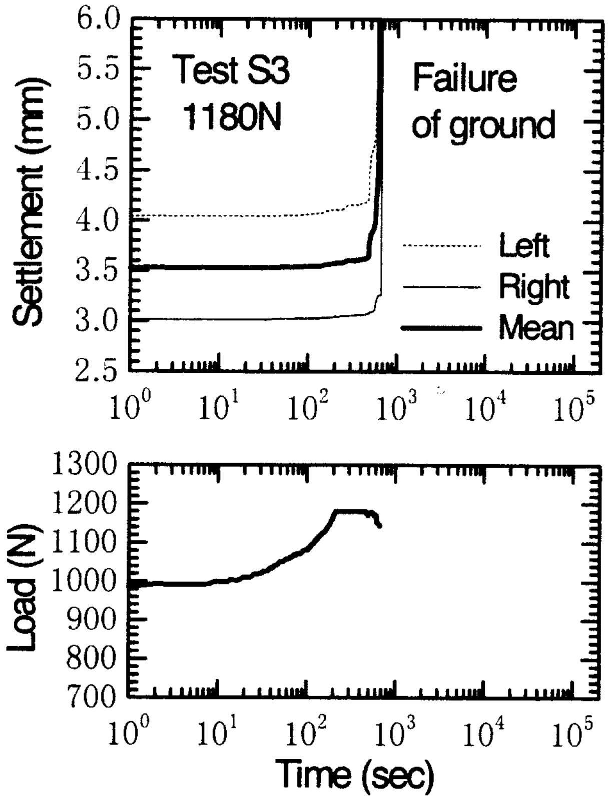


**Figure 5.7 Settlement or load vs. elapsed time(Test S3)** (e) 1180N

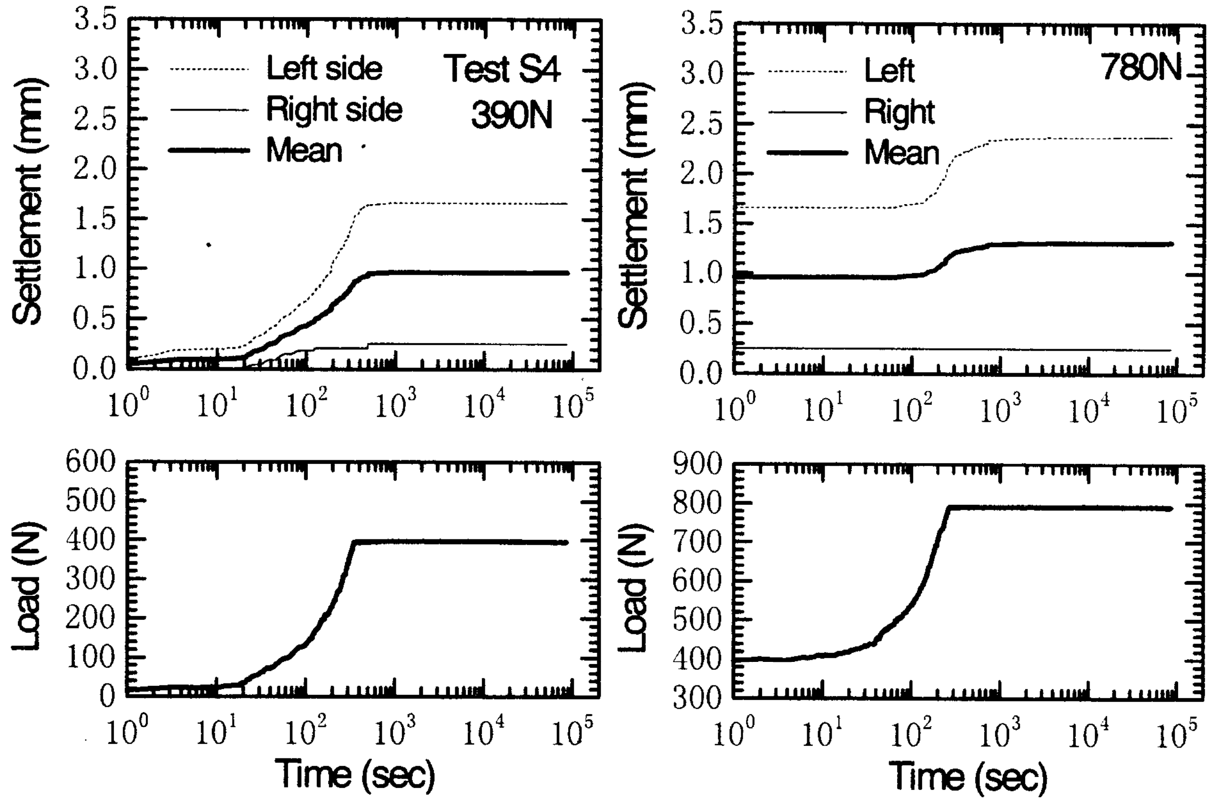


(a) 390N

(b) 780N

**Figure 5.8 Settlement or load vs. elapsed time curves (Test S4)**

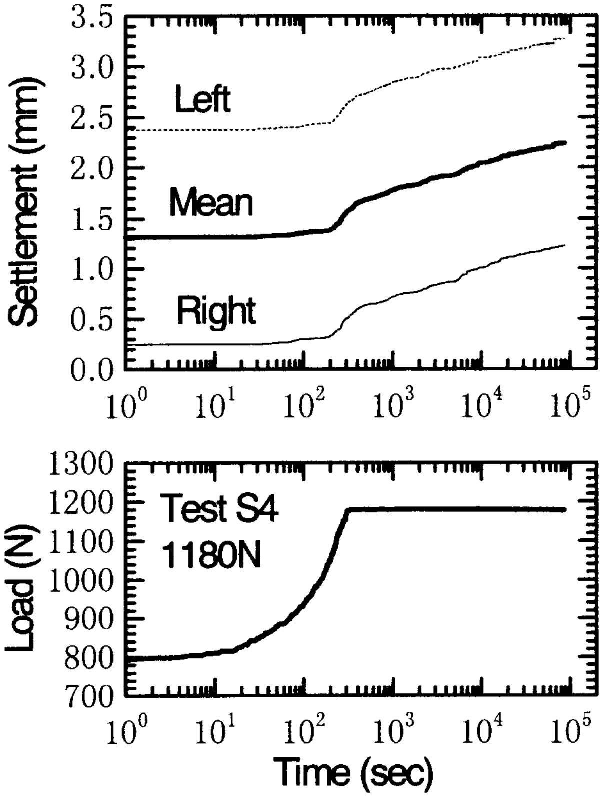


(c) 1180N

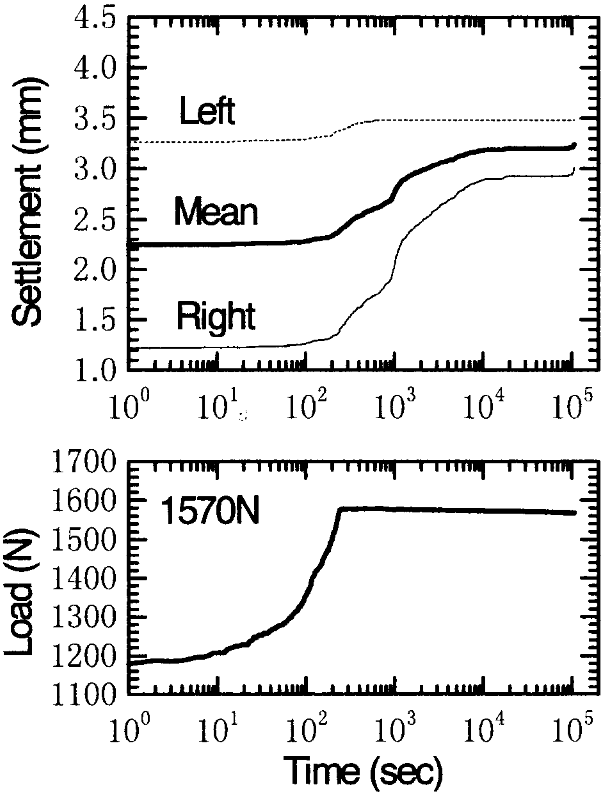


(d) 1570N

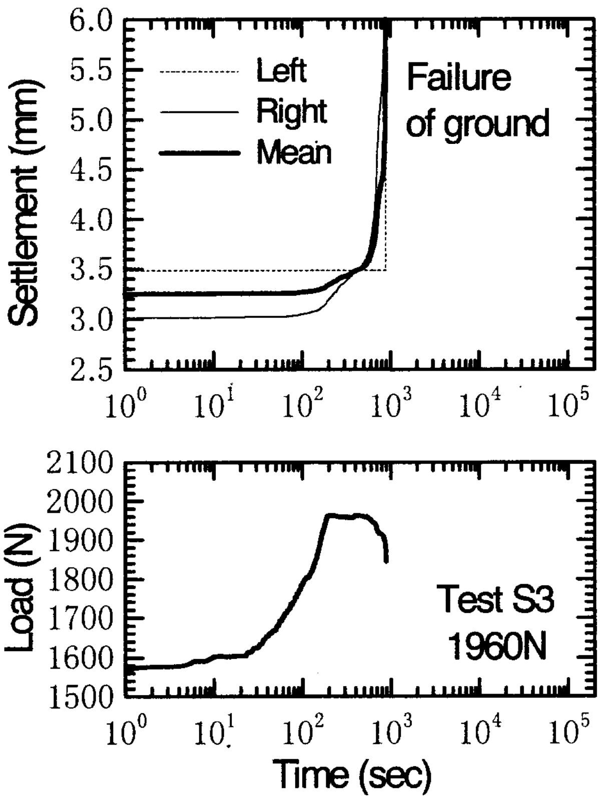


(e) 1980N

**Figure 5.8 Settlement or load vs. elapsed time curves (Test S4)**

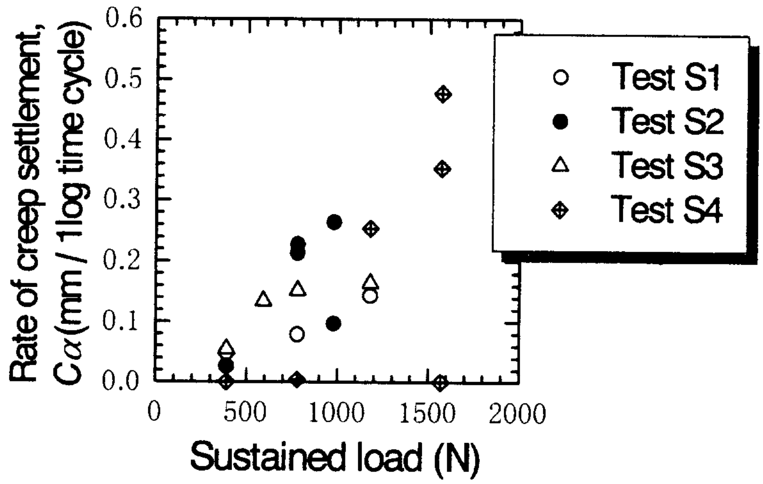


**Figure 5.9 The rate of creep settlement versus sustained load**

### 5.3.3 Mechanism of time-dependent settlement

**(1) Distribution of crushed particles**

Figures 5.10 – 5.13 illustrate the distribution of crushed chalk bars in each loading stage of each sustained loading test (Test S1 – S4). These figures were made from the sketches drawn in each experiment. These figures do not reflect the real width of each crack. The crushed chalk bars were spread over the fan-shaped region whose vertical angle was about 60° under the footing (see Figure 5.11(b)). There were some crushed chalk bars beyond the fan-shaped region in the depth deeper than 1*B*.

In the Figures 5.10 – 5.13, the cracks are grouped according to their time occurred. The numbers of crushed chalk bars increased with the passage of time even in the sustained loading period. In the one-dimensional compression tests of the chalk bar specimen, the increase in the number of crushed chalk bar occurred only in the first 45 seconds. In the footing loading tests, however, newly crushing occurred in the interval of several hours. Such a phenomenon occurred in the one-dimensional compression tests of the talc bar specimens. From the fact, it is considered that the contact forces must have been redistributed even in the sustained loading terms of the footing loading tests.

In all tests, particle crushing occurred firstly beneath the edges of the footing, and then spread over the region in the ground with load increasing and with passage of time. In Test S3 and S4, it is interesting that the crushing of chalk bars spreads in inclined lines.

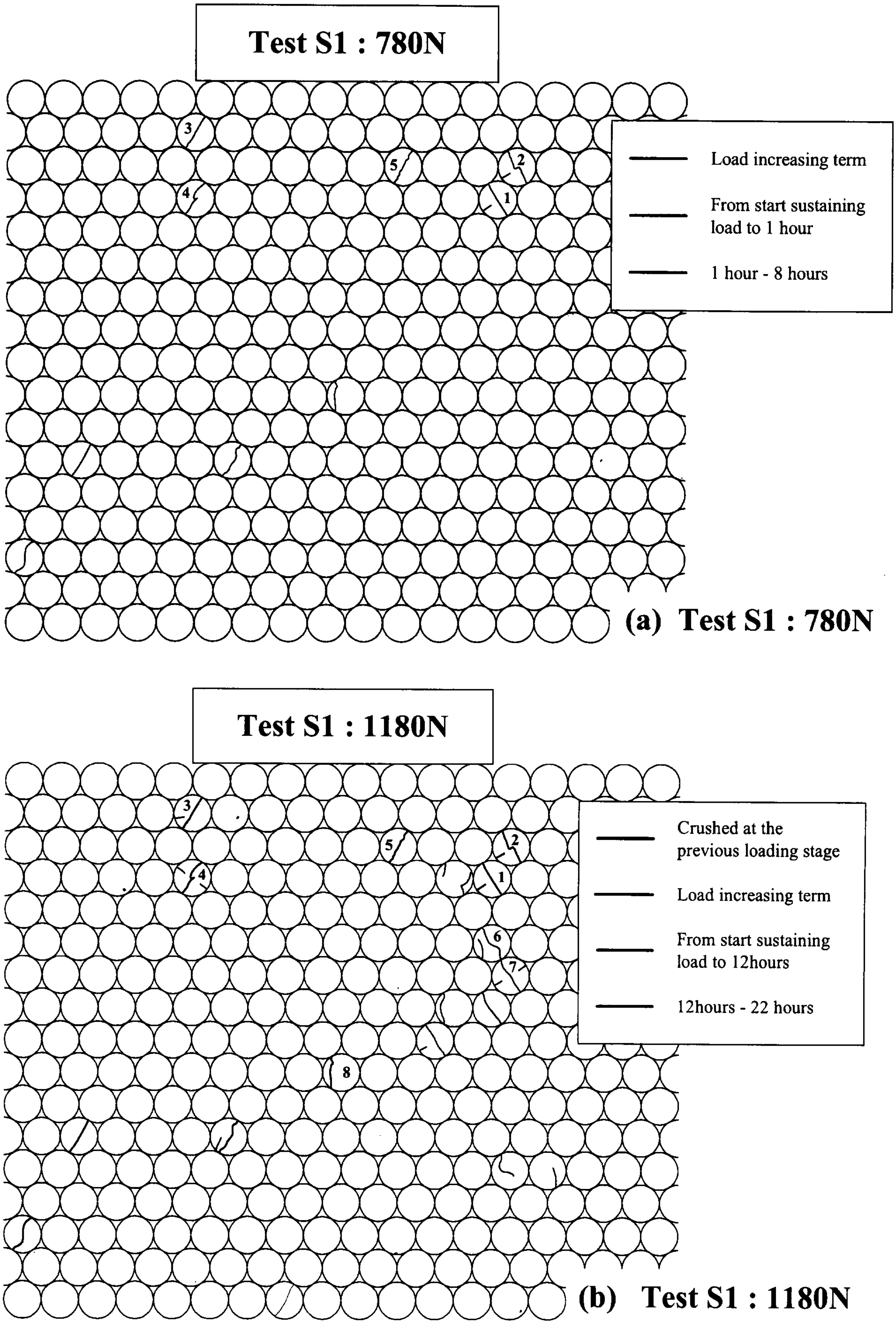


**Figure 5.10 Macroscopic crushing progress (Test S1)**

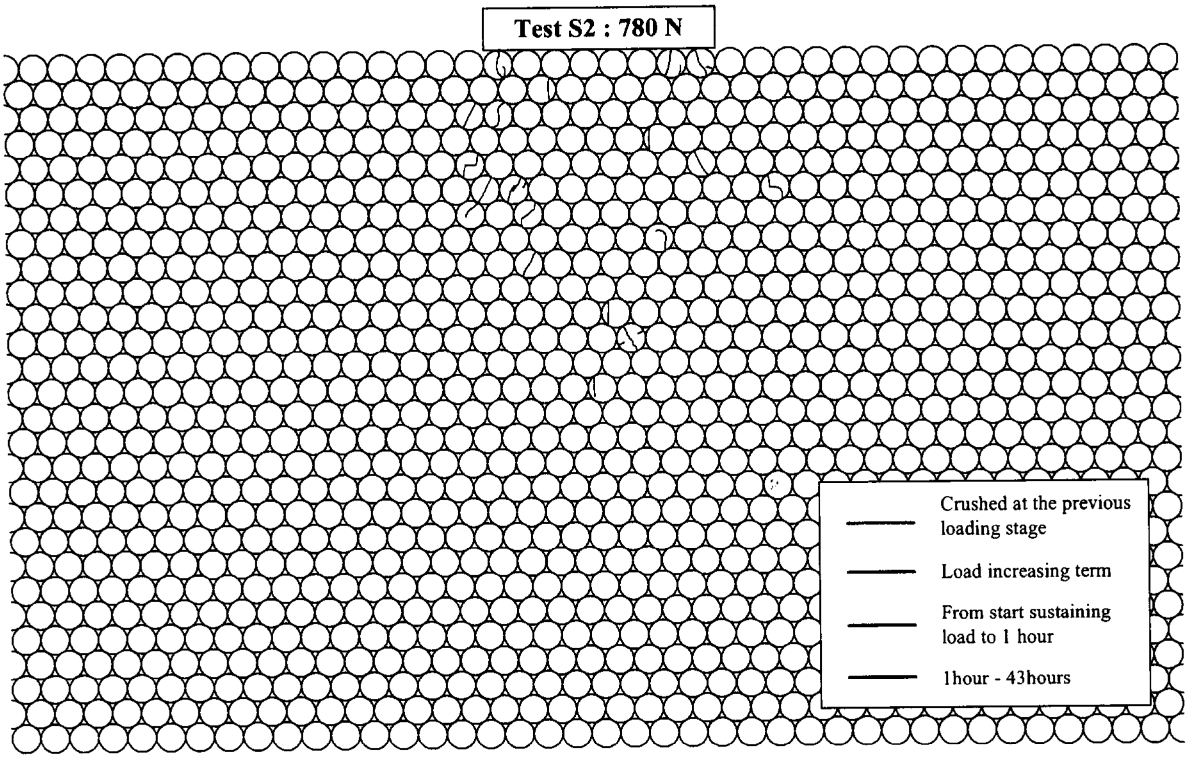


**(a) Test S2 : 780N**

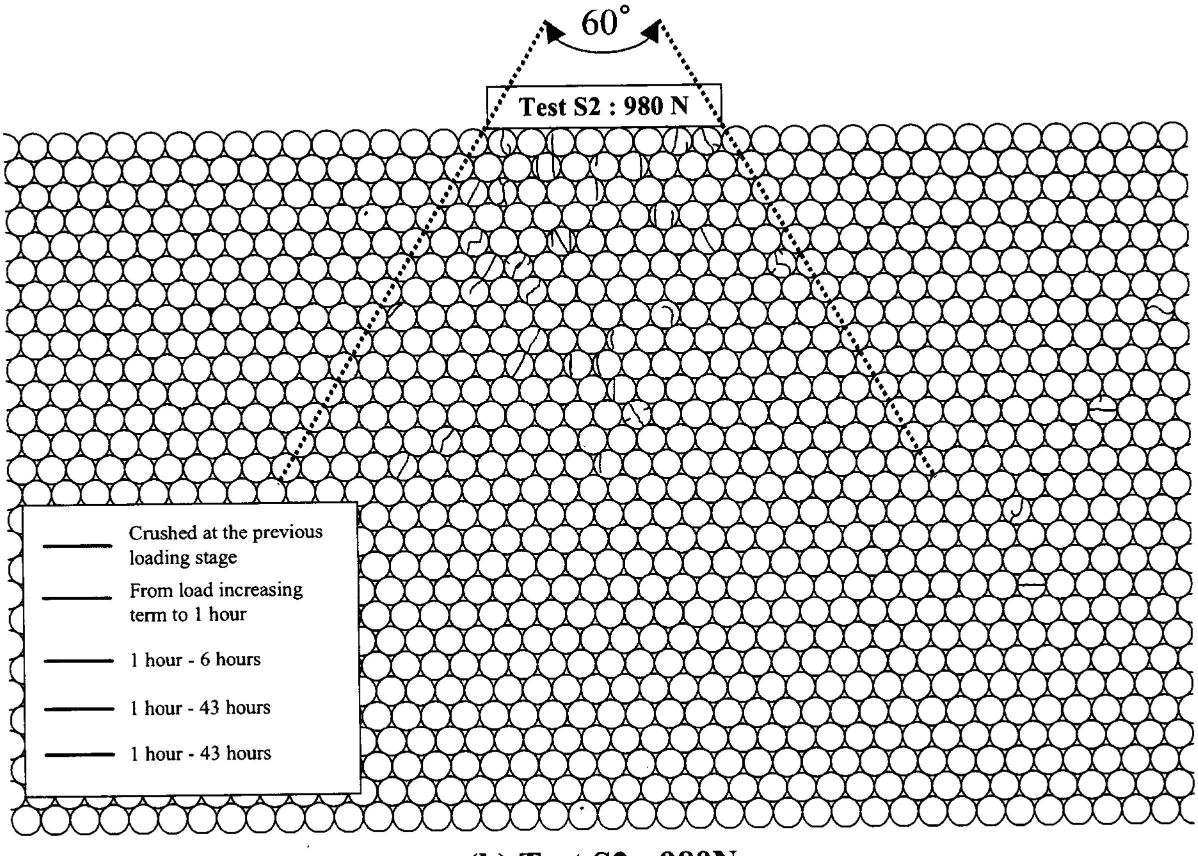


**(b) Test S2 : 980N**

**Figure 5.11 Macroscopic crushing progress (Test S2)**

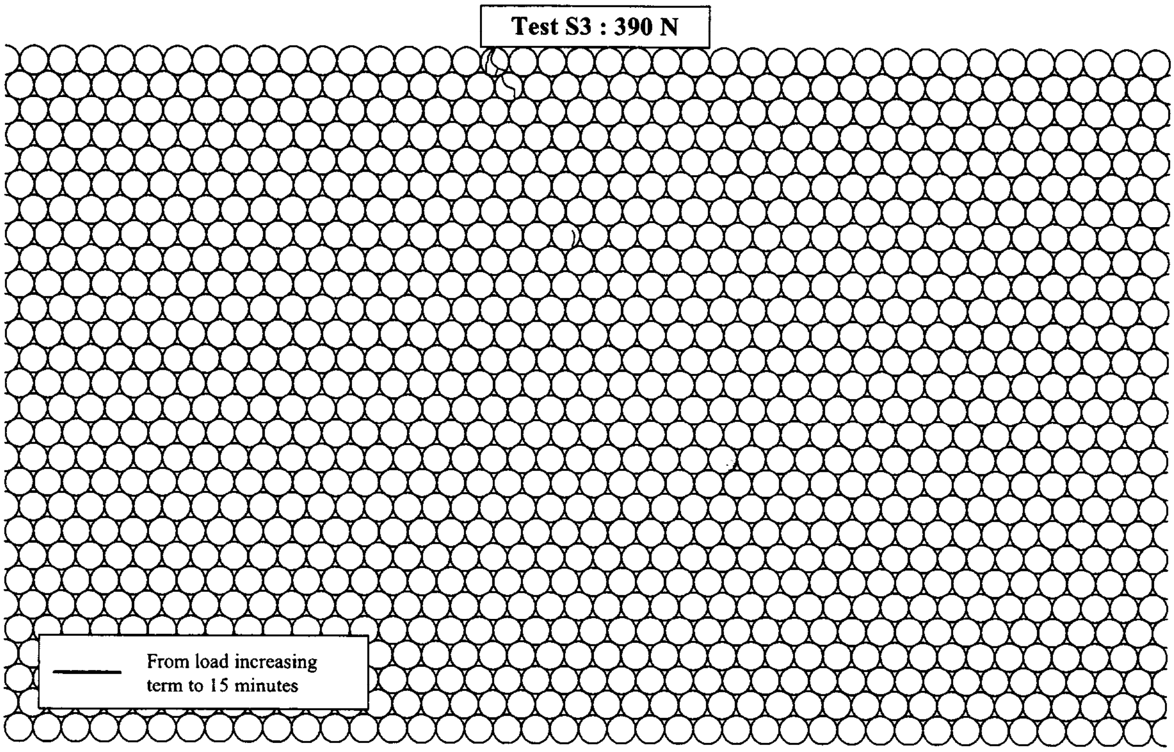


(a) Test S3 : 390N

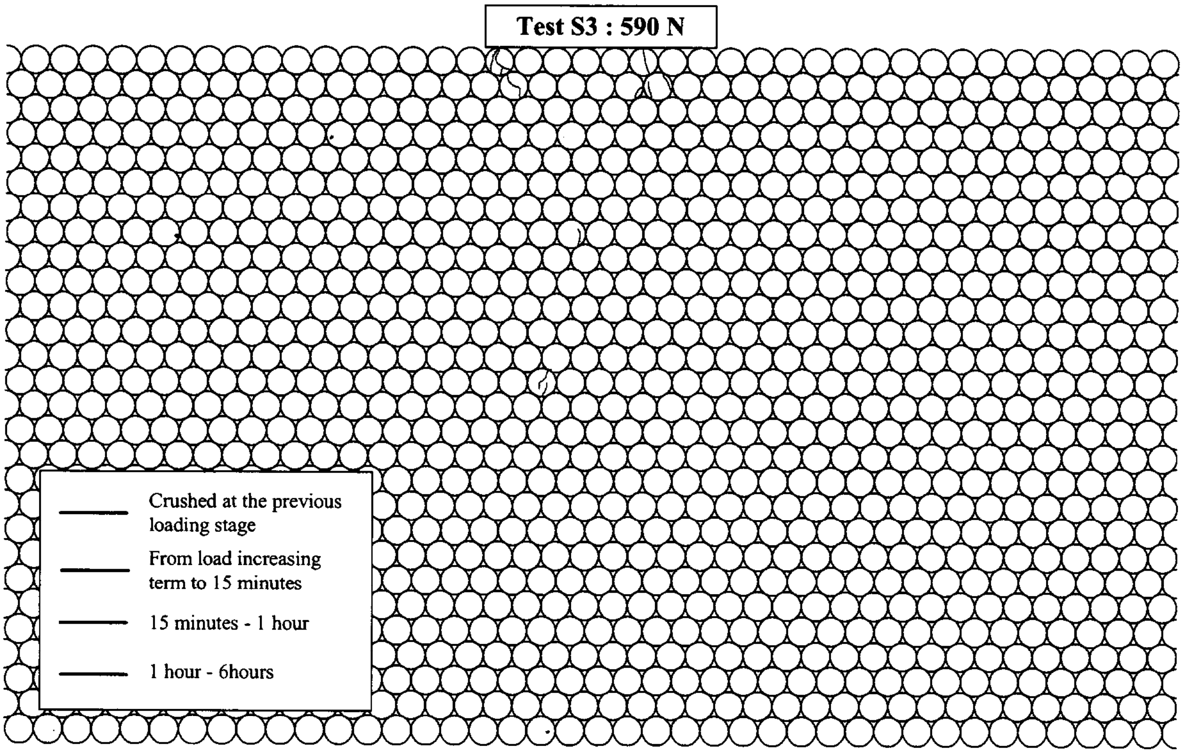


(b) Test S3 : 590N

**Figure 5.12 Macroscopic crushing progress (Test S3)**

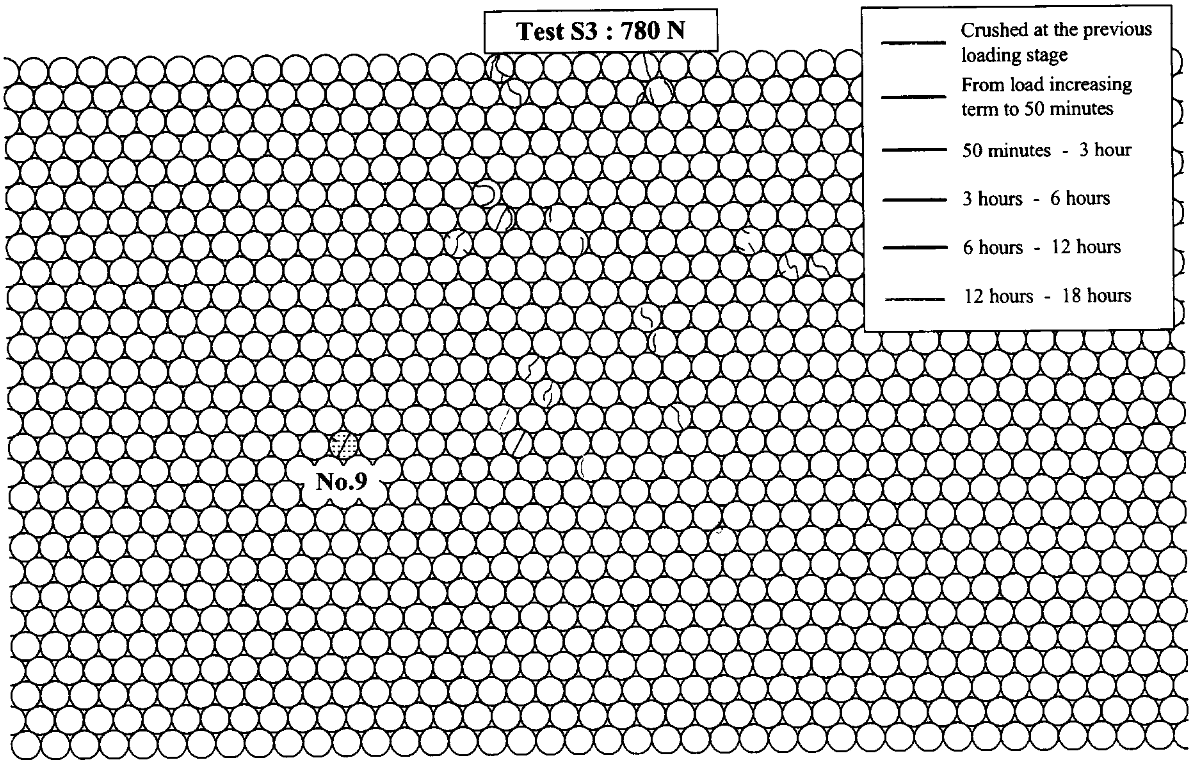


**(c) Test S3 : 780N**

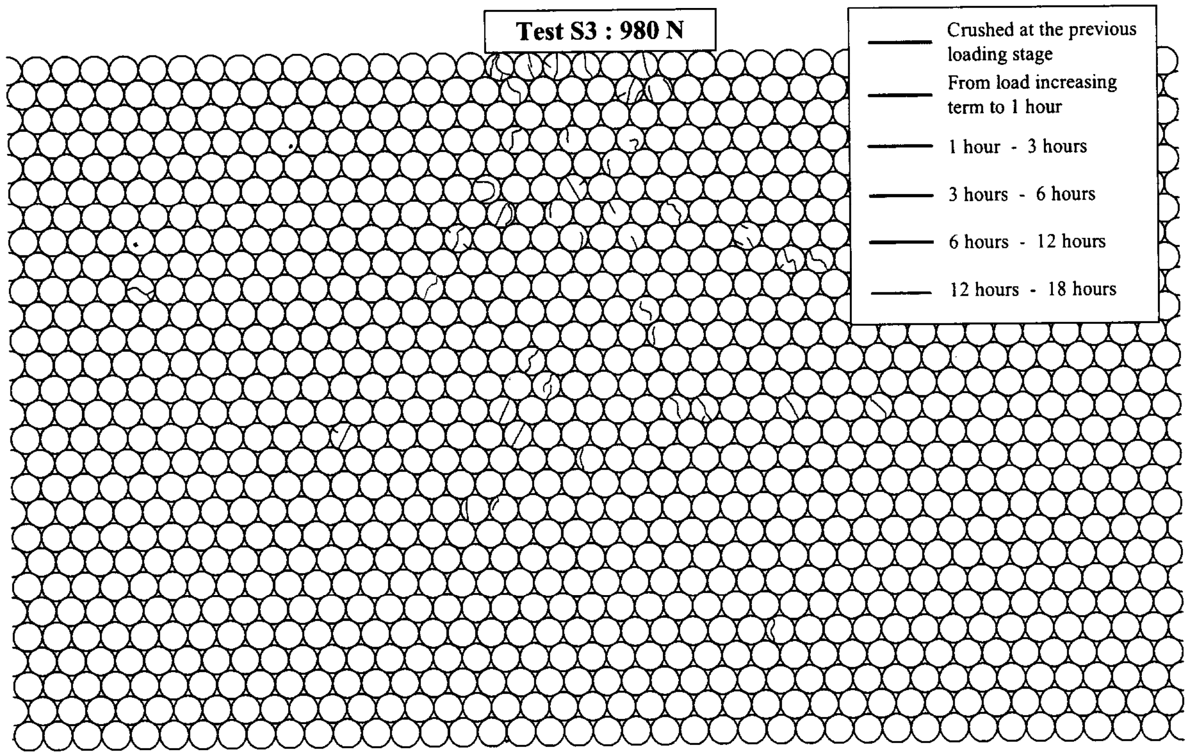


**(d) Test S3 : 980N**

**Figure 5.12 Macroscopic crushing progress (Test S3)**

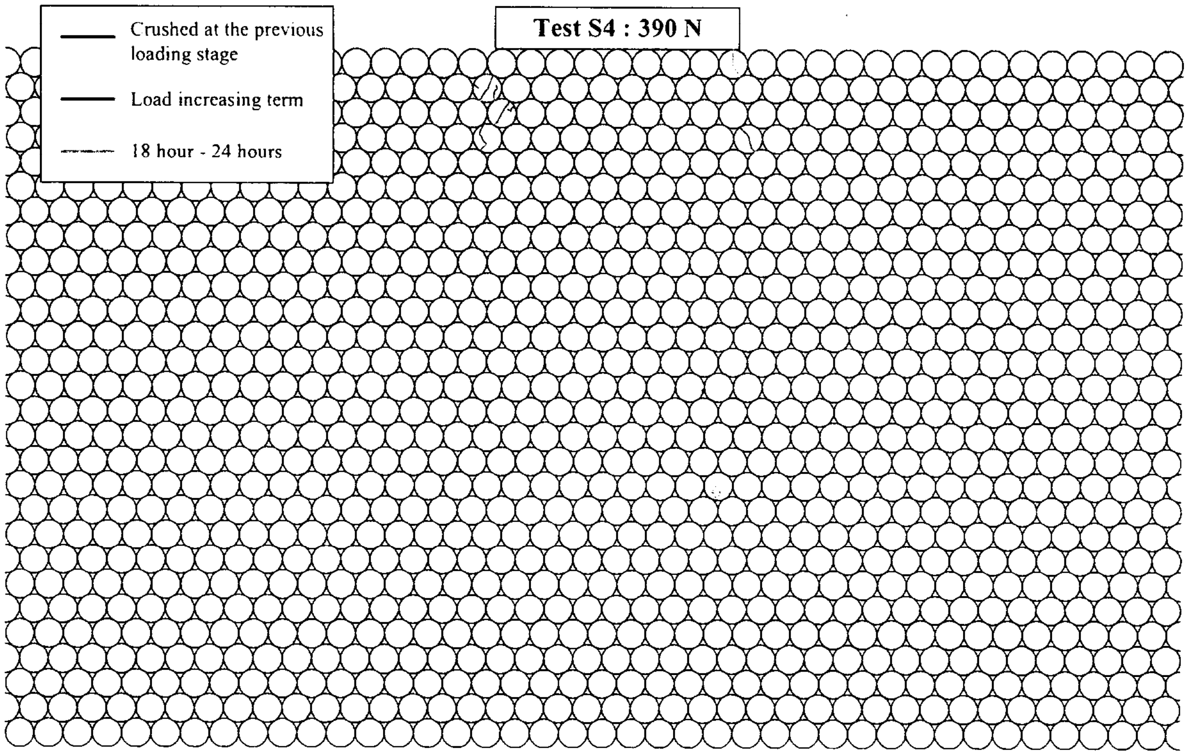


(a) Test S4 : 390N

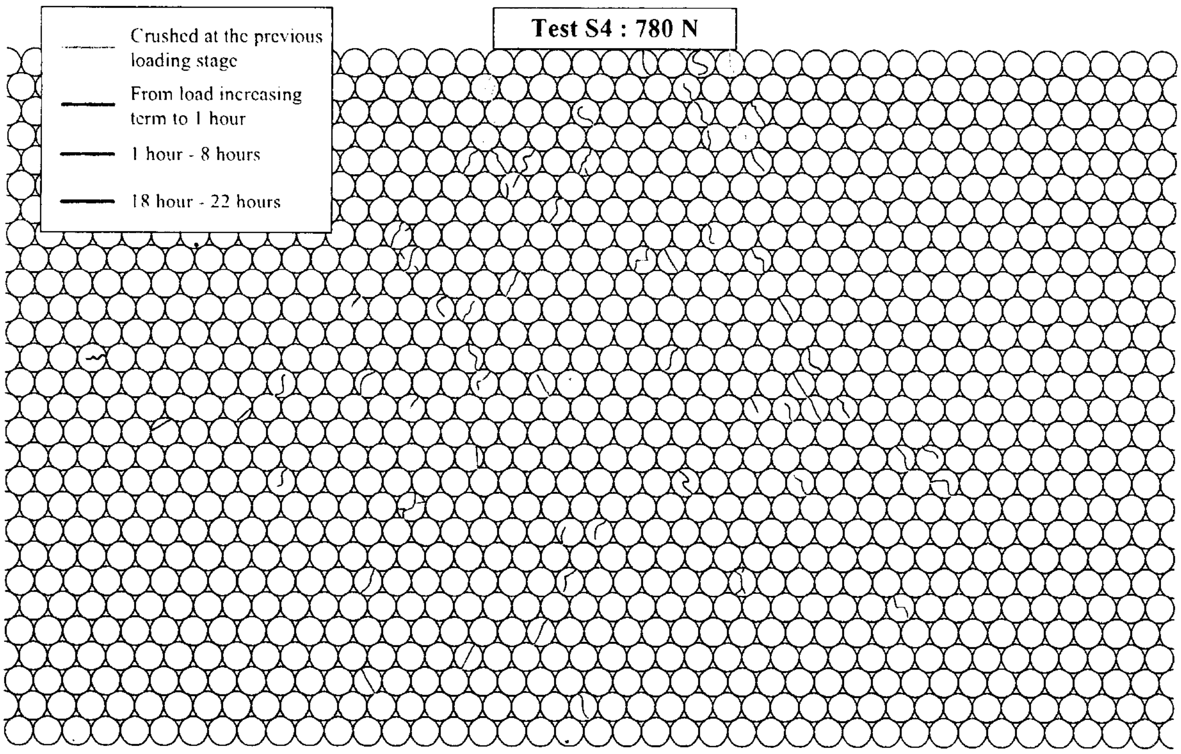


(b) Test S4 : 780N

**Figure 5.13 Macroscopic crushing progress (Test S4)**

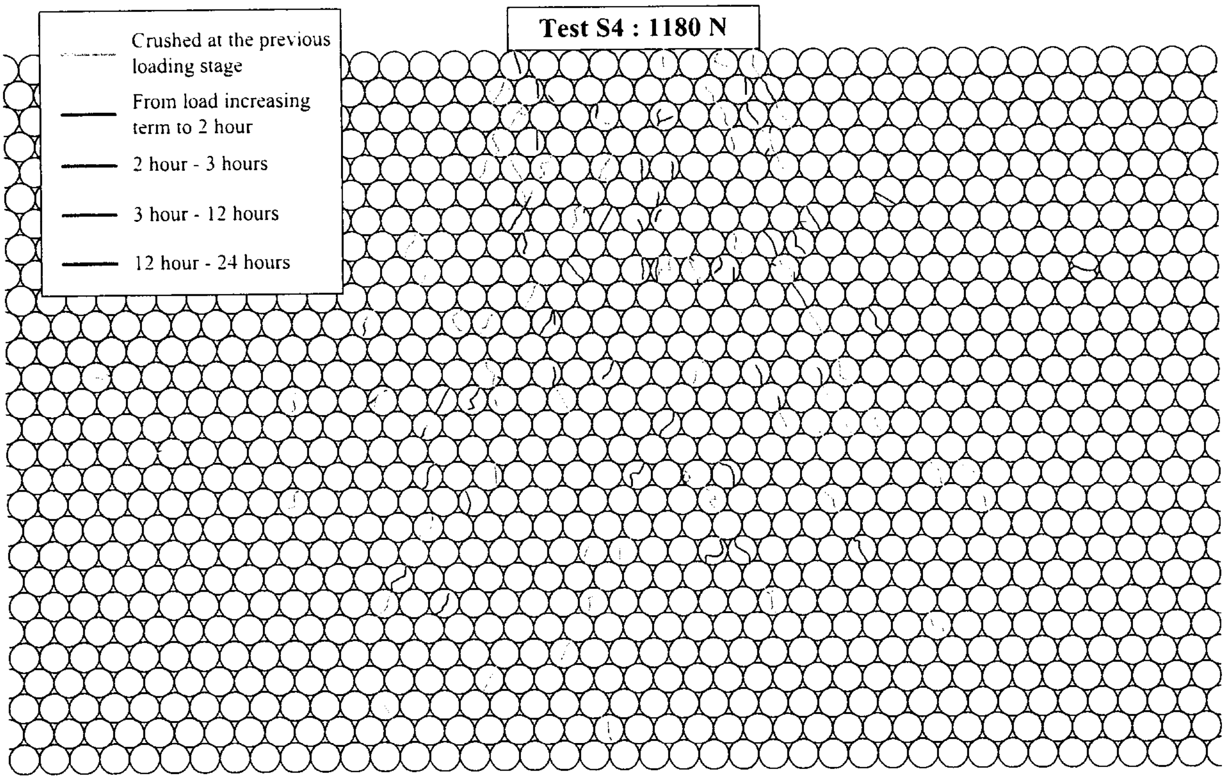


(c) Test S4 : 1180N

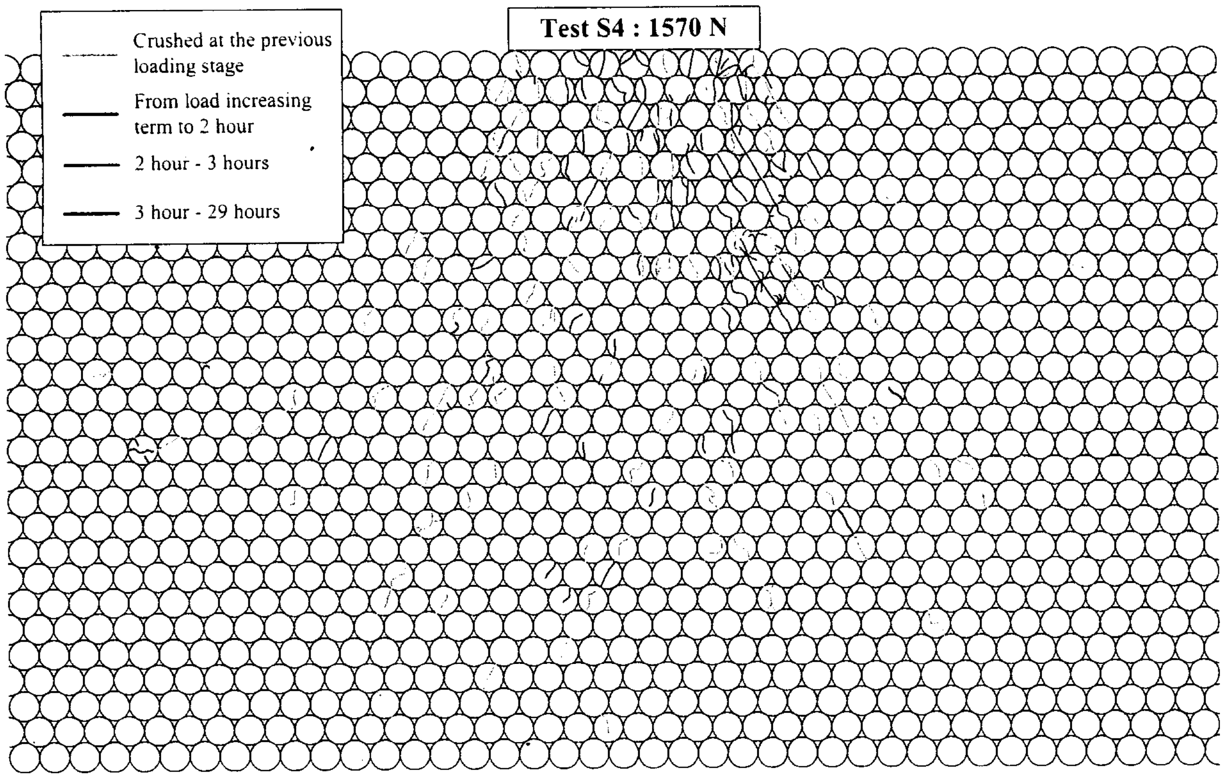


(d) Test S4 : 1570N

**Figure 5.13 Macroscopic crushing progress (Test S4)**

Figure 5.14 shows the numbers of crushed chalk bars at each loading stage. There was a variation in the number of crushed chalk bars even in the same loading stage. The largest numbers of crushed chalk bars occurred in Test S4. Such a variation would be due to the different situation of packing, i.e., the difference in configuration of skeleton made of contacted chalk bars and in the magnitude of the transferred forces along the skeletons. The distribution of the gaps shown in Figure 5.3 is one of the qualitative estimations of the configuration of the skeleton.

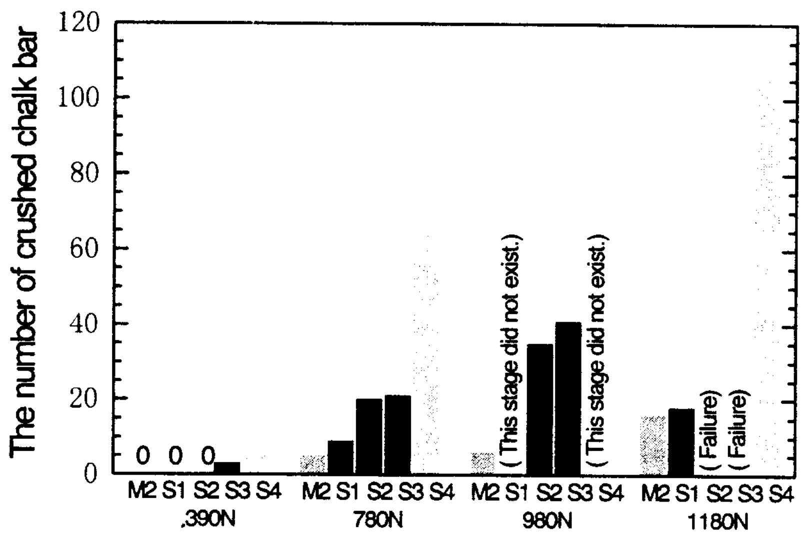


**Figure 5.14 The number of crushed chalk bars at each loading stage**

### (2) Crushing patterns of chalk bar

Figure 5.15 shows the crushing patterns observed in the model footing loading tests. There are the three crushing modes of Mode C, D, and E as observed in the one-dimensional compression test of hexagonal packed chalk bar specimen. And furthermore, Mode C is classified into Mode C, C1, and C2. Mode C is the normal "vertical splitting mode" described in Chapter 4. Mode C1 is a variety of the vertical splitting mode. In this mode, firstly, a chalk bar splits vertically, then one of the half-moon-shaped fragments or the both two fragments break or buckle by the splitting forces. Mode C2 is also a variety of the vertical splitting mode. In this mode, the splitting crack occurred in the s-shape, then both two fragments break at their projections as shown in Figure 5.15(c). Mode D and Mode E are the "sideways splitting mode" as shown in the one-dimensional compression tests. In addition, there existed the crushed chalk bars that belonged to none of these modes as shown in Figure 5.10 – 5.13. It is considered that the chalk bars contain a greater number of defects in their bodies. If there is an extremely large defect in the body or a number of defects gather in a part of the body, cracks may develop through the large defect or the gathered defects. Such cracks may sometimes exhibit a complicated configuration.

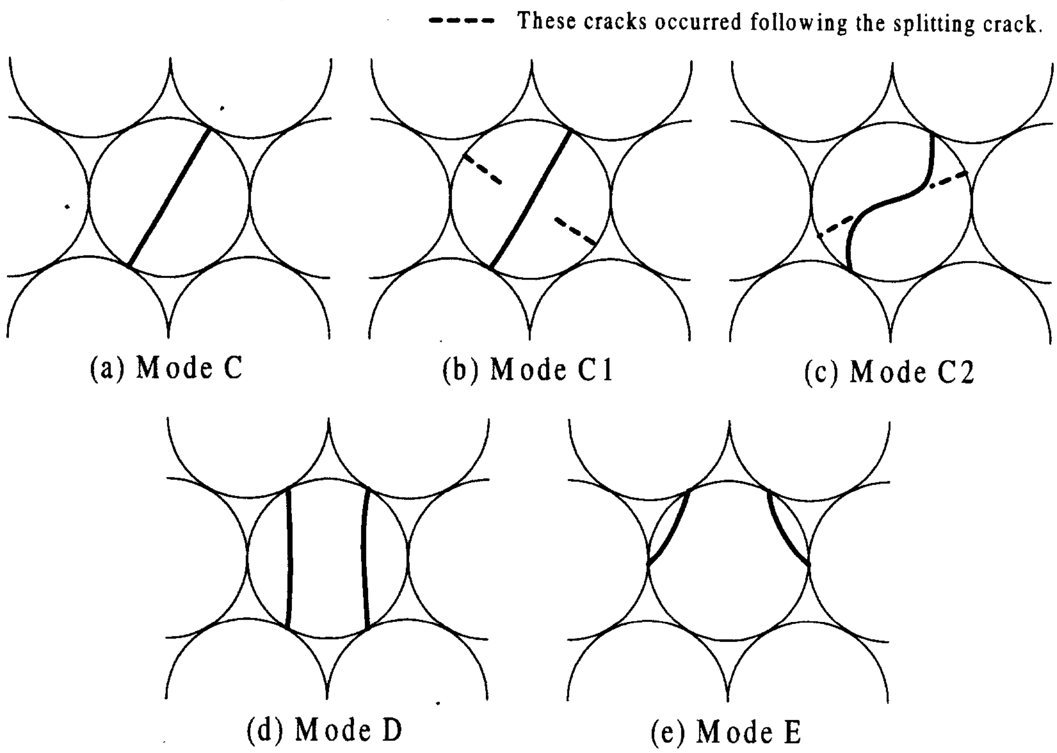


**Figure 5.15 Crushing patterns of chalk bar in footing loading test**

Figure 5.16 shows qualitative distributions of contact forces that are considered to cause each crushing mode. It is considered that the distribution of contact forces of a crushed chalk bar in Mode C would be the same as that in Mode C of hexagonal packed one-dimensional compression test. In Mode C, a pair of forces along a direction would surpass other two pairs of forces in magnitude of the forces. Each force would contain only normal component: not contain shear component. In Mode C1 and C2, the surpassed contact forces would contain shear component. If the magnitude of the shear component is relatively small, the chalk bar would be crushed in Mode C1. If the magnitude of the shear component is relatively large, the chalk bar would be crushed in Mode C2. It is considered that the surpassed contact forces that containing the shear components would make the splitting crack to curve. But in the case of Mode C1, it is considered that the condition of the contact forces shown in Figure 5.16(b) would not be only condition for causing Mode C1, and that the following factors would be related to occurring the crushing of Mode C1: distribution of defects in a body of chalk bar, distribution of contact forces after crushing, and others. For example, the curved crack that split the chalk bar unequally as shown in Figure 5.17 may cause the crushing of Mode C1. In Mode D, two pairs of contact forces would surpass other one pair of forces in magnitude of contact forces. In Mode E, no pair of contact forces would surpass, that is to say, all pairs of contact forces would be almost equal. It is necessary to discuss quantitatively the conditions of contact forces for each mode.

In such a footing loading test, that is one of the boundary value problems, the contact forces are not distributed uniformly in the ground. The directions of principal stresses for a semi-infinite elastic body that loaded by a shallow footing are shown in Figure 5.18(a). Compared to the sketches of cracks shown in Figure 5.10 – 5.13, it is observed that the directions of splitting cracks were relevant to the directions of maximum principal stress. A failure pattern of general shear failure observed in the dense sandy ground is shown in Figure 5.18(b). To which region the chalk belongs, or where the chalk positions in a region may be main factors of distribution of contact forces. A chalk bar that is in the active region beneath the footing would be loaded as a chalk bar that is under the one-dimensional compression test. Actually, Mode D and Mode E crushing were observed in the active region. Shear bands would be formed at boundaries between two regions. The chalk bar that belongs to the shear bands would be loaded the contact forces that contain a significant shear component. Thus such a chalk bar would be apt to crush in Mode C1 or C2.

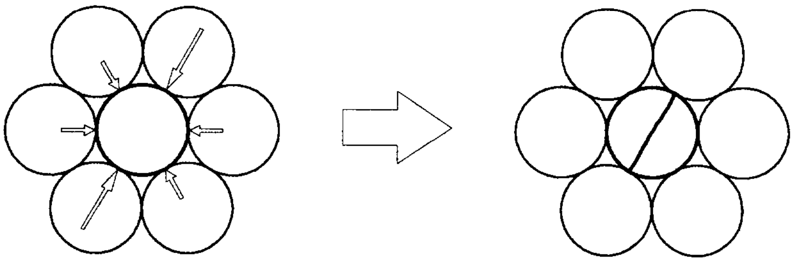

(a) Mode C

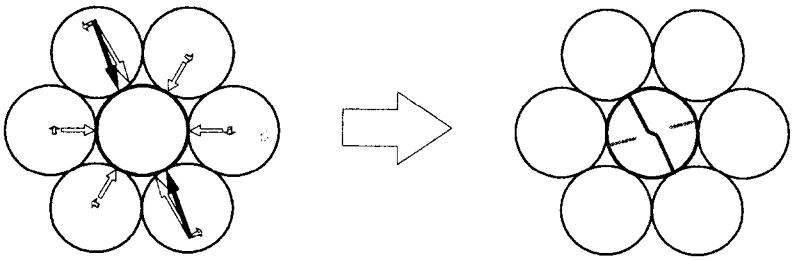

(b) Mode C1

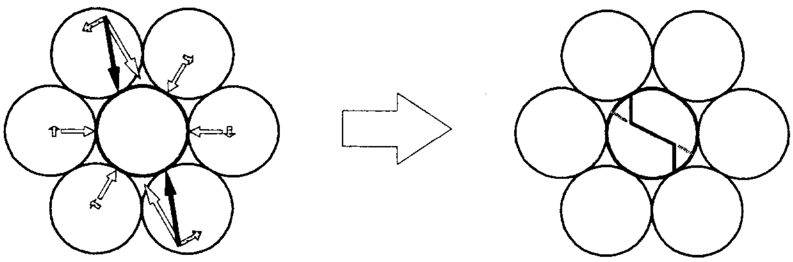

(c) Mode C2

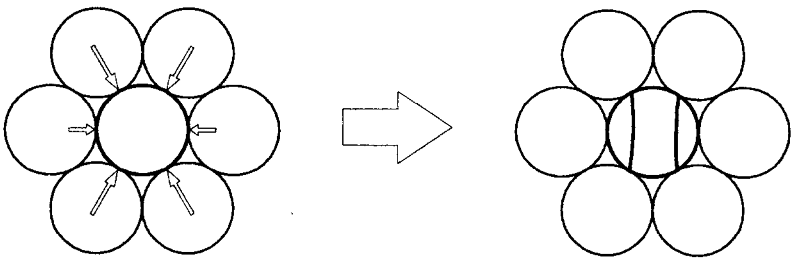

(d) Mode D

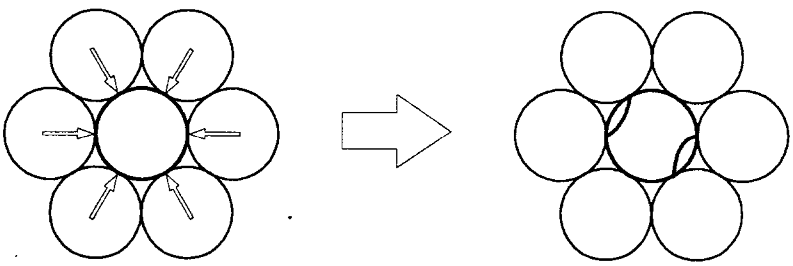

(e) Mode E

**Figure 5.16 Qualitative distributions of contact forces for each crushing mode**

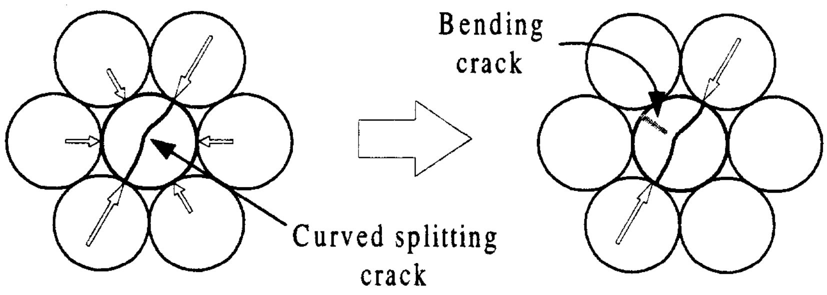


**Figure 5.17 Another condition for Mode C1 crushing**

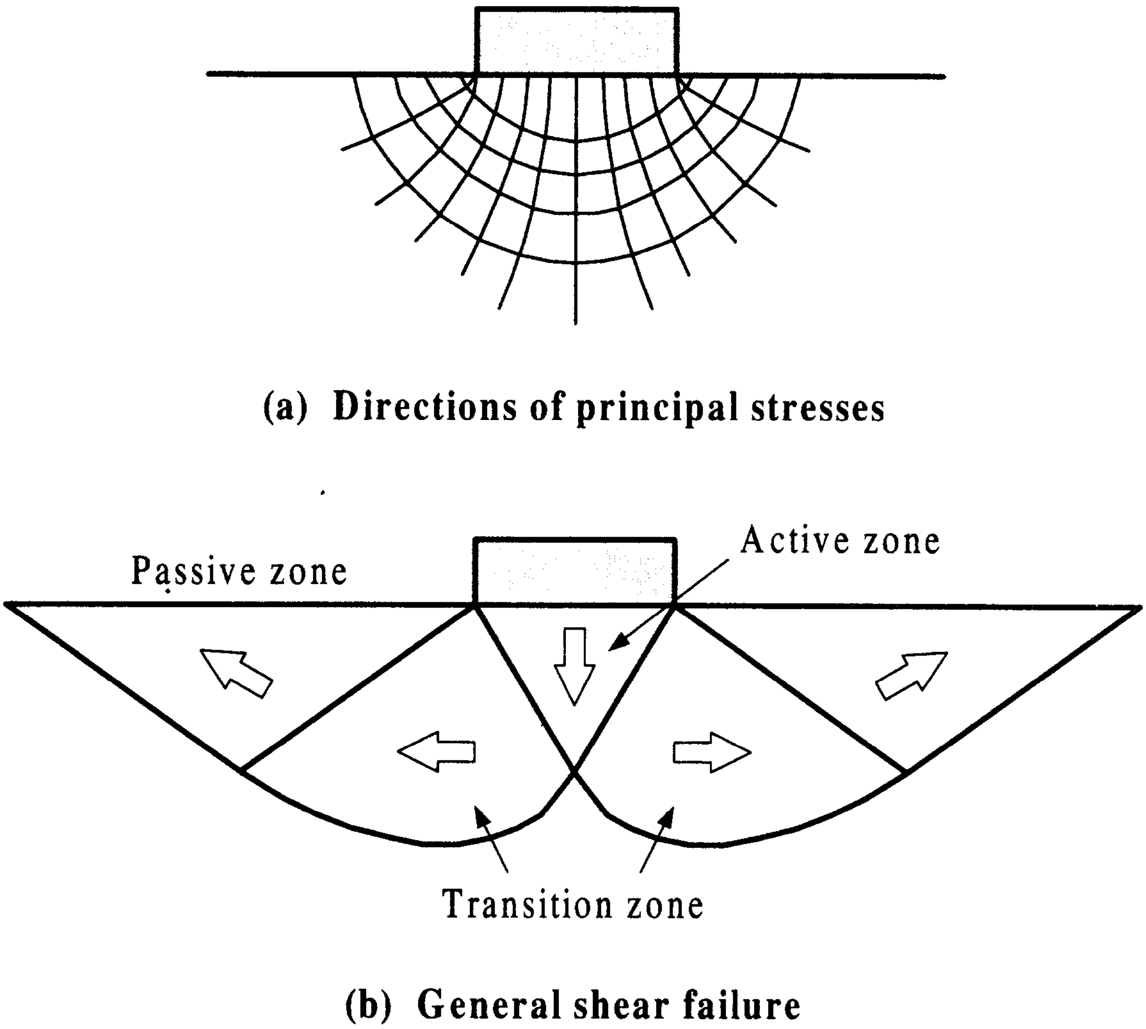


**Figure 5.18 Directions of principal stresses and general shear failure of general dense sandy ground**

The direction of principal stress and the failure mode of the ground (i.e., configuration of each region) would be affected by the following factors: magnitude of friction force between chalk bars (angle of internal friction), the magnitude of friction force between the under surface of the footing and chalk bars that are contacting with the footing, density of ground, and others. The distribution of the gaps shown in Figure 5.3 would also influence the distribution of contact forces of a chalk bar.

**(3) Crack opening with elapsed time**

In the footing loading tests, almost all crushed chalk bars were photographed by the digital microscope. The pictures of some crushed chalk bars are shown in Photographs 5.4 – 5.7. The chalk bars shown in these photographs are the examples of crushed chalk bars where some changes were observed during a sustained loading term. The crushed chalk bars were photographed two or three times during the loading stage at intervals of several hours. As seen in each photograph, the width of crack increased with the passage of time. The crushed chalk bars were numbered as shown in Figure 5.19.

Figure 5.19 also shows the distributions of the crushed chalk bars in which the crack openings were clearly observed during the sustained loading term of the loading stage. Only a few chalk bars showed the clear crack opening in each sustained loading term. Those crushed chalk bars were situated under the both edges of the footing at the depths of 0.2B – 1B. The positions of those crushed chalk bars crushed chalk bars would be in the share bands that were formed in the boundaries between the active zone and the transition zones.

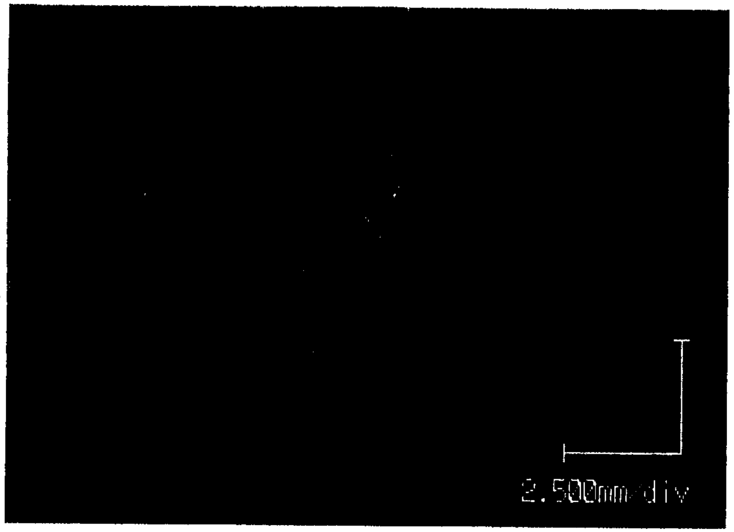


(a) Test S2 ; 780N : No.10 : 100 min.


(b) Test S2 ; 780N : No.10 : 43 hours

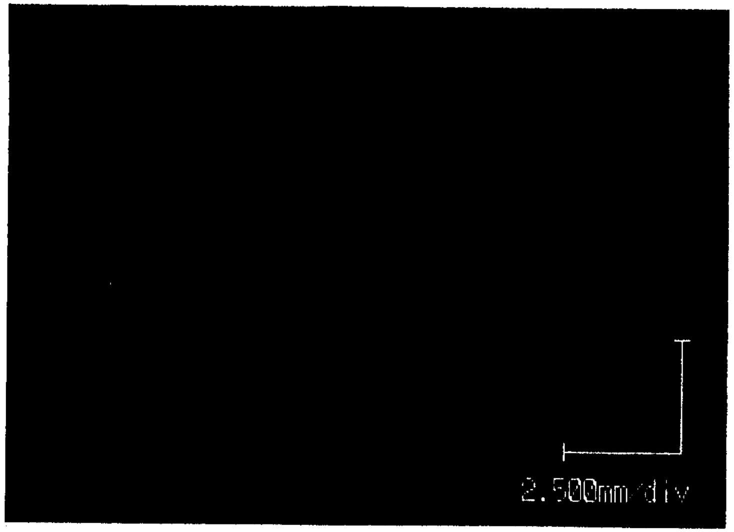


(c) Test S3 ; 590N : No.2 : 15min.

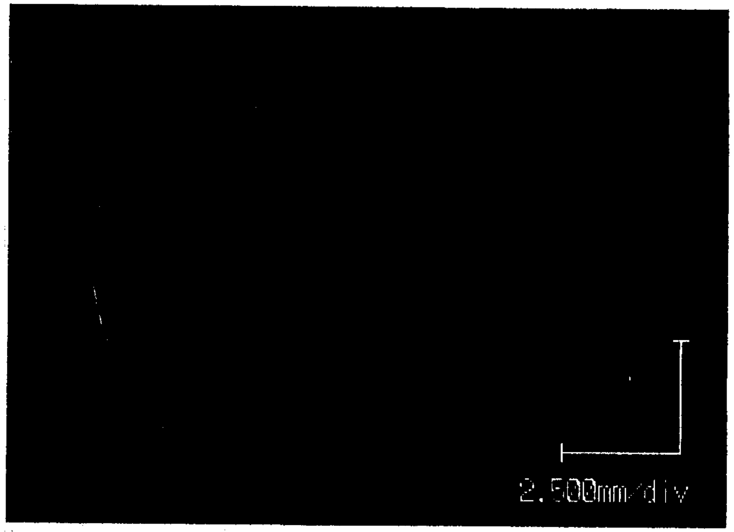


(d) Test S3 ; 590N : No.2: 24 hours

**Photo. 5.4 Crushing progress of chalk bar under a footing loading test ( Mode C )**

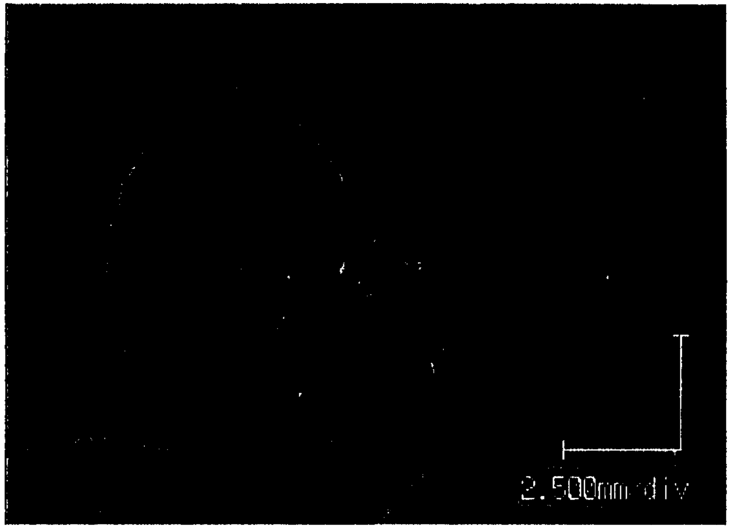


(a) Test S1 ; 780N : No.1 : 8 hours

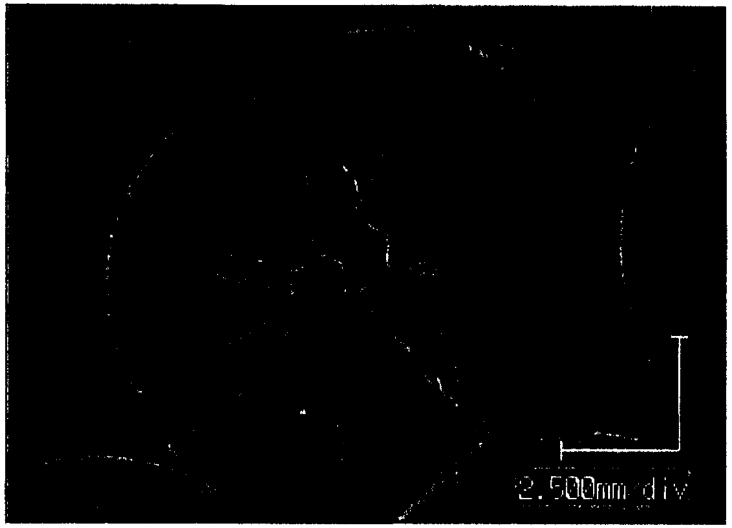


(b) Test S1 ; 780N : No.1 : 17 hours

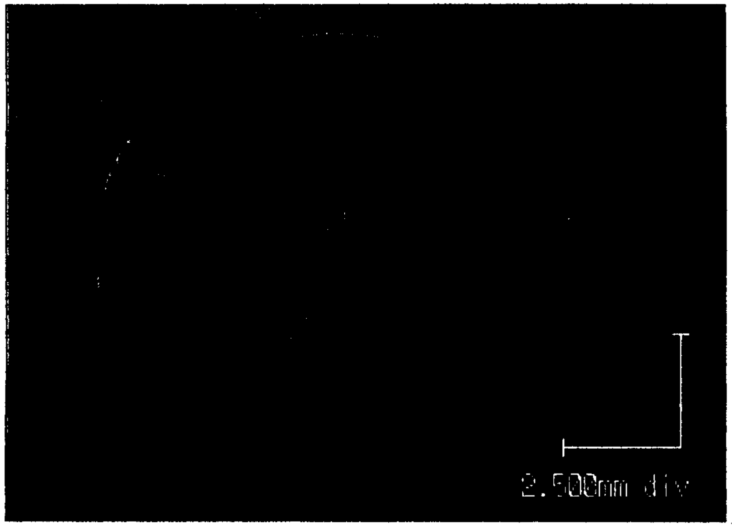


(c) Test S3 ; 780N : No.9 : 50min.


(d) Test S3 ; 780N : No.9 : 24 hours

**Photo. 5.5 Crushing progress of chalk bar under a footing loading test ( Mode C1 )**

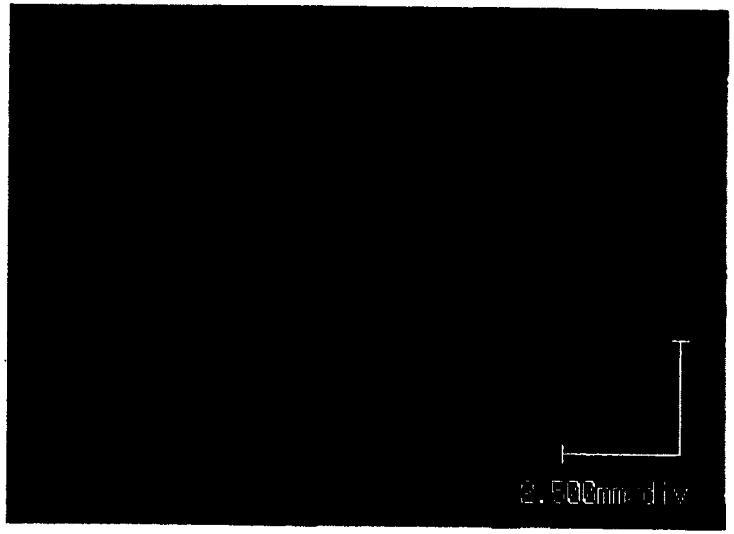


(a) Test S2 ; 780N : No.7 : 100 min.

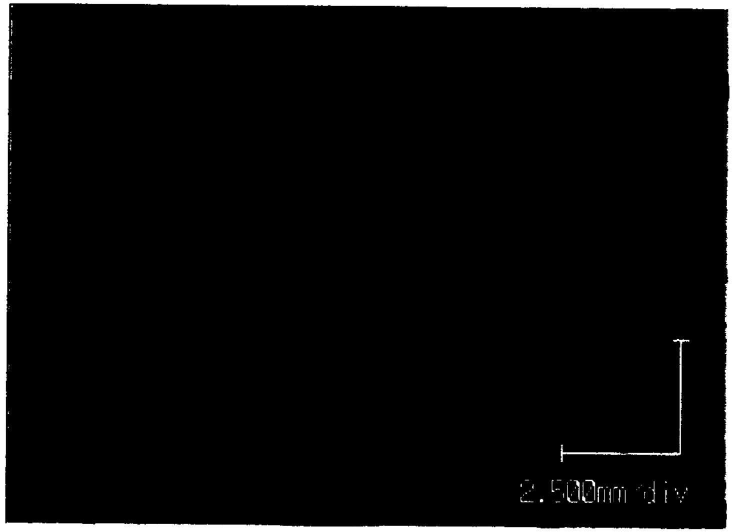


(b) Test S2 ; 780N : No.7 : 43 hours

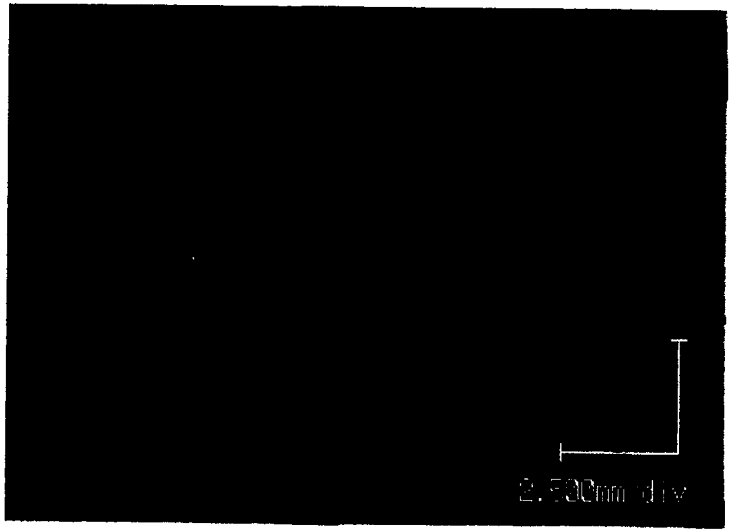


(c) Test S2 ; 780N : No.12 : 100 min.

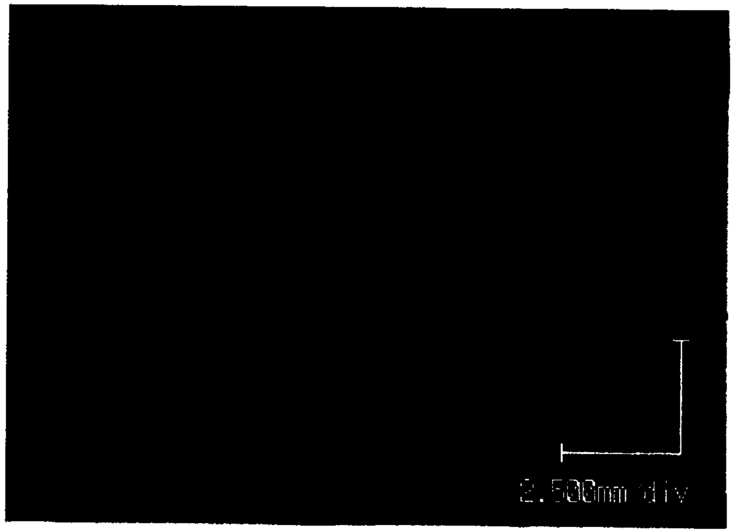


(d) Test S2 ; 780N : No.12: 43 hours

**Photo. 5.6 Crushing progress of chalk bar under a footing loading test ( Mode C2 )**

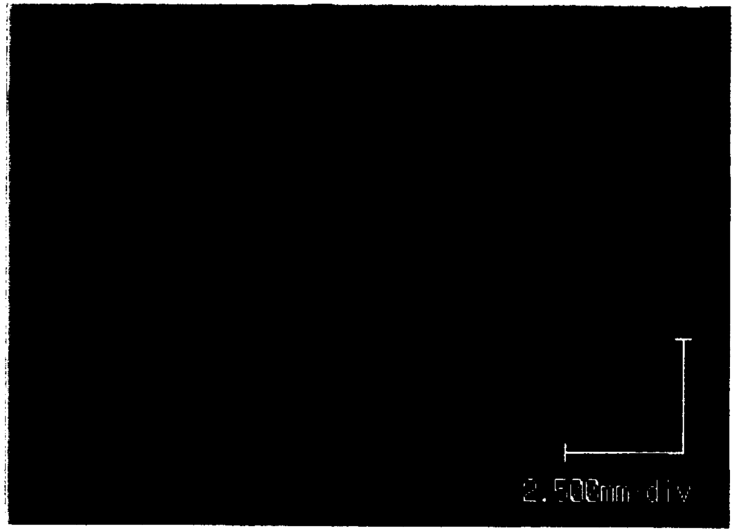


(a) Test S2 ; 980N : No.3 : 20 min.

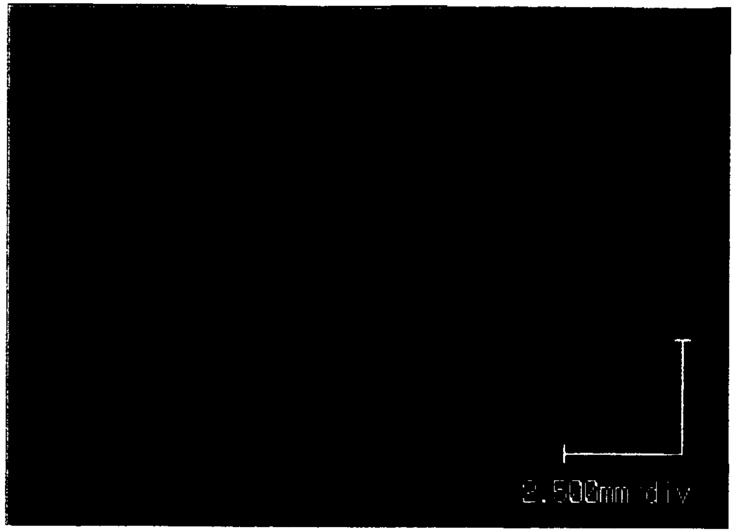


(b) Test S2 ; 980N : No.3 : 27 hours

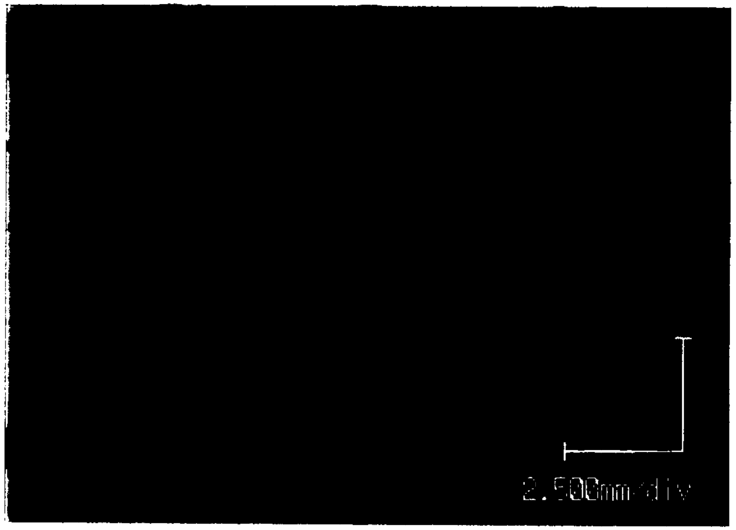


(c) Test S2 ; 980N : No.19 : 20 min.

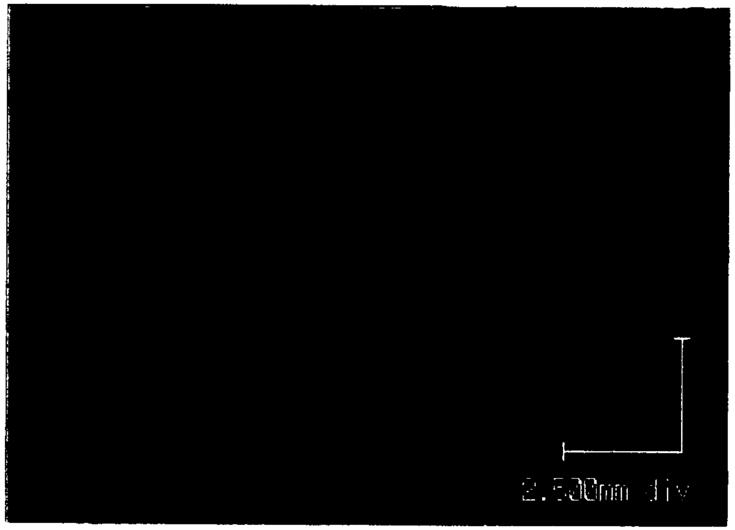


(d) Test S2 ; 980N : No.19 : 27 hours

**Photo. 5.7 Crushing progress of chalk bar under a footing loading test ( Mode D and E )**

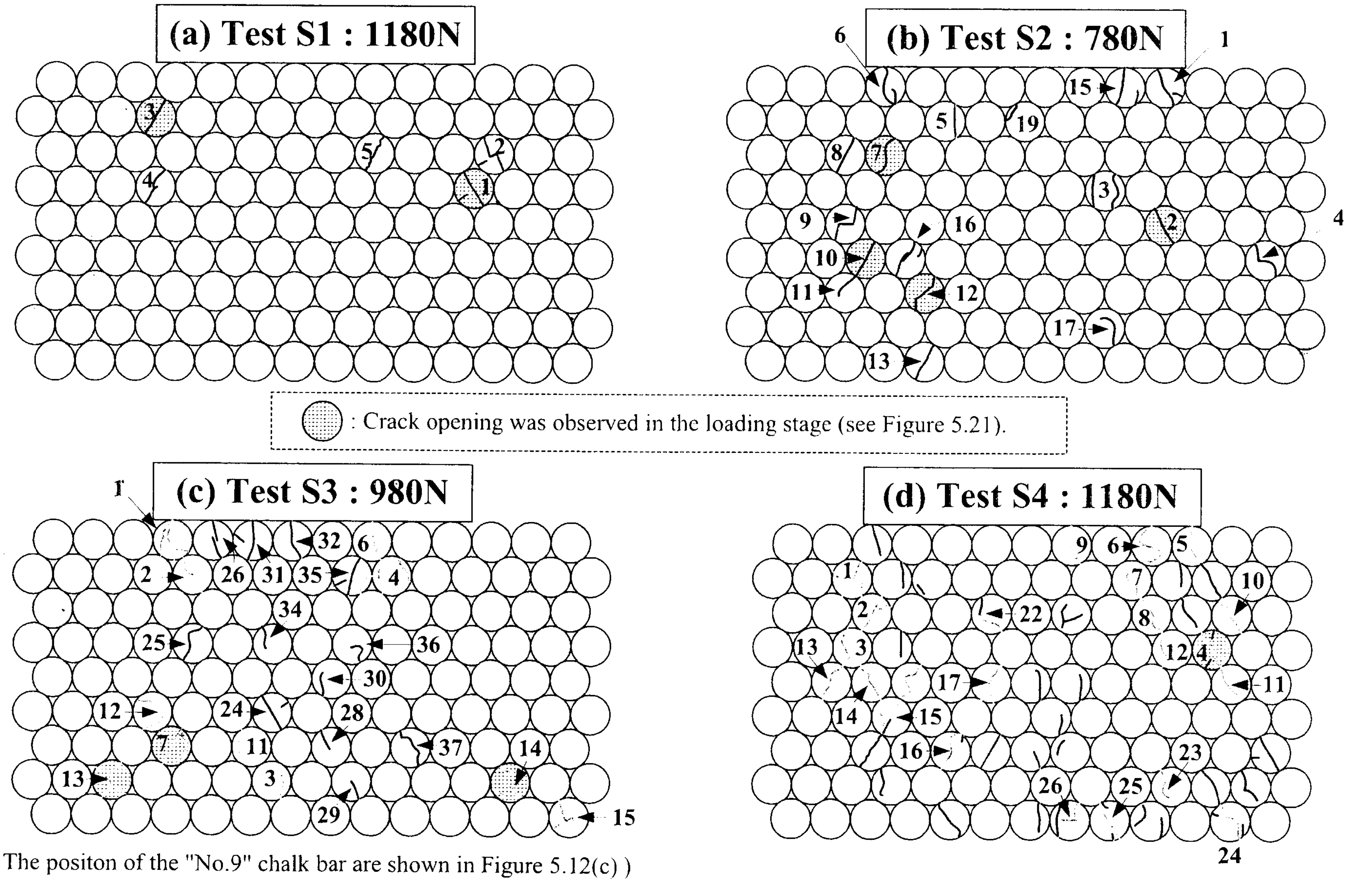


**Figure 5.19 Numbering of crushed chalk bars and the chalk bars observed crack opening**

Figure 5.20 presents the crack opening patterns in Mode C, C1 and C2. In the case of Mode C, the angular width of the vertical splitting crack increased with elapsed time. Each half-moon-shape fragment would be pushed to different directions. In the cases of Mode C1 and C2, the chalk bar was smashed by the splitting contact forces, (strictly speaking, by the normal components of the contact forces,) and widened. The crack opening would be attributed to crushing of the angular edges formed by the initial cracking. Those angular edges are marked by circles in Figure 5.20. Small confirming forces, that means the contact forces except the splitting contact forces, would be one of the factors for the crack opening. The local crushing progress at those angular edges would be the origin of the time-dependent behavior in the footing loading tests.

Figure 5.21 shows the magnitude of crack opening versus elapsed time with settlement of the footing. The magnitude of crack opening was measured from the photographs taken by the digital microscope. The trend of increment of crack opening is similar to that of the settlement of the footing. This fact shows that the crack opening is closely related with the time-dependent settlement of the footing.

In the cases of Mode D and E, slight crack openings were observed, as shown in Photograph 5.7. The crack openings in these modes would be due to the local crushing progress at the contact parts of fragmented chalk bars and the separation of the fragments from the original body into surrounding voids. These phenomena were observed in the one-dimensional compression tests of chalk bar specimen.

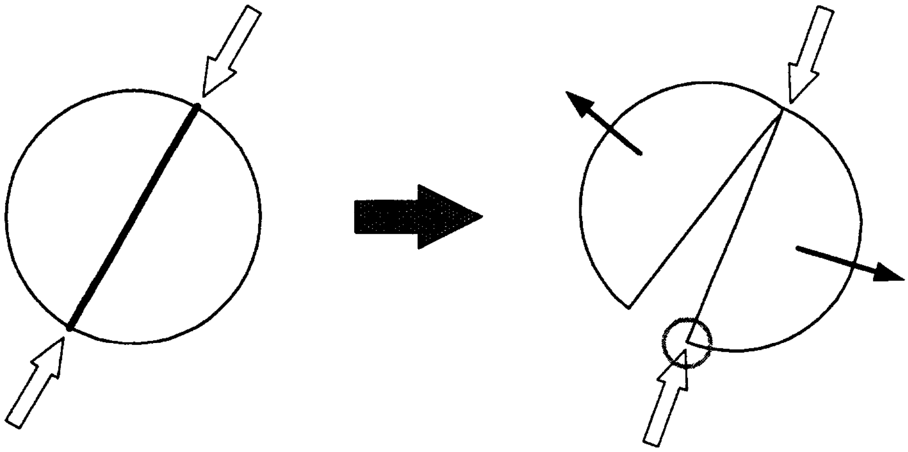

(a) Mode C

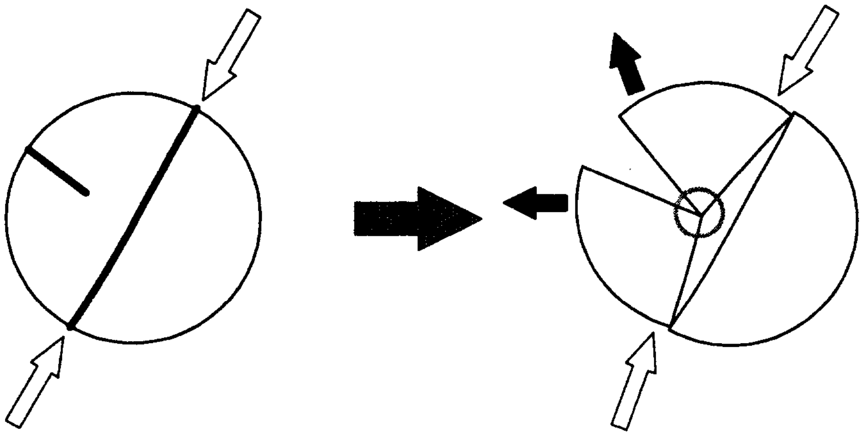

(b) Mode C1

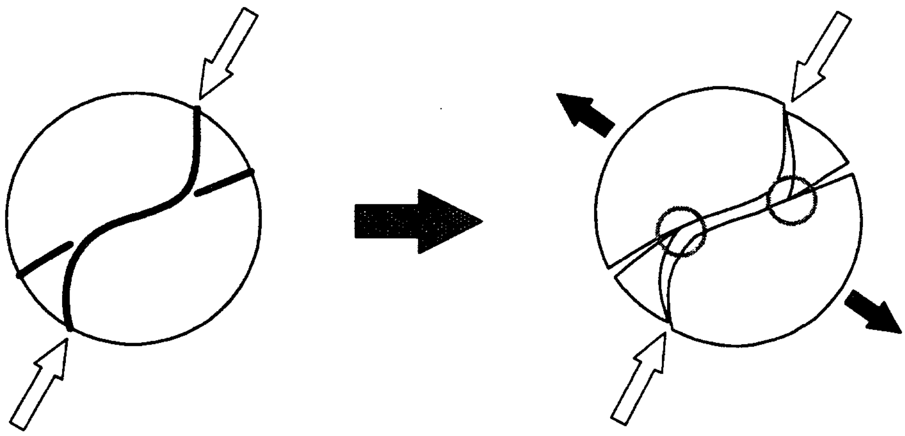

(c) Mode C2

**Figure 5.20 Crack opening styles (Mode C, C2 and C3 )**

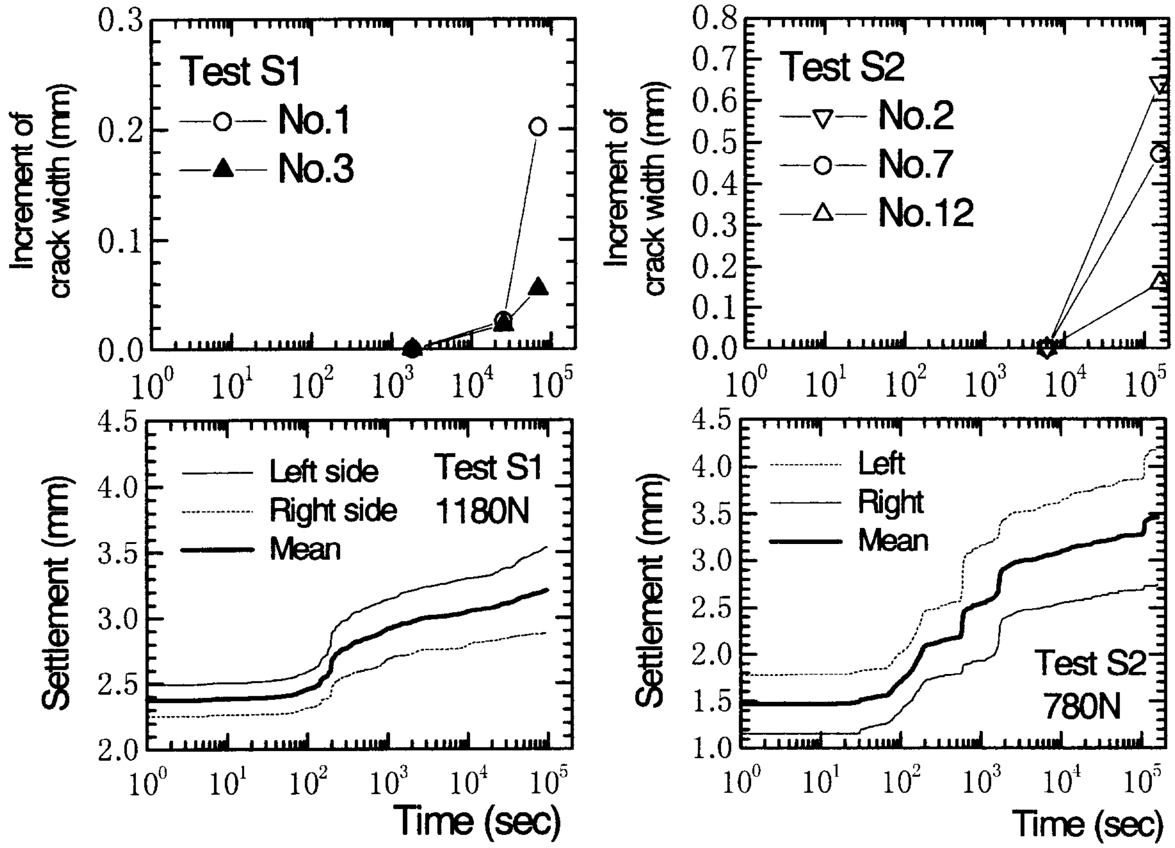


**(a) Test S1** **(b) Test S2**

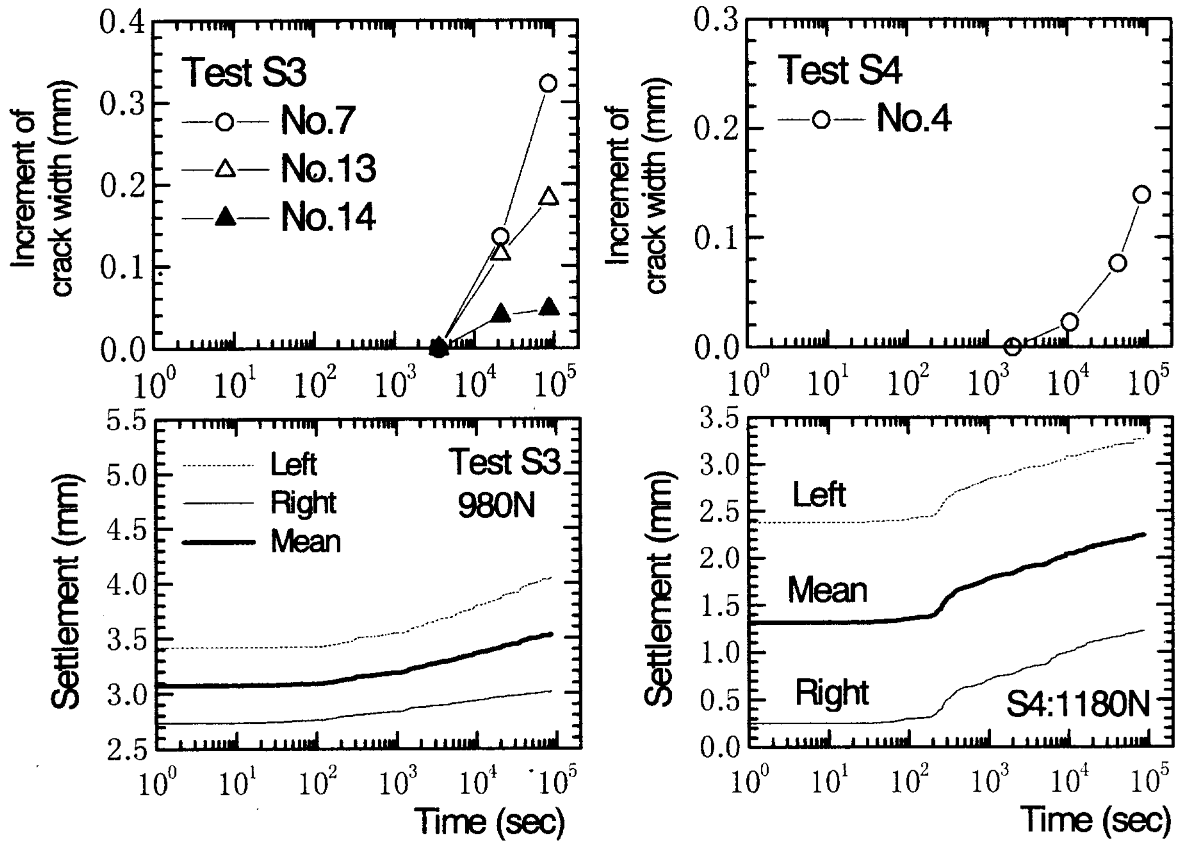


**(c) Test S3** **(d) Test S4**

**Figure 5.21 Increment of crack width**

**(4) Moving of chalk bars during sustained loading**

Here, the mechanism of time-dependent settlement of the footing will be discussed through tracing of movements of non-crushed chalk bars.

Figure 5.22 shows displacement vectors of chalk bars under the sustained load of 1180N of Test S4. This figure was made from pictures taken by the digital video camera. The coordinates of the targets drawn in each end of non-crushed chalk bars were read from pictures by a digitizer software. Each displacement vector was drawn as a straight line from the coordinate of the target of a chalk bar at a time to the coordinate of the corresponding target at the time after a time interval. Since resolution of the pictures was about 0.25mm/pixel, the displacement vectors whose length was below 0.25mm were not shown in the figure. The circles with crack sketches in the figure show crushed chalk bars. The displacement vectors for crushed chalk bars were not drawn.

The chalk bars located below the footing generally moved downward, while some chalk bars located on the surface of the ground moved upward and located in lower left and lower right of the footing moved sideward. Changes of the directions of the displacement vectors are observed around the crushed chalk bars. This fact indicates that the non-crushed chalk bars adjacent to a crushed chalk bar were moved downward by the smashing of the crushed chalk bars, or pushed to the direction of widening of the crushed chalk bars. Such a movement must have led to settlement of the footing.

The distributions of displacement vectors during rapid settlement of footing are shown in Figure 5.23. Two cases of rapid settlement are given: one is the loading stage of 780N in Test S2, the other is the loading stage of 1570N in Test S4. In the former case, the chalk bars located near the surface of ground moved upward largely. The upward movement occurred at the both side of the footing. The large upward displacement of chalk bars in the left side of the footing must have caused the rapid settlement of the left side of the footing, while the large upward displacement of chalk bars in the right side of the footing must have caused the rapid settlement of the right side of the footing (see Figure 5.6(b)). In the latter case, such large movements of chalk bars occurred only at the right side of the footing. The large movements of the chalk bars must have been corresponding to the rapid settlements of footing. It is considered that these rapid displacements of chalk bars resulted from unbalance of contact forces that was caused the progress of the crack opening.

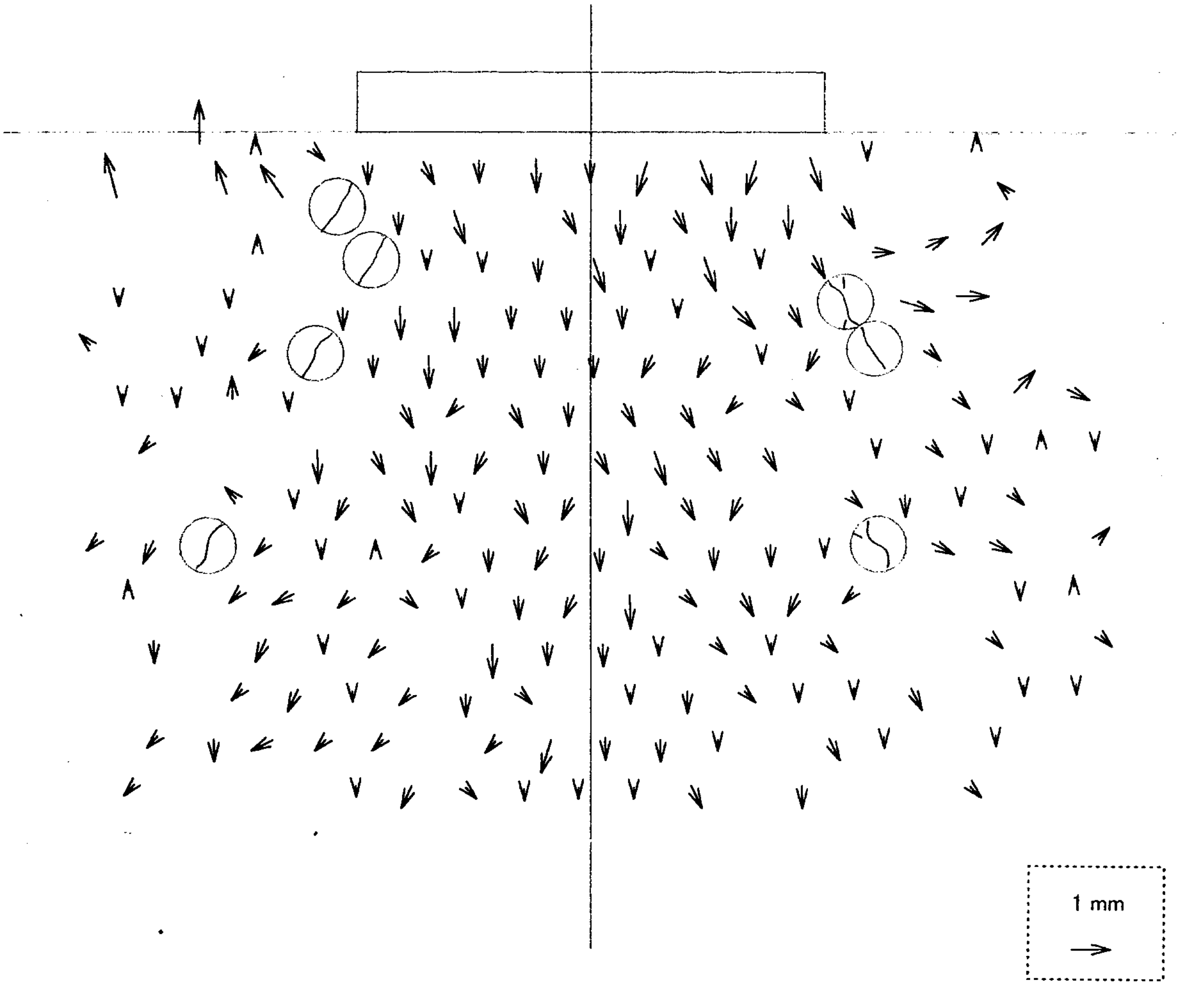


**Figure 5.22 Displacement vectors ( Test S4 : 1180N ; from the start of load sustaining to the end of the load sustaining )**

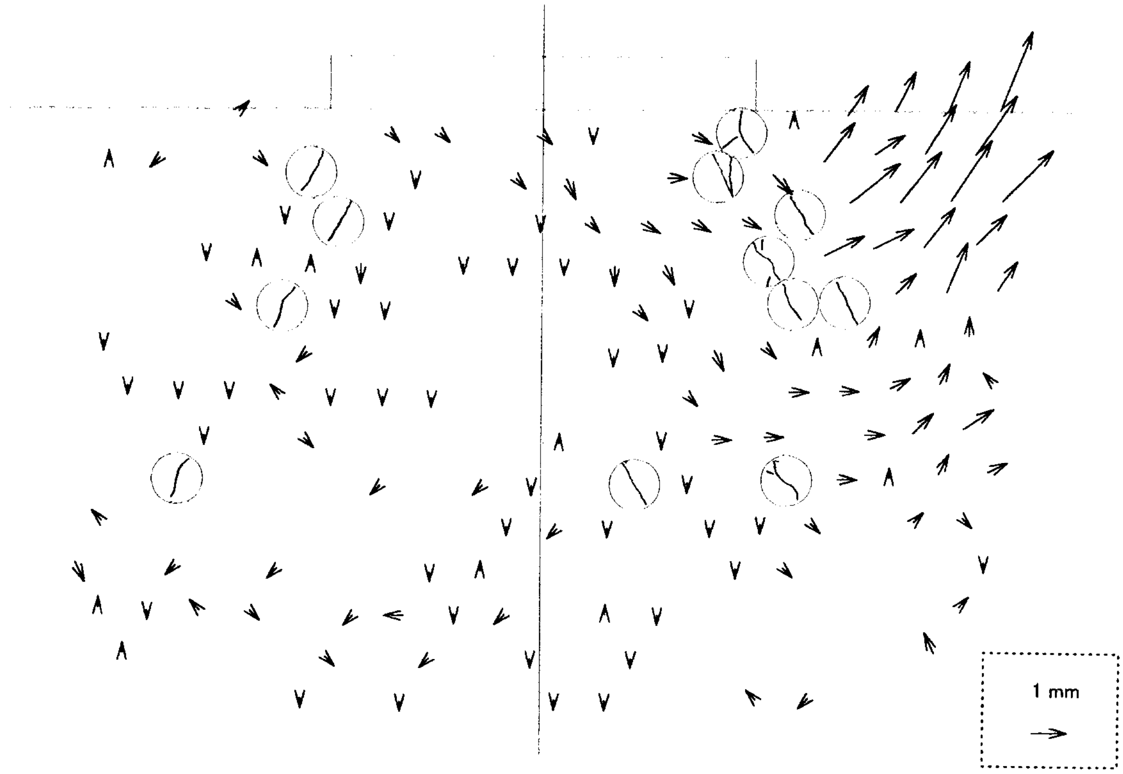


(a) Test S2 : 780N ; from the start of load sustaining to the elapsed time of 1 hour

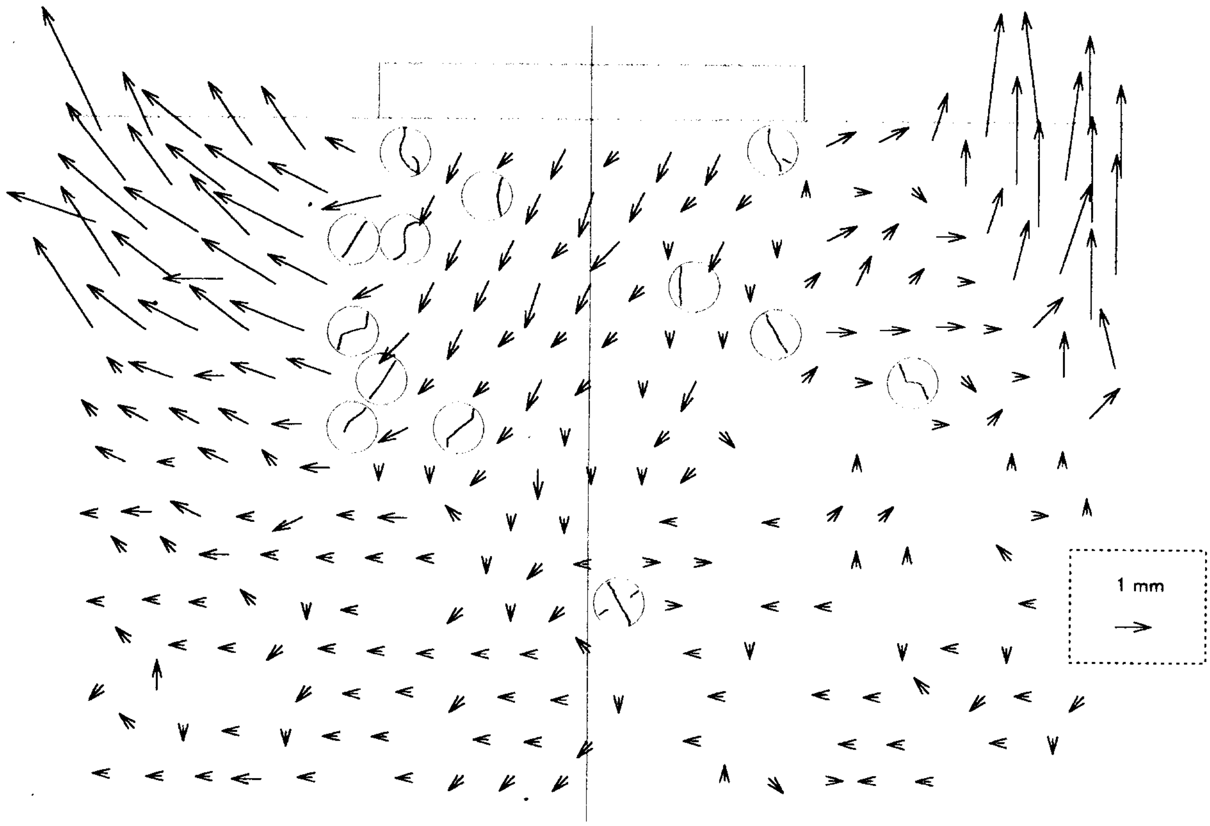


(b) Test S4 : 1570N ; from the start of load sustaining to the elapsed time of 3 hours

**Figure 5.23 Displacement vectors straddling the rapid settlement of footing**

## 5.4 Conclusions

In this Chapter, model footing loading tests were conducted on model crushable ground made of hexagonal packed chalk bars, and discussed the mechanism of the time-dependent behavior due to particle crushing. The following conclusions were drawn.

- Time-dependent settlement of footing occurred in the model footing loading tests on the model ground made of chalk bars. The settlement was proportional to the logarithm of time, in addition, sudden increase of settlement or change of the gradient of settlement – time curve also appeared.
- The cracks of crushed chalk bars were gradually opening under a sustained load. The crack opening would be caused by gradual collapsing of the angular edges formed in the chalk bars.
- The rapid settlement of the footing would be caused by the sudden displacements (rearrangements) of chalk bars that resulted from the progress of the crack openings.
- The process of crack opening is affected by position of particle, crushing mode, and distribution of contact forces around a chalk bar.

# CHAPTER 6

# MODELING OF CRUSHING PHENOMENA AND ANALYSIS BY DISTINCT ELEMENT METHOD

## 6.1 Introduction

In Chapters 4 and 5, time-dependent behavior due to particle crushing was discussed through observations of laboratory model tests with four crushable materials. In Chapter 6, the time-dependent behavior is discussed through numerical analyses. Two numerical methods are proposed for modeling of crushable particulate materials to analyze the time-dependent behavior due to particle crushing. Distinct element method (DEM) is adopted as a method of numerical analysis. The purpose of the analyses is to confirm whether these models could represent the chain events of particle crushing, subsequent rearrangement of particles and redistribution of contact stresses. The one-dimensional compression test of chalk bar specimen described in Chapter 4 is an objective for the analyses performed in this Chapter.

## 6.2 Modeling of particle crushing

In this study, the following two types of models of crushable particles are proposed : "Membrane model" and "Bonding model".

### (1) Membrane model

Figure 6.1 illustrates the membrane model. A crushable particle is modeled by a virtual aggregate of rigid particles wrapped in a membrane. Particle crushing is expressed by breaking of the membrane and followed scattering of the rigid particles. A magnitude of initial tension is introduced into the membrane. The rigid particles contact each other with a magnitude of contact force that comes from the membrane tension and the gravity. The contact forces are estimated from overlaps ("overlap" means the amount of contact deformation between two particles: refer to Figure 6.3) between particles at their contact points and contact constitutive models that provide the relationships between the contact force and the overlap.

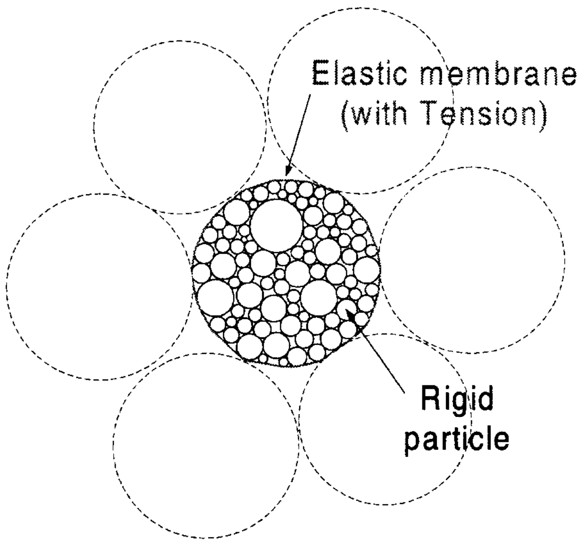


**Figure 6.1 Membrane model**

The membrane model is not discussed in this study, because the DEM calculation taking into account the model is very time-consuming.

**(2) Bonding model**

Figure 6.2 illustrates the bonding model. A crushable particle is modeled by a virtual aggregate of rigid particles bonded each other. Each bond has a certain magnitude of bonding strength. Particle crushing is expressed by breakage of the bonds. As shown in Figure 6.3, tensile or compressive forces at a bonding point are estimated from a normal force – displacement(overlap) law for the contact point, and shear forces at a contact point are also estimated from a shear force – displacement law. If the magnitude of a tensile force or a shear force exceeds the predetermined bonding strength, the bond breaks. Once breakage of bonding occurs at a bonding point, the bond does not restore. It should be mentioned here that the bonding model adopted does not include any viscous characteristics of the bonding properties.

The calculation incorporating the bonding model is also time-consuming, but the calculation rate using the bonding model is faster than that using the membrane model. The bonding model is discussed in this chapter.

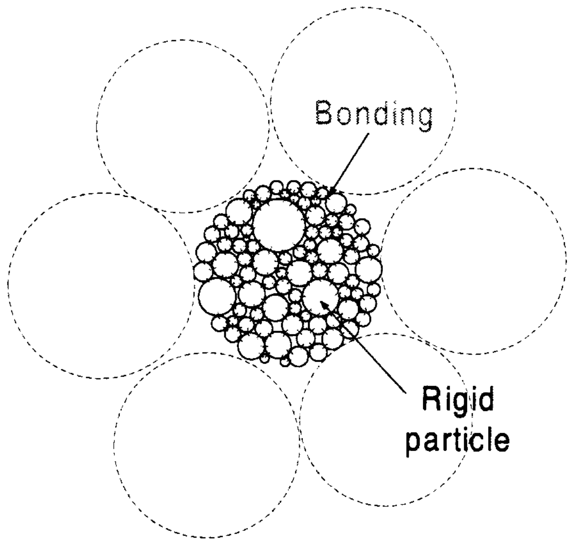


**Figure 6.2 Bonding model**

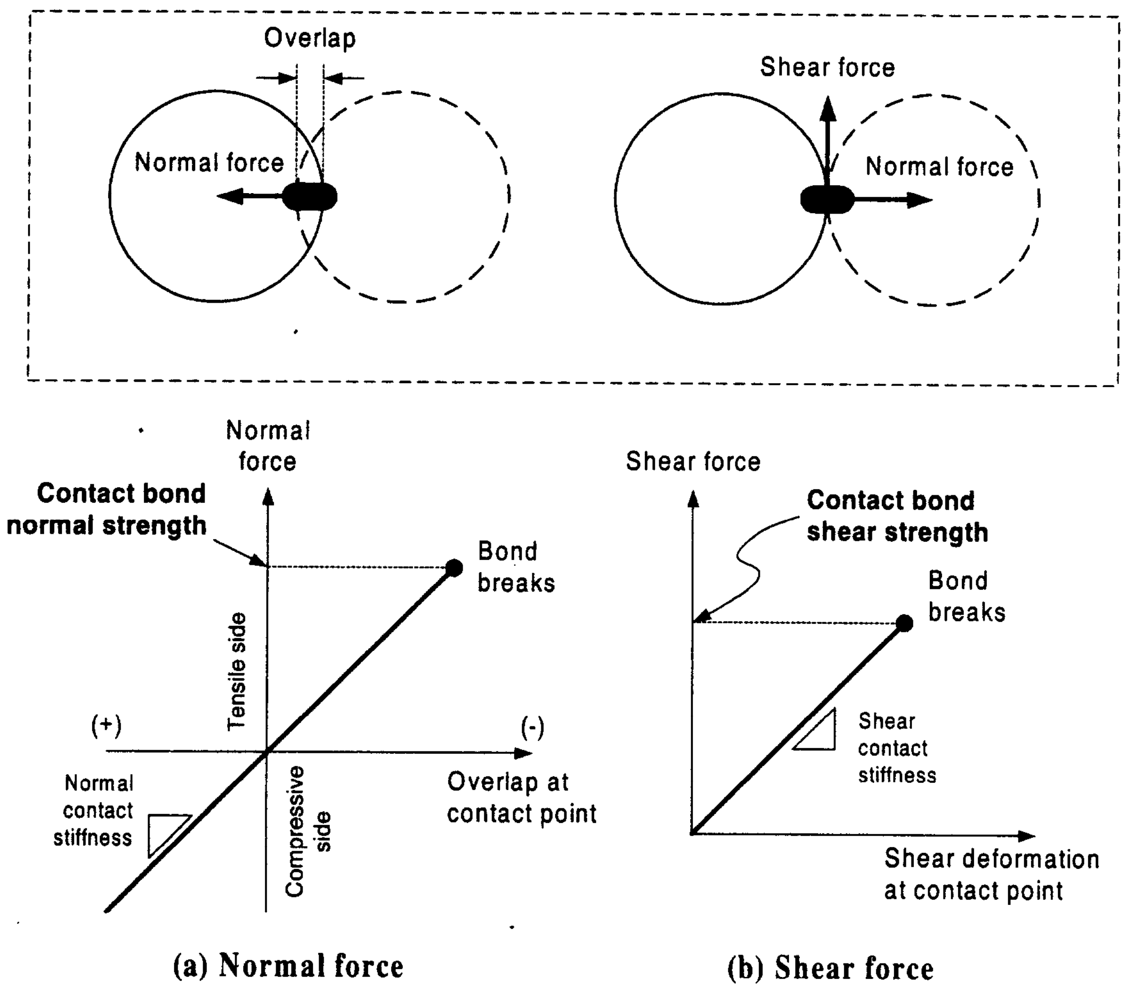


**Figure 6.3 Bond between two particles (Constitutive behavior for contact force)**

## 6.3 Analysis Method

Distinct element method (DEM) was adopted for the analyses in this Chapter. DEM can trace the movements or rotations of rigid particles. It is expected that rearrangement of particles or fragments, which is one of the events of time-dependent behavior due to particle crushing, could be represented by DEM as movements or rotations of the rigid particles.

### 6.3.1 Distinct Element Method

Distinct (or Discrete) element method was introduced by Cundall(1971) for the analysis of rock-mechanics problems and then applied to soils by Cundall and Strack(1979). In this method, an analytical objective is modeled as a crowd of distinct particles which displace independently from one another and interact only at contact points. The elements in DEM mean the distinct particles. In order to trace behavior of each element, an equation of motion is independently set up against each element divided by discontinuity planes, then each equation is solved numerically by a forward finite-difference method step by step. Consequently, the dynamic behavior of aggregate of elements was analyzed. It is assumed that the force that acts between two elements obeys the law of action and reaction. The force is transferred through contacts between elements.

DEM is, in principle, capable of handling particles of any shape (Cundall and Strack, 1979). However, in the case of circular or spherical element, it is easy to judge existence of contact points between two elements. Cundall and Strack (1979) developed a DEM program for modeling two-dimensional assemblies of circular elements (i.e. discs)

Figure 6.4 illustrates the calculation cycle of a DEM program used in this Chapter. The calculations performed in the DEM alternate between the application of Newton's second law to the discs and a force – displacement law at the contacts. Newton's second law gives the motion of a particle resulting from the forces acting on it. The force – displacement law is used to find contact forces from displacements.

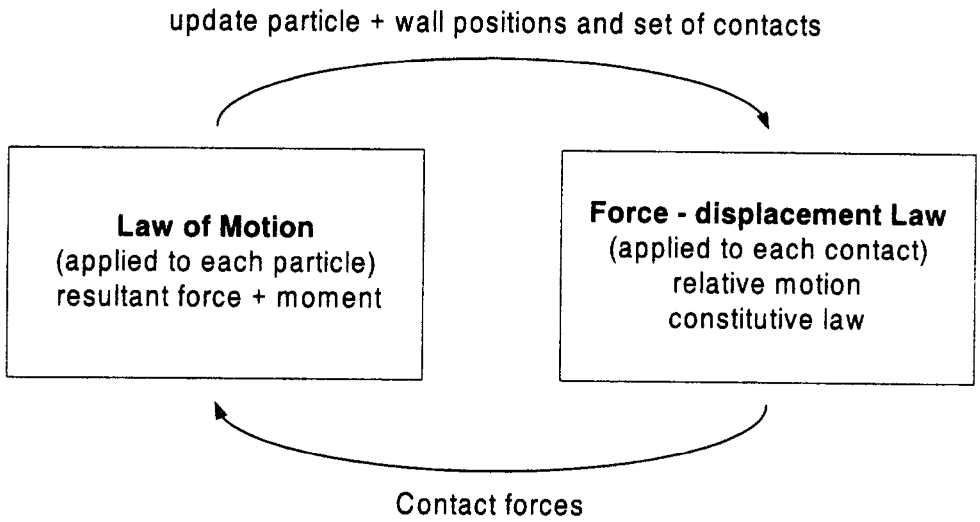


**Figure 6.4 Calculation flow of distinct element method**

### 6.3.2 DEM Code used

The two dimensional distinct element code "PFC2D(Version 2.0)" (Particle Flow Code in 2 Dimensions) package was used for analysis. This program package, developed by Itasca Consulting Group, Inc., USA, has been widely used.

The code PFC2D provides a particle-flow model containing the following assumptions (Itasca Consulting Group, Inc., 1999).

1. The particles are treated as rigid bodies.
2. The contacts occur a vanishingly small area (i.e. at a point).
3. Behavior at the contacts uses a soft-contact approach wherein the rigid particles are allowed to overlap one another at contact points.
4. The magnitude of the overlap is related to the contact force by means of the force – displacement law, and all overlaps are small in relation to particle size.
5. Bonds can exist at contacts between particles.
6. All particles are circular.

The main features of this code are as follows :

- This program allows particles to be bonded together at contacts. There are two forms of bonding at contacts ; bonds have finite strength in tension and shear.
- The linear contact model and the Heltz-Mindlin contact model can be used. Frictional sliding in both models can also be set.
- Built-in programming language to add user-defined features are mounted (e.g., model

generation and control, new variables, special boundary conditions).

- Every particle and contact may be assigned different properties, which may be changed at any time.
- Particles may be controlled : forces or velocities may be prescribed.

### 6.3.3 General formulation of DEM(PFC2D)

In this Subsection, general formulation of DEM(PFC2D) is presented briefly (Itasca Consulting Group, Inc., 1999).

#### (1) Law of motion

All points in a PFC2D model are described by $x_i$, where the index $i$ is in the set $\{1,2\}$. The plane of the model corresponds to the 1 and 2 directions. Moments and rotatonal velocities act only in the out-of-plane direction and are thus denoted $M_3$ and $\omega_3$ respectively. The translational motion of the center of mass is described in terms of its position $x_i$, velocity $\dot{x}_i$ and acceleration $\ddot{x}_i$ ; the rotational motion of the particle is described in terms of its angular velocity $\omega_i$ and angular acceleration $\dot{\omega}_i$.

The equation of motion of a single rigid particle can be expressed as two vector equations, one of which relates the resultant force to the translational motion and the other of which relates the resultant moment to the rotational motion.

$$F_i = m(\ddot{x}_i - g_i) \tag{6.1}$$

$$M_3 = I\dot{\omega}_3 \tag{6.2}$$

where $F_i$ is a resultant force, the sum of all externally applied forces acting on the particle, $m$ is the total mass of the particle, $g_i$ is the body force acceleration vector, $M_3$ is a component of the resultant moment, $I$ is a principal moment of inertia of the particle, and $\dot{\omega}_3$ is an angular acceleration about the principal axis.

The accelerations are calculated in terms of the velocity values at mid interval as

$$\ddot{x}_i(t) = \frac{\dot{x}_i(t + \Delta t/2) - \dot{x}_i(t - \Delta t/2)}{\Delta t} \tag{6.3}$$

$$\dot{\omega}_3(t) = \frac{\omega_3(t+\Delta t/2) - \omega_3(t-\Delta t/2)}{\Delta t}, \tag{6.4}$$

where $t$ is time and $\Delta t$ is time interval used for numerical calculation. Substituting these expressions into Equations(6.1)(6.2) and solving for the velocities at time $(t+\Delta t/2)$ result in

$$\dot{x}_i(t+\frac{\Delta t}{2}) = \dot{x}_i(t-\frac{\Delta t}{2}) + (\frac{F_i(t)}{m} + g_i)\Delta t \tag{6.5}$$

$$\omega_3(t+\frac{\Delta t}{2}) = \omega_3(t-\frac{\Delta t}{2}) + (\frac{M_3(t)}{I})\Delta t. \tag{6.6}$$

Finally, the position of the particle center is calculated as

$$x_i(t+\Delta t) = x_i(t) + \dot{x}_i(t+\Delta t/2)\Delta t. \tag{6.7}$$

**(2) Force – displacement law**

$F_i$ and $M_3$ at time $t$ are obtained from the positions of particles ($x_i(t)$) and force – displacement laws at contact points. Figure 6.5 illustrates the notation used to explanation.

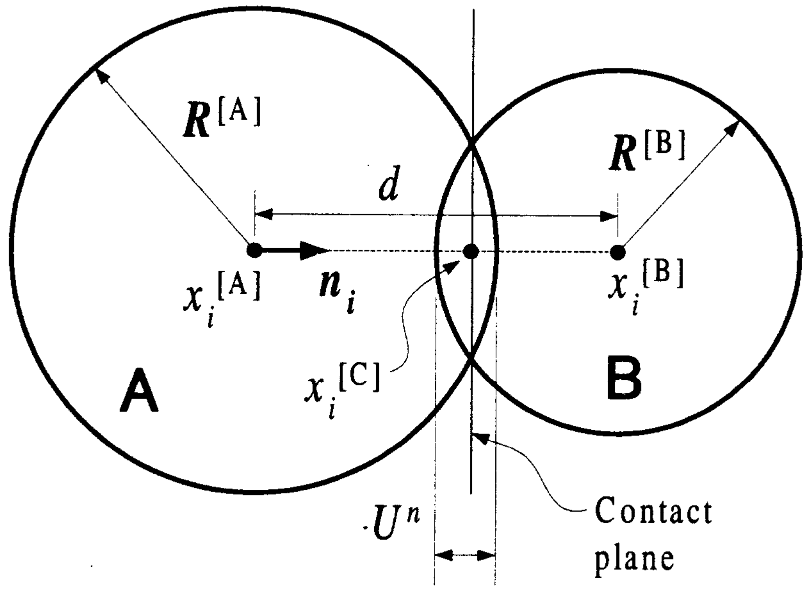


**Figure 6.5 Notation used to describe particle – particle (disc – disc ) contact**

For a contact point between two particles, the unit normal vector $n_i$ that defines the contact plane is given by

$$n_i = \frac{x_i^{[B]} - x_i^{[A]}}{d} \tag{6.8}$$

where $x_i^{[A]}$ and $x_i^{[B]}$ are the position vectors of the centers of balls A and B, and $d$ is the distance between the ball centers :

$$d = \left| x_i^{[B]} - x_i^{[A]} \right| \tag{6.9}$$

The overlap $U^n$, defined to be the relative contact displacement in the normal direction, is given by

$$U^n = R^{[A]} + R^{[B]} - d \tag{6.10}$$

where $R^{[\Phi]}$ is the radius of particle $\Phi$.

The location of the contact point is given by

$$x_i^{[C]} = x_i^{[A]} + \left( R^{[A]} - \frac{1}{2} U^n \right) n_i . \tag{6.11}$$

The contact force vector $F_i$ (which represents the action of particle A on particle B for the contact) can be resolved into normal and shear components with respect to the contact plane as

$$F_i = F_i^n + F_i^s \tag{6.12}$$

where $F_i^n$ and $F_i^s$ denote the normal and shear component vectors, respectively.

The normal contact force vector is calculated by

$$F_i^n = K^n U^n n_i \tag{6.13}$$

where $K^n$ is the normal stiffness [force/displacement] at the contact. The value of $K^n$ is determined by the linear contact model.

The shear contact force is computed in an incremental fashion. The relative motion at the contact, or the contact velocity $V_i$ (which is defined as the velocity of particle B relative to particle A at the contact point) is given by

$$\begin{aligned} V_i &= \left(\dot{x}_i^{[C]}\right)_B - \left(\dot{x}_i^{[C]}\right)_A \\ &= \left(\dot{x}_i^{[B]} + e_{i3k}\,\omega_3^{[B]}\left(x_k^{[C]} - x_k^{[B]}\right)\right) - \left(\dot{x}_i^{[A]} + e_{i3k}\,\omega_3^{[A]}\left(x_k^{[C]} - x_k^{[A]}\right)\right) \end{aligned} \tag{6.14}$$

where $\dot{x}_i^{[\Phi]}$ and $\omega_3^{[\Phi]}$ are the translational and rotational velocity, respectively, of particle $\Phi$. $e_{i3k}$ is the permutation symbol.

$$e_{ijk} = \begin{cases} 0, & \text{if 2 indices coincide;} \\ +1, & \text{if i, j, k permute like 1,2,3;} \\ -1 & \text{otherwise} \end{cases} \tag{6.15}$$

The contact velocity can be resolved into normal and shear components with respect to the contact plane. Denoting these components by $V_i^n$ and $V_i^s$ for the normal and shear components, respectively, the shear component of the contact velocity can be written as

$$V_i^s = V_i - V_i^n \tag{6.16}$$

The shear component of the contact displacement-increment vector occurring over a time step of $\Delta t$ is calculated by

$$\Delta U_i^s = V_i^s \Delta t \tag{6.17}$$

and is used to calculate the shear elastic force-increment vector

$$\Delta F_i^s = -k^s \Delta U_i^s \tag{6.18}$$

where $k^s$ is the shear stiffness [force/displacement] at the contact. The value of $k^s$ is determined by the linear contact model (The force – displacement law shown in Figure 6.2).

The new shear contact force is found by summing the old shear force vector existing at the start of the timestep with the shear elastic force-increment vector

$$F_i^s \leftarrow F_i^s + \Delta F_i^s \tag{6.19}$$

The value of normal and shear contact forces determined by Equ.(6.13) and (6.18) are adjusted to satisfy contact constitutive relations. ( For example, if $F_i^s$ exceed a value of $F_{\max}^s$ that is determined from the friction coefficient set on the contact point and $F_i^n$, a slip occur and the value of $F_i^s$ is reduced to $F_{\max}^s$. ) After this adjustment, the contribution of the final contact force to the resultant force and moment on the two particles in contact is given by

$$\begin{aligned}
&F_i^{[A]} \leftarrow F_i^{[A]} - F_i \\
&F_i^{[B]} \leftarrow F_i^{[B]} + F_i \\
&M_3^{[A]} \leftarrow M_3^{[A]} - e_{3jk}\left(x_j^{[C]} - x_j^{[A]}\right)F_k \\
&M_3^{[B]} \leftarrow M_3^{[B]} - e_{3jk}\left(x_j^{[C]} - x_j^{[B]}\right)F_k .
\end{aligned} \tag{6.20}$$

**(3) Local non-viscous damping in PFC2D**

DEM is one of the dynamic analysis methods. But DEM is used for static analysis. For example, it is necessary to obtain a stable condition of an analytical model under a sustained load by the static analysis: the stable condition is used as an initial condition for the following dynamic analysis. In the static analysis, a term of damping-force proportional to the velocity or acceleration of a particle is added to the equations of motion for convergence of calculations. A damping constant, that is a constant of proportionality between the damping-force and the velocity or acceleration of a particle, is set for static analyses. The damping constant is not a parameter related to geomaterials, but a tool for convergence of calculations (Uno et al., 1999). In the analysis that an excessive value is set for the damping constant, a solution after convergence makes sense, while solutions before convergence do not make sense.

Cundall and Strack(1979) introduced two types of viscous damping into their DEM program : contact damping and global damping. The contact damping operates on the relative velocities at the contacts. The global damping operates on the absolute velocities of the particles and is introduced in the calculations of motion as follows : $F_i - C\dot{x}_i = m(\ddot{x}_i - g_i)$, $M_3 - C^*\omega_3 = I\omega_3$, where $C$ and $C^*$ are the coefficients of global damping operating. Cundall and Strack(1979) mentioned that the use of damping other than by friction is necessary in order that the assemblies (i.e. particles or discs) reach a state of equilibrium for all conditions.

In PFC2D, a damping which is called "local non-viscous damping" has been introduced in order that the analytical model reaches a state of equilibrium. The equations of motion incorporating the local non-viscous damping can be written as follows :

$$F_i + F_i^d = m(\ddot{x}_i - g_i) \qquad (6.21)$$

$$F_i^d = -\alpha|F_i|sign(\dot{x}_i)$$

$$M_3 + M_3^d = I\dot{\omega}_3 \qquad (6.22)$$

$$M_3^d = -\alpha|M_3|sign(\omega_3)$$

$$sign(y) = \begin{cases} +1, & \text{if } y > 0 \ ; \\ -1, & \text{if } y < 0 \ ; \\ 0 & \text{if } y = 0 \ . \end{cases}$$

The developer of PFC2D comments from his experience that $\alpha = 0.7$ makes an analytical model reach a state of equilibrium rapidly (Itasca Consulting Group Inc., 1999). But for particles in free flight under gravity, the local non-viscous damping is obviously inappropriate.

In this chapter, the static analysis by DEM will be used to obtain a certain initial condition for the following dynamic analysis. The static analysis will lead the analytical model to a certain stable condition.

### 6.3.4 Objective of analysis

One-dimensional compression test of the chalk bar specimen described in Chapter 4 was chosen as the objective of analysis. The simple cubic packing case (corresponding to Case C1 to C4 in Chapter 4) was selected. The reasons why the test was chosen are as follows ;

1) the chalk bar specimen and the talc bar specimen of the test was two-dimensional specimen, and
2) the mass of a chalk bar was larger than the mass of a talc bar, that is to say, the mass of a rigid particle for the model of chalk bar was larger than the mass for the model of talc bar if a bar was divided into the same numbers of rigid particles. In PFC2D, the time interval $\Delta t$ is determined automatically from the minimum eigenperiod of the analytical model, that is to say, $\Delta t$ is proportional to square root of the mass of a rigid particle. The DEM analysis taking into account the bonding model is time-consuming because the mass of a rigid particle is very small. Thus the larger mass of a rigid particle is of advantage to the $\Delta t$ of DEM.

### 6.3.5 Analytical flow

Figure 6.6 shows the analytical flow in this chapter. Before the analysis of the one-dimensional compression test, the single particle crushing test of chalk bar described in Chapter 3 was also analyzed.

**(1) Analyses of single particle crushing test**

The analyses of single particle crushing test were performed to determine the following parameters of the bonding model : normal bonding strength, shear bonding strength, normal contact stiffness and shear contact stiffness. The analyses are performed iteratively until the analytical force – displacement curve is comparable with the curve obtained from the experiments. The parameters adopted for the comparable analysis are employed for the following analyses of one-dimensional compression test.

**(2) Analyses of one-dimensional compression test**

The analyses of one-dimensional compression test were performed using the values of the parameters determined from the iterative analyses of single particle crushing test. As shown later, the analytical model for one-dimensional compression test was made by packing the single particle models in cubic. Variations in the parameters were taken into account. Normal distributions were assumed for variations of parameters. The mean value of each parameter was the value determined from the analyses of the single particle crushing test.

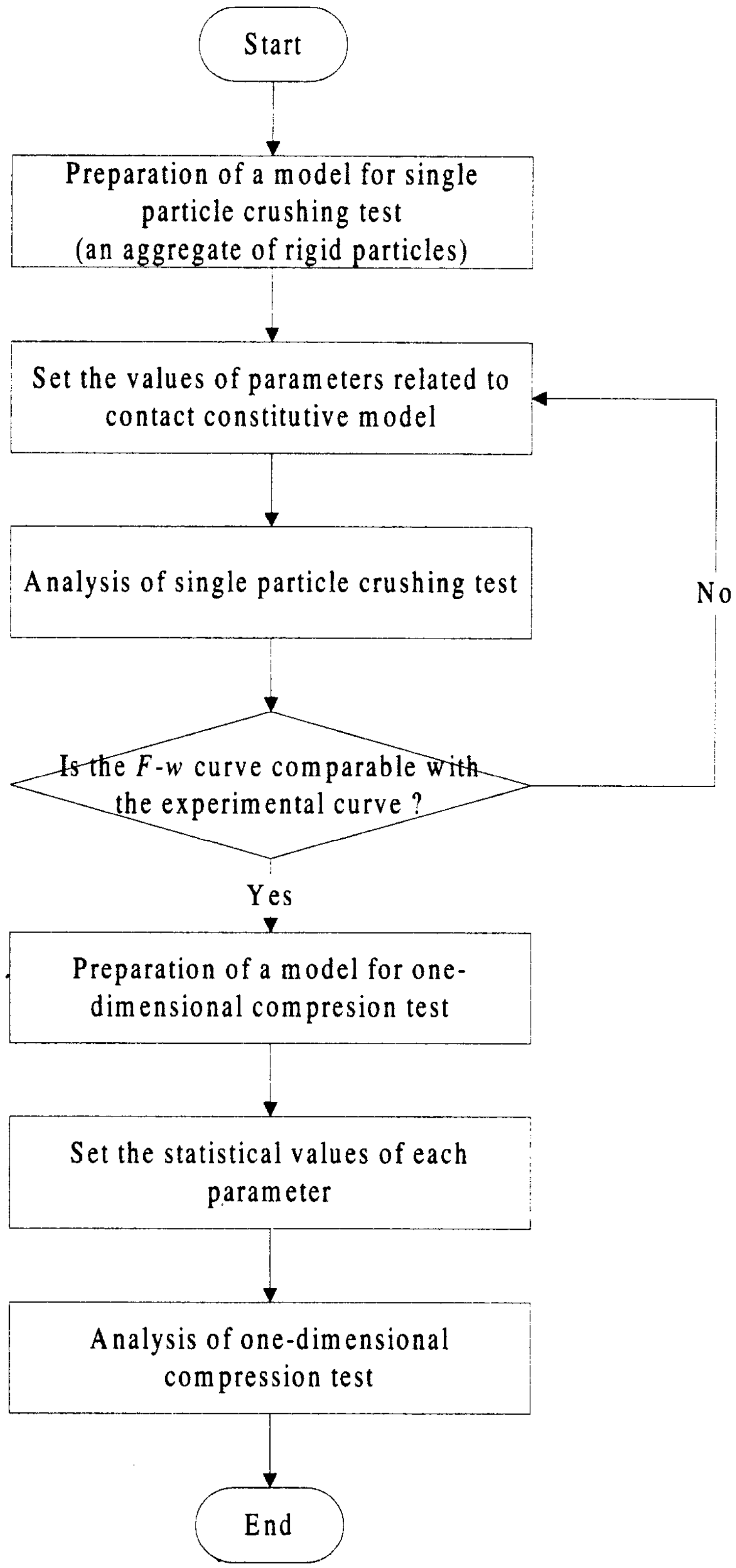


**Figure 6.6 Analytical flow**

## 6.4 Analyses of single particle crushing test

### 6.4.1 Analytical model and parameters required for analyses

The analytical model for single particle crushing test (hereafter referred to as a "(virtual) aggregate of rigid particles(or discs)" or simply as an "aggregate") is illustrated in Figure 6.7. The analytical conditions and parameters used in the analysis are summarized in Table 6.1. In DEM, packing of rigid particles is generally one of the important problems. But in the analyses of this study, for simplicity, the analytical model for single particle crushing test was made from 55 rigid particles (discs) that have the same diameter and were packed hexagonally in circular configuration. The dimension of each rigid particle is 0.6mm radius and 30mm length. The number of rigid particles of 55 was determined from the following reasons. The width of an aggregate of particles was 9.6mm, and the height of the aggregate was 9.514mm.

- If the number of particles is too large, the mass of a rigid particle becomes too small. As a result, the analysis needs a long period of time since $\Delta t$ becomes too small.
- If the number of particles is too small, the configuration of an aggregate of the rigid discs is far from a round shape, and it becomes difficult to distinguish the crushing mode (i.e. the shape of crack ; if a row of broken contact points appears in the aggregate, it is regarded as a crack).

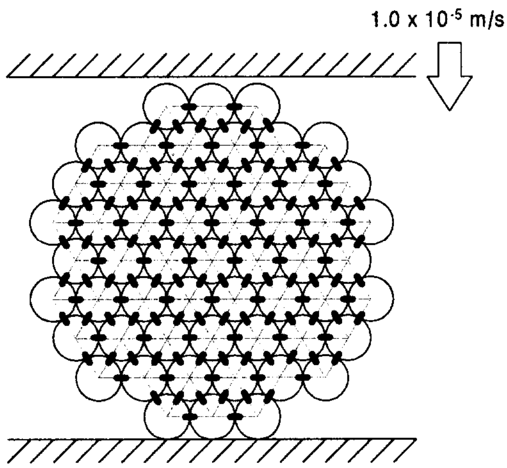


**Figure 6.7 Analytical model for single particle crushing test (An aggregate of rigid discs)**

**Table 6.1 Parameters for analysis of single particle crushing test**

| | | Value of parameter | Basis |
|---|---|---|---|
| Rigid constituent particle (disc) | Radius | 0.6 mm | assumed |
| | Length | 30 mm | experiment |
| | Density | 1640kg/m$^3$ | experiment |
| | Friction coefficient | 0.5 | assumed |
| | Normal stiffness $K^n$ (for linear contact model) | 6 x $10^6$ N/m | result of iterative analyses |
| | Shear stiffness $k^s$ (for linear contact model) | 6 x $10^6$ N/m | result of iterative analyses |
| | Contact bond normal strength $F_c^n$ | 25 N | result of iterative analyses |
| | Contact bond shear strength $F_c^s$ | 25 N | result of iterative analyses |
| Single particle (Aggregate of rigid constituent particles) | The number of particle | 55 | assumed |
| | Width of aggregate | 9.6 mm | experiment |
| | Height of aggregate | 9.514 mm | experiment |
| Loading plates ( Rigid wall ) | Normal stiffness (for linear contact model) | 1.0 x $10^8$ N/m | assumed |
| | Shear stiffness (for linear contact model) | 1.0 x $10^8$ N/m | assumed |
| | Friction coefficient | 0.5 | assumed |
| | Loading velocity | 1.0 x $10^{-5}$ m/s | experiment |
| Gravitational acceleration | | 9.81 m/s$^2$ | experiment |

Note) assumed : assumed value
experiment : determined from the single particle crushing test
result of iterative analyses : determined by iterative analyses

The normal bonding and shear bonding were introduced at each contact point. The linear contact model, that was shown in Figure 6.3, was adopted as the contact constitutive law. The value of the density of rigid disc is the same as the density of chalk bar (1640kg/m$^3$ : see Table 3.1). The value of frictional coefficient between the rigid discs is assumed as $\mu$=0.5. This value is based on the representative value of the angle of internal friction $\phi$=27.5° for dry, round and uniform sand (Terzaghi and Peck (1960); $\mu$ = tan $\phi$ = tan 27.5°=0.52≈0.5).

Two rigid walls are set for loading plates. The loading velocity of the upper wall is equal to the one in the single particle crushing tests described in Chapter 3 (0.625mm/minutes =1.0 x $10^{-5}$ m/s). Excessive values are assumed for the values of normal stiffness and shear stiffness of loading plates. These values are sufficiently larger than the normal stiffness and shear stiffness of the contact constitutive model for rigid particles. The value of frictional coefficient between the rigid disc and the rigid wall is assumed as 0.5. This value is the same as the value of the frictional coefficient between two rigid discs. As discussed in Chapter 3, this value would affect the result of the analysis. But in this study, the effect of friction of loading plates does not discuss analytically.

The analyses of single particle crushing tests were performed until the comparable $F - w$ curve with the experiments was found, changing the four parameters related to the contact constitutive model and bonding (i.e. normal stiffness, shear stiffness, normal strength and shear strength). The derived values of the parameters are also summarized in Table 6.1. It is assumed for simplicity that the value of shear stiffness($k^s$) is the same as the value of normal stiffness($K^n$) and that the value of shear strength($F_c^s$) is the same as the value of normal strength($F_c^n$).

From the result of computing, the information about $\Delta t$ and the time required for calculation was summarized as follows:

$\Delta t = 9.916 \times 10^{-7}$ sec

The number of timestep to obtain a $F - w$ curve : 14,000,000 steps,

Time required for calculation : 22 hours per 14,000,000steps,

CPU of the computer used : Intel, 433MHz, Celeron.

### 6.4.2 Results of analyses

The force – displacement curve obtained from the iterative analyses is compared with examples of the experimental curves in Figure 6.8. The calculated force, shown in Figure 6.8(a), increases linearly with the displacement, and indicates the peak value. After the peak force, the force drastically drops to zero. While the experimental force, shown in Figure 6.8(b), increases exponentially with the displacement, and reaches the peak value. After the peak, the force decreases to about 70% of the peak value, then continues to increase again. This increment of force after the peak was caused by the continuing support of two half-moon shaped fragments after crushed. The overall shape of the calculated curve is different from the experimental curve, particularly after the peak force. In order to select an appropriate set of parameters, the initial gradient and the maximum peak force of the calculated $F - w$ curve were matched with the experimental curves by changing the normal(shear) stiffness of rigid particles from $3.0 \times 10^6$ N/m to $6.0 \times 10^6$ N/m and the normal(shear) contact bond strength from 20N to 30N. Consequently, the combination of the value of $6.0 \times 10^6$ N/m for normal(shear) stiffness and the value of 25N for the normal(shear) contact bond strength obtained the comparable curve as shown in Figure 6.6(a).

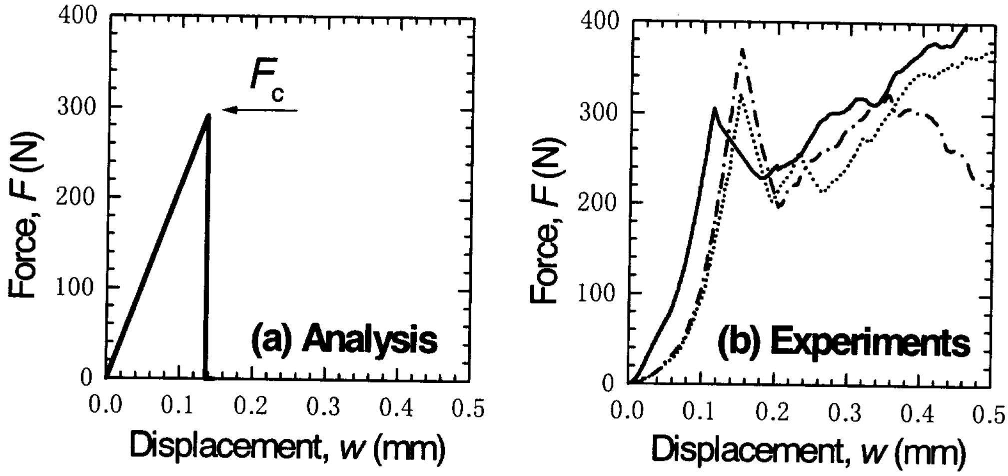


**Figure 6.8 Force – displacement curves**

The deformation of the single particle model is shown in Figure 6.9. Before the time of the peak force, the model compressed vertically without breakage of bonding points : the force were supported by linear deformation at the contact points(Figure 6.9(a)(b)). At the peak force, the model broke suddenly in four pieces(Figure 6.9(c)), then the two pieces in left side and right side flew out(Figure 6.9(d)). Thus it is clear that these four pieces could not support the load after the breakage.

Figure 6.10 shows the distribution of micro-cracks at the peak load. The breakages (micro-cracks) of normal bonds and shear bonds shown in the figure occurred almost simultaneously at the time of the peak force. Those micro-cracks appear to form a splitting crack. It is considered that more real splitting crack could be reproduced by the model made of smaller rigid particles or random-packed rigid particles.

From the analyses, it is revealed that the bonding model could reproduce the crushing mode (that is to say, splitting crushing) of a chalk bar or a talc bar under single particle crushing test. However, it is also revealed that the model could not reproduce the supporting behavior of load after splitting.

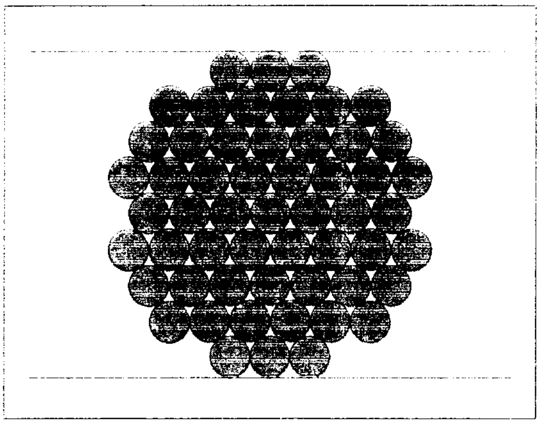

(a) 13850000step : 0.13617mm

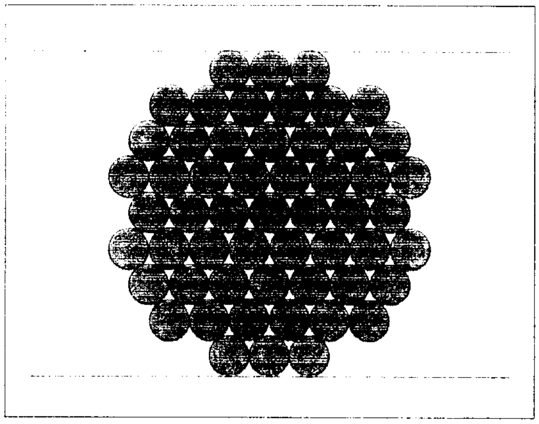

(b) 13851000step : 0.13618mm

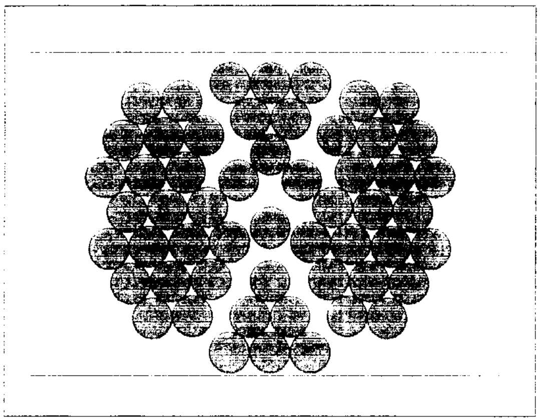

(c) 13852000step : 0.13619mm

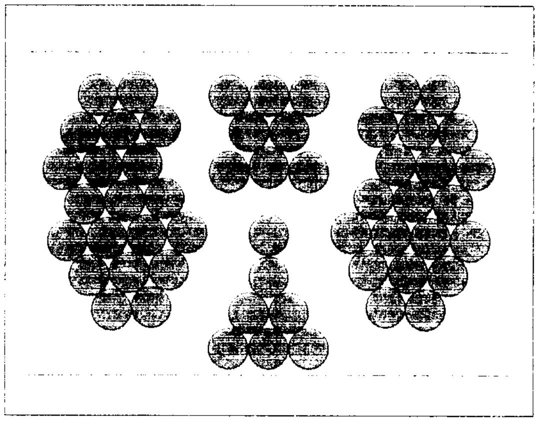

(d) 13853000step : 0.13620mm

**Figure 6.9 States of the single particle model during analysis**

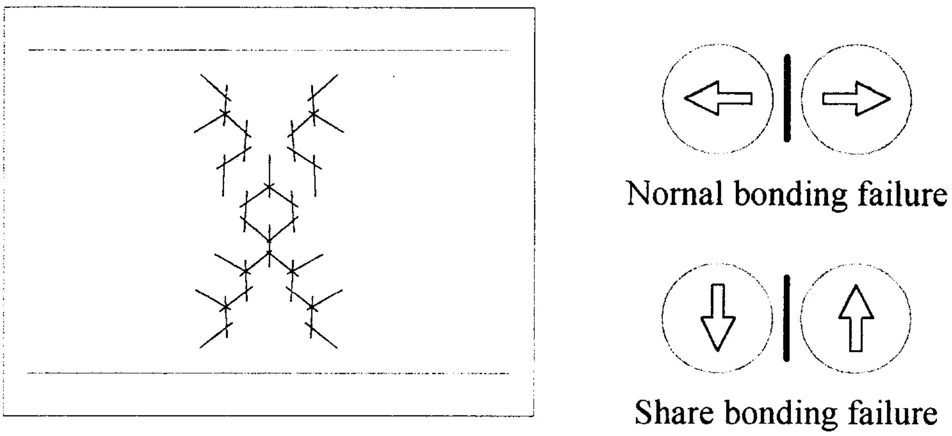


13851800step : 0.13619mm

**Figure 6.10 Distribution of micro-cracks**

## 6.5 Analyses of one-dimensional compression test

### 6.5.1 Analytical method

The analytical model is shown in Figure 6.11. The model is made of 100 aggregates of rigid particles cubical-packed in 10 rows and 10 columns. There exists no bonding between the neighboring aggregates. The model is surrounded with three rigid walls except the upper side. There exists a loading plate in the upper side of the model. The loading plate is made of 137 rigid particles clumped in line, and behaves as a rigid body.

In the analyses, the variations of the parameters that are related to the contact constitutive law were taken into account. Figure 6.12 shows the values of the parameters for each aggregate of rigid particles. Figure 6.13 presents the frequency distribution of the parameters. It was assumed that the contact stiffness($K$=$K^n$=$k^s$) and the bonding strength($F_c$=$F_c^{\,n}$=$F_c^{\,s}$) follow the standard normal distribution. The standard deviation of each parameter were set from the data of the single particle crushing tests of chalk bars. The coefficient of variation (COV) of the bonding strength($F_c$) was set at the COV of the crushing strength of the chalk bars. The COV of the contact stiffness($K$) was set at the COV of the characteristic initial stiffness obtained from the single particle crushing tests of chalk bar. The mean value of bonding strength $m(F_c)$ was set at the $F_c$ determined from the analyses of single particle crushing test. The mean value of the contact stiffness $m(K)$ was established at the $K$ determined from the analyses of the single particle crushing test. To obtain the practical values of each parameter, pseudo random numbers that followed the standard normal distribution were generated by a personal computer, and were employed for the parameters.

Other parameters used in the analyses are summarized in Table 6.2. The loading plate is constrained from movement in the horizontal direction and from rotation.

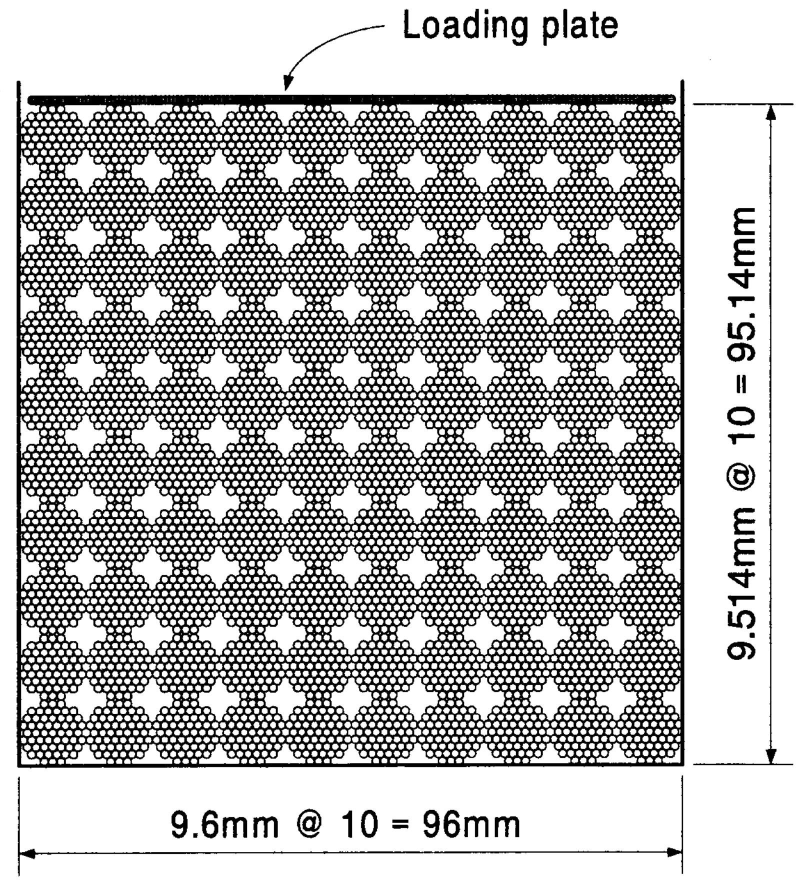


**Figure 6.11 Analytical model for one-dimensional compression test**

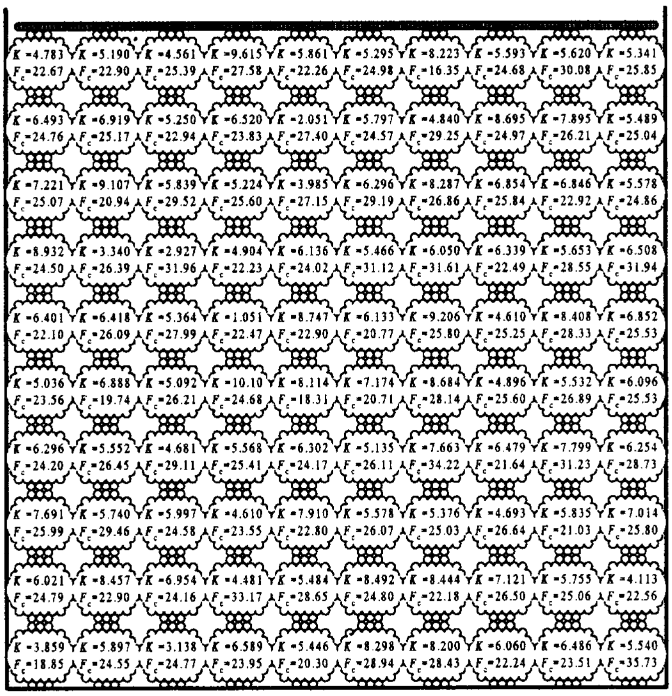

$K = K^n = k^s$ ($10^6$ N/m)
$K^n$ : Normal stiffness
$k^s$ : Shear stiffness

$F_c = F_c^n = F_c^s$ (N)
$F_c^n$ : Normal bonding strength
$F_c^s$ : Shear bonding strength

$m(K)$=6.0x$10^6$ (N/m)
$m(F_c)$=25 N
$m(K)$ : Mean value of $K$
$m(F_c)$ : Mean value of $F_c$

**Figure 6.12 Analytical model for one-dimensional compression test**

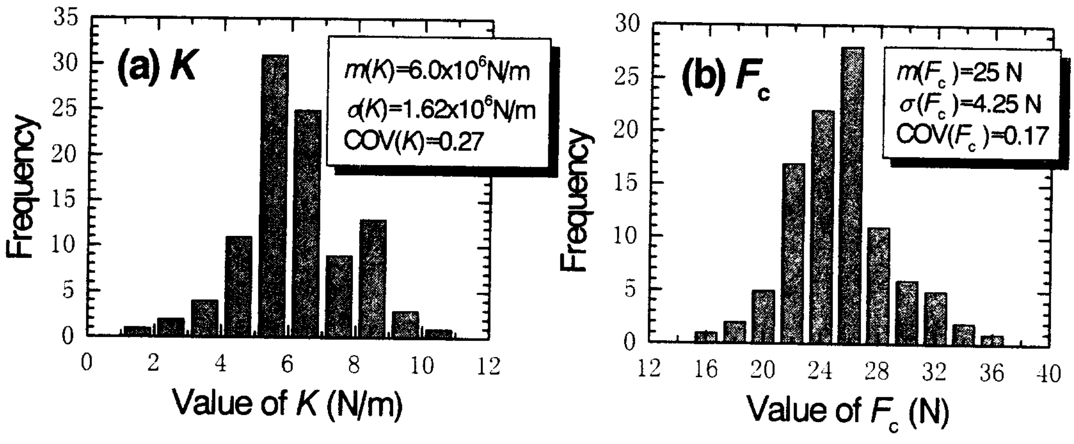


**Figure 6.13 Frequency distributions of parameter $K$ and $F_c$**

**Table 6.2 Parameters for analyses of one-dimensional compression test**

| | | Value of parameter | Basis |
|---|---|---|---|
| Rigid particles (discs) | Radius | 0.6 mm | assumed |
| | Length | 30 mm | experiment |
| | Density | 1630kg/m$^3$ | experiment |
| | Friction coefficient | 0.5 | assumed |
| | Normal stiffness $K^n$ Shear stiffness $k^s$ (for linear contact model) | Refer to Figure 6.12 - 13 | Result of analyses |
| | · Contact bond Normal strength $F_c^n$ Shear strength $F_c^s$ | Refer to Figure 6.12 - 13 | Result of analyses |
| Single particle (Aggregate of rigid discs) | The number of particles | 55 | assumed |
| | Width of aggregate | 9.6 mm | experiment |
| | Height of aggregate | 9.514 mm | experiment |
| Rigid walls | Normal & shear stiffness | 1.0 x 10$^8$ N/m | assumed |
| | Friction coefficient | 0.0 | assumed |
| Loading plate (A series of clumped discs) | The number of particles | 137 | assumed |
| | Radius of each disc | 0.6 mm | assumed |
| | Length of each disc | 30 mm | experiment |
| | Density of each disc | 1630 kg/m$^3$ | assumed |
| | Normal & shear stiffness | 1.0 x 10$^8$ N/m | assumed |
| Gravitational acceleration | | 9.81 m/s$^2$ | experiment |

Note) assumed : assumed value
experiment : determined from the single particle crushing test
result of analyses : determined by analyses of single particle crushing test

Figure 6.14 shows the loading history of the analyses. A constant load of 2354N(240kgf) was applied to the model continuously throughout the process of an analysis. This load corresponds to $0.8 MN/m^2$. During the first 5000 time steps, an excessive bonding strength of 100N and the maximum contact stiffness ($K(\max) = 1.05 \times 10^7$ N/m) were set to all bonding points. The calculation of first 5000 steps was performed in order to stabilize the analytical model under the constant load. The local non-viscous damping was set to 0.7 during the first 5000 steps for the purpose of leading the model to convergence. At the time step of 5001, bonding strength($F_c$) and contact stiffness($K$) of each aggregate were simultaneously decreased to the values shown in Figure 6.12. The calculation after the time step of 5001 was conducted in order to observe the time-dependent behavior of the model. The local non-viscous damping was changed to zero at the time step of 5001, that is to say, the analysis after the time step of 5001 was a dynamic analysis. The reason why the local non-viscous damping was set to zero is to remove any viscous characteristics from the analytical model.

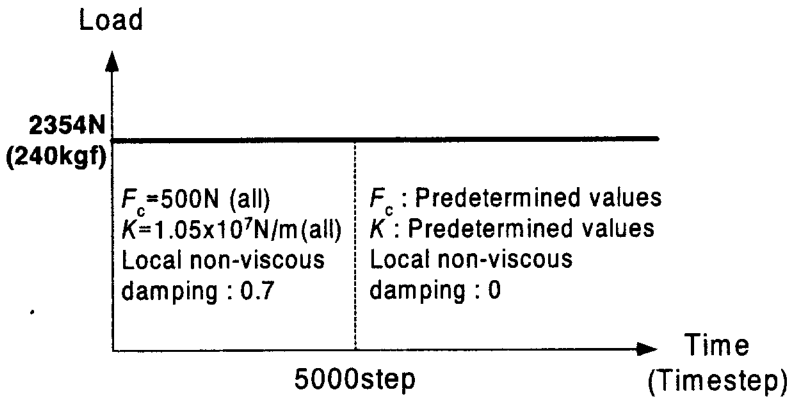


**Figure 6.14 Loading history of the analyses**

The performed analyses are summarized in Table 6.3. Two cases of analysis were performed. Case a1 is the analysis performed according to the above-mentioned method. The analysis Case a2 was performed to compare the behavior of the model with that of Case a1. In Case a2, at the time step of 5001, all bonding were removed simultaneously, that was to say, all bonding strength decreased to zero simultaneously. If the deformation of Case a1 is delayed in comparison with the behavior of Case a2, it is considered that the model is capable of representing the time-dependent behavior.

**Table 6.3 Analytical cases**

| Test Name | Sustained load | Change of $F_c$ and $K$ (at the time step of 5001) |
|---|---|---|
| Case a1 | 2354N(0.8MN/m$^2$) | $F_c$ : 100N ➔ Values described in Figure 6.12<br>$K$ : 1.05x10$^7$ N/m ➔ ditto. |
| Case a2 | 2354N(0.8MN/m$^2$) | $F_c$ : 100N ➔ 0 N (all bonding points)<br>$K$ : 1.05x10$^7$ N/m ➔ Values in Figure 6.12 |

### 6.5.2 Results of analyses and discussions

**(1) Displacement of loading plate versus elapsed time curve**

Figure 6.15 shows the displacement of the loading plate versus elapsed time curves of the two cases. Figure 6.15 also shows the compression load versus elapsed time curves. Although the time interval in which the behavior of the model was calculated was considerably short, i.e. about 0.004sec in both cases, the displacement increased with elapsed time. In Case a1, additional time about 0.00125sec compared with Case a2 was required to displace from the start of dynamic analysis ($t$ = 0.00375sec) to the peak displacement. The slope of the displacement – time curve increased at about 0.0052sec, after the time the slope of the curve was almost equal to the slope of Case a2. In Case a2, it took about 0.002sec for the loading plate to displace from start of the dynamic analysis to the peak displacement. It is considered that this term would be needed for loose rigid particles to fall down to the bottom of the specimen with collision and rearrangement of rigid particles under a sustained load. On the other hand, in Case a1, it is considered that the displacement increasing term would be needed for rigid particles to fall down with breaking of bonding, rearrangement of rigid particles, and collision, that is to say, the breaking of bonding would require the additional time.

The peak displacement was about 20mm. This was about 20% in strain. The strain was extremely larger than the strain of the one-dimensional compression tests of chalk bar specimen: In the one-dimensional compression tests, under the compression stress of about 0.8MN/m$^2$, the strain occurred was about 0.5% (refer to Figure 4.4). The mechanism of larger displacement in the analysis will be described later.

After the peak, the displacement decreased in both cases. The decrease is an initial part of an oscillation. If the loading will be continued, the displacement(loading plate) will indicate oscillation with a natural period. The oscillation will damp by the friction between the rigid particles.

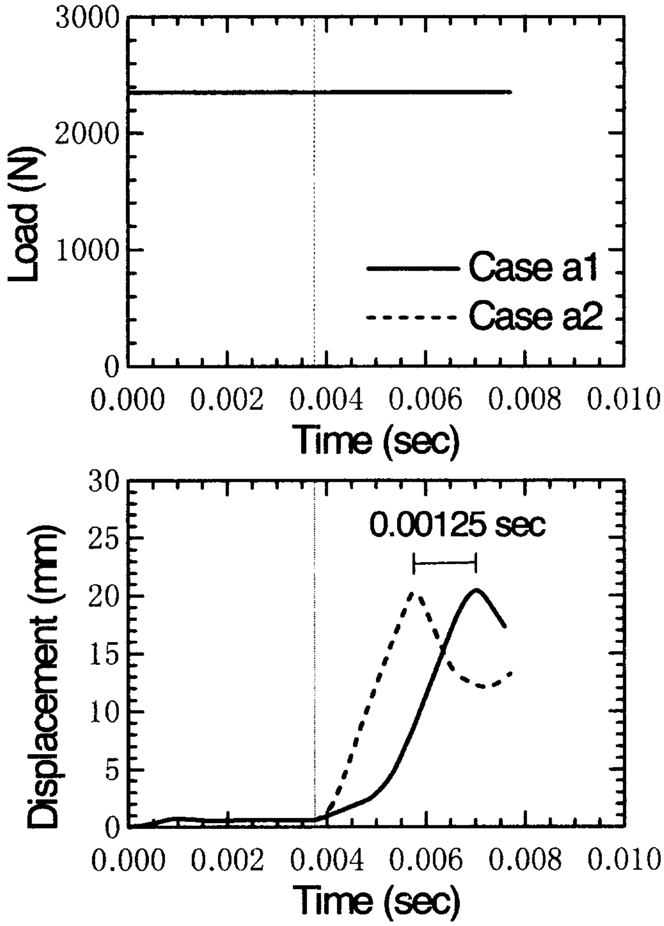


**Figure 6.15 Displacement versus elapsed time with load versus elapsed time**

**(2) Behavior of the analytical model**

Figure 6.16 shows the distributions of micro-cracks at some times in Case a1. The black line indicates normal bonding failure, while the red line shear bonding failure (see Figure 6.10). Each figure only shows the bonding failures newly occurred for the period of 50 or 100 or 200 steps from the time of the immediately former figure. At the time of Figure 6.16(b), there are three virtual aggregates of rigid particles with many micro-cracks. The bonding strength($F_c$) of the three aggregates ranges from 16N to 18N: this is the smallest range of strength of all aggregates in the analytical model (see Figure 6.12).

It is observed that new micro-cracks developed one after another with the passage of time. From the step of 5000 to 6500, the micro-cracks developed irregularly throughout the analytical model. After the step of 6500, localization of micro-cracks was observed. After about 6500step, the virtual aggregates of rigid particles, that illustrated by orange-colored circles in Figure 6.16, began to loosen due to breaking of bonding at almost all bonding points in the aggregates. Consequently, the loose rigid particles moved and filled the voids among the aggregates, and some high density areas where the loose rigid particles were packed closely were formed. As a result of the packing, the loading plate settled. The micro-cracks locally developed in the vicinity of the high density areas.

All micro-cracks developed during the term from 5000step to 6100step are drawn in Figure 6.17(a). Almost all cracked aggregates showed the same distribution of shear micro-cracks as that obtained from the analyses of the single particle crushing test (see Figure 6.10). However, the distribution of micro-cracks for normal bonding failure was beltlike distribution, and was different from that of the analyses of the single particle crushing test. The difference would be due to confining by neighboring aggregates. Figure 6.17(b) shows all micro-cracks developed during the term from 5000step to 6900step. Many normal and shear micro-cracks developed in almost all aggregates. For these micro-cracks, the aggregates crushed into pieces.

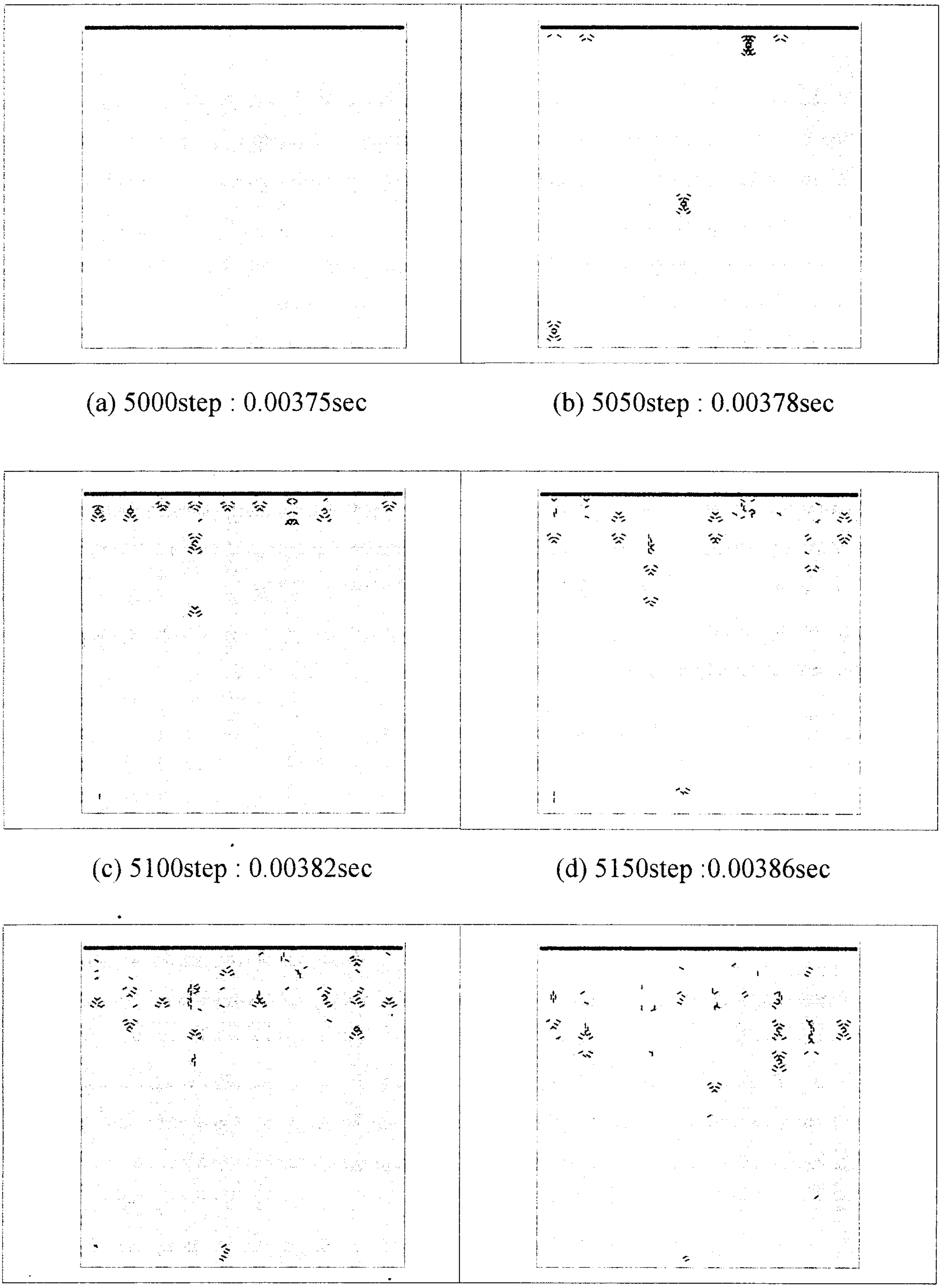

(a) 5000step : 0.00375sec
(b) 5050step : 0.00378sec

(c) 5100step : 0.00382sec
(d) 5150step :0.00386sec

(e) 5200steps : 0.00389sec
(f) 5250steps : 0.00393sec

Figure 6.16 Micro crack distributions (Case a1)

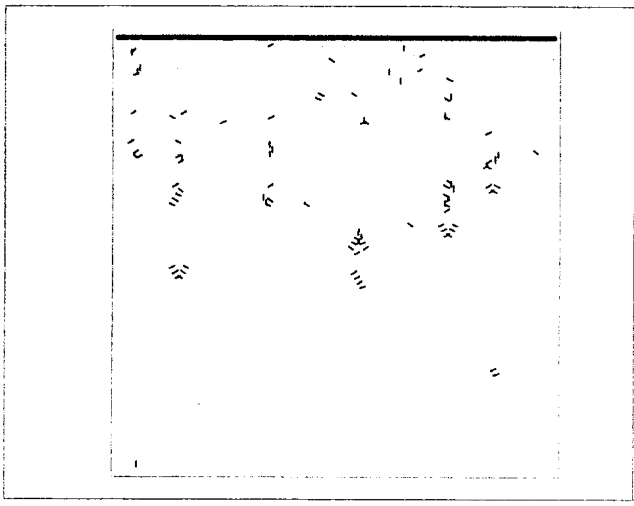

(g) 5300step : 0.00397sec

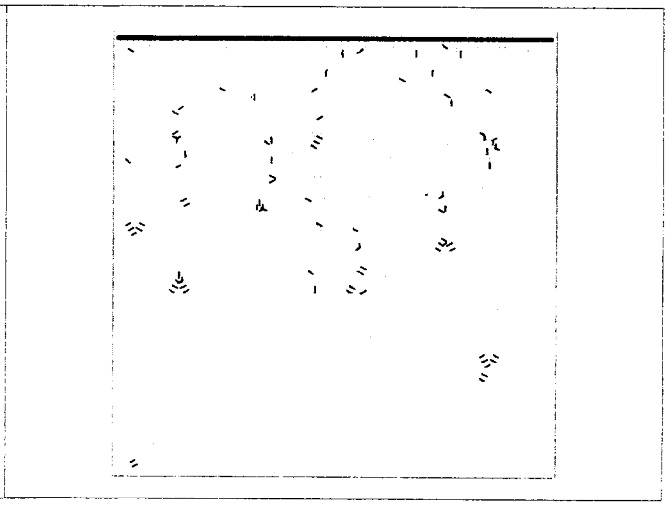

(h) 5350step : 0.00401sec

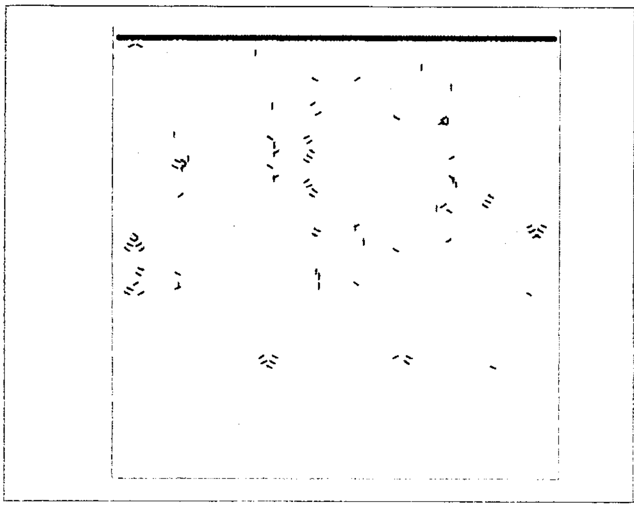

(i) 5400step : 0.00405sec

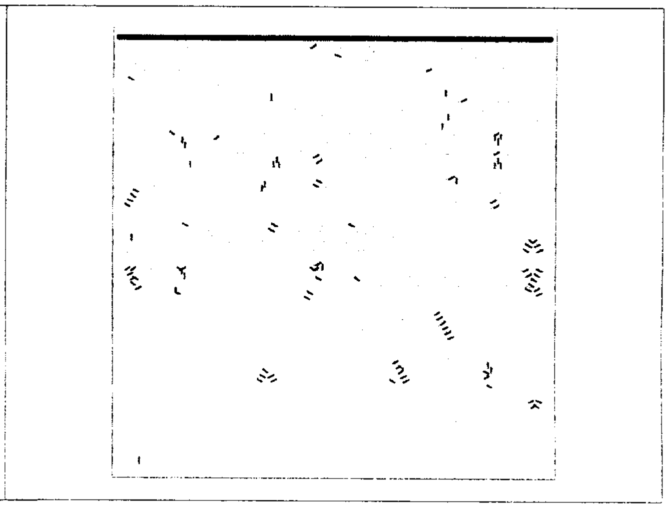

(j) 5450step :0.00408sec

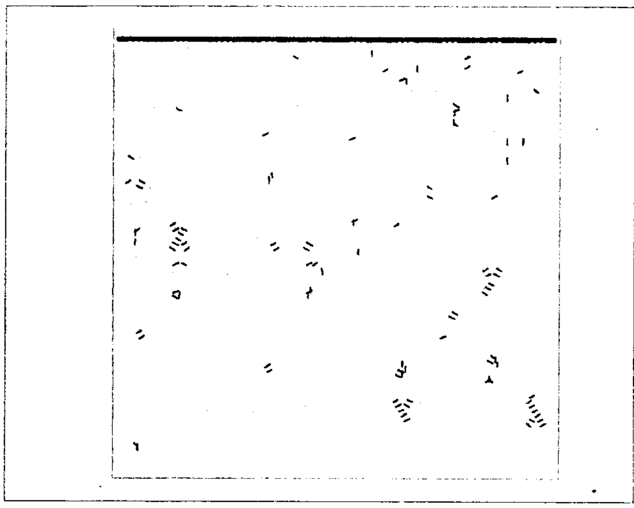

(k) 5500steps : 0.00412sec

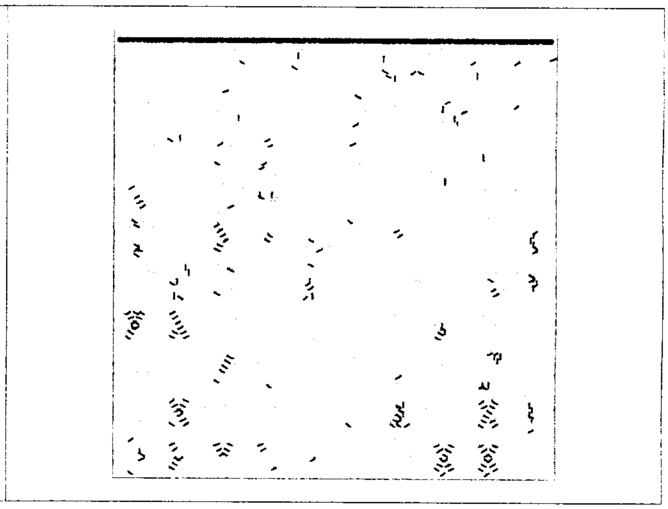

(l) 5600steps : 0.00420sec

Figure 6.16 Micro crack distributions (Case a1)

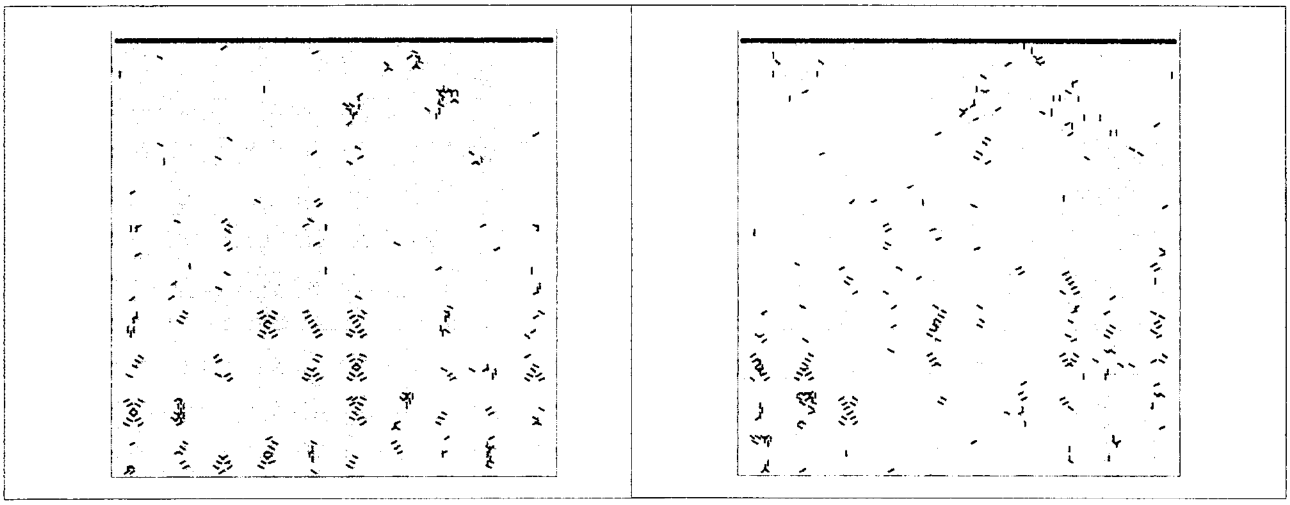

(m) 5700step : 0.00427sec　　　(n) 5800step : 0.00435sec

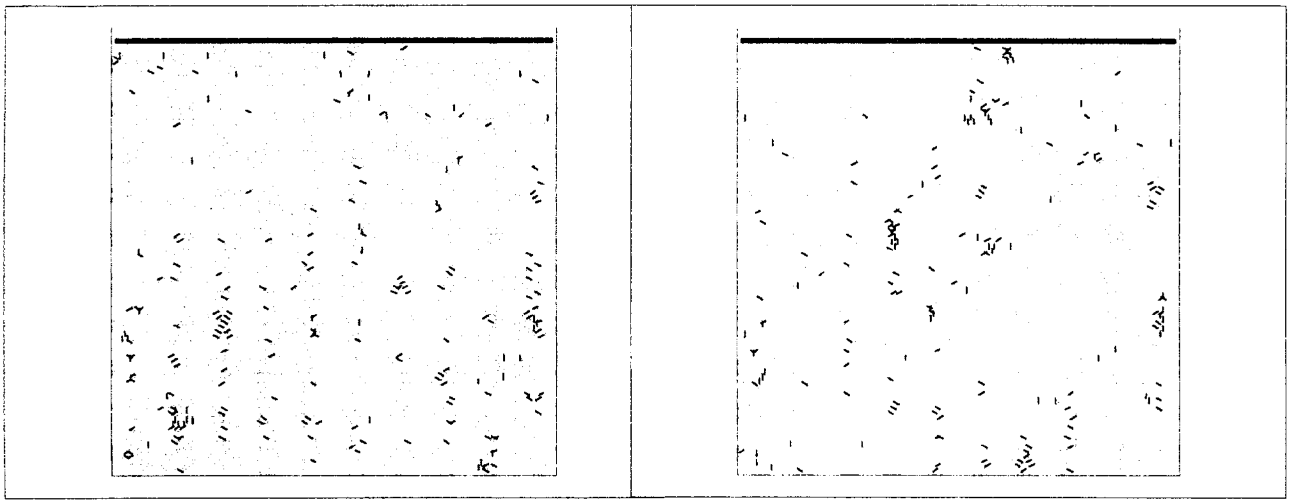

(o) 5900step : 0.00442sec　　　(p) 6000step : 0.00450sec

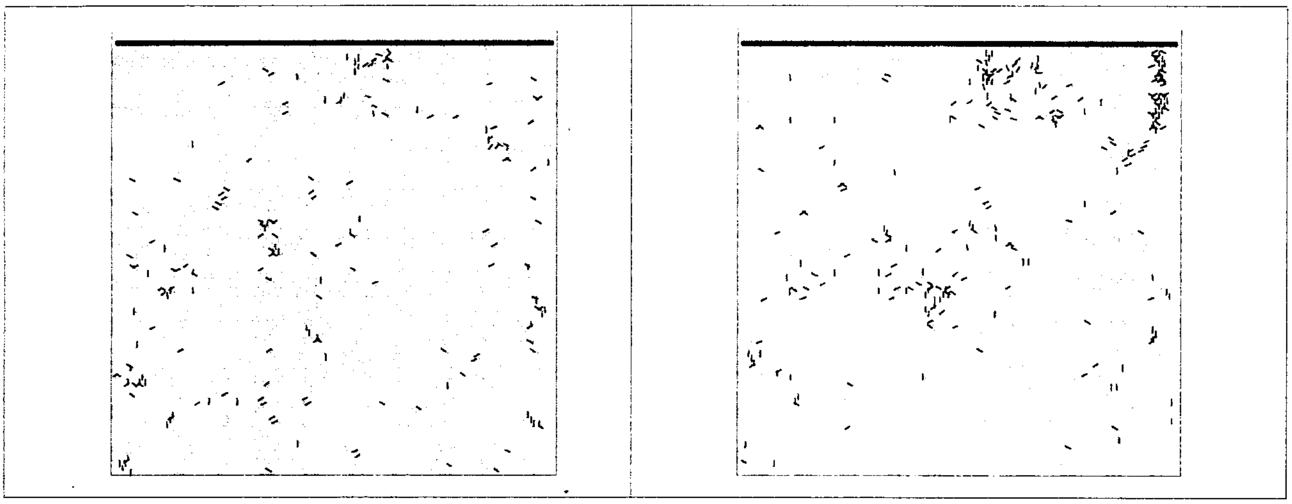

(q) 6100steps : 0.00457sec　　　(r) 6200steps : 0.00465sec

Figure 6.16 Micro crack distributions (Case a1)

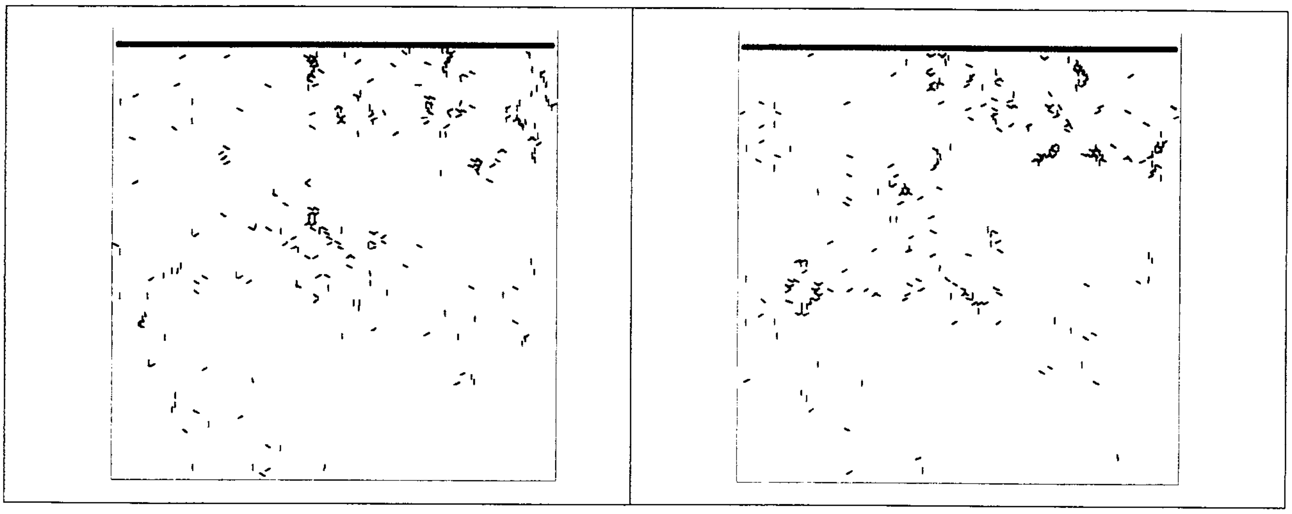

(s) 6300step : 0.00472sec (t) 6400step : 0.0048sec

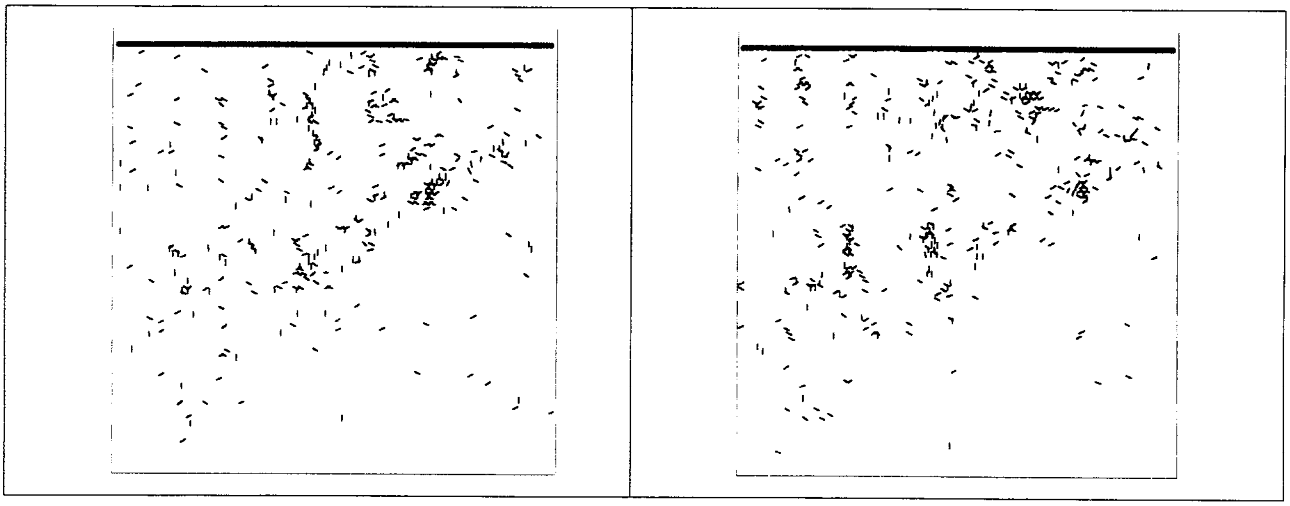

(u) 6500step : 0.00487sec (v) 6600step : 0.00495sec

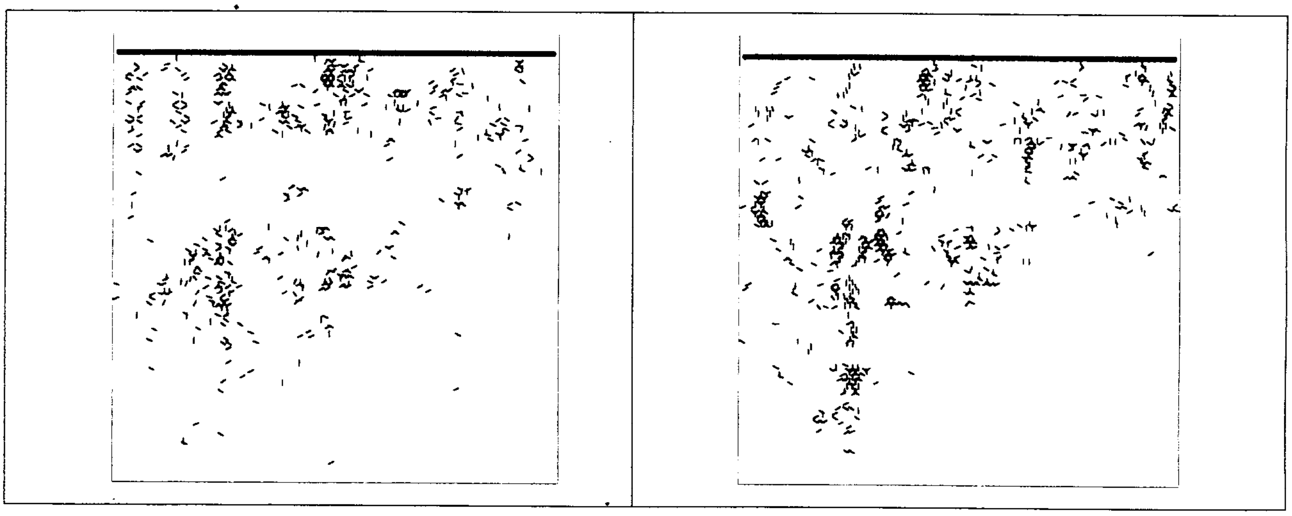

(w) 6700steps : 0.00502sec (x) 6800steps : 0.0051sec

Figure 6.16 Micro crack distributions (Case a1)

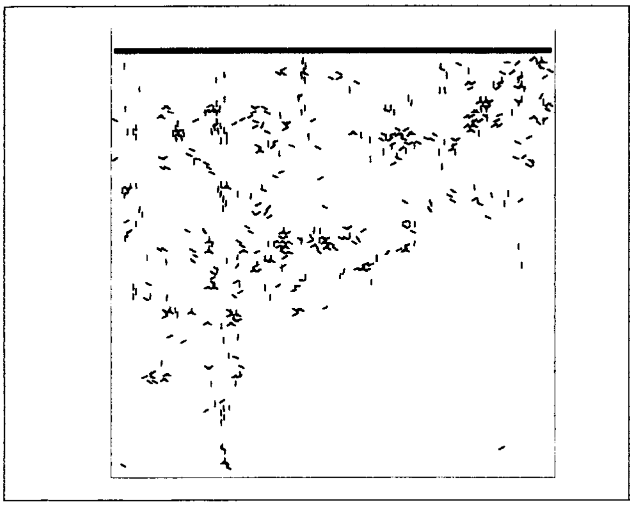

(y) 6900step : 0.00517sec

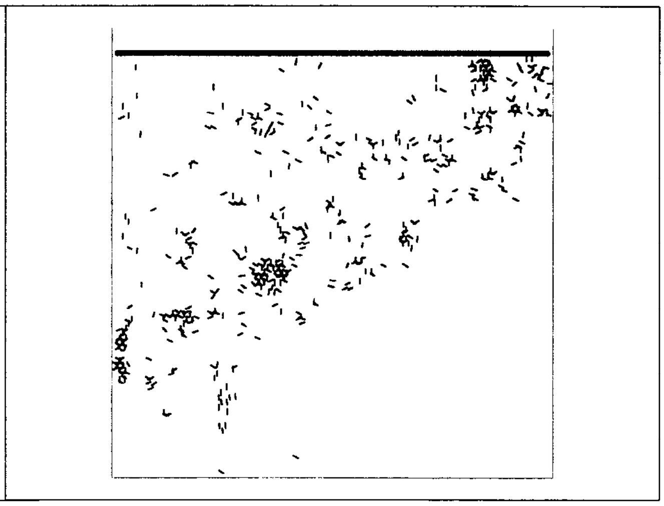

(z) 7000step : 0.00525sec

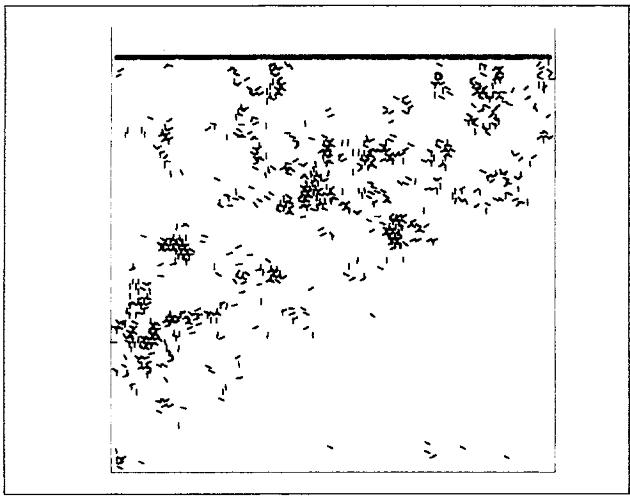

(α) 7200step : 0.00541sec

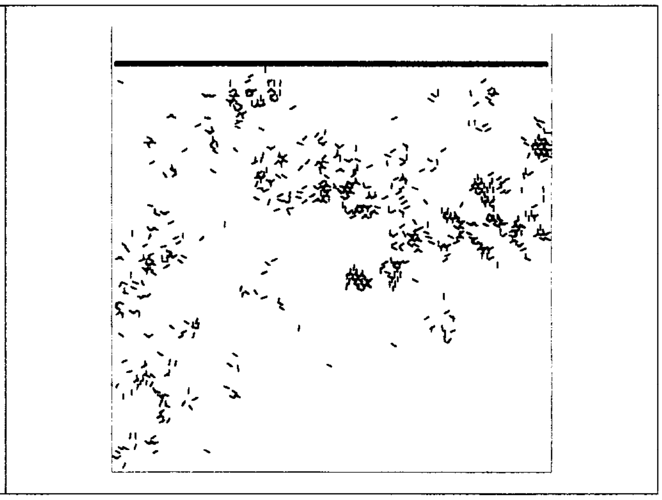

(β) 7400step : 0.00556sec

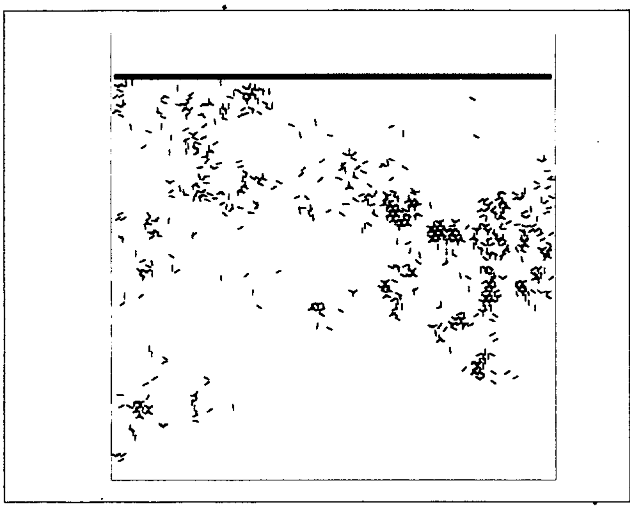

(χ) 7600steps : 0.00572sec

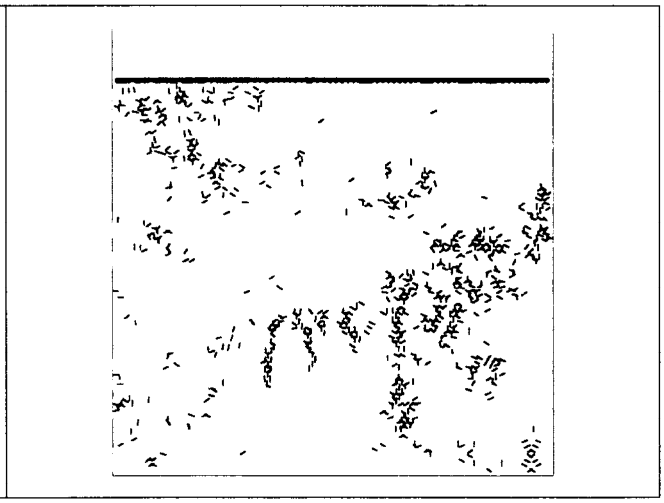

(δ) 7800steps : 0.00588sec

Figure 6.16 Micro crack distributions (Case a1)

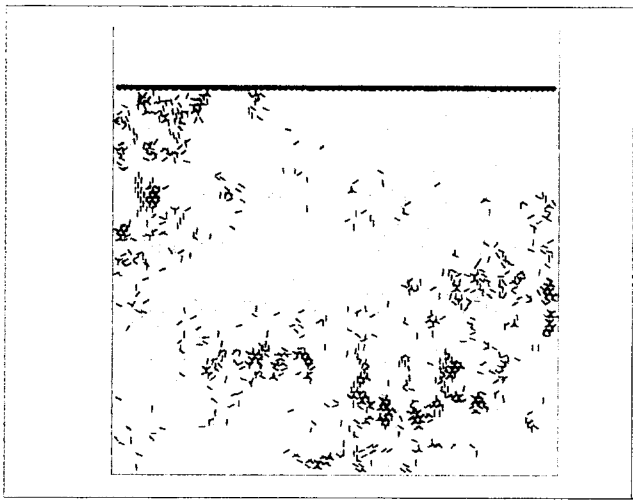

(ε) 8000step : 0.00604sec

(φ) 8200step : 0.0062sec

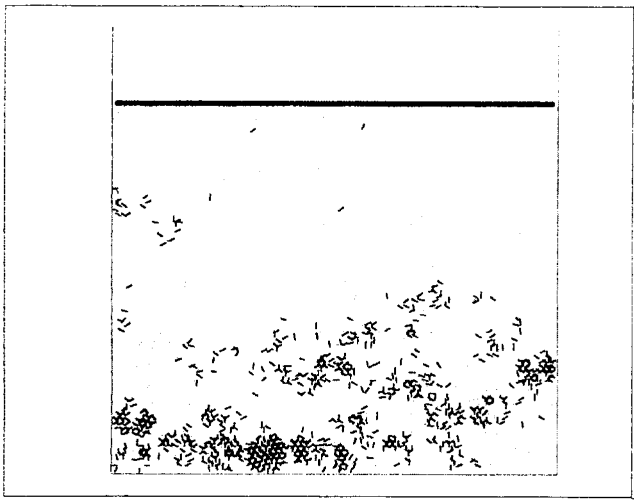

(γ) 8400step : 0.00636sec

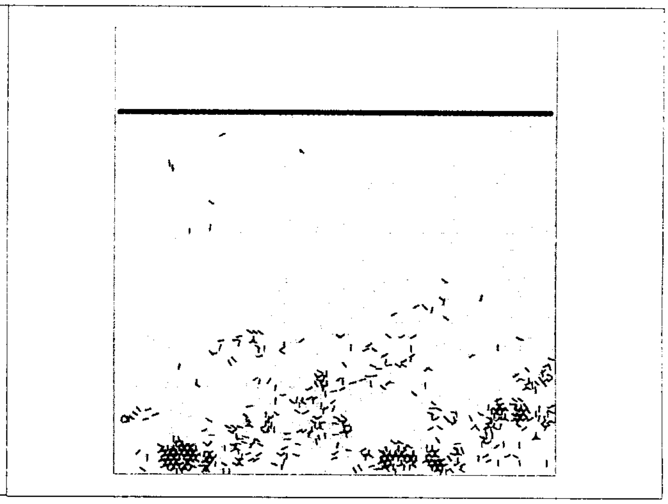

(η) 8600step : 0.00651sec

( Notes )

**Nornal bonding failure** **Share bonding failure**

Each figure only shows the bonding failures newly occurred for the period of 50 or 100 or 200 steps from the time of the immediately former figure.

**Figure 6.16 Micro crack distributions (Case a1)**

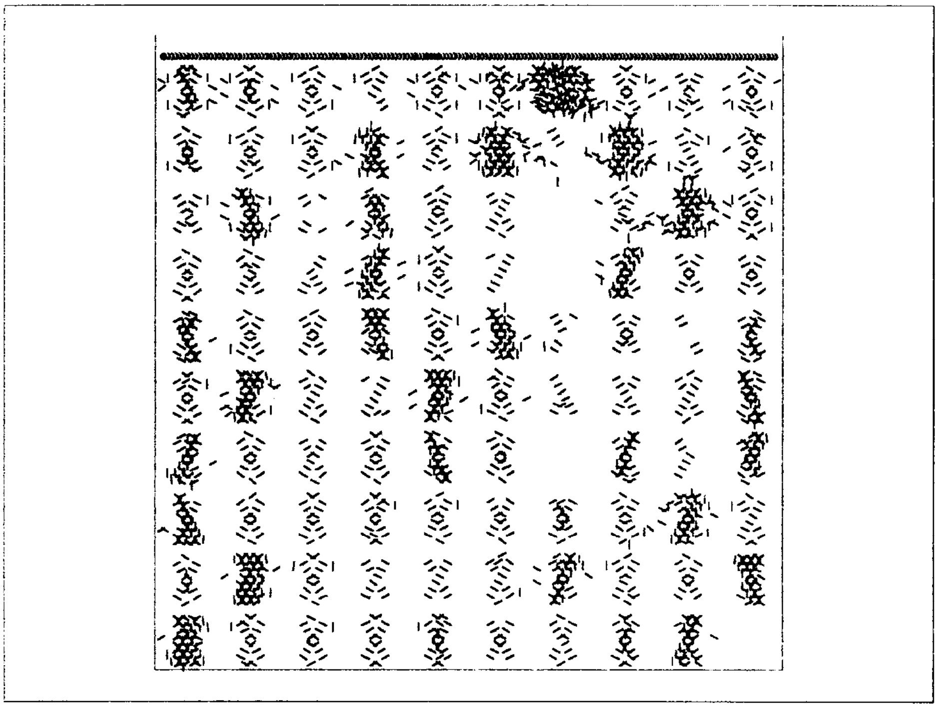

(a) 5000step - 6100step

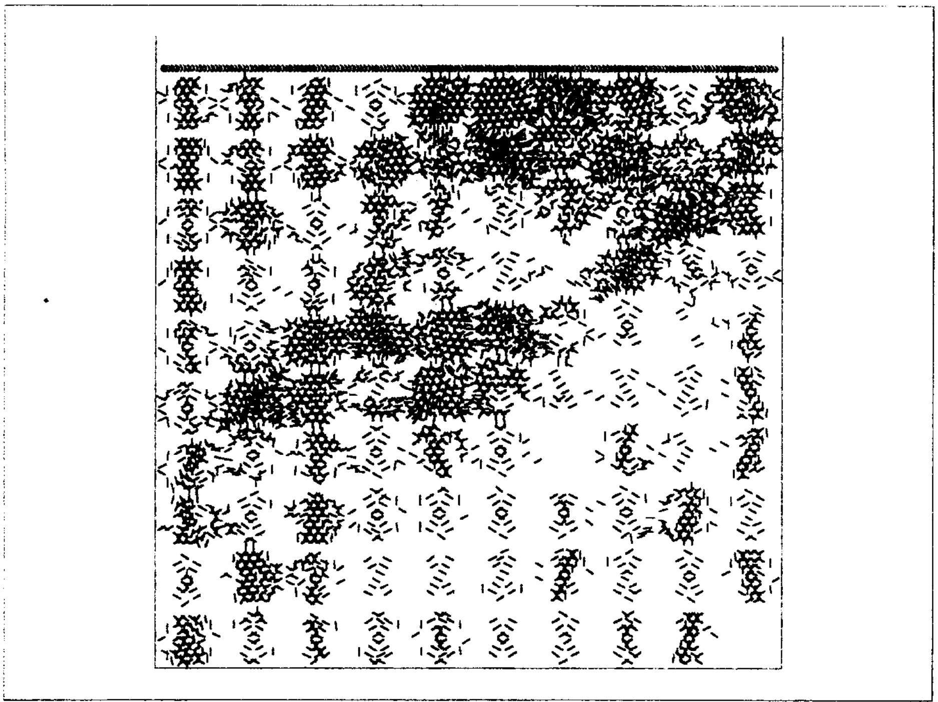

(b) 5000step - 6900step

Figure 6.17 Distributions of micro-crack (Case a1)

Figure 6.18 depicts the contact forces that developed in the model at some times. The contact-force distributions are depicted as bi-colored lines (for which the black line represents compression, and red line represents tension) through each contact location and oriented in the direction of the contact force, with a thickness proportional to force magnitude. The scales of thickness for contact forces are equal among all figures in Figure 6.18.

At 5000step, the analytical model was almost in a stable condition under the sustained load of 2354N, and the distribution of contact forces was almost uniform. From 5000step to around 5800step, redistribution of contact forces in some aggregates had occurred actively. It is considered that the redistribution of contact forces would be due to breakage of bonds between rigid particles in each aggregate. From around 5900step to around 6900step, redistribution of contact forces among aggregates had occurred actively. The region of low contact forces was spread from the aggregate that was located beneath the loading plate and 4th from the right as the starting point. This spread was accompanied by augmentation of contact forces in left-side columns that have non-loose aggregates. Figure 6.19 shows the enlarged figures of distribution of contact forces in a part of the model. The augmentation of contact forces could be confirmed from the figures. It is considered that the spread of the region of low contact forces and the augmentation of contact forces mean the redistribution of contact force posterior to the breakage of bonds. At around 6900step, the columns of aggregates that did not contain the non-loose aggregates (i.e. that transfer the load from the loading plate to the bottom of the model) almost disappeared. This timestep was in agreement with the time when the gradient of the settlement – time curve increased. After around 6900step, the loose rigid particles moved and filled the voids among the aggregates, following the settlement of the loading plate. New routes that transfer the load were gradually formed in the right-upper region of the model where the rigid particles were closely packed. The transferred load acted to the aggregates that located in the lower region of the model, and caused fragmentation of the aggregates. Finally, almost all aggregates were fragmented and the fragmented particles were deposited.

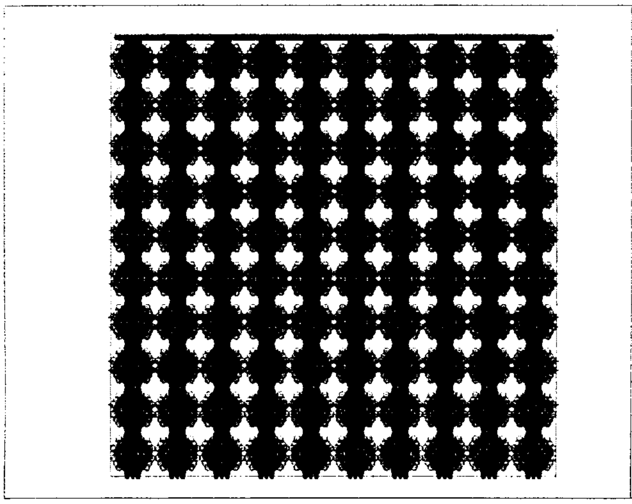
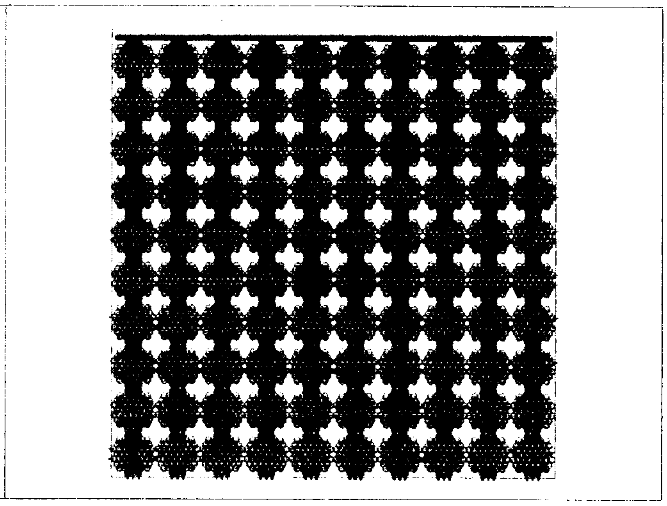

(a) 5000step : 0.00375sec

(b) 5050step : 0.00378sec

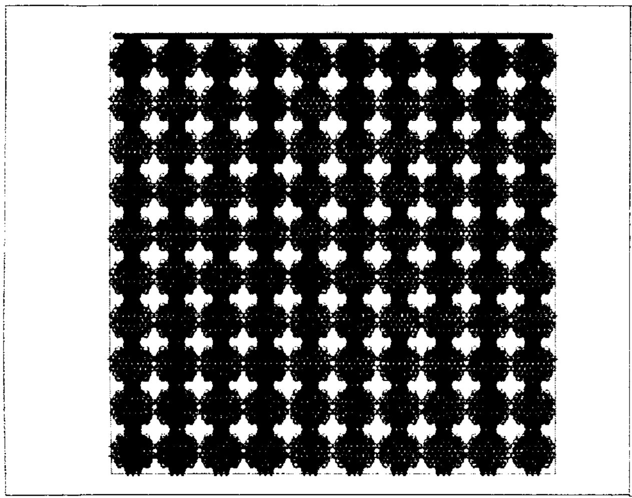
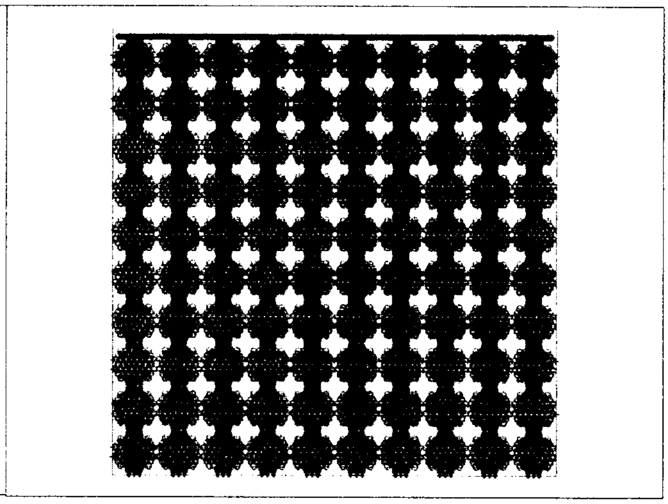

(c) 5100step : 0.00382sec

(d) 5150step :0.00386sec

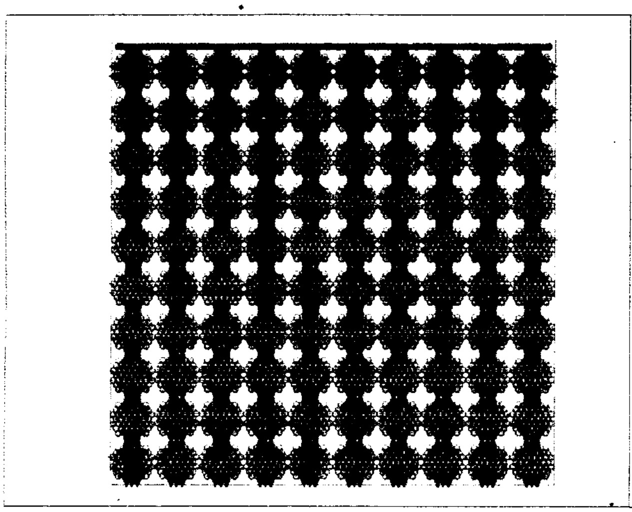
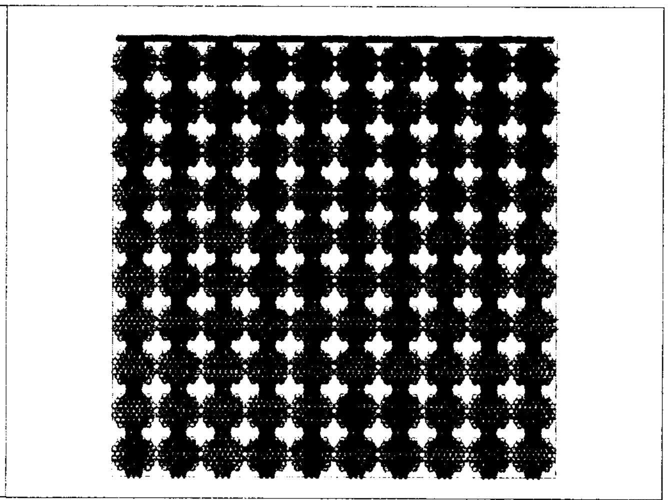

(e) 5200steps : 0.00389sec

(f) 5250steps : 0.00393sec

Figure 6.18 Contact force distributions (Case a1)

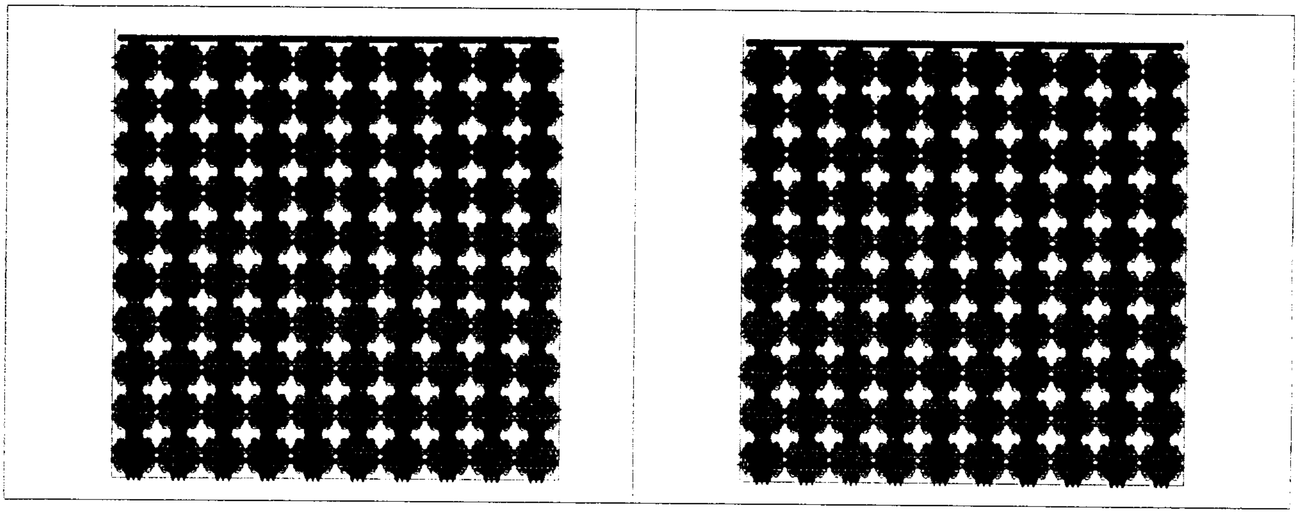

(g) 5300step : 0.00397sec (h) 5350step : 0.00401sec

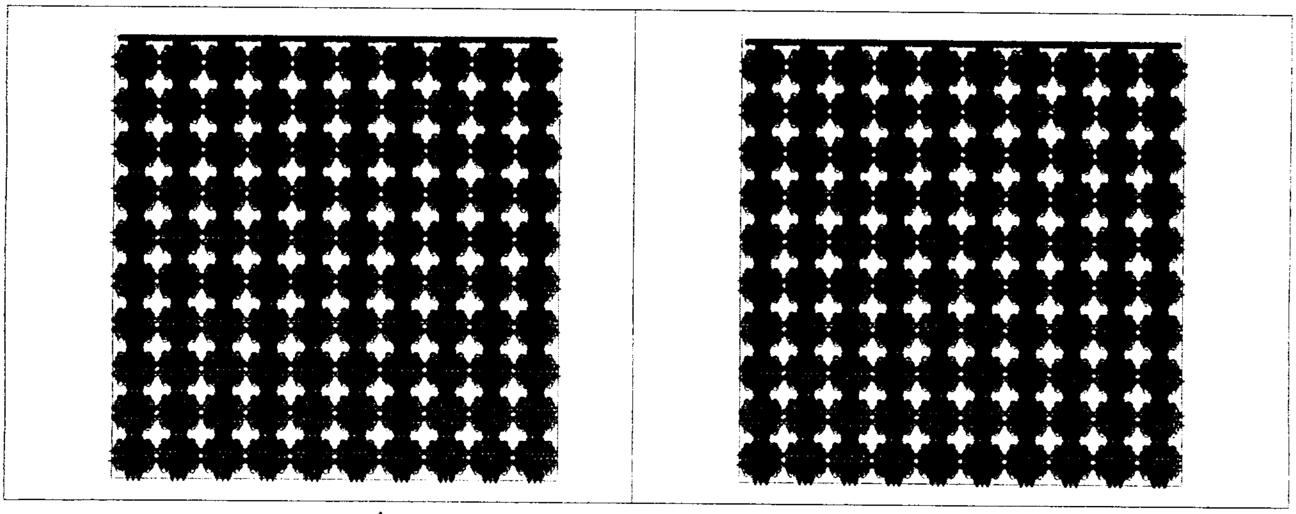

(i) 5400step : 0.00405sec (j) 5450step :0.00408sec

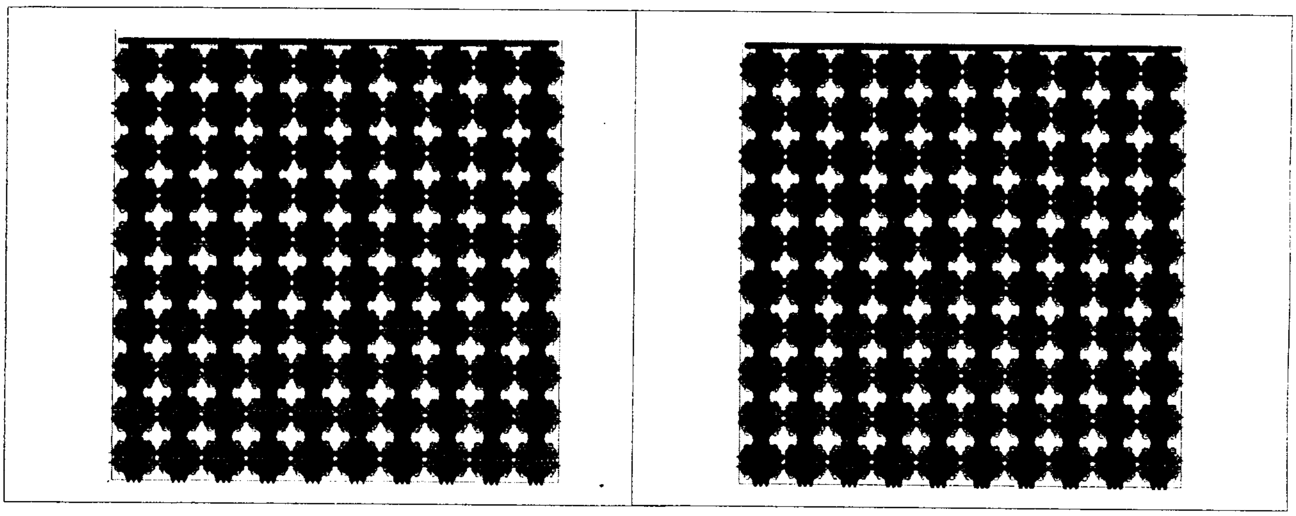

(k) 5500steps : 0.00412sec (l) 5600steps : 0.00420sec

Figure 6.18 Contact force distributions (Case a1)

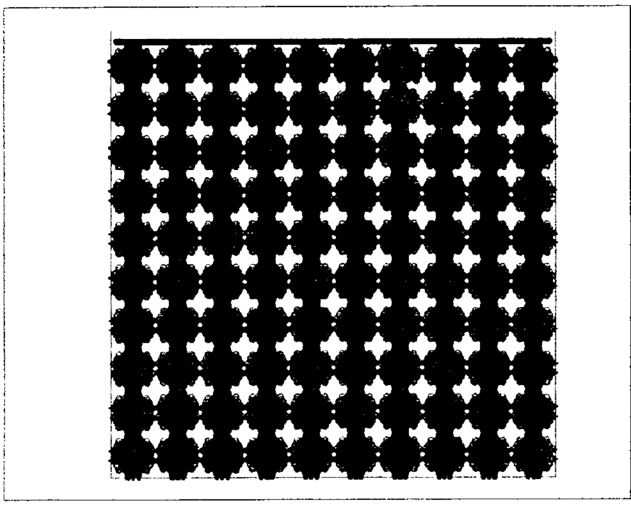

(m) 5700step : 0.00427sec

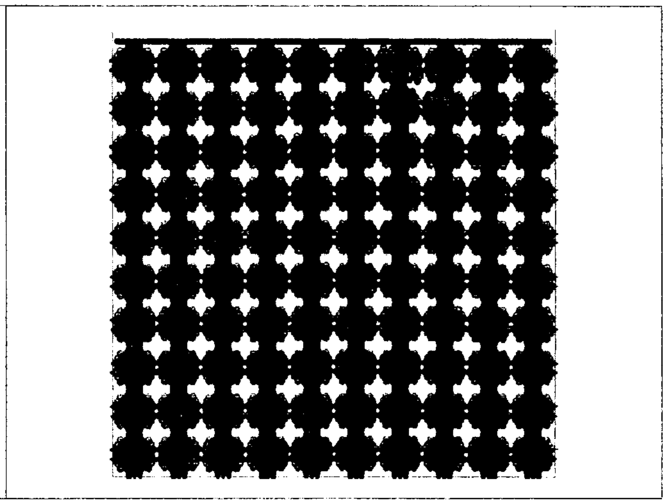

(n) 5800step : 0.00435sec

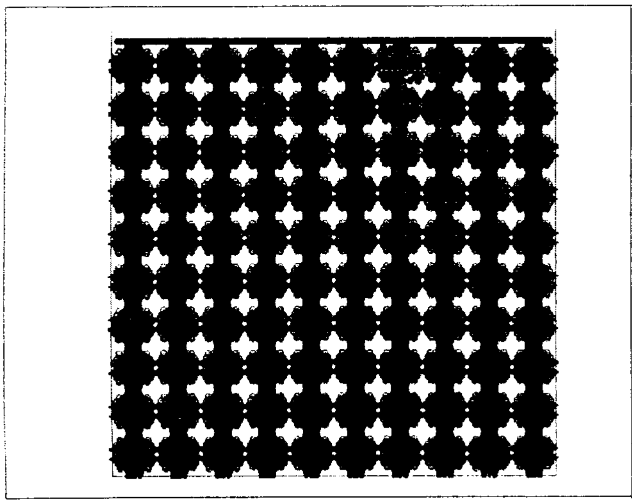

(o) 5900step : 0.00442sec

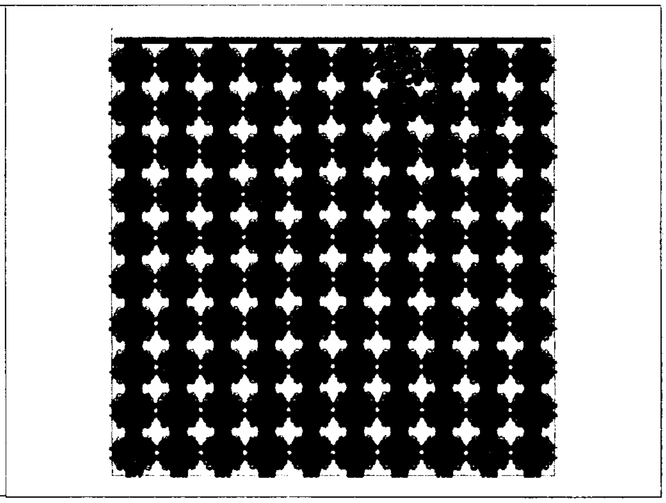

(p) 6000step : 0.00450sec

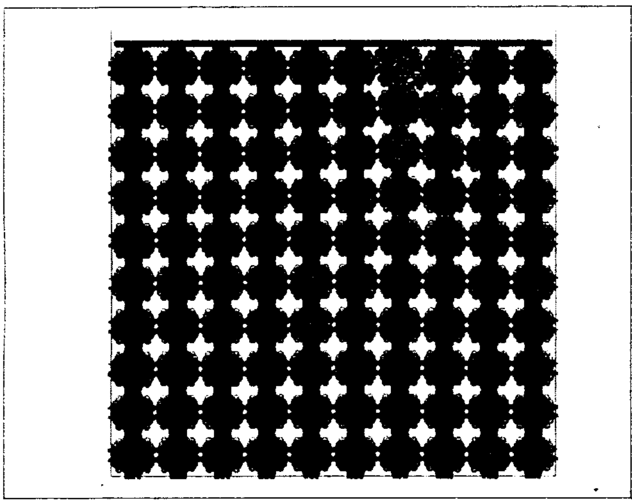

(q) 6100steps : 0.00457sec

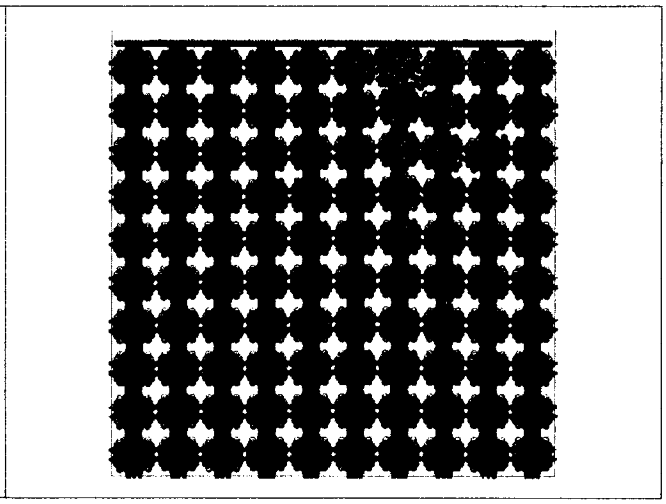

(r) 6200steps : 0.00465sec

Figure 6.18 Contact force distributions (Case a1)

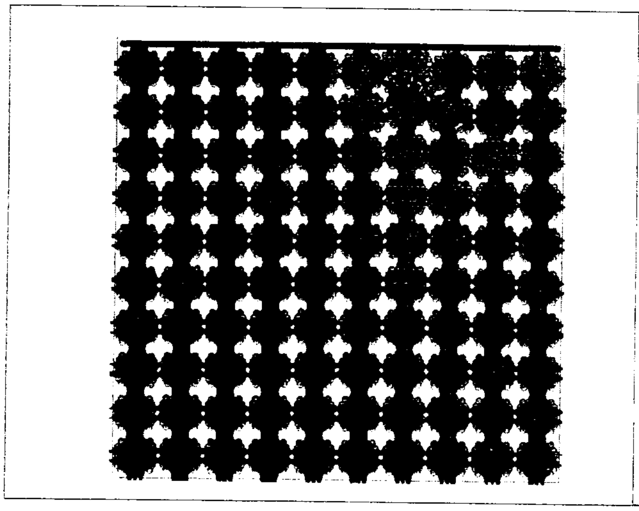
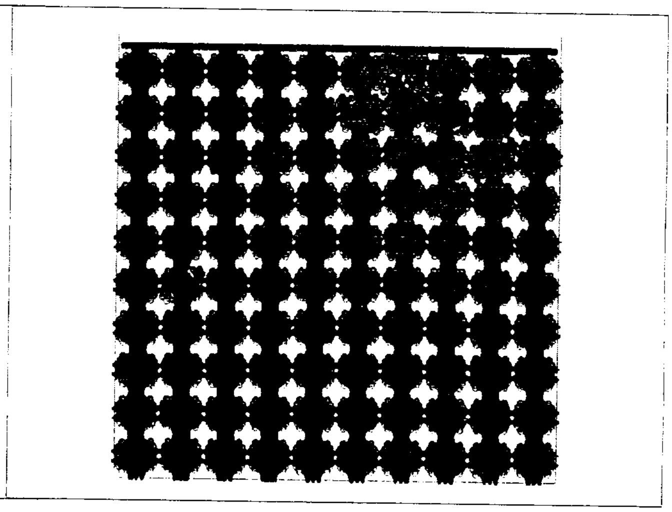

(s) 6300step : 0.00472sec

(t) 6400step : 0.0048sec

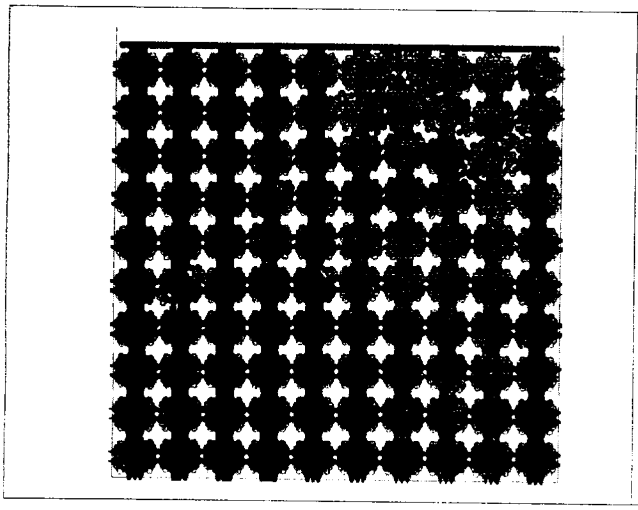
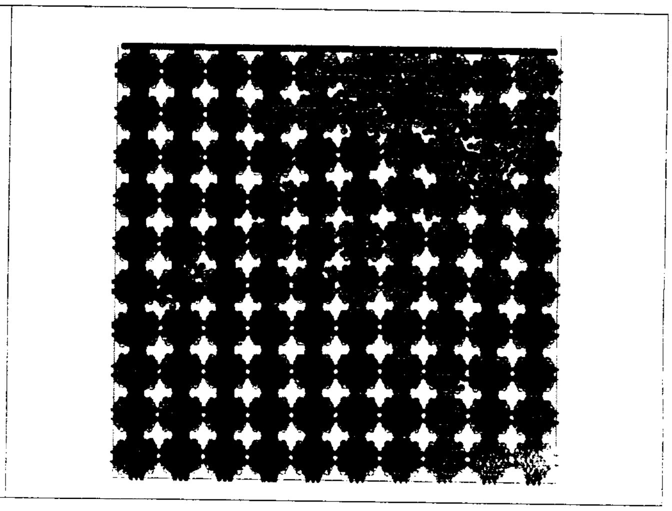

(u) 6500step : 0.00487sec

(v) 6600step : 0.00495sec

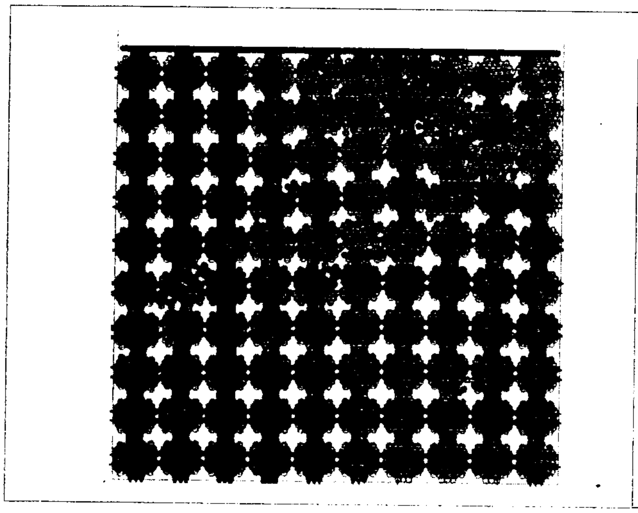
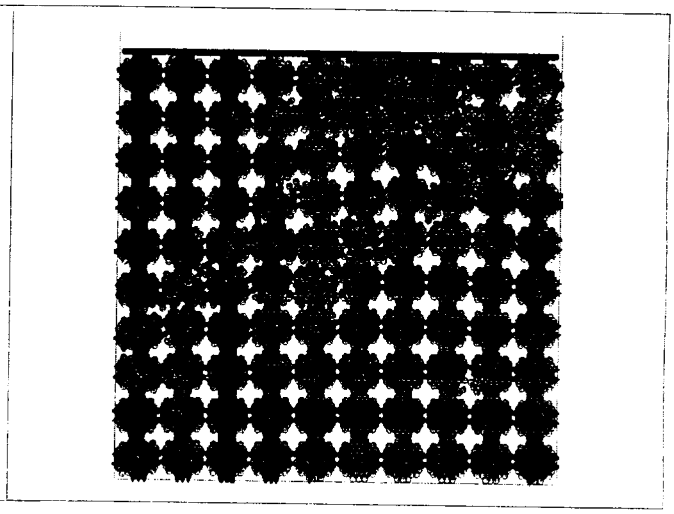

(w) 6700steps : 0.00502sec

(x) 6800steps : 0.0051sec

Figure 6.18 Contact force distributions (Case a1)

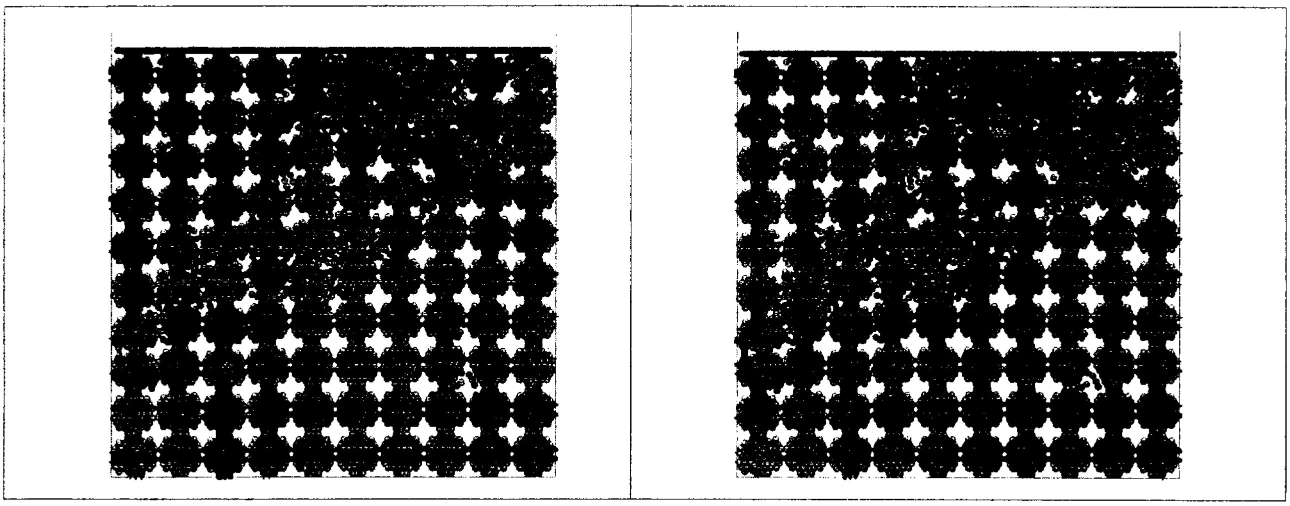

(y) 6900step : 0.00517sec

(z) 7000step : 0.00525sec

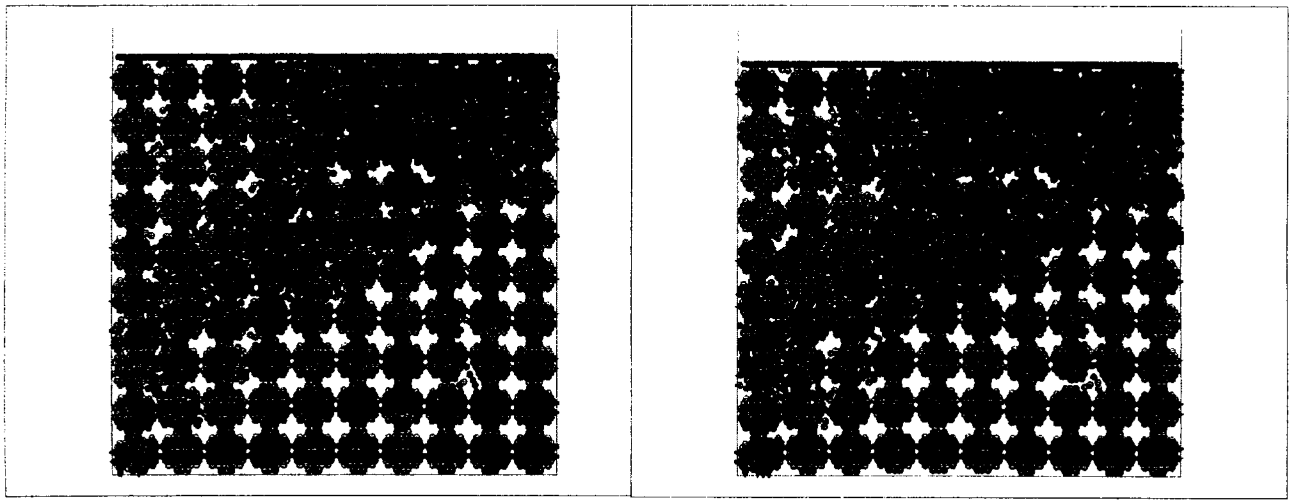

(α) 7200step : 0.00541sec

(β) 7400step : 0.00556sec

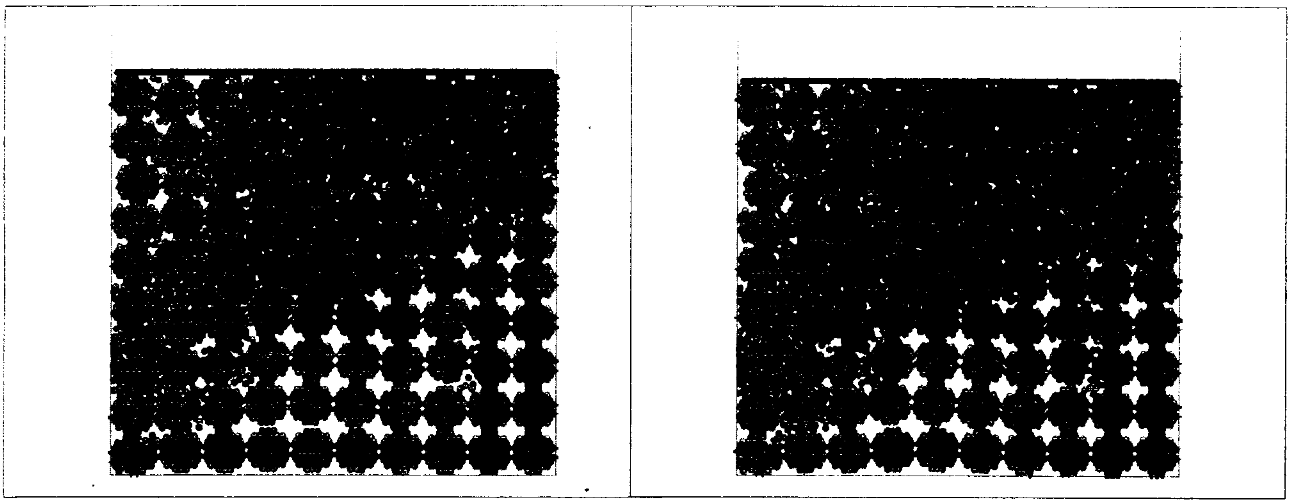

(χ) 7600steps : 0.00572sec

(δ) 7800steps : 0.00588sec

Figure 6.18 Contact force distributions (Case a1)

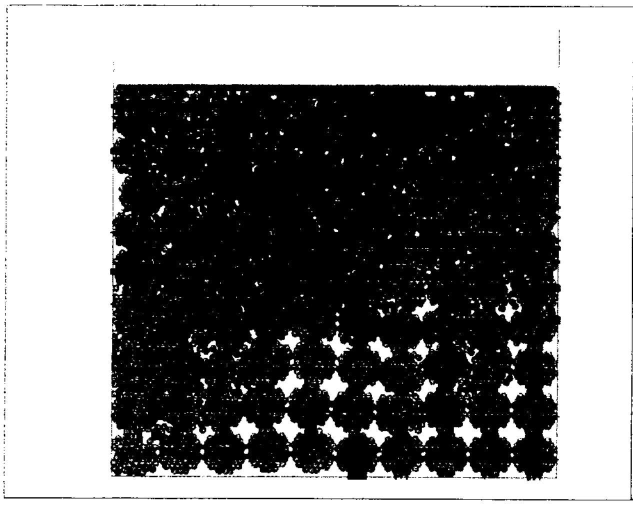

(ε) 8000step : 0.00604sec

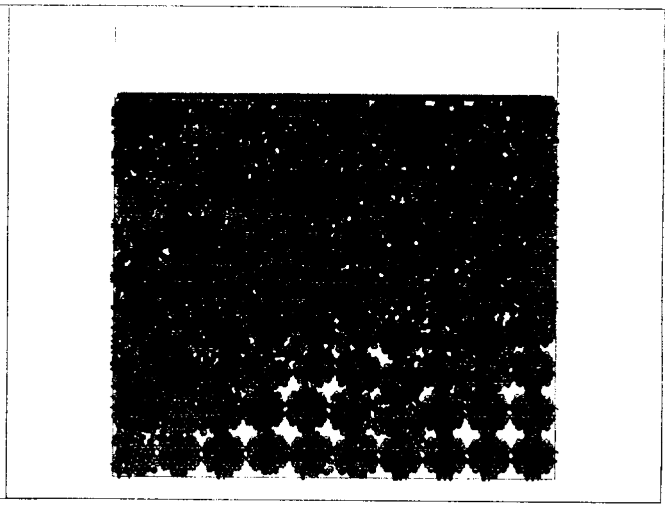

(ϕ) 8200step : 0.0062sec

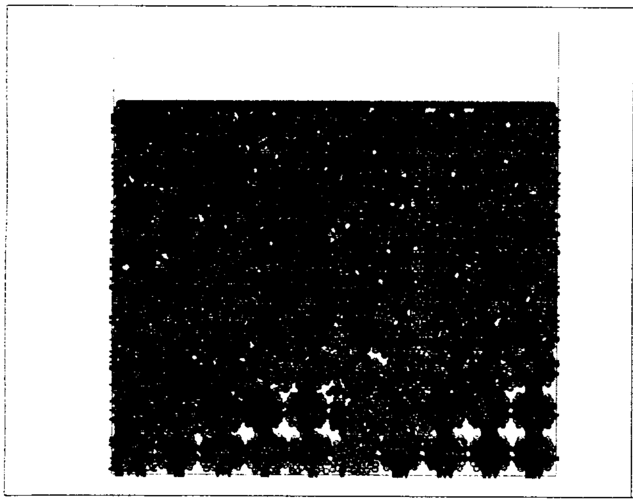

(γ) 8400step : 0.00636sec

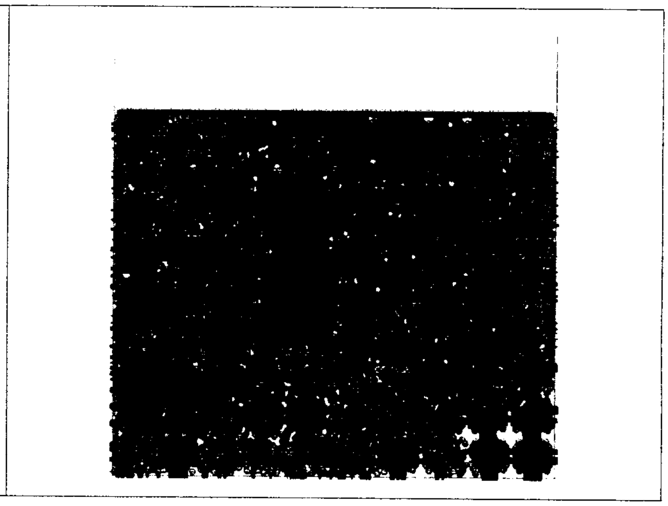

(η) 8600step : 0.00651sec

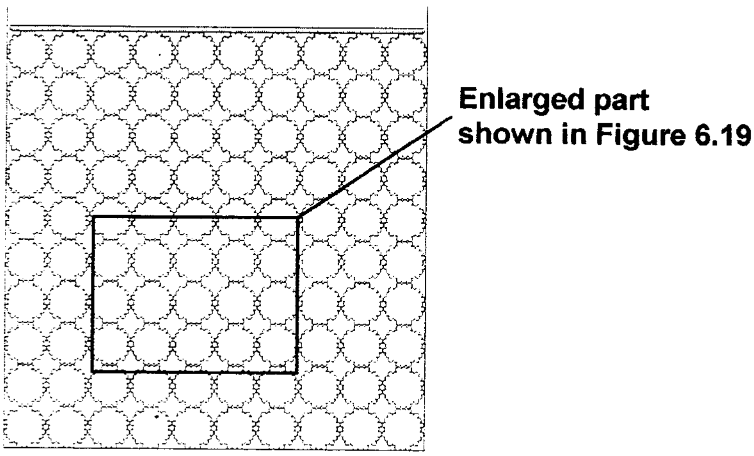


**Figure 6.18 Contact force distributions (Case a1)**

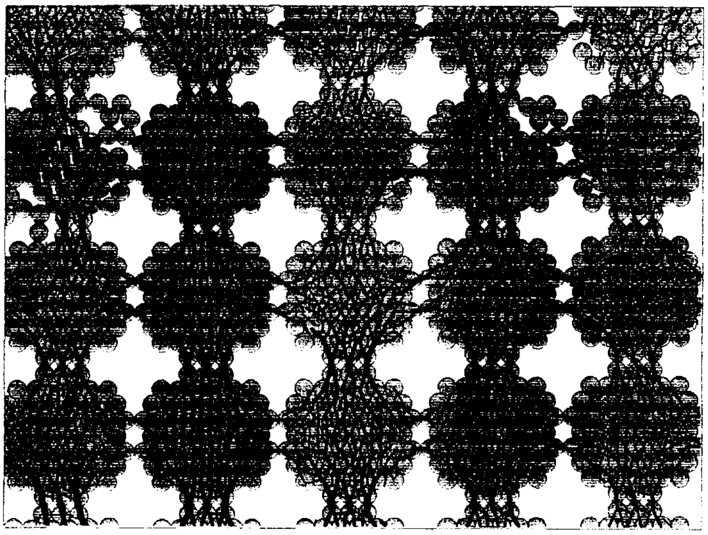

(a) 6500step : 0.00487sec

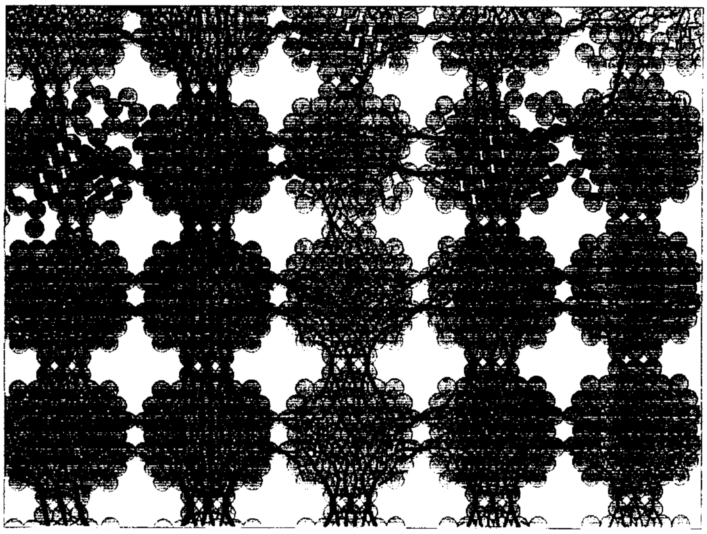

(b) 6600step : 0.00495sec

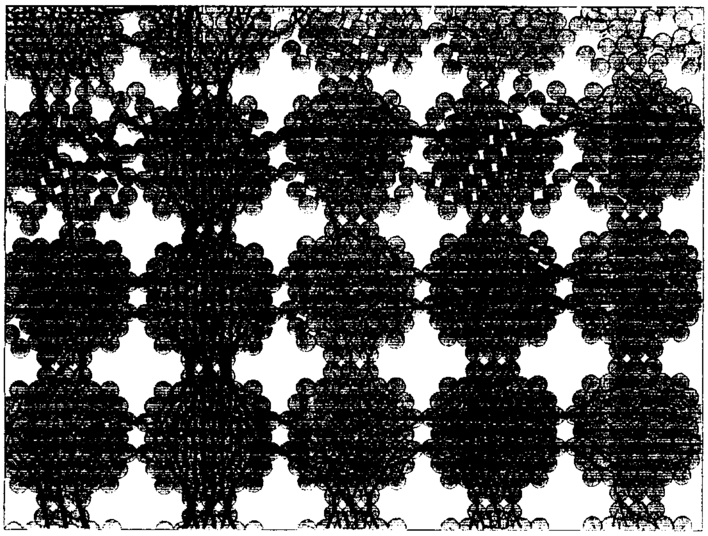

(c) 6700step : 0.00502sec

**Figure 6.19 Distributions of contact force (Case a1)**

### (3) Difference between experiments and analysis

The represented behavior of the analysis (Case a1) was greatly different from the observed behavior of the experiments. In the experiments of chalk bar specimen, the loading stage of $0.8MN/m^2$, the final axial strain of the specimen was about 0.5% (0.5mm in displacement), and the number of crushed chalk bars ranged from 5 to 18. In the analysis, the final axial strain of the model was about 20% (20mm in displacement), and almost all aggregates (i.e. chalk bars) of rigid particles were crushed.

The reasons for the difference would be as follows.

- The behavior of individual chalk bar in the experiments was different from the behavior of individual aggregate of rigid particles in analysis. In the experiments, chalk bars crushed in the pattern of Mode A and Mode B, and then the local crushing progressed from the edges of the crushed chalk bars. During the progress of the local crushing, the crushed chalk bars could support the contact forces. While in the analysis, firstly, the aggregates of rigid particles cracked like splitting crack shown in the analysis of single particle crushing test, then the aggregates crushed to pieces in a very short time. Thus, once the aggregates crushed, the aggregate could not support the loaded contact forces.
- The variation of the size (diameter) of chalk bar was not taken into account in the analysis. In the experiments, there was a slight variation in the diameter of chalk bars in a chalk bar specimen, thus the initial array of chalk bars must have been slightly irregular. At the original state of the specimen, the applied load would be supported with several columns of chalk bars that had relatively large diameters. But after the relatively large chalk bars crushed, the crushed chalk bars were slightly smashed, and some part of the contact forces that were acting to the crushed chalk bars would be distributed to other chalk bars. While in the analysis, all aggregates of rigid particles are entirely equal size. Thereby, at the original state of the analytical model, the applied load was supported with ten columns of aggregates uniformly. However, once crushing of aggregate occurred, the contact forces concentrated to non-crushed aggregates because of the above-mentioned crushing-to-pieces. The concentration of the contact force causes other succeeding crushing of aggregates.

The bonding model discussed in this chapter may be comfortable to represent the time-dependent behavior of the grass beads specimen considering the crushing behavior of the grass beads in the single particle crushing tests and the one-dimensional compression tests.

## 6.6 Conclusions

In Chapter 6, a modeling method of crushable materials was proposed for analyzing the time-dependent behavior due to particle crushing. One-dimensional compression test of chalk bar specimen was analyzed by DEM taking into account the modeling method. The following conclusions may be drawn.

- From the analyses of the single particle crushing test, that were conducted prior to the analyses of single particle crushing test, the proposed bonding model would represent the behavior of the single particle crushing test of chalk bar until the peak of load.
- From the analyses of one-dimensional compression test of chalk bar specimen, though it was a considerable short term, the proposed model could represent the time-dependent behavior due to particle crushing. The proposed model would be capable of expressing the time-dependent behavior due to particle crushing.
- More investigations are required to obtain the analytical results that are comparable with the experiments. The following investigation will be needed :
  - Improvement of the bonding model for supporting contact loads after crushing (cracking), expressing the crushing modes, and expressing the local crushing at the edges of fragments
  - Determination of the values of the analytical parameters with some physical explanation.

# CHAPTER 7

# CONCLUSIONS

## 7.1 Conclusions

In this dissertation, detailed mechanism of time-dependent behavior due to particle crushing was investigated through reappraisal of in-situ loading test data, laboratory model tests, and numerical analyses.

The conclusions of this dissertation are as follows :

(a) From the reappraisal of the plate loading tests conducted on the weathered granite ground, where crushing phenomena had been observed after the test, it was confirmed that the plate settled time-dependently in each loading stage. The time-dependent settlement was proportional to the common logarithm of time. The gradient of the settlement – log time curve, that is called the rate of creep settlement, increased with increasing of sustained load, area of plate, and weathered class of the ground. It was observed that the rate of creep settlement had a relation to elastic wave velocity of the ground.

(b) Single particle crushing tests of four crushable materials (chalk bars, talc bars, glass beads and quartz particles from weathered granite ground) clarified the mean crushing strength of each material, mean characteristic initial stiffness of $\sigma - \varepsilon$ curve of each material, standard deviations of these values, coefficient of variation of these values, and crushing patterns of each material. The crushing strengths of the crushable materials could be generally explained by the Weibull distribution. In the case of quartz particle from the weathered granite ground, the number of fragments were counted after each test, and it was found that the distribution of the number of fragments after a single particle crushing test was approximated with an exponential function.

(c) From the one-dimensional compression tests of the four crushable materials, the mechanism of time-dependent compression of each specimen was clarified as follows :

- Time-dependent compression of chalk and talc bar specimen is initiated by local crushing at contact areas, followed by the formation of continuous crack in the bar either in 'vertical splitting mode' or 'sideways splitting mode'. The formation of continuous crack accelerates further local crushing at the contact areas without noticeable rearrangement of particles for chalk bar.

- For the case of talc bar specimen, however, slippage occurs along contact areas, triggering other slippage and accelerating the chained-event of the rearrangement of the talc bars.
- Glass beads crush instantly into a number of fragments. Movement and rearrangement of particles after crushing mainly cause the time-dependent behavior of glass bead specimen.
- In specimens of natural quartz particles, the time-dependent behavior is predominately caused by a combination of the collapse of angular edges of particles and the local crushing at contact areas.
- From the results of separation of compression strain into the three components (instantaneous strain, strain due to material creep and strain due to particle crushing), the magnitude of the strain due to particle crushing was significant in the loading stages where the cumulative crushing ratio was over 40%.
- In one-dimensional compression tests, it was verified that the time-dependent behavior due to particle crushing is, in general, stemmed from progressive nature of a chained-event of "particle crushing" and subsequent "rearrangement of particles" and "stress redistribution" under the condition of one-dimensional compression. It was found that the detailed mechanism of each event for these four materials is different, depending upon the crushing characteristics of single particle.

(d) From the model footing loading tests on the model ground made of chalk bars, time-dependent settlement was observed. The settlement was proportional to the logarithm of time. In addition, a sudden increment of settlement or change of the gradient of settlement – time curve was also observed. These phenomena were caused by rearrangement of particles. The crushing modes appeared were the same as those of one-dimensional compression test of chalk bar specimen, but there were three types of "vertical splitting mode". Some cracks of the vertical splitting mode were gradually opening during sustained loading term and the fragments were pushing the neighboring chalk bars into the directions of crack opening. As a result of crack opening, rearrangement of chalk bars sometimes occurred suddenly. The crack opening would be caused by gradual collapsing of the angular edges formed in crushed chalk bars. The process of crack opening would be affected by position of particle, crushing mode, and distribution of contact forces around a chalk bar.

(e) In analytical investigations, a crushable particle was modeled by aggregates of rigid particles bonded each other, that was called bonding model. One-dimensional compression test of chalk bar specimen was analyzed by DEM that the bonding model was incorporated. From the results of the analysis of one-dimensional compression test, it was clarified that the bonding model could represent the chained-event and that the progress of the chained-event involved a time interval, though the time interval was very short. The variation of the diameters of chalk bars ought to be taken into account in the analysis. In addition, methods for determinating of the values of the parameters used in the analyses must be investigated.

## 7.2 Further research

In this section, future studies are described.

### (1) Multi-axial loading test for a cylindrical crushable bar

In Chapters 3, 4 and 5, crushing behavior of the cylindrical crushable bars was observed through the single particle crushing tests, one-dimensional compression tests and model footing loading tests. Conceptual distributions of contact forces of these tests are shown in Figure 7.1. The distribution of contact forces would differ in each test. Such different conditions of contact forces caused the different crushing modes and different aspects of time-dependent behavior due to particle crushing, though the chalk bars used in these tests were the same.

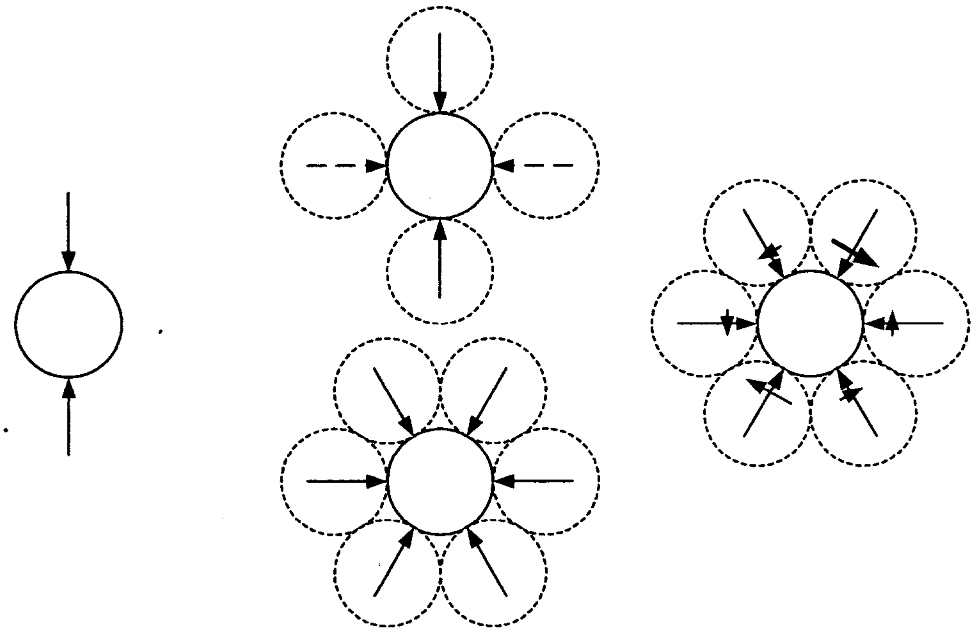

(a) Single particle crushing test

(b) One-dimensional compression test

(c) Footing loading test

**Figure 7.1 Contact forces of each test**

In the tests using chalk bars or talc bars, distribution of contact forces for occurrence of each crushing mode was not quantified rigorously, or a failure criterion for chalk bar or talc bar was not determined. To obtain the quantified distribution of contact forces and the failure criterion would be useful in creating a model for an analytical crushable particle and in verifying the model. Figure 7.2 shows an outline of an apparatus for investigating the quantified distribution of contact forces for each crushing mode. Controlled forces are loaded to a cylindrical crushable bar by the apparatus, and it is possible to observe the appeared crushing mode. The crushing behavior of a cylindrical crushable bar would be clarified by parametric experiments in which the number of contact points are changed or the ratio of a magnitude of compression forces to other contact forces are changed.

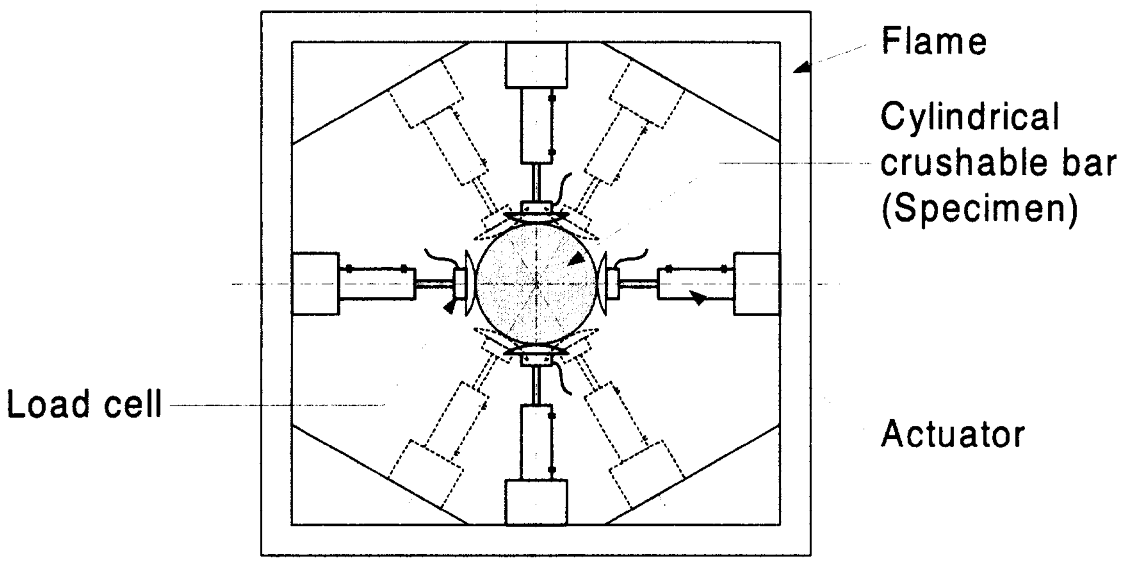


**Figure 7.2 An example of apparatus to investigate the crushing behavior of a cylindrical crushable bar**

By improving the apparatus, a spherical crushable particle could be tested. The crushing modes and the failure criterion of the spherical crushable bar would be clarified by the parametric experiments using the improved (three-dimensional) apparatus.

**(2) Investigation of parameters used in DEM analyses**

In the analyses conducted in Chapter 6, the bonding model, that was proposed in Chapter 6, could represent the chained-event of time-dependent behavior due to particle crushing, and the progress of the chained-event involved a time interval, though the time interval was a considerable short period of the time. More research will be required regarding determination of values of parameters used in the analyses in order to obtain analytical results that are comparable with the experiments. Based on the research, the applicability of the bonding model should be judged. The investigation of incorporating a damper into the bonding model or other modeling methods should be discussed after the research about the parameters.

As indicated in Chapter 6, DEM is a time-consuming calculation method. More development of computer is expected. In recent years, other analytical methods for calculation of granular materials have been developed (Kishino, 1989, Sakaguchi et al., 1996). The applicability of such methods should be investigated.

**(3) Model tests using natural deposit or field tests**

Natural deposit usually shows the following characteristics:

- The grain size is distributed,
- The configurations of particles are various,
- There exists pore water,
- The mineral of a particle is various, and
- Connectors develop among the particles.

Final destinations of this study are to understand physically the time-dependent behavior of such natural deposit due to particle crushing and to establish analytical methods for representing the behavior. In this dissertation, extremely special specimens or model grounds that were made from cylindrical crushable particles arranged regularly were used as a start of this study. If a method is developed to make an artificial specimen or a model ground that approximates the natural deposit, the artificial model ground or specimen should be used for the experiments described in this dissertation. But now, it is difficult to represent the natural deposit artificially.

It will be significant in the following respects to conduct the experiments using the natural deposit:

- The observed behavior in the experiments will be analyzed to verify an analytical method in future.
- The measured data of the experiments will be useful for establishing the below-mentioned simplified calculation methods of time-dependent settlement due to particle crushing.

In this dissertation, quartz particles from weathered granite ground were used as a natural geomaterial. But the observations in these tests were not necessarily sufficient, since the specimen of the quartz particles was three-dimensional specimen. It is necessary to invent some methods for observation of the crushing progress in the natural geomaterials or natural deposit.

**(4) Development of simplified calculation method**

It will take considerable time to apply the analytical method explained in Chapter 6 to practical problems. For the time being, an empirical simplified calculation method will be needed to estimate the time-dependent settlement of structures due to particle crushing in the ground. In order to make the simplified method, experimental data should be accumulated. For example, the following experiments are considered to be necessary; model footing or plie loading test on the model ground made of crushable geomaterials in 1G or nG, plate loading test on crushable ground as shown in Chapter 2, and long term measurement of structures based on the crushable ground. In these experiments, it will be necessary to separate the measured settlement into the following components; primary consolidation, settlement due to creep of geomaterials themselves, settlement due to creep behavior of structures (for example in the case of cast-in-place concrete pile), and others.

It is considered that time-dependent settlement of structures due to particle crushing may start from the beginning of construction of the structures, and continue after the completion of the structure. On the other hand, time-dependent settlement due to particle crushing may re-start just after an earthquake or a rapid change of groundwater level. The earthquake will change the arrangement of particles. The rapid change of groundwater level may change the magnitude of contact forces. They must change the rate of the settlement due to particle crushing. When the long term measurement of settlement of a structure is conducted, the occurrence of earthquakes and rapid changes of groundwater level should be checked during the measurement term.

**(5) Range of application of analysis and simplified calculation method**

Geomaterials are not always granular materials, but also continuous materials. It is rare, if anything, that geomaterials are discrete granular materials like the specimen or model ground described in Chapters 4 and 5. Natural deposit usually develops connectors among particles.

In the appendix of this dissertation, model pile loading tests were conducted on a tuff block, that is one of the crushable geomaterials. However, the tuff block were not much weathered unexpectedly, that is to say, it was a nearly continuous ground rather than granular ground. The matrices of the tuff block were pumice and many blocks of clay were scattered in the tuff block. It is considered that the time-dependent settlement of the model pile might be caused by compression of the matrices of pumice and the blocks of clay. It must be discussed whether such a compression could be treated as time-dependent behavior due to particle crushing. The range of application of the analyses described in Chapter 6 and the simplified calculation method should be clarified in future.

In the results of recent research in soil mechanics, constitutive equations for geomaterials have been studied based on an assumption that geomaterial is continuous material, and many phenomena in soil mechanics have been explained by the constitutive equations. But it is a fact that there are the phenomena of geomaterials that cannot be explained by the constitutive equations. Particle crushing is one of the phenomena. Thus, the basic research on mechanics of particulate media is important even in soil mechanics. In the near future, when we are faced with a certain practical problem in soil mechanics, we must use properly the approach from continuum mechanics and the approach from the mechanics of particulate materials according to the situation.

# APPENDIX

# OBSERVATIONS OF TIME-DEPENDENT SETTLEMENT OF MODEL PILE LOADING TESTS ON OHYA TUFF BLOCK

## A.1 Introduction

A series of model pile loading tests on models made of tuff were conducted to confirm the time-dependent behavior due to particle crushing. In the experiments, in addition to measurement of settlement of the model pile, observation of the model ground was conducted. Consequently, time-dependent settlement of the model pile was observed even though the model ground was dry. However, particle crushing could not observed since the model ground made of tuff block was considerably intact contrary to the author's expectation. The influence of water existence and configuration of pile tip (i.e. closed end or open end) on the time-dependent settlement was also discussed.

In this appendix, the outline of the model pile loading tests is described.

## A.2 Test procedures

Figure A.1 illustrates a general view of the test apparatus. A pneumatic actuator installed on the top of a strong steel flame, having a capacity of 30kN, generates a continuous vertical load for the test. A model pile was a steel pipe pile of 20mm diameter and 150mm length. The model pile was in contact with a model only by its tip, thereby the pile was supported only by the ground beneath the pile.

The model ground was made of a cylindrical block of Ohya stone having a diameter of 250mm and a height of 200mm. It was put in a cylindrical steel container, and the side of it was fixed by compacted sand and timber block. Ohya stone is a green tuff composed of pyroclastic sea deposits during the Miocene epoch, spreading over the northern Kanto area of Japan. Its main characteristics are given as follows : specific density = about 2.4 ; void ratio = 0.6 – 0.7 ; natural water content = 25 – 30% (Yokoyama et al., 1995).

Blocks of Ohya stone that prepared for these tests were commercially available. Thus these blocks were kept under room-dry conditions when they had been brought to the laboratory. Yokoyama et al.(1995) investigated the influence of wet-dry-wet histories on the strength of Ohya stone. Several unconfined compression tests were conducted on some specimens that had been subjected to the different number of wet(soaking in groundwater)-dry(oven drying)-wet cycles. They found out that values of the unconfined compression strength decreased after the first cycle, but kept constant for successive cycles.

Taking their experiments into account, the block of Ohya stone was experienced the wet-dry-wet-dry histories in the case of dry model ground, or the wet-dry-wet histories in the case of wet model ground. It was found that the unconfined compression strength was about 10MN/m$^2$ for the specimen experienced the wet-dry-wet-dry histories, and about 5MN/m$^2$ for the specimen experienced the wet-dry-wet histories.

The vertical load was measured through a 50kN load cell. The pile settlement was measured by means of two 10-mm-travel displacement transducers.

Table A.1 shows the test cases with their conditions and the summary of results. Four static load tests and five sustained load tests were performed. For the static load tests, the load was applied in controlled steps, with each step being 1 to 3 kN. At each step the load was maintained until the rate of settlement became less than 0.01mm/min before the next increment of load was applied. For the sustained load tests, the load was monotonically applied at the rate of 1kN/min until the load reached a sustained load, after that the load had been sustained for 7 days. The sustained loads were determined by predetermined ratios of sustained load to yield load. The yield load means here the load at the first deflection point appearing in a load - displacement curve. This ratio will be called "load ratio" in this study. The parameters of these tests are the load ratio, existence of water in ground (dry or saturated) and pile tip configuration (open end pile or close end pile).

Photograph A.1 shows (a) a block of model ground, (b) loading flame and (c) pile set to the model ground.

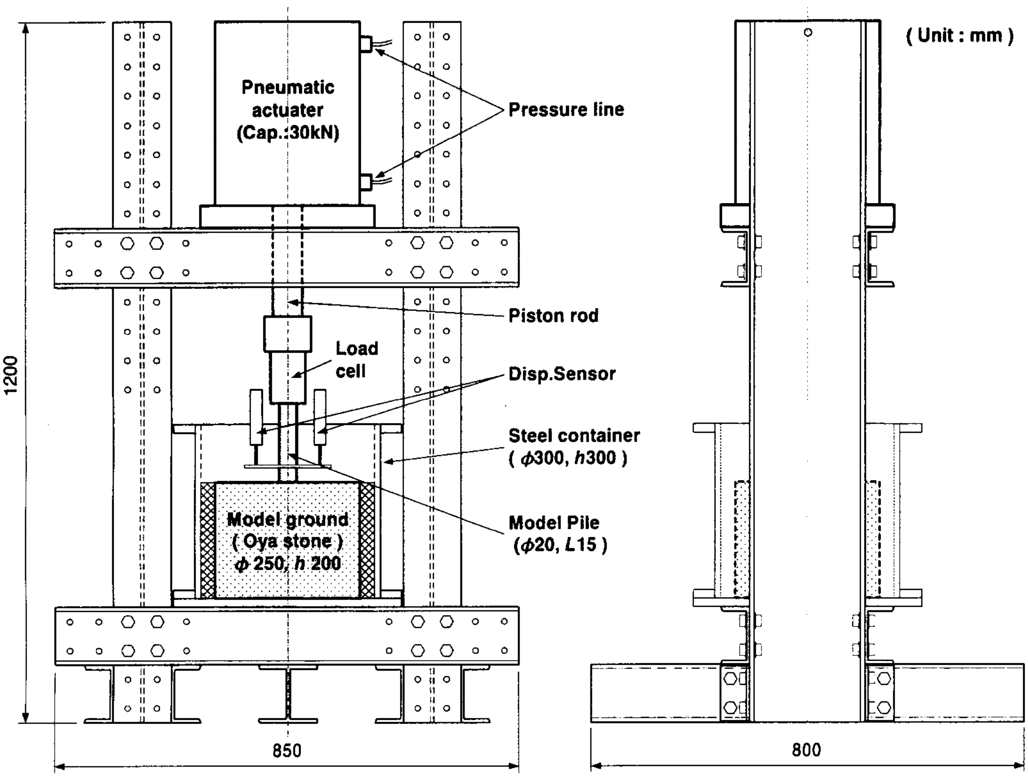


**Figure A.1 Test apparatus of model pile loading test**

**Table A.1 Test cases of model pile loading test and summary of results**

(a) Static load test ( SLT )

| Test No. | Water condition of model ground | Pile tip configuration | Yield load (kN) | Ultimate Load (kN) |
|---|---|---|---|---|
| SLT11 | Dry | Close | 19.6 | 21.5 |
| SLT12 | Dry | Close | 18.1 | 25.5 |
| SLT2 | Saturated | Close | 9.3 | 13.3 |
| SLT3 | Dry | Open | 13.7 | 23.5 |

(b) Sustained load test ( SUS )

| Test No. | Water condition of model ground | Pile tip configuration | Yield load (kN) | Sustained load (kN) | Load ratio† |
|---|---|---|---|---|---|
| SUS11 | Dry | Close | 18.6 | 18.6 | 1.0 |
| SUS12 | Dry | Close | 12.8 | 21.5 | 1.7 |
| SUS13 | Dry | Close | 10.3 | 19.6 | 1.9 |
| SUS2 | Saturated | Close | 6.87 | 10.8 | 1.6 |
| SUS3 | Dry | Open | 16.7 | 20.6 | 1.2 |

† Load ratio = Sustained load / Yield load

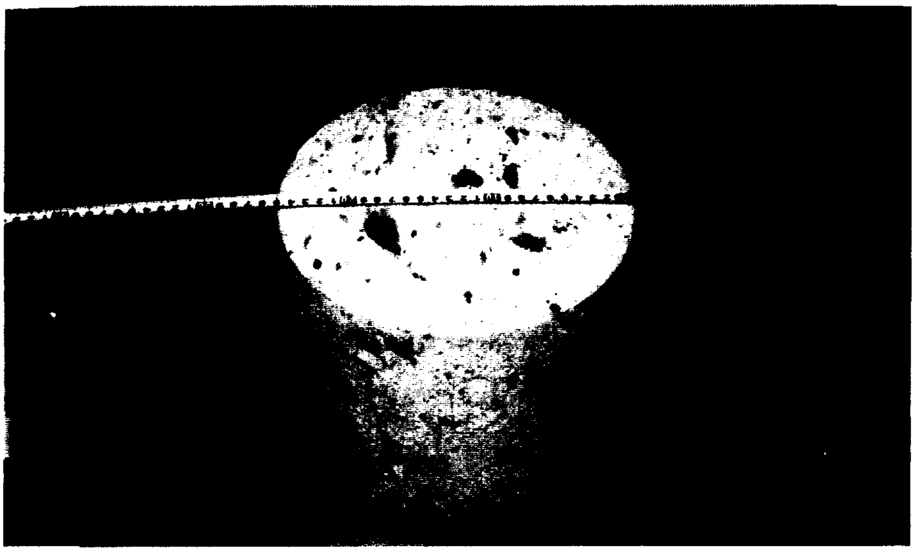

(a) Ohya tuff block

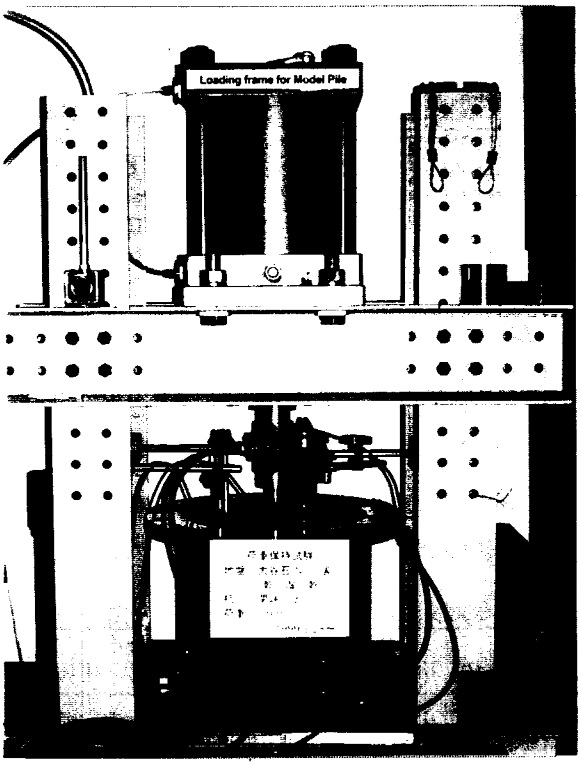


(b) Loading system

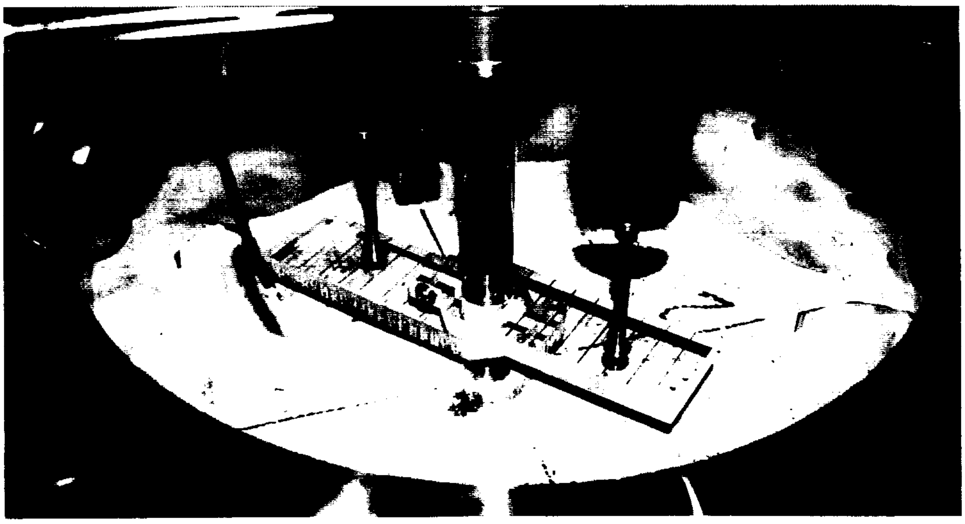

(c) Pile set to the model ground

Photo. A.1 Model pile loading test

## A.3 Test results

Figure A.2 shows the load – settlement curves of all the tests. The left figure shows the five curves obtained from the tests performed on dry model ground with close end pile. All these tests show a similar stiffness up to 10kN. But the ultimate loads of the test SLT11 and SLT12 differ in spite of the same test condition. Taking into account this result, the load ratio of the sustained load test was defined as the ratio of sustained load to yield load, which is different from the definition by Yet et al.(1996) who defined a load ratio in their model pile loading tests as a ratio of sustained load to ultimate capacity. In the case of SUS11, SUS12 and SUS13, the vertical part of each curve shows the creep settlement for one week. The right figure shows the four curves measured from the tests performed on saturated model ground with close end pile and on dry ground with open end pile. In the cases of SLT2 and SUS2 (the cases of saturated ground with close end pile), the initial stiffness and ultimate capacity are smaller than those of the cases of dry ground with close end pile. In the cases of SLT3 and SUS3 (the cases of dry ground with open end pile), the characteristics of the curves is similar to those of the cases of dry ground with close end pile except the amount of creep settlement of SUS3.

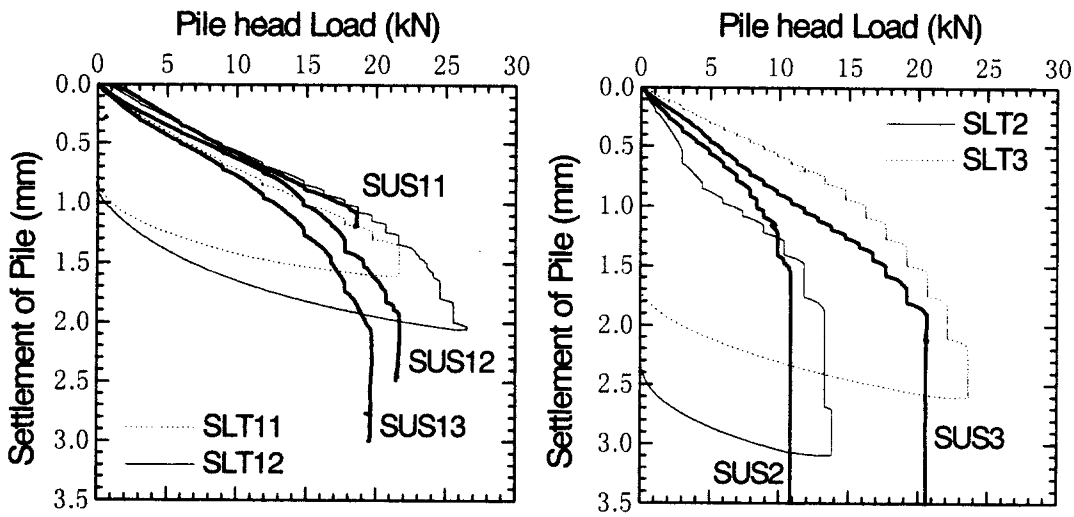


**Figure A.2 Load – settlement curves of model pile load tests**

A set of measurements of deformation at the ground surface are shown in Figure A.3. In some cases, vertical displacements of ground surface were measured by using two gap sensors with an accuracy of 0.00025mm. The vertical displacements at the distance of 40mm and 80mm from the center of pile appeared not upward but downward, and are much smaller than pile displacement. In other cases, the measurement of the displacement of ground surface did not show any bulging at the ground surface. Thus the failure mechanism of SLT may be the local shear failure.

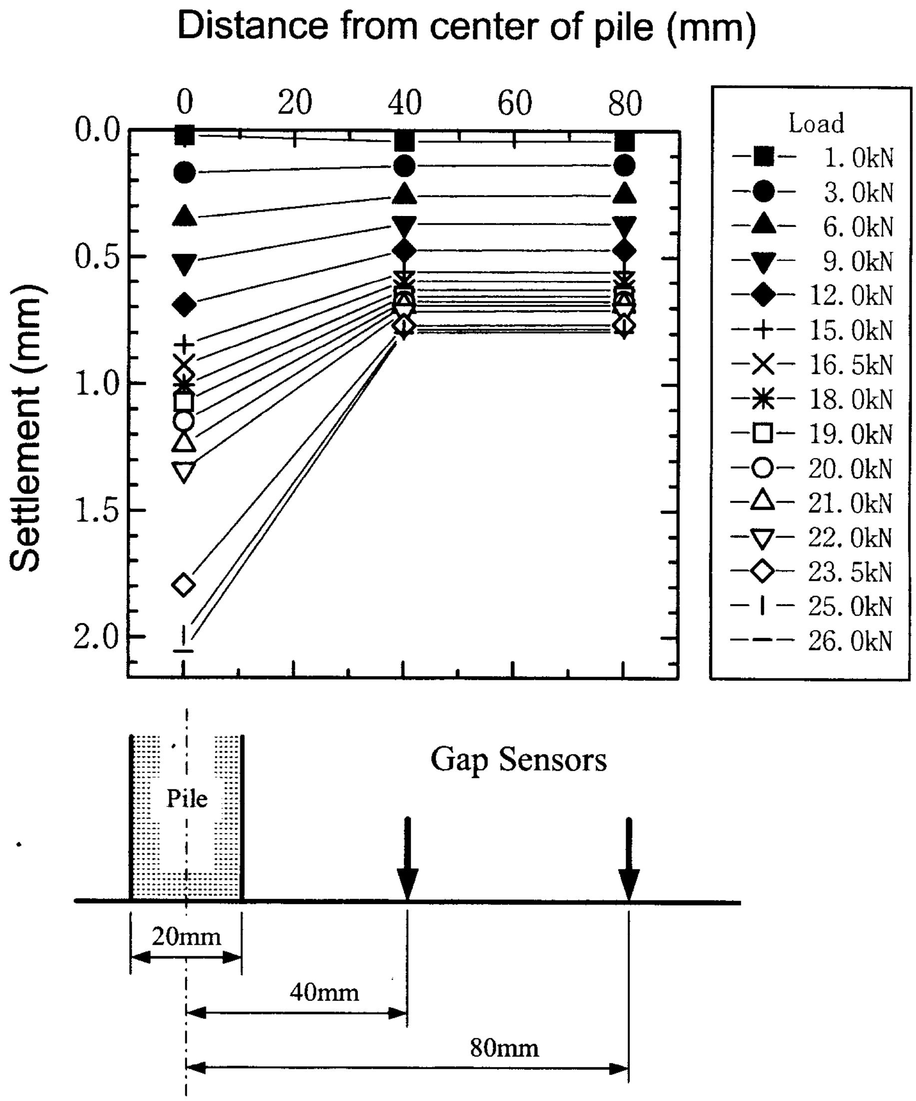


**Figure A.3 Deformation of ground surface (SUS12)**

Figure A.4 shows the increment of settlement with logarithmic time during the sustained load period in the loading test. As can be seen, the creep settlement of the piles initially increases almost linearly with the logarithm of time, but the gradients of the curves accelerate as time goes on, except the case SUS11. The similar trend was reported in a plate loading test on calcareous sediments (Sharp and Seters, 1988, see Figure 1.13 in Chapter 1).

Yet et al.(1996) and Leung et al.(1996) defined a creep coefficient as the magnitude of pile settlement for one logarithmic (to base 10) time cycle. In this study, the creep coefficient that they defined is called the rate of creep settlement. Thereby, the rate of creep settlement before the change of the gradient is defined as primary rate of creep settlement $C_{\alpha s1}$, and the rate of creep settlement after the change of the gradient is defined as secondary rate of creep settlement $C_{\alpha s2}$. From the curves of SUS11, SUS12 and SUS13 (all of dry ground and close end pile), it is clearly found that the $C_{\alpha s1}$ and $C_{\alpha s2}$ increases with load ratio. The curves of SUS2 (saturated ground and close end pile) and SUS3 (dry ground and open end pile) that have the lower load ratio of 1.6 or 1.2 respectively, show a larger secondary rate of creep settlement than SUS13 (dry ground and close end pile) that has the load ratio of 1.9. The case of SUS3 led to the ultimate condition after 4.5 days : The rate of creep settlement was over 0.1mm/sec.

The time-dependent settlement of pile in SUS2 would be caused not only by consolidation of model ground, but also by influence of water existence to disintegration of microscopic structure of model ground. The time-dependent settlement of pile in SUS3 during the term of $C_{\alpha s2}$ would be caused not only by creep of the model ground but also by influence of thin wall of pile to disintegration of microscopic structure of model ground. The mechanism of the acceleration of the rate of creep settlement will be discussed in the following paragraph.

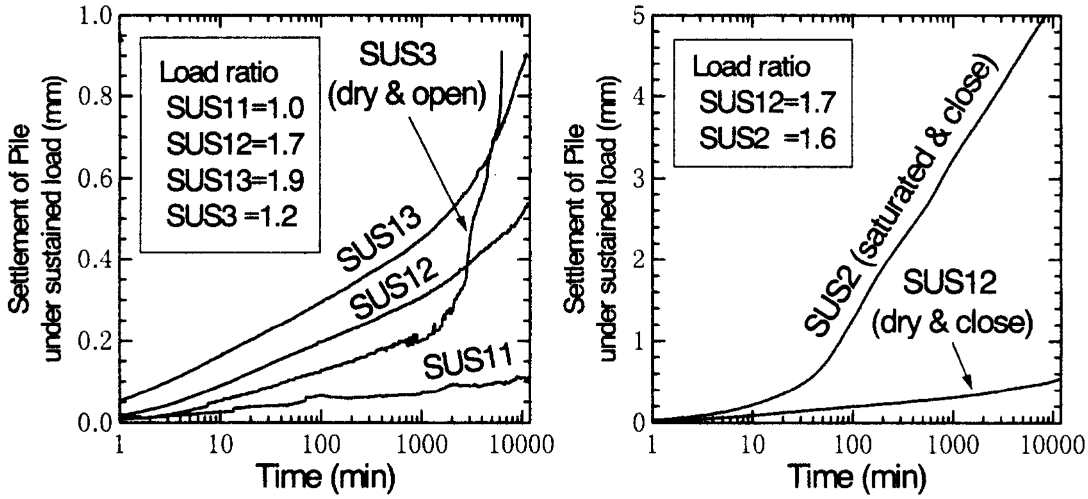


**Figure A.4 Settlement – time curves (Sustained load tests)**

In Figure A.5, the primary and secondary rates of creep settlement are plotted against the load ratio. This figure also shows that the rates of creep settlement increase with load ratio linearly in the cases of dry ground and close end pile. The plots of SUS2 are out of this trend. In the case of SUS3, the $C_{\alpha s1}$ is on the trend of SUS11-SUS13, but the $C_{\alpha s2}$ is out of the trend of SUS12 and SUS13. This suggests that the mechanism of time-dependent settlement of the primary region of $C_{\alpha s1}$ and that of the secondary region of $C_{as2}$ may differ. In the primary region, the open end pile will settle in the same mechanism of close end pile, while in the secondary region, the open end pile will settle with intrusion of soil into the pipe pile.

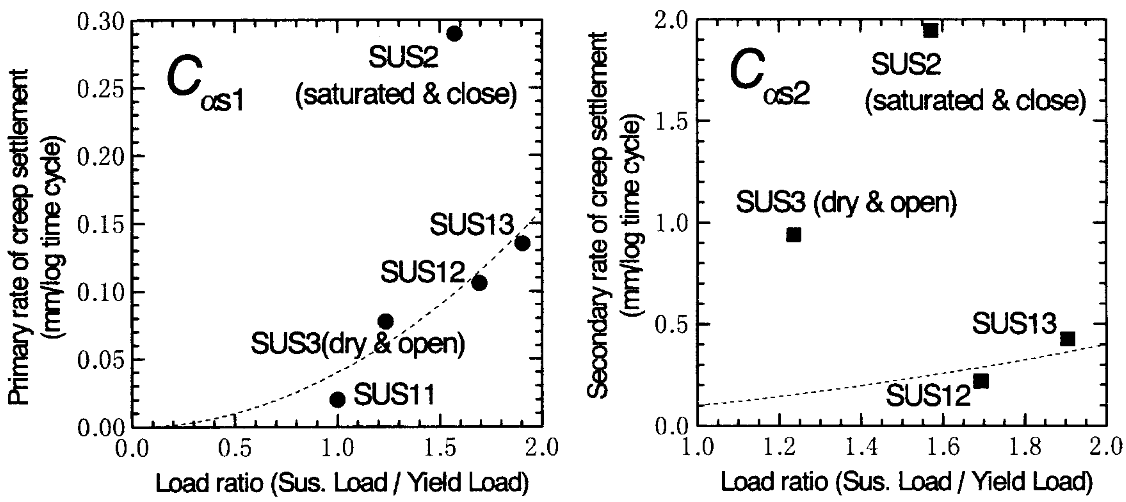


**Figure A.5 Rate of creep settlement versus load ratio**

After each test, the block of model ground was cut vertically passing through the contact area of the pile, as shown in Figure A.6, and the section was observed by the digital microscope (used in Chapter 3,4 and 5) to confirm the occurrence of particle crushing. But particle crushing was not observed since the Ohya stones used for the tests were unexpectedly intact. Three examples of pictures taken by the digital microscope are shown in Photograph A.2. These pictures show the ground beneath the model pile : The hollow in the upper part of each picture is a part of impression of the pile. The white parts in the ground are matrices made of pumice. The yellow or brown parts in the ground are blocks of clay called "Miso" in Japanese. Crystal particles --- for example quartz, Feldspar, and mica --- are scattered. In Photograph A.2(a) and (b), cracks occurred in the ground beneath the edge of the hollow of pile. In Photograph A.3(c), there were the blocks of clay under the hollow of pile. Kitaoka et al.(1977) described that the matrix made of pumice has large compressibility because of its porous structure consists of microscopic voids. The block of clay also has large compressibility. Hence, it is considered that the time-dependent settlement of pile was caused by time-dependent compression of the matrices and blocks of clay under the sustained load, and that the acceleration of the rate of settlement would be related to the cracking in the ground under the model pile. Unfortunately, it is impossible to observe the detail of the compression mechanism by the observation system of this study.

After the test of SUS3 finished, the soil inside the pile (soil plug) was observed. Photograph A.3 shows the pictures of the model ground and the soil plug. From these photographs, it is clear that the upper surface of the soil plug reached the same level of the surface of the ground, and the soil plug was not in a solid state but broken to pieces. The acceleration of the rate of creep settlement would be caused by the intrusion of soil into the pipe pile with crushing of the soil plug. This mechanism of settlement is different from the compression of the matrix of pumice or block of clay.

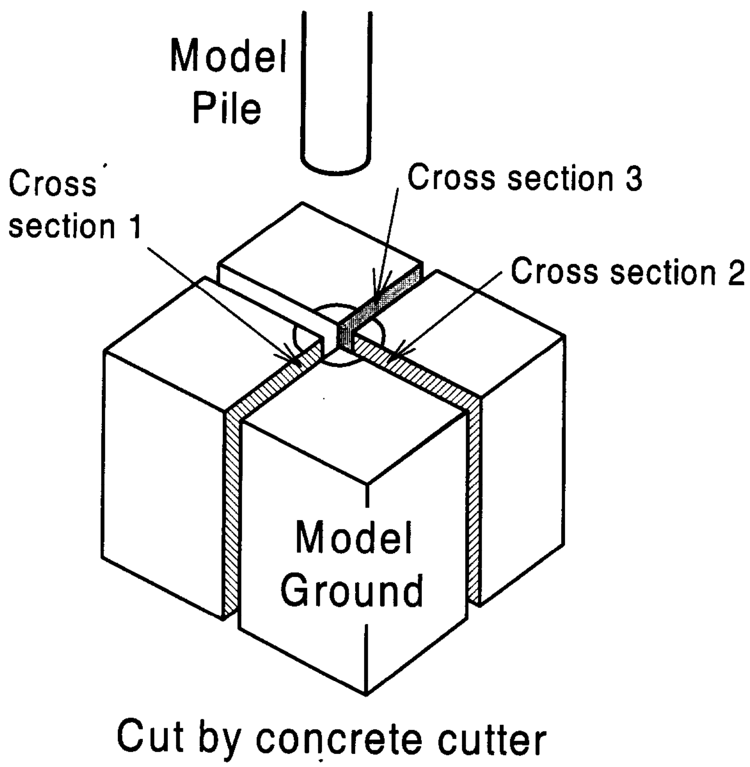


**Figure A.6 Observed cross section of Photograph A.2**

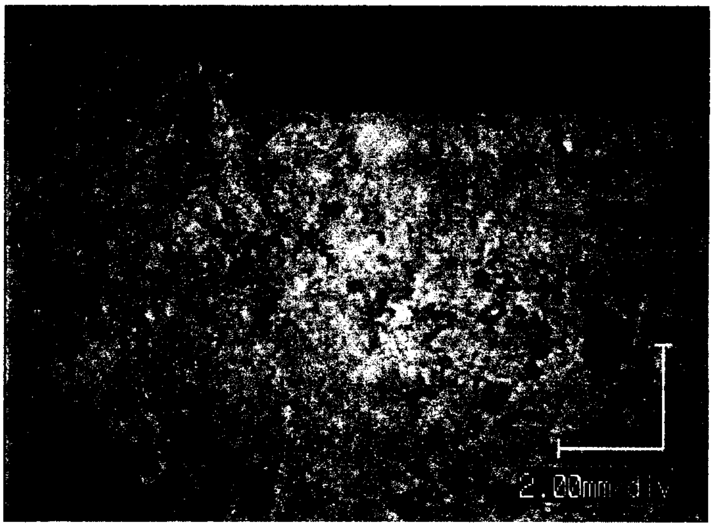


(a) Cross section 1

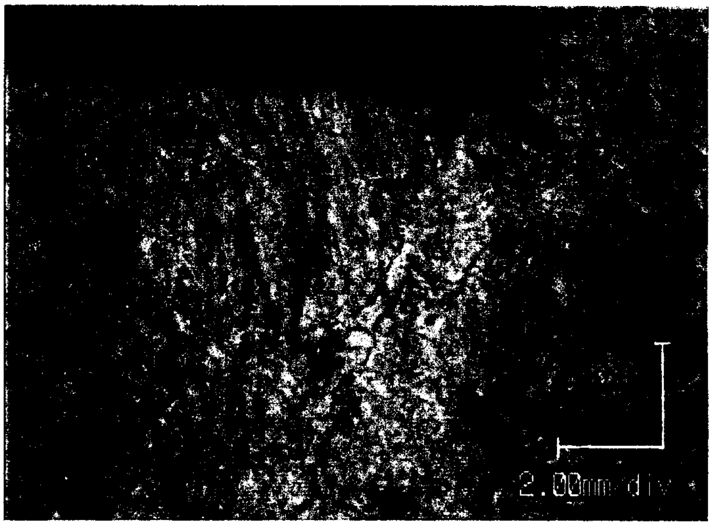


(b) Cross section 2

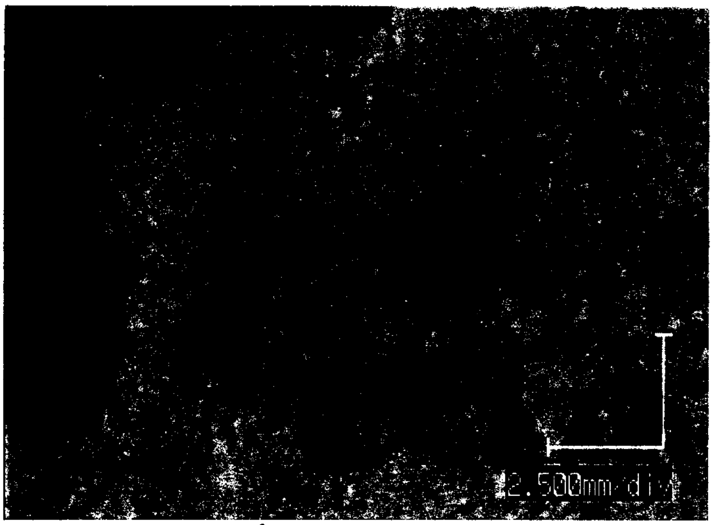


(c) Cross section 3

**Photo. A.2 Observation of the model ground beneath the pile by digital microscope (SUS12)**

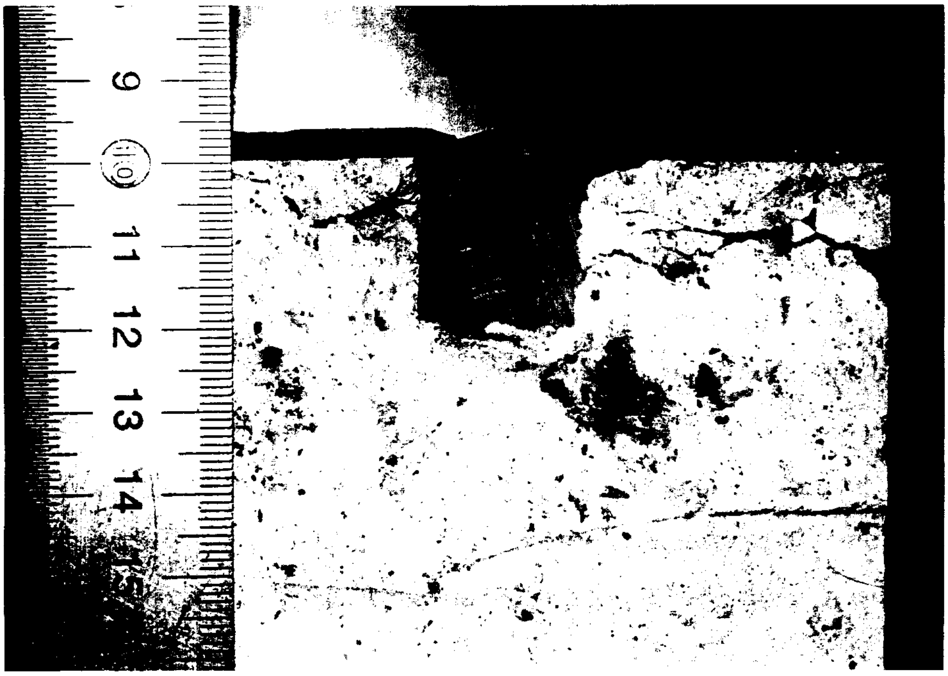


**(a) Socket of model ground after test (Case SUS3)**
**The model ground was fixed by resin**
**and cut vertically through the center of pile.**

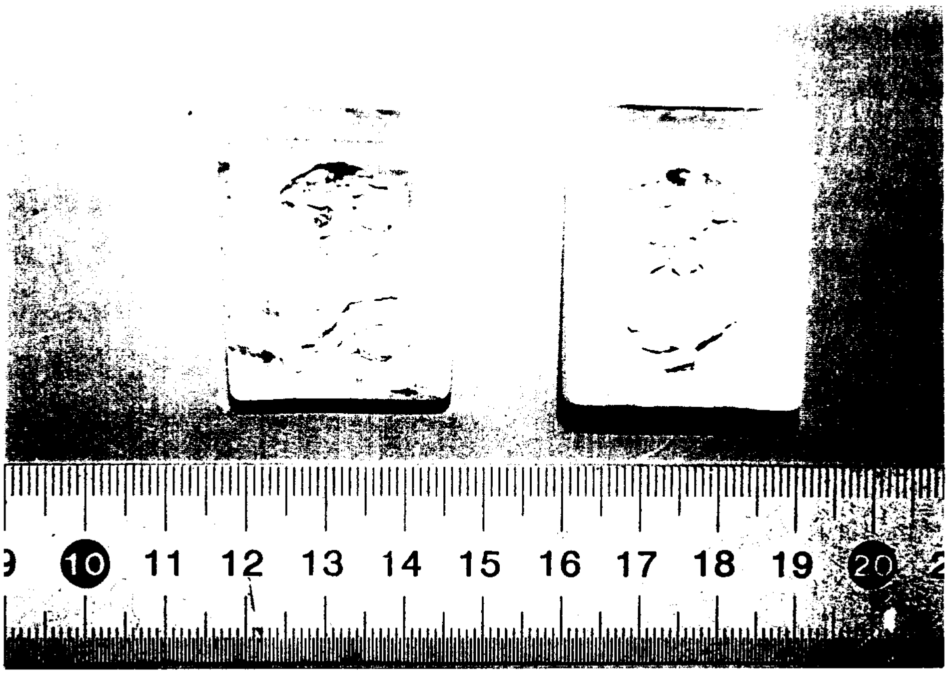


**(b) Soil plug (Case SUS 3)**
**The soil plug was fixed by resin and cut vertically.**

**Photo. A.3 Observation of the soil plug after the test SUS3**

## A.4 Conclusions

In this appendix, model pile loading tests on model ground made of Ohya tuff were conducted. The following conclusions are drawn.

- Time-dependent settlement of the model pile was occurred even on the dry ground.
- The settlement of the model pile increased linearly with time of logarithmic scale, but in a large load ratio case (in this experiment, when the load ratio is over 1.5 in the case of dry ground and close end pile), the rate of creep settlement accelerates under the sustained load.
- The following three factors would be concerned in the time-dependent settlement of pile and acceleration of the rate of creep settlement :
  - compression of matrices of pumice and blocks of clay,
  - cracking in the ground, and
  - intrusion of soil into the pipe pile accompanied by crushing of soil plug.

In this study, from Chapter 3 to 6, the time-dependency of particle crushing was investigated. Particle crushing is one of the failure patterns in geomaterials. In future study, the time-dependency of failure in geomaterials ("failure" means, for example, breakdown of soil structure, particle crushing, breaking of bonding or cementation, breaking to pieces of rock materials, and smashing of microscopic voids in geomaterials) should be investigated to obtain a proper interpretation of time-dependent behavior of soil structures and foundation structures.

# REFERENCES


1) Airey D. W., Randolph, M. F. and Hyden, A. M. (1988) : "The strength and stiffness of two calcareous sands," Proc. of the Int. Conf. on Calcareous Sediments, Perth, Vol.1, pp.43-50.

2) Barksdale, R. D. and Blight, G. E. (1997) : "Compressibility and settlement of residual soils," Mechanics of Residual Soils, Chapter 8, Balkema, Rotterdam, Brookfield, pp.95-154.

3) BCP Committee(1971) : "Field tests on piles in sand," Soils and Foundations, Vol.11, No.2, pp.29-49.

4) Bishop, A.W., Webb, D.L. and Skinner, A.E. (1965) "Triaxial test on soil at elevated cell pressures," Proceedings of the 6th International Conference on Soil Mechanics and Foundation Engineering, Montreal, Vol.1, pp.170-174.

5) Brenner, R. P., Garga, V. K. and Blight, G. E. (1997) : "Shear strength behavior and measurement of shear strength in residual soils," Mechanics of Residual Soils, Chapter 9, Balkema, Rotterdam, Brookfield, pp.155-220.

6) Cundall, P. A. (1971) : "A computer model for simulating progressive, large scale movements in blocky rock systems," Proceedings of the Symposium of the International Society of Rock Mechanics, Nancy, France, Vol.1, Paper No. II-8.

7) Cundall, P. A. and Strack, O. D. L. (1979) : "A discrete numerical model for granular assemblies", Geotechnique Vol.29, No.1, pp.47-65.

8) de Beer, E. E. (1963) : "The scale effect in the transposition of the results of deep-sounding tests on the ultimate bearing capacity of piles and caisson foundations," Geotechnique, Vol.13, No.1, pp.39-75.

9) Fukumoto, T. (1990) : "A grading equation for decomposed granite soil," Soils and Foundations, Vol.30, No.1, pp.27-34.

10) Fukumoto, T. (1992) : "Particle breakage characteristics of granular soils," Soils and Foundations, Vol.32, No.1, pp.26-40.

11) Galer, M. M., Sasaki, S. and Nakamura, Y. (1998) : "Field investigation of a decomposed granite site," Proceedings of the International Symposium on Problematic Soils – IS Tohoku 1998, Vol.1, Balkema, pp.453-456.

12) Galer, M. M., Sasaki, Y. and Hiraga, K.(1999) : "Time-dependent compressibility of some decomposed granites," Proceedings of the Symposium on Geotechnical Problems

of Crushable Soil, Japanese Geotechnical Society, pp.35-40.

13) Galer M. M. (1999) : "A study on the mechanical properties of undisturbed decomposed granite based on in-situ testing and triaxial testing results under elevated confining pressure," Ph. D. Thesis, Hiroshima Univ..

14) Haruyama, M. (1969) : "Effect of water content on the shear characteristics of granular soils such as Shirasu," Soils and Foundations, Vol.9, No.3, pp.35-57.

15) Hattori, T., Seto, K., Sakaguchi, M., Kitagawa, R. and Kusakabe, O. (1998a) : "The mechanical characteristics of Hiroshima granite," Jour. of Geotechnical Engineering, Proc. JSCE, No.589 / III-42, pp.1-10 (in Japanese).

16) Hattori, T., Kitagawa, R., Seto, K., Sokobiki, H. and Kusakabe, O. (1998b) : "Field investigation of weathering in Hiroshima granite," Jour. of Geotechnical Engineering, Proc. JSCE, No.589 / III-42, pp.359-368 (in Japanese).

17) Hattori, T., Xu, L., Galer M. M., Kitagawa, R. and Kusakabe, O. (1998c) : "Numerical simulation of stress-strain behavior of weathered granites from two different sites," Proceedings of the International Symposium on Problematic Soils – IS Tohoku 1998, Vol.1, Balkema, pp.465-468.

18) Hirano, K., Hashizume, T., Yamada, T., Fukushima, S. and Kitajima, A. (2000) : "Behavior and Stability investigation of high embankment constructed in large scale land development project at weathered granite rock district," Journal of Geotechnical Engineering, Proc. JSCE, No.666 / III-53, pp.303-320 (in Japanese).

19) Hull T. S., Poulus, H. G. and Alehossein, H. (1988) : "The static behavior of various calcareous sediments," Proc. of the Int. Conf. on Calcareous Sediments, Perth, Vol.1, pp.87-96.

20) ISO(1996) : "Soil quality --- Determination of aggregate strength --- Part 1 : Tensile strength measurement (crushing test)", Draft International Standard ISO/DIS 11273-1, ISO/TC 190/SC 5.

21) Itasca consulting group (1999) : "Particle Flow Code in 2 Dimensions (Version 2.0), Theory and background," pp.1-1 – 2.11.

22) Jaeger, J. C. (1967) : "Failure of rocks under tensile conditions," Int. Jour. Rock. Min. Sci., Vol.4, pp.219-227.

23) Jaros, M. B. (1978) : "The settlement of two multi-storey buildings on residual Ventersdorp laba. S. A.," Instn. Civil Engs. Symp. on Soil-Structure Interraction, Durban, South Africa, 20p. (From Barksdale, R. D. and Blight, G. E. (1997) :

"Compressibility and settlement of residual soils," Mechanics of Residual Soils, Chapter 8, Balkema, Rotterdam, pp.95-154.)

24) Kishino, Y. (1989) : "Investigation of the quasi-static behavior of granular materials with a new simulation method," Journal of Geotechnical Engineering, Proc. JSCE, No.406 / III-11, pp.97-106 (in Japanese).

25) Kitaoka, M., Tanaka, S., Kusuniki, K. and Endo, G. (1977) : "Mechanical properties of Ohya tuff --- Correspondence of experimental results of in-situ and laboratory tests and effects of rock texture on mechanical properties ---," Journal of the Mining and Metallurgical Institute of Japan, Vol.93, No.1067, pp.1-32 (in Japanese).

26) Kojima, S.(1993) : "The micro-rheological interpretation for time-dependent behavior of clayey soil," Graduation Thesis, Dept. of Civil and Environmental Engineering, Hiroshima University, 45p (in Japanese).

27) Kusakabe, O., Maeda, Y., Ohuchi, M. and Hagiwara, T. (1991) : "Strength-deformation characteristics of an undisturbed scoria and effects of sample disturbance," Jour. of Geotechnical Engineering, Proc. JSCE, No.439 / III-17, pp.69-78 (in Japanese).

28) Kusakabe, O., Maeda, Y. and Ohuchi, M. (1992) : "Large-scale loading tests of shallow footings in pneumatic caisson," Jour. of Geotechnical Engineering, Proc. ASCE, Vol.118, No.11, pp.1681-1695.

29) Lee, D. M. (1992) : "The angles of friction of granular fills," Ph.D. Dissertation, University of Cambridge. (From McDowell, G. R. and Bolton, M. D. (1998) : "On the micromechanics of crushable aggregates," Geotechnique, Vol.48, No.5, pp.667-679.)

30) Lee, K. L. and Farhoomand, I. (1967) : "Compressibility and crushing of granular soil in anisotropic triaxial compression," Canadian Geotechnical Journal, Vol.9, No.1, pp.68-86.

31) Lee, K.L., Seed, H.B. and Dunlop, P. (1967) : "Effect of moisture on the strength of a clean sand," Journal of Soil Mechanics and Foundation Engineering Division, ASCE, Vol.39, No.SM6, pp.17-40.

32) Leung, C. F., Lee, F. H. and Yet, N. S. (1996) : "The role of particle breakage in pile creep in sand," Canadian Geotechnical Jour., Vol.33, No.6 , pp.888-898.

33) McDowell, G. R. and Bolton, M. D. (1998) : "On the micromechanics of crushable aggregates," Geotechnique, Vol.48, No.5, pp.667-679.

34) McDowell, G.R. (1999) : "Micro mechanics of clastic soil," International Workshop on Soil Crushability, Ube, Yamaguchi.

35) McDowell, G.R. and Amon, A. (2000) : "The application of Weibull statistics to the fracture of soil particles," Soils and Foundations, Vol.40, No.5, pp.133-141.

36) Mikasa, M.(1963) : "Consolidation of soft clay," Kajima Institute Publishing Co., Ltd. (in Japanese) (From Aboshi, H.(1969) : "Chapter 4 Consolidation," Soil Mechanics, Edited by Mogami, T., Supervised by JSCE, Gihodo Suppan Co., Ltd., pp.370-371(in Japanese)).

37) Miura, N. and Yamanouchi, T. (1971) : "Drained shear characteristics of standard sand under high confining pressures," Proceedings of the Japan Society of Civil Engineers, No.193, pp.69-79 (in Japanese).

38) Miura, N. and Yamanouchi, T. (1972) : "Compressibility of sand under high isotropic pressures," Proceedings of the Japan Society of Civil Engineers, No.203, pp.45-52 (in Japanese).

39) Miura, N. and Yamanouchi, T. (1977) : "Effect of particle-crushing on the shear characteristics of a sand," Proceedings of the Japan Society of Civil Engineers, No.260, pp.109-118 (in Japanese).

40) Miura, N. and O-hara, S. (1979) : "Particle-crushing of a decomposed granite soil under shear stresses," Soils and Foundations, Vol.19, No.3, pp.1-14.

41) Miura, N., Murata, H. and Yasufuku, N. (1984) : "Stress-strain characteristics of sand in a particle crushing region," Soils and Foundations, Vol.24, No.1, pp.77-89.

42) Miura, N.(1985) : "Point resistance of piles in sand," Proc. 11th Int. Conf. on SMFE, San Francisco, Vol.3, pp.1445-1448.

43) Miura, S., Yagi, K. and Kawamura, S. (1996) : "Static and cyclic shear behavior and particle crushing of volcanic coarse grained soils in Hokkaido," Jour. of Geotechnical Engineering, Proc. JSCE, No.547 / III-36, pp.159-170 (in Japanese).

44) Miura, S.and Yagi, K. (1997) : "Particle breakage of volcanic coarse-grained soils and its evaluation," Jour. of Geotechnical Engineering, Proc. JSCE, No.561 / III-38, pp.257-269 (in Japanese).

45) Miyake, M. and Kusakabe, O. (1997) : "Shear band observed in loading tests," Proc. of Deformation and Progressive Failure in Geomechanics – IS Nagoya 1997, pp.887-898.

46) Mukai, M., Takino, Y. and Yamazaki, H. (1999) : "Long term measurement of super-high banking with decomposed granite soil," Proc. of the 54th Annual Conf. of JSCE, 3-(A), pp.780-781 (in Japanese).

47) Mukunoki, T., Otani, J. and Obara, Y. (1999a) : "Evaluation of the property of crushable

soils around pile tip due to vertical loading using X-ray CT scanner," Proceedings of the Symposium on Geotechnical Problems of Crushable Soil, Japanese Geotechnical Society, pp.89-94 (in Japanese).

48) Mukunoki, T., Otani, J., Sugawara, K. and Obara, Y. (1999b) : "Evaluation of crushability in soils around pile tip using X-ray CT scanner," Proceedings of the 44th Symposium on Geotechnical Engineering, Japanese Geotechnical Society, pp.101-106 (in Japanese).

49) Mukunoki, T. and Otani, J. (2000) : "The behavior of the ground at the tip and around the pile due to loading using X-ray CT method," Proc. 35th Japan National Conf. on Geotechnical Engineering, 169, pp.333-334 (in Japanese).

50) Nakata, Y., Hyde, A.F.L., Hyodo, M. and Murata, H. (1999) : "A probabilistic approach to sand particle crushing in the triaxial test," Geotechnique Vol.49, No.5, pp.567-583.

51) Nonami, S., Akita, S. and Karube, D (1998) : "Effect of grain shape and particle breakage on shear strength of coarse materials," Proc. 33th Japan National Conf. on Geotechnical Engineering, pp.37-38 (in Japanese).

52) Ohno, S. and Sawada, S. (1999) : "Bearing capacity of piles in sands with different crushabilities under various stress conditions," Proceedings of the Eleventh Asian Regional Conference on Soil Mechanics and Geotechnical Engineering, Seoul, Vol.1, pp.249-252.

53) Ohuchi, M., Kusakabe, O. Hagiwara, T. and Abe, S. (1994) : "Development of shear band and particle crushing observed in in-situ loading tests on a sedimented sand," Jour. of Geotechnical Engineering, Proc. JSCE, No.487 / III-26, pp.207-216 (in Japanese).

54) Randolph, M., Finnie, I. and Joer, H. (1993) : "Performance of shallow and deep foundations on calcareous soil," International Seminar in Kagoshima '93 – Regional soils –, Geomechanics Group of Kagoshima University, Kyushu Branch of JSSMFE, pp.169-220.

55) Roscoe, K. H., Schofield, A. N. and Thurairajah, A. (1963) : "Yield of clay in states wetter than critical," Geotechnique, Vol.13, pp.211-240.

56) Roscoe, K.H. and Burland, J.B.(1968) : "On the generalized stress strain behavior of 'wet' clay," Engineering Plasticity, Heyman, J. and Leckie, F.(eds.), pp.535-609. (From Handbook of Geotechnical Engineering (1999) : "Section 3.3 Constitutive equation of soils," Chapter 2, JGS, pp.98-116(in Japanese).)

57) Rowe, P.W. (1962) : "The stress-dilatancy relation for static equilibrium of an assembly

of particles in contact," Proc. Royal Soc., London, Series A. ( From Yamaguchi, H. (1969) : "Soil Mechanics," Gihodo Suppan Co., Ltd., pp.179-181(in Japanese). )

58) Sakaguchi, H., Murakami, A., Hasegawa, T. and Shirai, A. (1996) : "Connected lattice cellular-automation particles: a model for pattern formation in vibrating granular media," Soils and Foundations, Vol.36, No.1, pp.105-110.

59) Schofield, A. N. and Wroth, C. P. (1968) : "Critical state soil mechanics," McGraw-Hill, London.

60) Sharp, D. E. and A. J. van Seters (1988) : "Results and evaluation of plate load test results," International Conference on Calcareous Sediments, Perth, Balkema, Vol.2, pp.473-483.

61) Shinjo, T. (2000) : "Time dependent behavior of crushable sand under one-dimensional compression", Tsuchi-to-Kiso, Japanese Geotechnical Society, Vol.48, No.10, pp.19-22(in Japanese).

62) Terzaghi, K. (1923) : Die Berechung der Durchlassigkeitziffer des Tones aus dem Verlauf der Hydri dynamischen Spannungserscheinungen. (From Terzaghi, K. and Peck, R. B. (1967) : "Soil Mechanics in Engineering Practice, Second Edition," John Wiley and Sons, pp.84-85.)

63) Terzaghi, K. and Peck, R. B. (1967) : "Soil Mechanics in Engineering Practice, Second Edition," John Wiley and Sons, pp.107.

64) Turcotte, D. L. (1986) : "Fractals and Fragmentation," Journal of Geophysical Research, Vol.91,.No.B2, pp.1921-1926.

65) Uno, H., Higuchi, Y. and Sueoka, T. (1999) "A study on interpretation of time in distinct element method," Proceedings of 34th Japan National Conference on Geotechnical Engineering, Tokyo, Vol.2, pp.453-454.

66) Vesic, A. S. and Clough, G. W. (1968) : "Behavior of granular materials under high stresses," Jour. of Soil Mechanics and Foundations Division, Proc. ASCE, Vol.94, No.SM3, pp.661-688.

67) Weibull, W.(1951) : "A statistical distribution function of wide applicability," Journal of Applied Mechanics, ASME, Vol.18, pp.293-297.

68) Yamagata, M. and Kurino, S. (1984) : "An engineering classification of weathered granites and its application in designing of bridge," Journal of the Japan Society of Engineering Geology, Special Issue, pp.91-102 (in Japanese).

69) Yasufuku, N. and Hyde, A. F. L. (1995) : "Pile end-bearing capacity in crushable

sands," Geotechnique, Vol.45, No.4, pp.663-676.

70) Yasufuku, N. and Kwag, J.M. (1999) : "Significance of soil particle fragmantation strength related to soil crushability," Proceedings of the Eleventh Asian Regional Conference on Soil Mechanics and Geotechnical Engineering, Seoul, Vol.1, Balkema, pp.149-152.

71) Yet, N. S., Leung, C. F. and Lee, F. H. (1996) : "Post-installation behavior of pile," Twelfth Southeast Asian Geotechnical Conference, Kuala Lumpur, Vol.1, pp.429-434.

72) Yoshida, T.(1995) : "Strain localization and shear banding during failure of sands," Doctoral thesis, University of Tokyo (in Japanese).

73) Yokoyama, Y., Ueno, K. and Mizunuma, T. (1995) : "Subsidence of underground quarries in Ohya district, Japan," Proceedings of the Fifth International Symposium on Land Subsidence, The Hague, pp.225-236.

## Acknowledgements

The present study was carried out under the guidance of Prof. Osamu Kusakabe of Tokyo Institute of Technology (TIT) from April 1998 to March 2001. I would like to express my sincere gratitude to Professor Osamu Kusakabe for his kind advice, constant encouragement and guidance during the course of my study.

I would like to acknowledge Professor Hideki Ohta, Professor Jun-ichiro Niwa, Associate Professor Jiro Takemura and Associate Professor Jiro Kuwano, all of TIT for their participation in the examination of this dissertation and for their advice and fruitful comments.

I am very thankful to Dr. Masayuki Kohda formerly Research Associate of TIT and now connected with the Railway Technical Research Institute. I am also grateful to the following research associates of TIT : Mr. Akihiro Takahashi, Dr. Ichizo Kobayashi and Dr. Shin-ichi Miyazato, for their kind support in the conduct of my experiments and analyses and to my student life at TIT.

To Dr. Takayuki Hattori (Pacific Consultants Co., Ltd.) and Dr. Mircea Mihai Galer (formerly Doctoral student of Hiroshima University), I extend my grateful appreciation for their permission to use the plate loading test data for this study. To Dr. Katsutoshi Ueno (Lecturer of Tokushima University), I am grateful for his advice about the treatment of Ohya stone. To Dr. Hitoshi Nakase (Tokyo Electric Power Co., Ltd.), I am thankful for his fruitful comments about the DEM analyses in this study.

I wish to acknowledge the assistance of Mr. Tomonobu Yoneima, Toa Corporation (formerly graduate student of TIT), and Mr. Taketo Hayashi, and Mr. Takuro Yamakawa, graduate students of TIT, for their help in carrying out the laboratory tests. I also wish to thank all members of Kusakabe laboratory for their kind support.

I acknowledge the financial support provided by the Ministry of Education, Science and Culture (Monbusho, No.12650488), Japan.

I am very much thankful to Technical Research Institute of Nishimatsu Construction Co., Ltd. for providing me the financial support to pursue this study. I wish to acknowledge Dr. Kazuo Kurihara (adviser of Nishimatsu Construction Co., Ltd., formerly General Manager of Technical Research Institute of Nishimatsu Construction Co., Ltd.), Dr. Takeshi Hosoi (General Manager, Technical Research Institute of Nishimatsu Construction Co., Ltd.) and Dr. Toshi Nomoto (Deputy General Manager, ditto) for giving me the chance to start and complete this study. I wish to express my thanks to Mr. Kenji Saito (Director of Geotechnical group, Technical Research Institute of Nishimatsu Construction Co., Ltd.) and to Mr. Keiichi Miyazaki (Manager of Geotecnical group, ditto) for their consideration to lighten my work load for me to be able to concentrate on this study. It is a pleasure to acknowledge the encouragement of the members of the Geotechnical group of Technical Research Institute of Nishimatsu Construction Co., Ltd..

I would like to express my sincere appreciation to Professor Tatsunori Matsumoto of Kanazawa University, who was my master's thesis advisor, for giving me a recommendation to Tokyo Institute of Technology and for his fruitful discussion about this study and continuous encouragement.

Finally, I express my gratitude to my wife Michiko, my sons Kohei and Shingo, my brother Yoshihiko, my parents and my wife's parents for their hearty support and kind encouragement.

March, 2001

武井正孝

Masataka Takei